UCC

University College Cork, Ireland
Coláiste na hOllscoile Corcaigh

Airborne ultrasonic communications using multiple parallel channels

Wentao Jiang

MSc

Thesis submitted for the degree of
Doctor of Philosophy
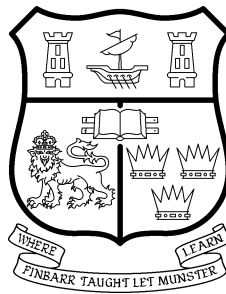
NATIONAL UNIVERSITY OF IRELAND, CORK

SCHOOL OF ENGINEERING
DEPARTMENT OF ELECTRICAL AND ELECTRONIC ENGINEERING

December 2016

Head of Department: Prof. William P. Marnane

Supervisor: Dr. William M. D. Wright

Contents

List of Figures

x

List of Tables

List of Acronyms

ADC	Analogue-to-Digital Converter
ADLS	Asymmetric Digital Subscriber Line
AOA	Angle-Of-Arrival
ASK	Amplitude-Shift Keying
AWGN	Additive White Guassian Noise
BER	Bit Error Rate
BFSK	Binary Frequency-Shift Keying
BPSK	Binary Phase-Shift Keying
CDMA	Code Division Multiple Access
CMUT	Capacitive Micromachined Ultrasonic Transducer
CP	Cyclic Prefix
CRC	Cyclic Redundancy Check
DAC	Digital-to-Analogue Converter
FDM	Frequency Division Multiplexing
FFT	Fast Fourier Transform
FSK	Frequency-Shift Keying
GI	Guard Interval
GPS	Global Positioning System
HCI	Human-Computer Interaction
ICI	Inter-Carrier Interference
IFFT	Inverse Fast Fourier Transform
IR	InfraRed
ISI	Inter-Symbol Interference

LED	Light-Emitting Diode
LFM	Linear Frequency Modulation
LFSR	Linear Feedback Shift Register
LOS	Line-Of-Sight
ML	Maximum Likelihood
NDE	Non-Destructive Evaluation
NDT	Non-Destructive Testing
NLOS	Non Line-Of-Sight
OEM	Original Equipment Manufacturer
OFDM	Orthogonal Frequency Division Multiplexing
OOK	On-Off Keying
PAPR	Peak-to-Average Power Ratio
QAM	Quadrature Amplitude Modulation
QPSK	Quadrature Phase-Shift Keying
RF	Radio Frequency
RSS	Received Signal Strength
SNR	Signal-to-Noise Ratio
SONAR	SOund Navigation And Ranging
STO	Symbol Timing Offset
TOA	Time-Of-Arrival
TOF	Time-Of-Flight
WHO	World Health Organization
WLAN	Wireless Local Area Network
XOR	eXclusive-OR

I, Wentao Jiang, certify that this thesis is my own work and has not been submitted for another degree at University College Cork or elsewhere.

_____

Wentao Jiang

Acknowledgements

I would first like to thank my supervisor, Dr. Bill Wright, for his insightful guidance and endless encouragement throughout my research. Without his support and patience, this thesis would never have been completed.

I would also like to thank the technical staff in the Control and Power Laboratory, Hilary Mansfield and James Griffiths, for giving their assistance on making the peripheral circuitry and cabling of the ultrasonic transducers, Michael O'Shea and Timothy Power in the Mechanical Workshop, for manufacturing the casings used in construction of transducers and building the metal frame for the ceiling-mounted base stations. Special thanks go to Peter Flynn in UCC IT Services unit who has continuously supported me for editing this thesis using LaTeX.

I would like to thank Dr. Guangbo Hao in Mechanical Engineering of UCC for sharing his knowledge and experience in academic researches. Thanks are also due to Alison, Brian, Dave, Haiyang, James, Megan, Oksana and Rehan, fellow PhD students in the post-graduate room, for their companionship and helpful suggestions in both work and life. Additional thanks to all my Chinese friends, Ao Xia, Qiulin Liu, Xiaolin Chen and Zichuan Fan, who previously did their researches in UCC, for providing inspiration and assistance during my PhD study. Finally, I would like to thank my parents for their endless love, support and understanding, and to members in UCC mountaineering club and photography society for allowing me to get away from work occasionally.

Abstract

Concerns still exist over the safety of prolonged exposure to radio frequency (RF) wireless transmissions and there are also potential data security issues due to remote signal interception. Airborne ultrasound may be used as an alternative to RF for indoor wireless communication systems for securely transmitting data at short ranges. This thesis describes the design and evaluation of an airborne ultrasonic communication system using capacitive transducers.

Most ultrasonic data communication systems developed in the past have looked at single-channel modulations, achieving relatively low bandwidth efficiency. In this study, basic digital modulation schemes, such as ON-OFF keying (OOK) and binary phase-shift keying (BPSK), were implemented successfully over multiple parallel channels over an air gap of up to 10 m with wireless synchronization using ultrasonic means. A simulation model that can precisely predict ultrasonic signals through the air channel was also created to help with signal characterisation. Error free decoding was achieved over ranges up to 5 m using multichannel OOK with a data transfer rate of 60 kb/s. This range could be extended up to 10 m using BPSK with a reduced rate of 30 kb/s. To further improve the bandwidth utilisation and eliminate the need for filtering, quadrature amplitude modulation (QAM) using orthogonal frequency division multiplexing (OFDM) method was investigated. The recorded data rate was 800 kb/s at 0.7 m with no measurable errors using prototype broadband ultrasonic transducers, and 180 kb/s at 6 m using relatively narrowband commercially available transducers. In comparison to the previous systems, this work has achieved improved data rates at both short and long ranges.

Non line-of-sight (LOS) conditions may occur in an indoor environment and the effects of reflection and diffraction on wireless data transmission were studied in this thesis. The experimental results indicate that modulations with low-

order format at low frequency channels are more robust in terms of system bit error rate through a non-LOS path. Full-duplex communication using both separated and interleaved channel allocations for forward and reverse links were investigated. By using 16QAM-OFDM with recently obtained SensComp transducers, the achieved data rates at 5 m were 40 kb/s and 20 kb/s, respectively.

This thesis has also looked at implementing an indoor communication network with ceiling-mounted base stations and a mobile communicator for practical applications. An asynchronous ultrasonic location technique using Gold Code modulated ranging signals was chosen to optimise the modulation schemes, and offer automatic handover between different cell regions on a switch on and off basis as all base stations use the same frequency bands for data transmission. Within a circular range of 0.15 m, 16QAM-OFDM can be used to achieve a higher uplink data transfer rate of 37.4 kb/s while the range can be extended up to 0.35 m by using QPSK-OFDM with a data rate of 18.7 kb/s. For the uplink connection, the achieved data rates using 16QAM-OFDM and QPSK-OFDM are 36.1 kb/s and 18.1 kb/s, respectively. A more robust handover technique using received signal strength with hysteresis was also proposed to improve system efficiency when multiple mobile users subscribed to the service.

Chapter 1

Introduction

1.1 Introduction

Sound is a mechanical vibration that moves as a pressure wave through solids, liquids and gases. In physiology and psychology, the term sound refers to the auditory sensation produced by the human ear due to the perception of the vibrations [1]. Sound is also used by most species in the animal kingdom for detecting danger, navigation, predation and communication. The frequency of vibration of the sound, f, is related to the velocity of the wave in the medium, c, and the wavelength of the oscillation, λ, expressed by the well-known formula

$$f = \frac{c}{\lambda}. \tag{1.1}$$

The frequency f is measured in Hertz (Hz), where 1 Hz = 1 cycle per second. If this frequency is within the approximate range 20 Hz to 20 kHz, the sound is audible; above 20 kHz, the sound waves are referred to as ultrasound; beneath 20 Hz, they are called infrasound which usually occur naturally in earthquakes, ocean waves, volcanoes, etc. Though ultrasound is beyond the range of human hearing, it is especially useful for animals like bats [2], which live in dark caves and need to locate prey and obstacles at night, and porpoises [3], which use ultrasound to detect the position and speed of objects in turbid water. Ultrasound

has also been used extensively in the medical profession [4], for diagnosis, imaging and therapeutic applications, and in engineering applications such as flaw detection [5], dimensional measurements [6] and material characterization [7].

This introductory chapter begins with a brief history of ultrasonics. This is followed by the basic properties of ultrasonic waves such as propagation mechanisms through a medium, atmospheric absorption and diffraction from a source transducer. Air-coupled ultrasonic transducers will be introduced, and the use of ultrasound in wireless communications in air will also be discussed. An overview of the remaining chapters of this thesis will then be given in the final section.

1.2   A brief history of ultrasound

Long before the use of ultrasound in modern science, the stage was set with the investigation of sound. As early as 1826, Jean-Daniel Colladon, a Swiss physicist, and his assistant Jacques-Charles-François Sturm, a mathematician, measured the speed of sound in the fresh water of Lake Geneva in Switzerland [8]. In their experiment, an underwater bell was struck simultaneously with ignition of gunpowder on one boat, while the sound of the bell and the flash from the gunpowder were observed in another boat 13 km away. By measuring the time interval between these two events, the reported speed of sound in water at 8 °C was 1435 m/s, compared with the presently accepted value of about 1439 m/s [9]. Many years later, in 1877, Lord Rayleigh published his famous book *The theory of sound* [10], which became the foundation for the science of ultrasound.

In 1880, French physicists Pierre and Jacques Curie discovered the piezo-electric effect [11]. The Curie brothers observed when pressure was applied to

a quartz crystal, an electric charge will appear on its faces. This charge was directly proportional to the force applied to it. Conversely, vibration of the crystal was measured if it was placed in an alternating electric field. The phenomenon was named "piezoelectricity" as the word "piezo" means "to press" in Greek. Unfortunately, due to the underdeveloped status of electronics during that time, the importance of this discovery in ultrasound generation was not realised until more than 30 years later, in 1912, after the sinking of Titanic. The research of underwater object detection was extensively developed. Together with the outbreak of World War I, the use of this technology was focused on underwater signalling and navigation for the purpose of detecting submarines. By 1917, a powerful high frequency ultrasonic SONAR (SOund Navigation And Ranging) system [12] was developed by Pierre Curie's doctoral student Paul Langevin and a Russian scientist Constantin Chilowsky. This technique was further improved in classified research activities during World War II and finally became acceptably practical.

In 1928, the concept of ultrasonic metal flaw detection was first suggested by Soviet Physicist Sergei Sokolov at the Electrotechnical Institute of Leningrad [13]. He showed that by observing the variations in ultrasonic energy transmitted across the metal, the hidden flaws inside the metal can then be detected. Over the following two decades, a number of systems were developed for this task. One of the early pioneers of such reflective metal flaw detecting devices was Floyd Firestone at the University of Michigan [14]. Since 1941, the devices were manufactured by Sperry Inc. to detect the flaws in metal for industrial purposes [15]. The same principle was employed by Josef and Herbert Krautkrämer who produced their first German version pulse-echo metal flaw detector in Cologne in 1949 [16], followed by equipment from Karl Deutsch in Wuppertal [17]. The technique is now known as non-destructive evaluation (NDE) or non-destructive testing (NDT).

The use of ultrasound in the field of medicine through the 1930s was initially confined to therapeutic applications such as cancer treatments and physical therapy for various ailments, utilising its heating and disruptive effects on animal tissues [18]. In 1942, Karl Dussik, a Neurologist and Psychiatrist at University of Vienna, was generally regarded as the first person attempted to locate brain tumours by measuring the transmission of ultrasound beams through the skull [19]. Later in 1949, George Ludwig and Francis Struthers, working at the Naval Medical Research Institute in Bethesda, Maryland, investigated the use of reflective pulse-echo ultrasound methodology on detecting gallstones and foreign bodies in animal tissues [20]. Since the 1940s, Douglass Howry, at the University of Colorado, and Joseph Holmes, a nephrologist at the Veteran's Administration Hospital in Denver, had started pioneering ultrasonic research on the development of B-mode (brightness-mode) equipment, visualising soft tissue structure in the body in a 2-dimensional and sectional manner [21]. The 1960s and 1970s, saw the introduction of linear and phased-array transducers into commercial instruments, further improve the ultrasound images and expand the use of the ultrasonic technology.

Up until now, piezoelectric transducers are still most commonly used for the generation and detection of ultrasound in solids, however, usually with expensive couplant gels or using immersion tanks, which could be impractical in some cases. Since the 1990s, there are an increased number of researches that have focused on building high sensitivity, broadband transducers for air-coupled applications. Compared with piezoelectric transducers, capacitive (or electrostatic) transducers have improved impedance matching to air, and were found to be a good alternative for the use of non-contact inspection methods. Recently, the use of airborne ultrasound for wireless communication and positioning has been proposed by several authors [22–25] due to its high security features (this is discussed further in Section 1.5). The study of a secure commu-

nications network using modulated ultrasound in air is the focus of this thesis. Therefore, the basic properties of ultrasound relevant to the work in this thesis will be covered in the next section.

1.3 Basic properties of ultrasound

1.3.1 The propagation of ultrasound through a medium

An ultrasonic wave is the propagation of a mechanical vibration through a medium at frequencies above human hearing. If the particles of the material move in the same direction as the propagation of the wave, the resulting wave is called a longitudinal or compressional wave as shown schematically in Fig. 1.1. Such waves may exist in solids, liquids or gases. If the motion of the material particles is perpendicular to the direction of the wave as shown in Fig. 1.2, such waves are known as transverse or shear waves. Shear waves only exist in solids or a very few viscous liquids that can support shear stresses. The velocity of an ultrasonic wave through a medium varies with the physical properties of the medium. In low-density materials such as gases, particles may move relatively large distances before they influence neighbouring particles. In these media, the velocity of an ultrasonic wave is relatively low. While in solids, particles are constrained in their motions, and the velocity of ultrasound is relatively high.

The velocity of longitudinal waves through a medium can be calculated from the bulk modulus, B, and the mass density of the medium, ρ, as [26]

$$c = \sqrt{\frac{B}{\rho}}. \qquad (1.2)$$

The velocity of sound in air is dependent on humidity, frequency, temperature and pressure [27–29]. However, for an approximate calculation, the effects of humidity, frequency and pressure can be neglected, and the velocity is mainly

5
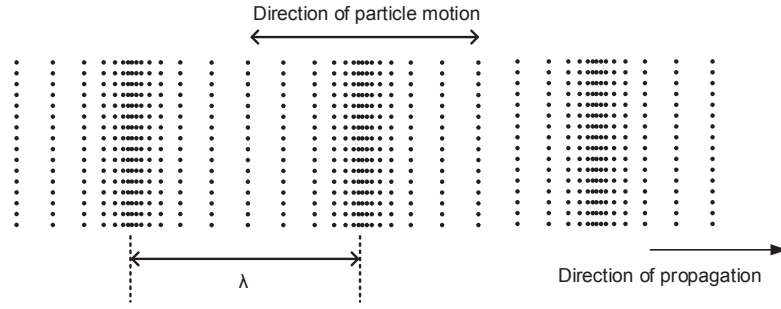
Figure 1.1: Particle motion for a compressional wave.
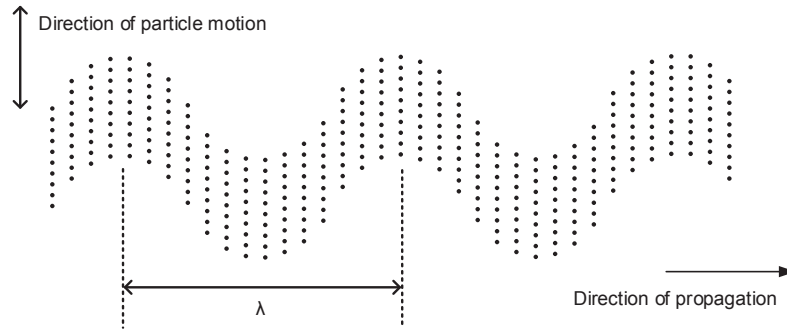
Figure 1.2: Particle motion for a shear wave.

dependent on temperature according to the equation [30]

$$c = 331.31\sqrt{T/273.16}, \tag{1.3}$$

in m/s, where T is the air temperature in Kelvin. Therefore, at 20 °C (293.15 K), the velocity of sound is approximately 343.2 m/s.

Besides compression and shear waves, various different types of waves can also be produced in solids. Surface waves or Rayleigh waves can be generated when particle movement is elliptical and such waves exist only in the surface of solids to a depth of about a wavelength [31]. Lamb waves can exist in plate material, containing a component of oscillation at right angles to the surface [32]. Other complex waves which occur between the interfaces of materials are Stoneley waves [33] and Love waves [34], and as they are not required for this thesis will not be described further.

6

1.3.2 Ultrasonic absorption in air

The propagation of ultrasonic waves through air is not lossless due to effects such as internal friction and thermal conductivity. This results in the loss of oscillation energy accompanied by an increase in temperature of the air. The sound pressure decays exponentially with propagation distance, d, due to absorption attenuation, and for plane waves it can be calculated as [31]

$$p = p_0 e^{-\alpha d}, \tag{1.4}$$

where p is the sound pressure at a distance d from an initial pressure p_0, and α is taken as the sound attenuation coefficient in Np/m. Note that 1 Np = $20/ln10$ dB ≈ 8.686 dB.

Accurate calculation of this absorption can be difficult as the air is a variable mixture of gases [35]. However, only two mechanisms are assumed to be important in atmospheric absorption. The first one is known as classical loss associated with the transfer of the kinetic energy of the molecules into heat, while the second one is called relaxation loss which is caused when the translational energy of the molecules is absorbed into the gas molecules themselves. The classical absorption due to viscous and thermal conduction losses at a particular frequency f, is a function of temperature and pressure, according to [35]

$$\alpha_{cl} = 4.85 \times 10^{-8} \frac{T/T_0}{T + 110.4} f^2 / (P/P_0), \tag{1.5}$$

in dB/m, where T is the measured temperature (in K) and T_0 is the standard atmospheric temperature (293.15 K). P and P_0 are the measured atmospheric pressure and the standard pressure (101.325 kPa), respectively. The two main forms of loss that contribute to the relaxation loss are the rotational relaxation loss and vibrational relaxation loss. Rotational relaxation loss is also a function of frequency, temperature and pressure. Therefore, rotational absorption can

be combined with classical absorption as α_{cr}:

$$\alpha_{cr} = 1.59 \times 10^{-10} \frac{(T/T_0)^{1/2} f^2}{P/P_0}, \tag{1.6}$$

in dB/m. Vibrational loss depends on the particular atmospheric constituent and the per cent mole fraction of water vapour as well as frequency, temperature and pressure [36]. The composition of air can be seen as a mixture of four normal atmospheric constituents: nitrogen (N_2), oxygen (O_2), carbon dioxide (CO_2) and water vapour (H_2O). The studies in [35] discovered that during vibrational energy-transfer processes, all the reactions including CO_2 can be ignored without affecting the results. Therefore, only the absorption associated with the relaxation of vibrationally excited oxygen and nitrogen molecules, and their interaction with water vapour are considered. The vibrational attenuation constant can be divided into two separate formulas

$$\alpha_{vib,O} = 1.11 \times 10^{-1} (T_0/T)^{5/2} \frac{e^{-2239.1/T}}{f_{r,O} + f^2/f_{r,O}} f^2, \tag{1.7}$$

and

$$\alpha_{vib,N} = 9.29 \times 10^{-1} \frac{e^{-3352/T}}{f_{r,N} + f^2/f_{r,N}} f^2, \tag{1.8}$$

in dB/m, where

$$f_{r,O} = (P/P_0)(24 + 4.41 \times 10^4 h \frac{0.05 + h}{0.391 + h}), \tag{1.9}$$

$$f_{r,N} = (P/P_0)(T/T_0)^{-1/2} \{9 + 350h e^{-6.142[(T/T_0)^{-1/3} - 1]}\}. \tag{1.10}$$

Here $f_{r,O}$ and $f_{r,N}$ are scaled relaxation frequencies for oxygen and nitrogen in Hertz, and h is the absolute humidity which is calculated as

$$h = h_r(P_{sat}/P), \tag{1.11}$$

in percent, where h_r is the relative humidity for a given sample of moist air under pressure P and at a temperature T, and P_{sat} is the saturation vapour pressure of pure water at the same temperature T. The total absorption coefficient, α, can then be expressed as

$$\alpha = \alpha_{cr} + \alpha_{vib,O} + \alpha_{vib,N}. \tag{1.12}$$
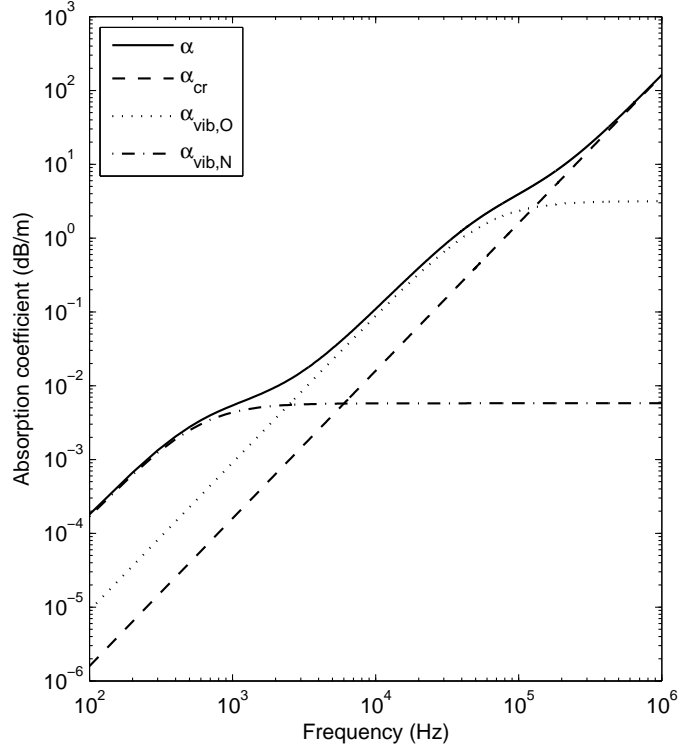
Figure 1.3: Absorption coefficient for sound propagation in air as a function of frequency.

According to (1.12), the absorption coefficient for sound propagation in air, α, can be estimated as plotted in Fig. 1.3. Note that the factors which contribute to the absorption coefficient in the simulation were set at $P = P_0 = 1$ atm, $T = T_0 = 293.15$ K (20°C), and $h_r = 70\%$. It can be seen from Fig. 1.3, the
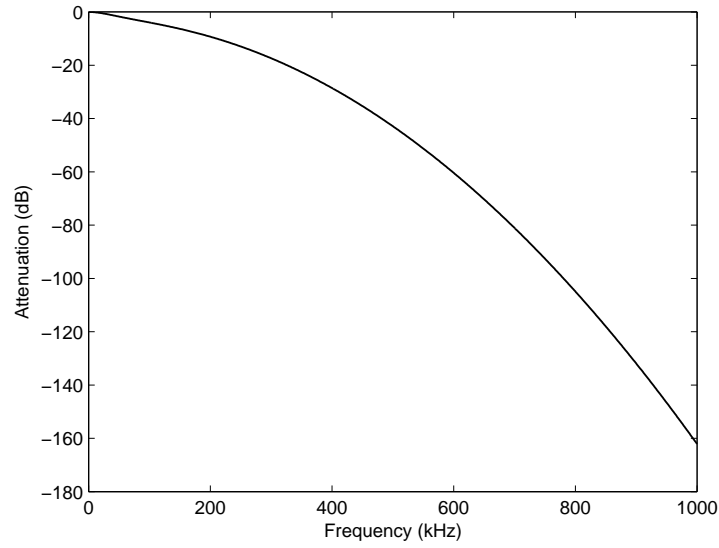
Figure 1.4: Total absorption attenuation of sound transmitted through an air gap of 1 m as a function of frequency at 1 atm, 20°C and 70% relative humidity.

classical-plus-rotational absorption coefficient, α_{cr}, is proportional to the sound frequency, and it becomes a dominant contribution to overall absorption, α, when the frequency is in excess of 300 kHz. Therefore, vibrational absorption can be neglected at higher frequencies where the air humidity has no effect on the total absorption. Fig. 1.4 shows a attenuation curve of sound at different frequencies from 0 to 1 MHz transmitted through an air gap of 1 m. As can be seen, the air has a low-pass filtering effect on sound signals, and the attenuation drops below -160 dB when the sound frequency is 1 MHz at 1 m. It indicates that for an effective ultrasonic transmission in air the upper frequencies are limited to around 1 MHz due to excessive atmospheric absorption.

1.3.3 Diffraction effects

It is important to understand how the wave motion propagates as a sound field. If a plane wave travels through an aperture in a screen as shown in Fig. 1.5, the sound field is changed due to diffraction effects. According to Huygens' principle, the annular waves caused by the edge effects, on superposition upon
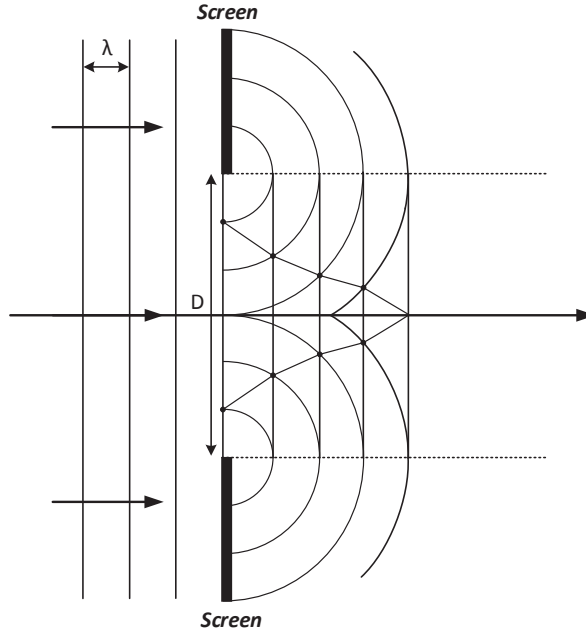
Figure 1.5: Interference structure of sound field according to Huygens' principle.

the plane waves, produce a field of maxima and minima of the sound pressure due to constructive and destructive interference. As can be seen from Fig. 1.5, in instantaneous exposures of the sound field, the maxima travel with the wave along the dotted curves towards the axis. The position of the last pressure maxima on the axis at a distance N from the source, depends on the values of the aperture opening D and wavelength λ can be described in the following relationship [37]

$$N = \frac{D^2 - \lambda^2}{4\lambda}.$$ (1.13)

The field beyond N is known as the far field or 'Fraunhöfer region', and the one between the source and the last maxima is called the near field. N is therefore named as the near-field length. The variation of the sound pressure along the axis at a distance z is given by

$$p = p_0 2 sin\left(\frac{\pi}{\lambda}[\sqrt{(D/2)^2 + z^2} - z]\right),$$ (1.14)

where p_0 is the sound pressure at a distance of $z = 0$. Fig. 1.6 gives an illustrative example of the sound pressure along the axis of a 10 mm, 300 kHz ultrasonic transmitter. According to (1.13), the calculated near-field length N here is 21.6 mm. As can be seen, after a series of pressure variations, the sound pressure gradually drops from its last maxima towards to zero with the increase of distance z on the axis.
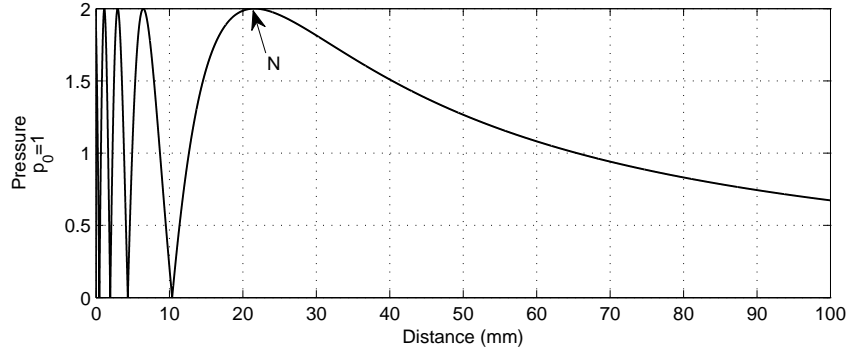
Figure 1.6: Sound pressure p on the axis of a 10 mm, 300 kHz piston source in air.

It is important to note that the maximum sound pressure is always found along the axis in the far-field. The sound pressure field outside the central axis with an angle γ at a distance z can be calculated by the formula [37]

$$p = 2p_z \frac{J_1(X)}{X},\tag{1.15}$$

where $X = \pi(D/\lambda)sin\gamma$. Here $J_1(X)$ represents the first-order Bessel function and p_z is the pressure on the axis at z where $J_1(X)/X = 1$. Therefore, the theoretical far-field sound pressure curve as a function of the angle γ can be plotted as shown in Fig. 1.7. Note the value of D/λ is 8.75, the same parameter settings as used in Fig. 1.6. The radiation pattern shows a steep decay of the sound pressure with the increase of the angle γ at both sides of the source. For this special case when $D/\lambda = 8.75$, the first zero point occurs at $\gamma = 8°$, and this is called the angle of divergence, γ_0. Based on a plane piston ultrasonic source,

the profile of the emitted sound beam can be illustrated diagrammatically in Fig. 1.8, showing the divergence angle γ. Since $X = 3.83$ is the first root of the first-order Bessel function, the angle γ to the first nulls of the radiation pattern can then be calculated as

$$sin\gamma_0 = \frac{3.83\lambda}{\pi D} \approx 1.22(\lambda/D), \tag{1.16}$$
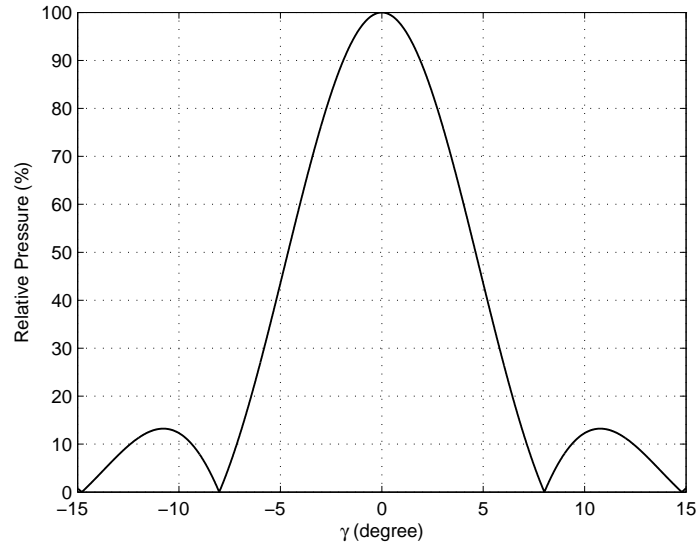
Figure 1.7: Relative sound pressure in the far-field as a function of divergence angle γ for $D/\lambda = 8.75$.

Note this equation is only valid for $\lambda \ll D$ and thus becomes increasingly inaccurate with low frequency signals using small diameter ultrasonic sources [31]. It is more intuitive to display the sound pressure field as a function of radial distance as illustrated in Fig. 1.9. As compared in Fig. 1.9 (a) and (b), the angular characteristics show that a high frequency sound will have a more directional beam while a low frequency sound with larger wavelength will have a more diverged beam.

For the theoretical prediction of the ultrasonic radiation field in front of a plane piston, an impulse response method [38, 39] can be used to efficiently calculate the pressure field. The mathematical model assumes that the pres-
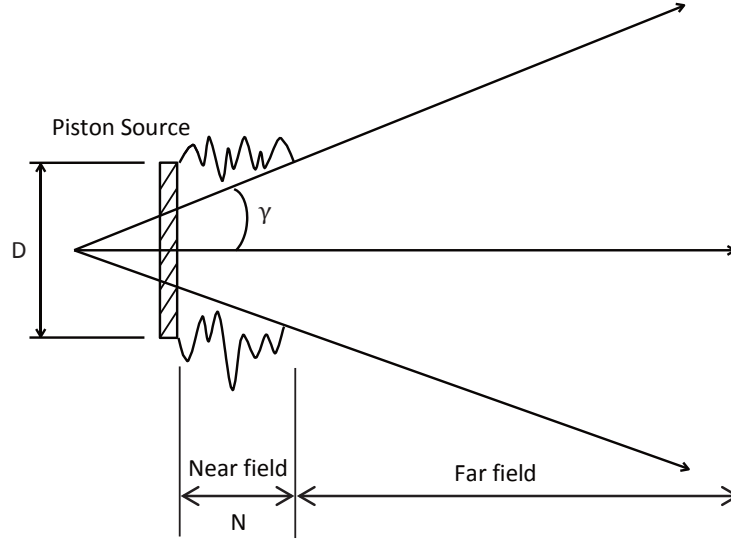
Figure 1.8: Schematic diagram of the sound field of a piston source.
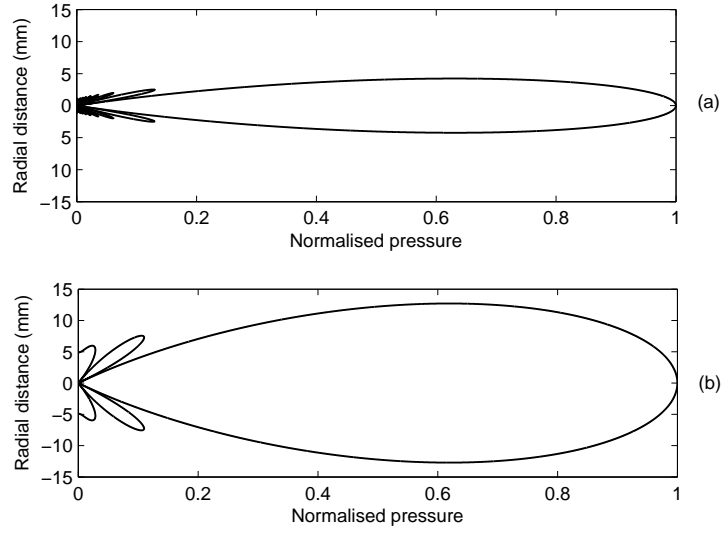
Figure 1.9: Sound pressure fields in air as a function of radial distance with different sound frequencies: (a) $f = 300$ kHz and $D/\lambda = 8.75$, (b) $f = 100$ kHz and $D/\lambda = 2.92$.

sure at the observation point M as shown in Fig. 1.10 can be computed from the interference of the plane wave from the source, and edge waves which are diffracted at the boundaries of the source [40, 41]. The velocity potential impulse response $\Phi(M, t)$ can be written as
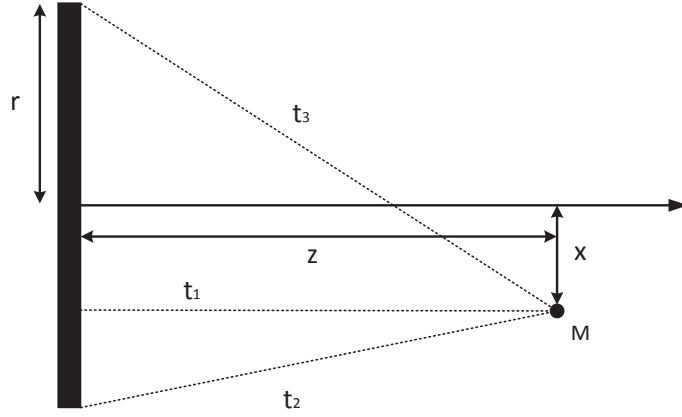
Figure 1.10: Location of an observation point M, showing transit times of plane and edge waves.

$$\Phi(M,t) = c|A|H(t - t_1) + (\frac{c}{2\pi})\cos^{-1}\{\frac{(ct)^2 - z^2 + x^2 - r^2}{2x[(ct)^2 - z^2]^{1/2}}\}H(t - t_2)H(t_3 - t),$$

(1.17)

where

$$t_1 = z/c,$$

(1.18)

$$t_2 = [(r - x)^2 + z^2]^{1/2}/c,$$

(1.19)

$$t_3 = [(r + x)^2 + z^2]^{1/2}/c.$$

(1.20)

Here c is the wave velocity within the medium, t is time, and H is the Heaviside step function, which is defined as unity for $t > 0$ and zero for all other cases. r represents the transducer radius, x and z are the radial and axial distances respectively. The value of $|A|$ depends on the field position. For M opposite the front face the value is 1. If $x = r$, the value drops to 0.5, and $|A|$ is zero at greater radial distances when $x > r$. The pressure impulse response $p(M, t)$

15

for an arbitrary point M is defined as the differential of the velocity potential impulse response:

$$p(M,t) = \rho_0(\delta\Phi/\delta t)(M,t), \qquad (1.21)$$

where ρ_0 is the density of the medium. Equation (1.21) is only valid for values when $t_1 \leq t \leq t_3$; elsewhere $p(M,t) = 0$. Fig. 1.11 shows the predicted radiated beam profile for a 10 mm diameter piston source driven by a 300 kHz ultrasonic signal. As can be seen, the theoretical pressure field plot is divided into two distinct regions. A series of maxima and minima which occurred by constructive and destructive interference is found in the near field region. In the far field region, the pressure decays gradually from a maximum to zero along the axis. It can also be found that the beam is diverged in the radial axis, consisting of a strong central lobe and numerous side lobes.
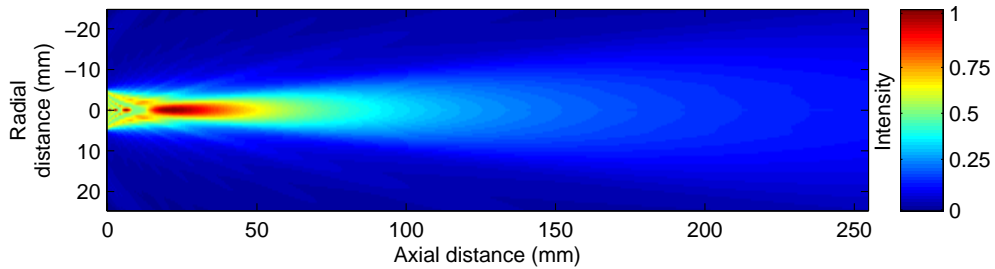
Figure 1.11: Theoretical prediction of sound field for a 10 mm diameter piston source driven by a 300 kHz ultrasonic signal using impulse response method. Note that the colour scale is normalised intensity.

1.4 Ultrasonic transducers

A transducer is any device that converts one form of energy into another. An ultrasonic transducer converts electrical energy into mechanical energy, in the form of ultrasound, and vice versa. A well-designed ultrasonic transducer with good sensitivity, sufficient bandwidth, and effective operational range in air

is an essential requirement for air-coupled ultrasonic communication systems. There are several types of devices to generate and detect ultrasonic waves in air. Two of the most popular ones are piezoelectric and capacitive (or electrostatic) transducers.

1.4.1 Piezoelectric transducers

Piezoelectric transducers are the most widely used devices for ultrasonic transduction. This is mainly because the transducers are generally low-cost, highly effective, and thus well suited to an industrial environment. They have been successfully developed for the use in the area of NDE [37]. However, the main problem with conventional ultrasonic methods is the need for a liquid or gelatinous couplant between the transducer and the test material [42]. For instance, the use of the ultrasonic water immersion method will cause permanent damage to some test objects such as wood products, explosives, art objects, and certain electronic-packaging materials. In addition, water is not compatible with some industrial manufacturing processes, and may bring inconvenience especially in the aerospace industry [43].

For air-coupled applications, the energy conversion efficiency of piezoelectric devices is very low due to the large acoustic impedance mismatch that occurs at the boundary between the transducer and air. Generally, when an ultrasonic wave is incident on a plane boundary between two media, some ultrasonic energy will be reflected, and some will be transmitted or refracted through the interface [31]. The quantities of transmitted and reflected energy are dependent on the specific acoustic impedance Z of a medium, which is the product of the density ρ of the medium and the acoustic velocity c in the medium:

$$Z = \rho c.$$ (1.22)

17

The transmission coefficient, T, is given by

$$T = \frac{4Z_1 Z_2}{(Z_1 + Z_2)^2}, \tag{1.23}$$

and the reflection coefficient, R, by

$$R = \left(\frac{Z_1 - Z_2}{Z_1 + Z_2} \right)^2, \tag{1.24}$$

where Z_1 and Z_2 are the acoustic impedances of the two media. From (1.24), it is obvious that a large difference in the values of Z_1 and Z_2 results in a large reflection coefficient, and thus a small transmission coefficient. The basic approach to design an air-coupled piezoelectric transducer is to attach an impedance matching layer to the front of the device, therefore partially mitigating the impedance mismatch between the air and piezoelectric element [44]. This layer should have an acoustic impedance between that of air and the piezoelectric, with an optimum value of Z_L, given by

$$Z_L = \sqrt{Z_1 Z_2}. \tag{1.25}$$

To maximise the energy transfer, a matching layer of thickness equal to a quarter wavelength at the centre frequency is required [18], and this reduces the overall bandwidth of the device. A wide set of different materials such as epoxy resin [44], silicon rubber [45], aerogel [46], balsa wood [46, 47], and piezopolymer foil [48–51] have been selected. The transducer sensitivity can be improved by a single matching layer, but multiple matching layers are needed to widen the frequency bandwidth at the expense of signal intensity [52]. Another approach to reduce the impedance mismatch between the piezoelectric and air is to use micromachined 1-3 piezocomposite ceramic elements [53]. Though improved sensitivity and bandwidth were found from the proposed solution, the complexity of the manufacturing process is still a major concern for wider application.

1.4.2 Capacitive transducers

Capacitive or electrostatic transducers are efficient devices for the transduction of ultrasound in air. The devices are essentially a parallel-plate capacitor with a thin flexible membrane fixed over a rigid immovable conducting backplate. They are similar in form to a condenser microphone that the motion of the membrane serves to change the capacitance which results in a change in the electrical potential [26]. The first condenser microphone used as an acoustic detector dates back as early as 1917 [54]. However, the use of capacitive transducers for airborne ultrasonics is reported in the 1950s [55]. The construction of the transducer consists of a very thin flexible metallised polymer membrane and a conducting contoured backplate, allowing the frequency response of the transducers to be increased well into the ultrasonic region, with low acoustic impedance and wide bandwidth. A schematic diagram of the device is shown in Fig. 1.12. As can be seen, one side of the membrane is metallised with a conducting layer as the upper electrode, and the contoured backplate is the lower electrode. A D.C. bias voltage is usually applied between the two electrodes, electrostatically trapping tiny air pockets between the membrane and the backplate. Consequently, the trapped air acts as a natural spring, mak-
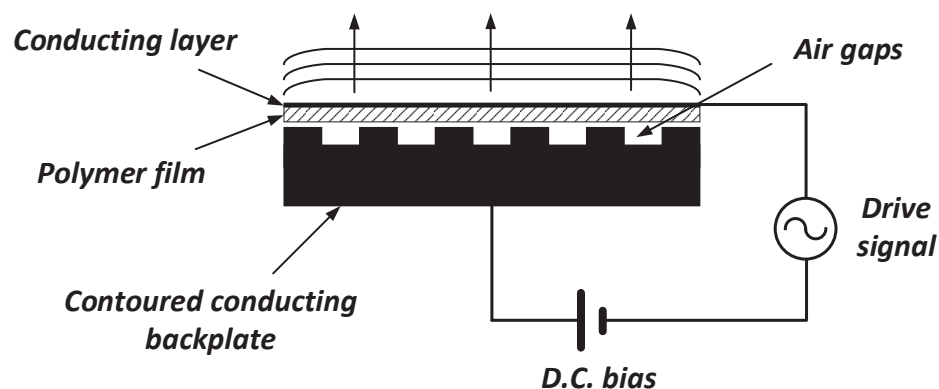
Figure 1.12: Schematic diagram of a capacitive transducer for generation and detection of ultrasound in air.

ing the acoustic impedance of the device more closely matched to that of air. When operating as an ultrasonic transmitter, an alternating voltage driven by the source signal is superimposed over the D.C. bias, causing the charge on the two electrodes to vary. Accordingly, the movement of the metallised polymer film produces longitudinal pressure oscillations in the air, so that an ultrasonic wave is generated with a frequency corresponding to that of the alternating voltage applied to the transducer. Acting as a detector, an ultrasonic wave striking the membrane causes it to vibrate, vary the air gaps behind it and thus the capacitance of the device. The change in capacitance can then be amplified with a charge amplifier.

The behaviour of the capacitive transducer, in terms of centre frequency, bandwidth and sensitivity, is determined by many factors such as the surface profile of the backplate [56, 57], membrane thickness and density [58, 59], and the D.C. bias voltage used [60, 61]. The response of capacitive transducers has been both modelled theoretically and measured experimentally in the past literature [56, 58, 62–65].

The structures of backplates used in the design of ultrasonic capacitive transducers in air can be broadly divided into two categories, those using a roughened or a grooved surface finish. The first assumes that the metal-coated membrane acts as a frictionless piston constrained by an air spring. Therefore, the approximate resonant frequency, f, can be calculated by [56]

$$f = \frac{1}{2\pi}\sqrt{\frac{\gamma P_a}{\rho d_m d_a}}, \qquad (1.26)$$

where γ is the adiabatic constant of air, P_a is the atmospheric pressure, ρ is the density of the membrane, and d_m and d_a are the thickness of the membrane and the air gap, respectively. This model suggests that the resonant behaviour is controlled by the air-gap and membrane thickness. It has been found by several authors [56, 62, 63] that the air-gap model predicts the resonant frequency

20

of the random-backplate transducer reasonably well. However, for randomly roughened backplate transducers, the detailed surface finish varies from one plate to another even produced by the same manufacturing process. Thus, it is difficult to get consistent results from these devices.

Alternatively, grooved backplate transducers which consist of either parallel or circular rails and grooves can be manufactured to fairly precise specifications. As the grooved pattern provides many individual resonant elements, the resonant frequency of the device can be predicted by applying Helmholtz's resonator model [36, 66]

$$f = \frac{c}{\pi}\sqrt{\frac{\rho_0}{2\sigma h}},$$

(1.27)

where c is the speed of sound in air, ρ_0 is the air density, σ is the mass per unit area of the membrane, and h is the depth of the groove. In this model, the groove width is ignored, and experimental results suggest that the tension of the membrane has little effect on the resonant frequency [59, 61].

Various studies have been reported on the characterization of capacitive transducers, but it has been found that the bandwidth and sensitivity of the devices is largely dependent on the backplate geometry. For this reason, new designs of capacitive transducers based on silicon micromachining techniques [67] have been introduced for precise control over the backplate surface features. Another reason for developing micromachined structures is the possibility of integrating transducers and peripheral circuits on the same chip, as the same standard silicon processing is used during fabrication [67–69]. These devices, also known as capacitive micromachined ultrasonic transducers (CMUTs), have been investigated by many authors [60, 70–72] for use in air, and some have developed systems in the field of ultrasound medical imaging [73–75].

It should be noted that piezoelectric ultrasonic transducers are more robust, and require no extra bias voltage compared to capacitive ultrasonic transduc-

ers. However, as the air-pocket/membrane transduction system of a capacitive transducer has a higher coupling efficiency, and more importantly, much wider operating bandwidth compared with that of piezoelectrics [76, 77], only capacitive ultrasonic transducers are used as the transmitters and receivers for the communication systems presented in this thesis.

1.5 Air-coupled ultrasonic communications

The use of modulated ultrasound as a way of communication has existed for many years. Most ultrasonic communication systems have been developed for underwater applications because the physical properties of liquids tend to allow sound waves travelling via molecular vibrations to cover relatively long distances. However, sound propagation in air is more difficult, in that it is much more susceptible to changes in atmospheric conditions and attenuation is significant. As ultrasonic signals do not travel long distances in air, it is not surprising that most ultrasonic communication systems are designed for indoor use [22–24, 78]. This section will give a insight into the field of ultrasonic communications in air including its advantages compared to existing wireless communication methods, a review of air-coupled ultrasonic transmissions and the past literature in the area.

1.5.1 Comparison to existing methods

Radio frequency (RF) waves, or electromagnetic radiation with frequencies ranging from 30 kHz to 300 GHz, have been utilized for wireless communications by civilian or military personnel for decades. Wireless RF connectivity has now become a fundamental part of our daily lives and is being regarded as an essential commodity similar to gas, water and electricity. The most well-known applications of RF wireless communications are, for example, radio broadcast-

ing, Bluetooth, wireless local area network (WLAN), mobile communication and satellite communication [79]. However, the huge success of these technologies makes the RF spectrum overcrowded, and the frequency band is in short supply. It is also strictly regulated to control the performance of and prevent interference from different communication systems [80]. This partly constrains the system flexibility in allocating spectrum resources. In addition, due to the radiative nature of the RF communications, the signals can be easily intercepted remotely [81], therefore limiting their ability to provide a secure system to ensure confidentiality of information. Furthermore, RF methods are inappropriate in some circumstances where communication is required, such as explosive atmospheres in industry, which require intrinsically safe devices. Long term exposure to RF radiation is also considered as a potential threat to public health as the World Health Organization (WHO) classifies the emitting RF electromagnetic fields as a possible human carcinogen [82]. Some countries are also restricting the use of RF, for example, in 2015, the Assemblée Nationale in France passed a bill prohibiting the installation of Wi-Fi equipment in areas dedicated to the activities of children under 3 years of age [83].

Infrared (IR) light is invisible electromagnetic radiation with a spectrum between microwaves (300 GHz) and visible light (400 THz) [84]. Wireless infrared communication uses a light-emitting diode (LED) to transmit a signal as bursts of non-visible light, and receives the light pulses using a photodiode or photodetector before retrieving the information they contain [85]. Compared with RF technology, IR transmissions are virtually unregulated, and the high directionality of the beam makes the system relatively immunity to multipath interferences. In addition, like visible light, infrared radiation does not pass through solid barriers, so that infrared signals are confined to an indoor environment, preventing malicious interventions such as eavesdropping and jamming. Though IR method can provide more secure data transmission, line-of-

sight (LOS) connection is necessary. Its output power is also limited due to eye safety regulations [86]. Besides, direct sunlight or some artificial-light sources like tungsten and fluorescent lamps may contribute to high levels of shot noise in a photodetector which degrades the performance of IR transmissions [87].

Ultrasonic communications in air have several advantages over conventional RF- and IR-based solutions. Unlike RF communications, ultrasonic transmissions can be implemented by simple and inexpensive means at unregulated frequency bands, and in an interference-free manner in circumstances where radio emission is restricted. On the other hand, ultrasonic signals in air are difficult to intercept through solid barriers as ultrasonic waves are not as penetrating as radio waves. Thus, ultrasound and IR technology share the same advantage that allows the establishment of more secure communication links. However, ultrasonic transmissions are more immune to environmental electromagnetic noise sources, and they are not limited to LOS operation. The medical experience of therapeutic and diagnostic ultrasound in the last few decades has shown that the use of ultrasound is relatively harmless, as long as the overall acoustic output intensity is limited to safe levels, preventing hazardous bioeffects such as heating and cavitation in tissues [88]. Diagnostic ultrasound is also supported by WHO in that it is recognized as a safe, effective, and highly flexible imaging modality capable of providing clinically relevant information about most parts of the body in a rapid and cost-effective fashion [89]. In summary, the license-free ultrasonic transmissions eliminate any potential conflict with existing RF systems, and provide secure data delivery without harmful effects on the human body. Therefore, the use of ultrasonic technology in wireless communications can be considered as an ideal alternative to both RF and IR systems.

1.5.2 Prior works

In general, a communication system is an operational assembly to transfer information from one side to the other. Fig. 1.13 shows a collection of functional blocks that comprise a communication system. As can be seen, coding and modulation are the two key components to construct the system. Therefore, the objectives to enable a good communication system are to implement appropriate modulation schemes over suitable frequency bands, achieving sufficient data transfer rates at ranges with acceptable reliability.
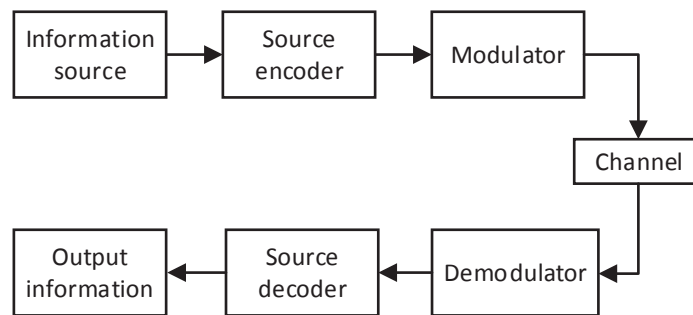
Figure 1.13: Basic elements of a communication system.

The use of ultrasonic waves as a means of signal transmission in air has been patented by several authors. For instance, the design of an ultrasonic communication system including an omnidirectional transducer and a cordless earpiece with an ultrasonic microphone has been proposed [90]. Similar work looked at the invention of a hands-free ultrasonic telephone with a designed bit rate of 1-10 kb/s at a frequency band between 200 and 400 kHz [91]. Other patents such as a personal sound system [92], a speech translator [93], and a wireless mobile headset [94] using ultrasonic connections have also been proposed.

The first generation batteryless, wireless remote control system for TV receivers was designed by Robert Adler for Zenith televisions in the 1950s [78]. Distinctive high frequency sounds at ultrasonic frequencies of around 40 kHz

were produced by striking different lengths of aluminium rod with a set of hammer buttons. These sounds were decoded at the TV, which changed channels appropriately. Research conducted by Oak Ridge National Laboratory in 2000 has successfully demonstrated transmitting and receiving ultrasonic data across a 3-m distance through air at 31 kHz, with a system rate of 75 b/s [95]. In [22], an indoor data communication system was developed by emitting frequency-shift keying (FSK) modulated ultrasonic signals. In this work, the attainable transmission range achieved was above 10 m, with a data rate of 100 b/s on a 4 kHz bandwidth at 40 kHz. Later work on multichannel data communication investigated high frequency amplitude-shift keying (ASK) and ON-OFF keying (OOK) at 250 kHz with only a 0.5 m transmission distance and achieved an 80 kb/s data transfer rate using prototype transducers [96]. In [24], the authors studied the performance of air-coupled ultrasonic transmission over directional short-range links using OOK, binary frequency-shift keying (BFSK) and binary phase-shift keying (BPSK) modulations. The system started to experience error decoding at a range of 1.6 m and the maximum data rate achieved was 83 kb/s using a physical hard wired synchronization link between the transmitter and the receiver in a laboratory environment. Another later study implemented quadrature phase-shift keying (QPSK) modulation using the same custom-made capacitive transducers in [24] and achieved a bit rate of 200 kb/s over 1.2 m in air [97]. Fig. 1.14 compares the above airborne ultrasonic data communication systems in terms of their data rates and attainable transmission ranges. It has to be noted that all these previous works considered only line-of-sight (LOS) path, and with proper error correction methods used, the system can potentially be more robust, however, sacrificing part of the system data rate.

Compared with RF based systems, ultrasonic systems can provide more accurate measurement of time-of-flight (TOF) for location estimation at low cost, owing to the low propagation speed of ultrasonic waves in air. Therefore, a vari-
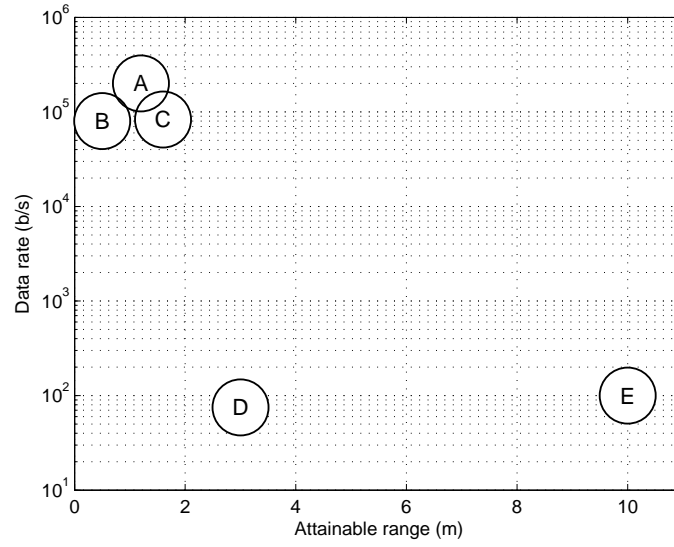
Figure 1.14: Comparison of different airborne ultrasonic data communication systems and their data rates at attainable transmission ranges. A, B, C, D, E refer to the works referenced in [97], [96], [24], [95] and [22], respectively.

ety of ultrasonic communication systems used for indoor positioning and localization have been reported in the past literature. In [98], an indoor positioning system used in hospitals was developed based on ultrasound, achieving a data rate of 100 b/s with a channel efficiency of 0.025 b/s/Hz. This work addressed some of the major challenges in air-coupled ultrasonic communications due to Doppler shift and reverberation for more robust and practical use, however, at the sacrifice of data rate. Another later work also implemented an indoor location system, using broadband ultrasonic transmitter and receiver units [23]. This broadband system allowed the use of spread spectrum, multiple access techniques in its ranging signals and improved the overall data rate to 20 kb/s with a higher bandwidth efficiency of 0.26 b/s/Hz. More recent work looked at a 2-channel orthogonal frequency division multiplexing (OFDM) scheme for the use in localization systems [25]. However, as piezoelectric transducers were used in the work, the achieved data rate was only 5.7 kb/s and the measured packet error rate was 13% at a distance of 18 m. Other works proposed high accuracy 2D and 3D ultrasonic positioning systems as an extension of Global

27

Positioning System (GPS) for indoor applications [99, 100].

There also have been some studies of airborne ultrasound in the field of human-computer interaction (HCI) [101]. For example, an ultrasonic system looked at implementing a computer input device containing a writing instrument coupled to ultrasonic transmitters which allowed the system to continuously determine the position of the stylus [102]. In [103], a touchless human computer interface has been designed with a plurality of ultrasonic transducers as user input devices. Another recent work proposed a prototype networking framework for wearable medical devices based on ultrasonic communications [104]. To meet the privacy and security requirements, the health information of a patient can be collected and transmitted through an ultrasonic link.

1.6 Outline of the thesis

The research work described in this thesis aims to achieve a practical indoor ultrasonic data communication network, implementation and evaluation of the most efficient modulation schemes for the limited bandwidth available using air-coupled capacitive transducers, and create a simulation model that can precisely predict ultrasonic signals through the air channel.

In Chapter 2, multicarrier modulation schemes including OOK and BPSK using a pair of commercially available air-coupled capacitive transducers are investigated. A simulation model for estimating ultrasonic signals through the air channel is also proposed. In addition, system performance metrics including data transfer rate, transmission range and bit error rate result are evaluated.

Chapter 3 presents pilot-aided orthogonal multicarrier modulation methods for airborne ultrasonic communication using both prototype and commercially available transducers. The ultrasonic propagation model for signal prediction is also used to simulate received signals, and compared with the experimental

results. System performance in both LOS and multipath scenarios is evaluated.

Chapter 4 looks at the ultrasonic data communication under non-LOS transmission conditions including reflection and diffraction. Different OFDM modulation methods are analysed and compared in possible non-LOS propagation configurations. Full-duplex communications using both separated and interleaved forward and reverse bands are also investigated.

Chapter 5 describes an indoor full-duplex communication network with ceiling-mounted base stations and a mobile unit. A RF-free ultrasonic positioning method for estimating the user location is investigated with its ranging accuracy evaluated. The handover mechanism is discussed later in this chapter for seamless switching data connections between different cells.

Chapter 6 gives the main contributions and the conclusions of the work. Suggestions for future research are also proposed in this chapter.

1.7 References

[1] D. Wright, *Human Physiology and Health*. Harlow, U.K.: Pearson Education Limited, 2000.

[2] A. Surlykke, *Animal Sonar*, ch. Interaction Between Echolocating Bats and Their Prey, pp. 551–566. Boston, MA, USA: Springer, 1988.

[3] T. Akamatsu, D. Wang, K. Wang, and Y. Naito, "Biosonar behaviour of free-ranging porpoises," *Philos. Trans. R. Soc. Lond., B, Biol. Sci.*, vol. 272, no. 1565, pp. 797–801, 2005.

[4] M. Repacholi, M. Grandolfo, and A. Rindi, *Ultrasound: Medical Applications, Biological Effects, and Hazard Potential*. New York, NY, USA: Springer, 1987.

[5] A. Abbate, J. Koay, J. Frankel, S. C. Schroeder, and P. Das, "Signal detection and noise suppression using a wavelet transform signal processor: application to ultrasonic flaw detection," *IEEE Trans. Ultrason., Ferroelectr., Freq. Control*, vol. 44, pp. 14–26, Jan. 1997.

[6] S. Kocis and Z. Figura, *Ultrasonic Measurements and Technologies*. New York, NY, USA: Springer, 2012.

[7] R. Smith, "Ultrasonic materials characterization," *NDT Int.*, vol. 20, no. 1, pp. 43–48, 1987.

[8] C. H. Sherman and J. L. Butler, *Transducers and arrays for underwater sound*. New York, NY, USA: Springer, 2007.

[9] M. Greenspan and C. E. Tschiegg, "Speed of sound in water by a direct method," *J. Res. Natl. Bur. Stand.*, vol. 59, no. 4, p. 249, 1957.

[10] J. W. S. B. Rayleigh, *The Theory of Sound*, vol. 1. London, U.K.: Macmillan and Co., 1894.

[11] J. Curie and P. Curie, "Développement, par pression, de l'électricité polaire dans les cristaux hémièdres à faces inclinées," *Comptes Rendus*, vol. 91, pp. 294–295, 1880.

[12] C. Constantin and L. Paul, "Production of submarine signals and the location of submarine objects." U.S. Patent 1 471 547, Oct. 23, 1923.

[13] R. M. Gowda, I. A. Khan, B. C. Vasavada, T. J. Sacchi, and R. Patel, "History of the evolution of echocardiography," *Int. J. Cardiol.*, vol. 97, no. 1, pp. 1–6, 2004.

[14] F. A. Firestone, "The supersonic reflectoscope, an instrument for inspecting the interior of solid parts by means of sound waves," *J. Acoust. Soc. Amer.*, vol. 17, no. 3, pp. 287–299, 1946.

[15] P. G. Newman and G. S. Rozycki, "The history of ultrasound," *Surg. Clin. North Am.*, vol. 78, no. 2, pp. 179–195, 1998.

[16] C. Meola and C. Toscano, "NonDestructive evaluation of carbon fiber reinforced polymers with ultrasonics and infrared thermography: An overview on historical steps and patents," *Recent Pat. Mater. Sci.*, vol. 5, no. 1, pp. 48–67, 2012.

[17] J. Woo, "A short history of the development of ultrasound in obstetrics and gynecology." [Online]. Available: `http://www.ob-ultrasound.net/history1.html`. accessed Aug. 2016.

[18] W. R. Hendee and E. R. Ritenour, *Medical imaging physics*. Hoboken, NJ, USA: John Wiley & Sons, 2003.

[19] K. T. Dussik, "Über die möglichkeit, hochfrequente mechanische schwingungen als diagnostisches hilfsmittel zu verwerten," *Z. Gesamte Neurol. Psy.*, vol. 174, no. 1, pp. 153–168, 1942.

[20] G. D. Ludwig and F. W. Struthers, "Considerations underlying the use of ultrasound to detect gallstones and foreign bodies in tissue," tech. rep., Naval Medical Research Institute, 1949.

[21] J. H. Holmes, D. H. Howry, G. J. Posakony, and C. R. Cushman, "The ultrasonic visualization of soft tissue structures in the human body," *Trans. Am. Clin. Climatol. Assoc.*, vol. 66, p. 208, 1955.

[22] S. Holm, O. Hovind, S. Rostad, and R. Holm, "Indoors data communications using airborne ultrasound," in *Proc. IEEE Int. Acoust. Speech. Signal (ICASSP)*, vol. 3, pp. 957–960, 2005.

[23] M. Hazas and A. Hopper, "Broadband ultrasonic location systems for improved indoor positioning," *IEEE Trans. Mobile Comput.*, vol. 5, pp. 536–547, May 2006.

[24] C. Li, D. Hutchins, and R. Green, "Short-range ultrasonic digital communications in air," *IEEE Trans. Ultrason., Ferroelectr., Freq. Control*, vol. 55, no. 4, pp. 908–918, 2008.

[25] A. Ens and L. Reindl, "Multicarrier airborne ultrasound transmission with piezoelectric transducers," *IEEE Trans. Ultrason., Ferroelectr., Freq. Control*, vol. 62, pp. 905–914, May 2015.

[26] M. J. Crocker, *Handbook of acoustics*. Hoboken, NJ, USA: John Wiley & Sons, 1998.

[27] C. L. Morfey and G. P. Howell, "Speed of sound in air as a function of frequency and humidity," *J. Acoust. Soc. Amer.*, vol. 68, no. 5, pp. 1525–1527, 1980.

[28] G. S. K. Wong and T. F. W. Embleton, "Variation of the speed of sound in air with humidity and temperature," *J. Acoust. Soc. Amer.*, vol. 77, no. 5, pp. 1710–1712, 1985.

[29] G. P. Howell and C. L. Morfey, "Frequency dependence of the speed of sound in air," *J. Acoust. Soc. Amer.*, vol. 82, no. 1, pp. 375–376, 1987.

[30] R. Hickling and S. P. Marin, "The use of ultrasonics for gauging and proximity sensing in air," *J. Acoust. Soc. Amer.*, vol. 79, no. 4, pp. 1151–1160, 1986.

[31] R. Halmshaw, *Non-destructive testing*. London, U.K.: Edward Arnold, 1987.

[32] D. N. Alleyne and P. Cawley, "The interaction of lamb waves with defects," *IEEE Trans. Ultrason., Ferroelectr., Freq. Control*, vol. 39, pp. 381–397, May 1992.

[33] D. M. Barnett, J. Lothe, S. D. Gavazza, and M. J. P. Musgrave, "Considerations of the existence of interfacial (Stoneley) waves in bonded anisotropic elastic half-spaces," *Proc. R. Soc. A., Math. Phys. Eng. Sci.*, vol. 402, no. 1822, pp. 153–166, 1985.

[34] M. Schoenberg, "Elastic wave behavior across linear slip interfaces," *J. Acoust. Soc. Amer.*, vol. 68, no. 5, pp. 1516–1521, 1980.

[35] W. Mason and R. Thurston, eds., *Physical acoustics: principles and methods*. New York, NY, USA: Academic Press, 1984.

[36] K. Nakamura, ed., *Ultrasonic Transducers: Materials and Design for Sensors, Actuators and Medical Applications*. Cambridge, U.K.: Woodhead Publishing Limited, 2012.

[37] J. Krautkrämer and H. Krautkrämer, *Ultrasonic testing of materials*. Berlin, Germany: Springer-Verlag, 1990.

[38] P. R. Stepanishen, "Transient radiation from pistons in an infinite planar baffle," *J. Acoust. Soc. Amer.*, vol. 49, no. 5B, pp. 1629–1638, 1971.

[39] J. C. Lockwood and J. G. Willette, "High-speed method for computing the exact solution for the pressure variations in the nearfield of a baffled piston," *J. Acoust. Soc. Amer.*, vol. 53, no. 3, pp. 735–741, 1973.

[40] A. G. Bashford, D. W. Schindel, D. A. Hutchins, and W. M. D. Wright, "Field characterization of an air-coupled micromachined ultrasonic capacitance transducer," *J. Acoust. Soc. Amer.*, vol. 101, no. 1, pp. 315–322, 1997.

[41] D. A. Hutchins, J. S. McIntosh, A. Neild, D. R. Billson, and R. A. Noble, "Radiated fields of capacitive micromachined ultrasonic transducers in air," *J. Acoust. Soc. Amer.*, vol. 114, no. 3, pp. 1435–1449, 2003.

[42] D. Schindel, D. Forsyth, D. Hutchins, and A. Fahr, "Air-coupled ultrasonic NDE of bonded aluminum lap joints," *Ultrasonics*, vol. 35, no. 1, pp. 1 – 6, 1997.

[43] W. A. Grandia and C. M. Fortunko, "NDE applications of air-coupled ultrasonic transducers," in *Proc. IEEE Int. Ultrason. Symp. (IUS)*, vol. 1, pp. 697–709, Nov. 1995.

[44] T. E. G. Alvarez-Arenas, "Acoustic impedance matching of piezoelectric transducers to the air," *IEEE Trans. Ultrason., Ferroelectr., Freq. Control*, vol. 51, pp. 624–633, May 2004.

[45] G. Hayward and A. Gachagan, "An evaluation of 1-3 connectivity composite transducers for air-coupled ultrasonic applications," *J. Acoust. Soc. Amer.*, vol. 99, no. 4, pp. 2148–2157, 1996.

[46] J. Stor-Pellinen, M. Okasanen, R. Vuohelainen, J. Rantala, J. Hartikainen, and M. Luukkala, "Photoacoustic inspection of matching layers of ultrasonic air-coupled transducers," in *Proc. IEEE Int. Ultrason. Symp. (IUS)*, vol. 1, pp. 665–668, Oct. 1989.

[47] S. Schiller, C.-K. Hsieh, C.-H. Chou, and B. T. Khuri-Yakub, *Review of Progress in Quantitative Nondestructive Evaluation*, ch. Novel High-Frequency Air Transducers, pp. 795–798. Boston, MA, USA: Springer US, 1990.

[48] W. Manthey, N. Kroemer, and V. Magori, "Ultrasonic transducers and transducer arrays for applications in air," *Meas. Sci. Technol.*, vol. 3, no. 3, p. 249, 1992.

[49] L. Durris, L. Goujon, A. Pelourson, P. Gonnard, M. Brissaud, and C. Richard, "Airborne ultrasonic transducer," *Ultrasonics*, vol. 34, pp. 153 – 158, 1996.

[50] A. Gachagan, G. Hayward, S. P. Kelly, and W. Galbraith, "Characterization of air-coupled transducers," *IEEE Trans. Ultrason., Ferroelectr., Freq. Control*, vol. 43, pp. 678–689, July 1996.

[51] L. F. Brown, "Design considerations for piezoelectric polymer ultrasound transducers," *IEEE Trans. Ultrason., Ferroelectr, Freq. Control*, vol. 47, pp. 1377–1396, Nov. 2000.

[52] T. Gudra and K. J. Opieliński, "Influence of acoustic impedance of multilayer acoustic systems on the transfer function of ultrasonic airborne transducers," *Ultrasonics*, vol. 40, pp. 457 – 463, 2002.

[53] M. I. Haller and B. T. Khuri-Yakub, "Micromachined 1-3 composites for ultrasonic air transducers," *Rev. Sci. Instrum.*, vol. 65, no. 6, pp. 2095–2098, 1994.

[54] E. C. Wente, "A condenser transmitter as a uniformly sensitive instrument for the absolute measurement of sound intensity," *Phys. Rev.*, vol. 10, pp. 39–63, Jul. 1917.

[55] W. Kuhl, G. Schodder, and F.-K. Schröder, "Condenser transmitters and microphones with solid dielectric for airborne ultrasonics," *Acta Acust. united Ac.*, vol. 4, no. 5, pp. 519–532, 1954.

[56] H. Carr and C. Wykes, "Diagnostic measurements in capacitive transducers," *Ultrasonics*, vol. 31, no. 1, pp. 13 – 20, 1993.

[57] P. Mattila and J. Hietanen, "Bandwidth control of an electrostatic ultra-sonic transducer," *Sensor. Actuat. A: Phys.*, vol. 45, no. 3, pp. 203 – 208, 1994.

[58] M. Rafiq and C. Wykes, "The performance of capacitive ultrasonic trans-ducers using v-grooved backplates," *Meas. Sci. Technol.*, vol. 2, no. 2, p. 168, 1991.

[59] J. Hietanen, P. Mattila, J. Stor-Pellinen, F. Tsuzuki, H. Vaataja, K. Sasaki, and M. Luukkala, "Factors affecting the sensitivity of electrostatic ultra-sonic transducers," *Meas. Sci. Technol.*, vol. 4, no. 10, p. 1138, 1993.

[60] D. W. Schindel, D. A. Hutchins, L. Zou, and M. Sayer, "The design and characterization of micromachined air-coupled capacitance trans-ducers," *IEEE Trans. Ultrason., Ferroelectr., Freq. Control*, vol. 42, pp. 42–50, Jan. 1995.

[61] L. Pizarro, D. Certon, M. Lethiecq, and B. Hosten, "Airborne ultrasonic electrostatic transducers with conductive grooved backplates: tailoring their centre frequency, sensitivity and bandwidth," *Ultrasonics*, vol. 37, no. 7, pp. 493 – 503, 1999.

[62] K. Matsuzawa, "Condenser microphones with plastic diaphragms for air-borne ultrasonics, i," *J. Phys. Soc. Jpn.*, vol. 13, no. 12, pp. 1533–1543, 1958.

[63] K. Matsuzawa, "Condenser microphones with plastic diaphragms for air-borne ultrasonics, ii," *J. Phys. Soc. Jpn.*, vol. 15, no. 1, pp. 167–174, 1960.

[64] P. Mattila, F. Tsuzuki, H. Vaataja, and K. Sasaki, "Electroacoustic model for electrostatic ultrasonic transducers with v-grooved backplates," *IEEE Trans. Ultrason., Ferroelectr., Freq. Control*, vol. 42, pp. 1–7, Jan. 1995.

[65] L.-F. Ge, "Electrostatic airborne ultrasonic transducers: modeling and characterization," *IEEE Trans. Ultrason., Ferroelectr., Freq. Control*, vol. 46, pp. 1120–1127, Sept. 1999.

[66] J. Hietanen, J. Stor-Pellinen, M. Luukkala, P. Mattila, F. Tsuzuki, and K. Sasaki, "A helmholtz resonator model for an electrostatic ultrasonic air transducer with a v-grooved backplate," *Sensor. Actuat. A: Phys.*, vol. 39, no. 2, pp. 129 – 132, 1993.

[67] K. Suzuki, K. Higuchi, and H. Tanigawa, "A silicon electrostatic ultrasonic transducer," *IEEE Trans. Ultrason., Ferroelectr., Freq. Control*, vol. 36, pp. 620–627, Nov. 1989.

[68] M. I. Haller and B. T. Khuri-Yakub, "A surface micromachined electrostatic ultrasonic air transducer," *IEEE Trans. Ultrason., Ferroelectr., Freq. Control*, vol. 43, pp. 1–6, Jan. 1996.

[69] A. S. Ergun, Y. Huang, X. Zhuang, O. Oralkan, G. G. Yarahoglu, and B. T. Khuri-Yakub, "Capacitive micromachined ultrasonic transducers: fabrication technology," *IEEE Trans. Ultrason., Ferroelectr., Freq. Control*, vol. 52, pp. 2242–2258, Dec. 2005.

[70] D. Hutchins, D. Schindel, A. Bashford, and W. Wright, "Advances in ultrasonic electrostatic transduction," *Ultrasonics*, vol. 36(1-5), pp. 1–6, 1998. Ultrasonics International 1997.

[71] J. McIntosh, D. Hutchins, D. Billson, T. Robertson, R. Noble, and A. Jones, "The characterization of capacitive micromachined ultrasonic transducers in air," *Ultrasonics*, vol. 40, pp. 477–483, 2002.

[72] D. W. Schindel and D. A. Hutchins, "Applications of micromachined capacitance transducers in air-coupled ultrasonics and nondestructive eval-

uation," *IEEE Trans. Ultrason., Ferroelectr., Freq. Control*, vol. 42, pp. 51–58, Jan. 1995.

[73] J. Johnson, Ömer Oralkan, U. Demirci, S. Ergun, M. Karaman, and P. Khuri-Yakub, "Medical imaging using capacitive micromachined ultrasonic transducer arrays," *Ultrasonics*, vol. 40, pp. 471 – 476, 2002.

[74] G. Caliano, R. Carotenuto, E. Cianci, V. Foglietti, A. Caronti, A. Iula, and M. Pappalardo, "Design, fabrication and characterization of a capacitive micromachined ultrasonic probe for medical imaging," *IEEE Trans. Ultrason., Ferroelectr., Freq. Control*, vol. 52, pp. 2259–2269, Dec. 2005.

[75] A. Caronti, G. Caliano, R. Carotenuto, A. Savoia, M. Pappalardo, E. Cianci, and V. Foglietti, "Capacitive micromachined ultrasonic transducer (CMUT) arrays for medical imaging," *Microelectr. J.*, vol. 37, no. 8, pp. 770 – 777, 2006.

[76] D. Schindel, D. Hutchins, and W. Grandia, "Capacitive and piezoelectric air-coupled transducers for resonant ultrasonic inspection," *Ultrasonics*, vol. 34, no. 6, pp. 621 – 627, 1996.

[77] A. S. Ergun, G. G. Yaralioglu, and B. T. Khuri-Yakub, "Capacitive micromachined ultrasonic transducers: Theory and technology," *J. Aerospace Eng.*, vol. 16, no. 2, pp. 76–84, 2003.

[78] R. Adler, P. Desmares, and J. Spracklen, "An ultrasonic remote control for home receivers," *IEEE Trans. Consum. Electron.*, vol. CE-28, pp. 123–128, Feb. 1982.

[79] D. Agrawal and Q. Zeng, *Introduction to Wireless and Mobile Systems*. Boston, MA, USA: Cengage Learning, 2015.

[80] I. F. Akyildiz, W.-Y. Lee, M. C. Vuran, and S. Mohanty, "NeXt generation/-dynamic spectrum access/cognitive radio wireless networks: A survey," *Comput. Netw.*, vol. 50, no. 13, pp. 2127 – 2159, 2006.

[81] N. Borisov, I. Goldberg, and D. Wagner, "Intercepting mobile communications: the insecurity of 802.11," in *Proc. 7th Annu. Int. Conf. Mobile Comput. Netw. (MobiCom)*, pp. 180–189, 2001.

[82] R. Baan, Y. Grosse, B. Lauby-Secretan, F. E. Ghissassi, V. Bouvard, L. Benbrahim-Tallaa, N. Guha, F. Islami, L. Galichet, and K. Straif, "Carcinogenicity of radiofrequency electromagnetic fields," *Lancet Oncol.*, vol. 12, no. 7, pp. 624 – 626, 2011.

[83] Assemblée Nationale (2016, Aug.). [Online]. Available: `http://www.assemblee-nationale.fr/14/ta/ta0468.asp`.

[84] J. Whitaker, *The Electronics Handbook, Second Edition*. Electrical Engineering Handbook, Boca Raton, FL, USA: CRC Press, 2005.

[85] J. Krenz, *Electronic Concepts: An Introduction*. Cambridge, U.K.: Cambridge University Press, 2000.

[86] R. Ramirez-Iniguez, S. Idrus, and Z. Sun, *Optical Wireless Communications: IR for Wireless Connectivity*. Abingdon, U.K.: Taylor & Francis, 2008.

[87] X. N. Fernando, K. Srithar, H. Sun, and K.-M. Kamyar, "Adaptive denoising at infrared wireless receivers," in *Proc. SPIE* (B. F. Andresen and G. F. Fulop, eds.), vol. 5074, pp. 199–207, Infrared Technology and Applications XXIX, 2003.

[88] S. B. Barnett, G. R. T. Haar, M. C. Ziskin, H.-D. Rott, F. A. Duck, and K. Maeda, "International recommendations and guidelines for the safe

use of diagnostic ultrasound in medicine," *Ultrasound Med. Biol.*, vol. 26, no. 3, pp. 355 – 366, 2000.

[89] "Training in diagnostic ultrasound: essentials, principles and standards," Tech. Rep. 875, Geneva, Switzerland: World Health Organization, 1998.

[90] R. A. Zurek, A. Dietrich, and M. L. Charlier, "Omnidirectional ultrasonic communication system." U.S. Patent 6 363 139, Mar. 26, 2002.

[91] L. Hofmann, "Transmission of data by ultrasound." U.S. Patent 6 363 139, Sept. 27, 2005.

[92] H. Olson, "Signal transmission and receiving apparatus." U.S. Patent 2 461 344, Feb. 8, 1949.

[93] M. Akerman, C. Ayers, and H. Haynes, "Ultrasonic speech translator and communications system." U.S. Patent 5 539 705, July 23, 1996.

[94] Y. Tsfaty, "System and method for using ultrasonic communication." U.S. Patent 13 175 790, July 5, 2012.

[95] H. D. Haynes, M. A. Akeman, and V. M. Baylor, "Ultrasonic communication project, phase 1, FY 1999," tech. rep., Oak Bridge, TN, USA, Jun. 2000.

[96] W. M. D. Wright, O. Doyle, and C. T. Foley, "Multi-channel data transfer using air-coupled capacitive ultrasonic transducers," in *Proc. IEEE Int. Ultrason. Symp. (IUS)*, pp. 1805–1808, 2006.

[97] C. Li, D. Hutchins, and R. Green, "Short-range ultrasonic communications in air using quadrature modulation," *IEEE Trans. Ultrason., Ferroelectr., Freq. Control*, vol. 56, no. 10, pp. 2060–2072, 2009.

[98] S. Holm, "Airborne ultrasound data communications: the core of an indoor positioning system," in *Proc. IEEE Int. Ultrason. Symp. (IUS)*, vol. 3, pp. 1801–1804, Sept. 2005.

[99] T. Ito, T. Sato, K. Tulathimutte, M. Sugimoto, and H. Hashizume, "A scalable tracking system using ultrasonic communication," in *Proc. IEEE 3rd Int. Conf. Sens. Technol. (ICST)*, pp. 31–36, Nov. 2008.

[100] S. I. Lopes, J. M. N. Vieira, and D. Albuquerque, "High accuracy 3d indoor positioning using broadband ultrasonic signals," in *Proc. IEEE 11th Int. Conf. Trust, Security, Privacy Comput. Commu. (TrustCom)*, pp. 2008–2014, June 2012.

[101] T. Dahl, J. L. Ealo, H. J. Bang, S. Holm, and P. Khuri-Yakub, "Applications of airborne ultrasound in human-computer interaction," *Ultrasonics*, vol. 54, no. 7, pp. 1912–1921, 2014.

[102] M. Stefik and J. Heater, "Ultrasound position input device." U.S. Patent 4 814 552, Mar. 21, 1989.

[103] Z. Radivojevic, Y. Zou, K. Wang, R. Takala, V. Lantz, R. Lehtiniemi, J. Rantala, and R. Vatanparast, "Apparatus, methods and computer program products providing finger-based and hand-based gesture commands for portable electronic device applications." U.S. Patent 8 086 971, Dec. 27, 2011.

[104] G. E. Santagati and T. Melodia, "U-wear: Software-defined ultrasonic networking for wearable devices," in *Proc. 13th Annu. Int. Conf. Mobile Syst., Applicat., Services (MobiSys)*, pp. 241–256, 2015.

Chapter 2

Evaluation of Frequency Division Multiplexing (FDM) Schemes in Ultrasonic Communications

2.1 Introduction

The work described in this chapter investigates a practical wireless ultrasonic communication system with multicarrier modulation schemes using a pair of commercially available air-coupled capacitive transducers, and proposes a simulation model for estimating ultrasonic signals through the air channel. The instrumentation used for the experiment work will be introduced in Section 2.2, followed by wireless signal characterization including bandlimiting filtering, synchronization techniques, modulation and demodulation methods in Section 2.3. Section 2.4 will evaluate the system reliability based on bit error rate (BER) measurements. In Section 2.5 and 2.6, ultrasonic transmissions in air using range-dependent modulation schemes with variable data transfer rates and in misaligned conditions are presented, respectively. Section 2.7 gives the conclusion of this chapter.

2.2 Instrumentation

There is a capacitive ultrasonic transducer widely available commercially, designed by Polaroid as a range finder for autofocus cameras but can be purchased on its own. These ultrasonic sensors are now manufactured by SensComp Inc., which is an original equipment manufacturer products division of Polaroid. The transducers used in this work are series 600 environmental grade ultrasonic sensors [1] as shown in Fig. 2.1. The transducers are specially designed for operation in air at an ultrasonic frequency of 50 kHz with a beam angle of $15°$ at -6 dB. These devices are composed of a gold coated polymer membrane and a rigid contoured aluminium backplate with an aperture size of 38.4 mm. The SensComp series 600 capacitive transducers have been used for different scientific research such as robotic applications [2], ultrasonic tomography of concrete structures [3], and acoustic separation of suspending submicron solid particles in gases [4].
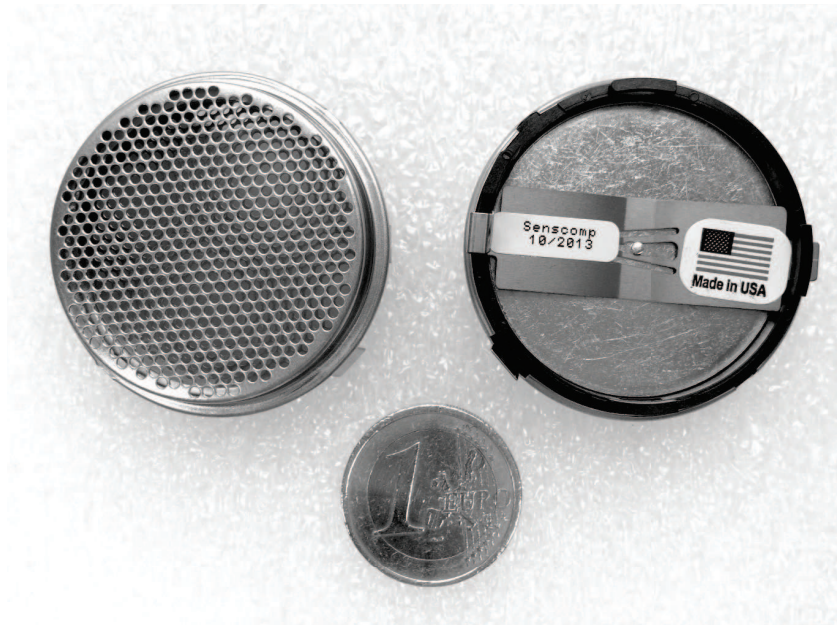
Figure 2.1: SensComp series 600 environmental grade ultrasonic transducer.

2.2.1 Experimental set-up

Fig. 2.2 illustrates the experimental setup of the ultrasonic communication system. The data to be transmitted were encoded and modulated using MATLAB (The Math Works, Inc.) before sending to a TTi TGA 12102 arbitrary waveform generator (Thurlby Thandar Instruments Ltd.) via a GPIB interface. The voltage signal was then amplified by a Falco WMA-300 amplifier (Falco Systems B.V.) and combined with a bias voltage of +200 V generated by a Delta Elektronika SM3004-D power supply (Delta Elektronika B.V.). The receiver transducer was connected to a Cooknell CA6/C charge amplifier (Cooknell Electronics Ltd.) powered by a Cooknell SU2/C power supply unit and followed by a high-performance PicoScope 6403A PC oscilloscope (Pico Technology). After that, the signal was sent to another PC through a USB interface for signal processing.
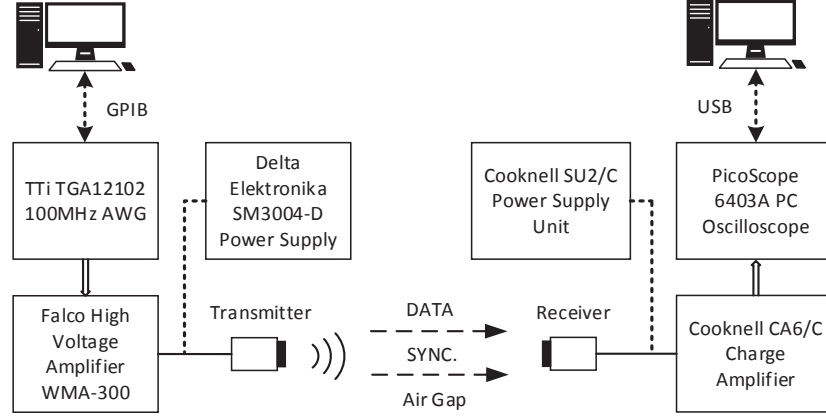
Figure 2.2: Schematic diagram of the experimental set-up.

2.2.2 System and noise characteristics

The overall system impulse response, frequency response and phase response over a typical range of 2 m are shown in Fig. 2.3(a), (b), and (c), respectively. The received impulse was measured by sending a pulse signal generated by a

Panametrics 500PR pulser (Panametrics, Inc.) from the transmitter transducer to the receiver transducer through the air gap. As can be seen in Fig. 2.3(b), the spectrum peaks at about 50 kHz as expected, and it indicates using data channels at ultrasonic frequencies from 46 kHz to 113 kHz is appropriate in terms of 6-dB bandwidth which is about 68 kHz. The phase response of the channel is nearly linear across the 6-dB bandwidth as shown in Fig. 2.3(c). It means that there is no phase distortion due to the time delay of frequencies relative to one another.
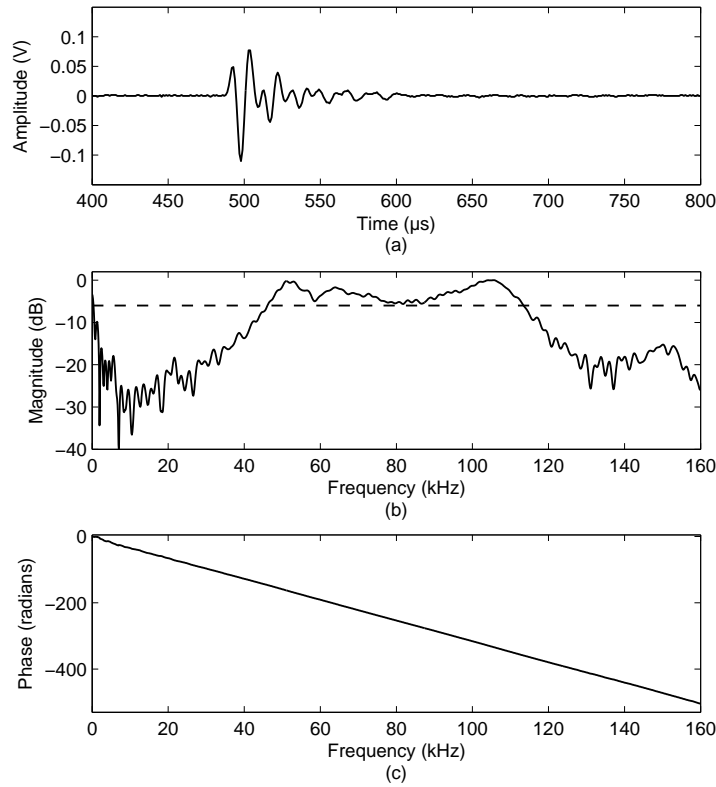
Figure 2.3: System characteristics over 2 m: (a) impulse response; (b) frequency response; and (c) phase response.

In addition, to analyse the background noise, a signal was captured by sending no data from the transmitter transducer in an indoor laboratory environment as Fig. 2.4(a) shows. Accordingly, its frequency spectrum is illustrated in Fig. 2.4(b). As can be seen, within the audio frequency range up to 20 kHz,

the magnitude response is relatively higher. But it stays relatively constant afterwards, extending to ultrasonic frequencies. Therefore, most ambient noise is audio noise which can be easily filtered out. It should be noted that in many industrial applications, a maximum spectral density of acoustic noise is observed at frequencies up to 40 kHz [5]. Thus, higher operating frequencies are preferred. The recorded impulse peak-to-peak signal amplitude was approximately 187 mV and the background noise level was about 3 mV giving a signal-to-noise ratio (SNR) of 35.8 dB at this range.
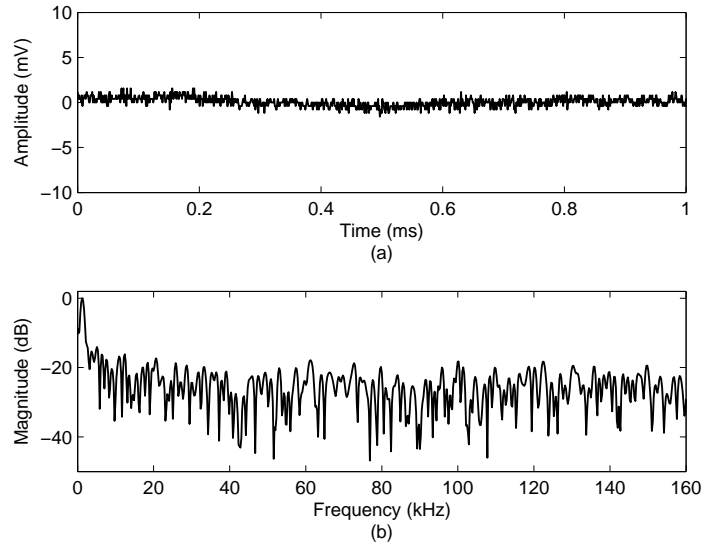
Figure 2.4: Background noise in: (a) time domain; and (b) frequency domain.

2.3 System description

2.3.1 Signal design

In practical digital wireless communications, inter-symbol interference (ISI) is an unavoidable consequence [6] after the signal has been transmitted through non-ideal channels where the symbol duration is significantly smaller than the time dispersion. In such a case, a channel equalizer is usually employed at the receiver to compensate for the channel distortion [7]. However, ISI still causes a

certain amount of performance degradation, even when an optimum detector is used to recover the information symbols at the receiver [8]. An alternative approach is to divide the available bandwidth into a number of equal-bandwidth subchannels, where the bandwidth of each subchannel is sufficiently narrow so that the frequency response characteristics of the subchannels are nearly ideal. Consequently, the data can be transmitted by frequency-division multiplexing (FDM).

Assuming that a sequence of transmitted data symbols can be denoted as $\{d_k\}$, $k = -\infty, ..., \infty$. The transmitted signal $s(t)$ with linear modulation is then given by

$$
\begin{aligned}
s(t) &= h_T(t) * \sum_{k=-\infty}^{\infty} d_k \delta(t - kT) \\
&= \sum_{k=-\infty}^{\infty} d_k h_T(t - kT)
\end{aligned}
\tag{2.1}
$$

where T is the symbol interval, $h_T(t)$ is the impulse response of the transmit filter and $\delta(t)$ is the Dirac delta function. The modulator can be regarded as a pulse-shape filter and the impulse response of this filter is therefore rectangular of duration T. All the pulses are then summed at the output of the filter. As a result, the filter produces a baseband transmitted signal. However, sharp transitions occur when rectangular pulse filtering is applied. It leads to significant spectral leakage and thus produces severe interference to other sub-channel signals operating at neighbouring frequencies. Therefore, in pursuit of utilizing the limited bandwidth more efficiently and eliminating adjacent channel interference, introducing a proper pulse shaping technique is necessary to improve the signal transmission. In practice, the pulse shape filter with the following frequency response is often used [8]:

$$H_T(f) = \begin{cases} T, & |f| \leq \frac{1-\alpha}{2T} \\ \frac{T}{2}\{1 + cos[\frac{\pi T}{\alpha}(|f| - \frac{1-\alpha}{2T})]\}, & \frac{1-\alpha}{2T} \leq |f| \leq \frac{1+\alpha}{2T} \\ 0, & otherwise \end{cases} \quad (2.2)$$

where α, ranging from 0 to 1, is a design parameter called the roll-off factor. This spectrum $H_T(f)$ is called the raised-cosine spectrum. The corresponding impulse response in the time domain is

$$h_T(t) = sinc(\frac{t}{T})\frac{cos(\frac{\alpha \pi t}{T})}{1 - (\frac{2\alpha t}{T})^2}. \quad (2.3)$$

The roll-off factor α defines the shape of the impulse response as well as the shape of the frequency response. A value of $\alpha = 0$ gives a rectangular-shaped spectrum with the narrowest bandwidth and $h_T(t)$ becomes a sinc. As the value of α increases from 0 to 1, the effective bandwidth also increases and the rate of decay becomes faster in the time domain. Thus, by choosing a proper value of α, most of the channel power can be effectively limited to a specific defined bandwidth. After the transmit filter, all the sub-channel signals at individual frequencies were linearly added together, giving a single waveform for transmission.

Baseband modulation methods chosen were amplitude-shift keying (ASK) and binary phase-shift keying (BPSK). For ASK, the source generates carrier signals with large amplitude when a bit "1" occurs, and small amplitude when bit a "0" occurs. A simplified but more power efficient version of ASK is ON-OFF keying (OOK) [6], in which the source sends no signal when a bit "0" occurs. For BPSK, it uses two opposite signal phases (0 and 180 degrees) to convey information bits "1"s and "0"s. It should be noted that another popular digital modulation scheme, binary frequency-shift keying (BFSK), is not studied in this work due to its poor bandwidth efficiency. This has been investigated by other authors [14].
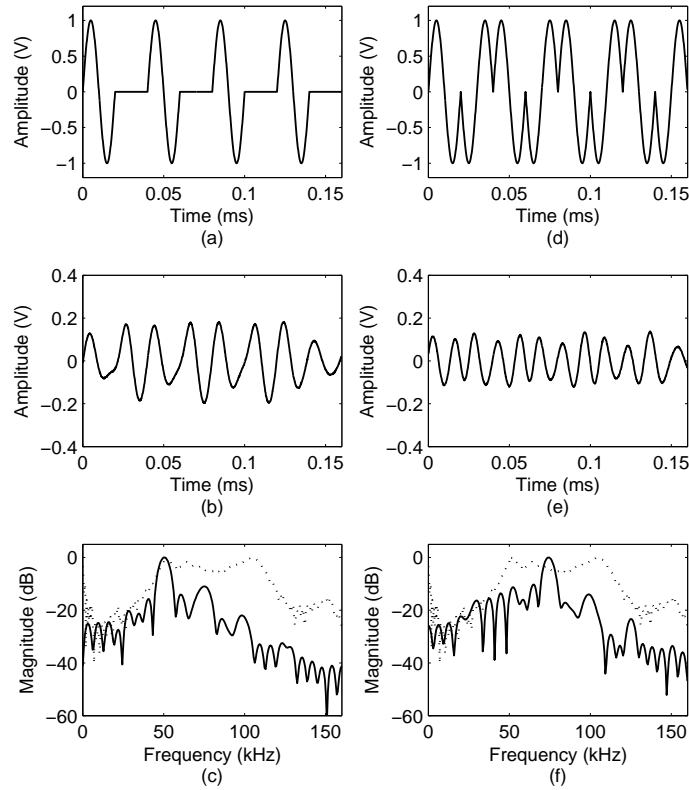
Figure 2.5: OOK modulation of a binary stream ("10101010") with a symbol duration of 0.02 ms at 50 kHz: (a) transmitted OOK signal; (b) received OOK signal at 2 m; (c) its spectrum. BPSK modulation with a symbol duration of 0.02 ms at 50 kHz: (d) transmitted BPSK signal; (e) received BPSK signal at 2 m; and (f) its spectrum. The dotted lines in (c) and (f) show the overall channel frequency response.

In binary modulations, each symbol can represent only one bit of data (i.e. "0" or "1"). Therefore, the symbol rate is equal to the bit rate. In order to maximise the data rate at each sub-channel, a short symbol duration is preferred. For a 50 kHz (nominal operating frequency of SensComp series 600 transducers) carrier frequency, the shortest symbol duration is 0.02 ms, allowing only one cycle of a sinusoid wave to be transmitted at one time at a data rate of 50 kb/s. The modulated OOK and BPSK signals of a binary stream ("10101010") at 50 kHz are shown in Fig. 2.5(a) and (d), respectively. However, both the received OOK and BPSK signals in different symbol durations tended to get elongated and smeared into each other after being transmitted

49
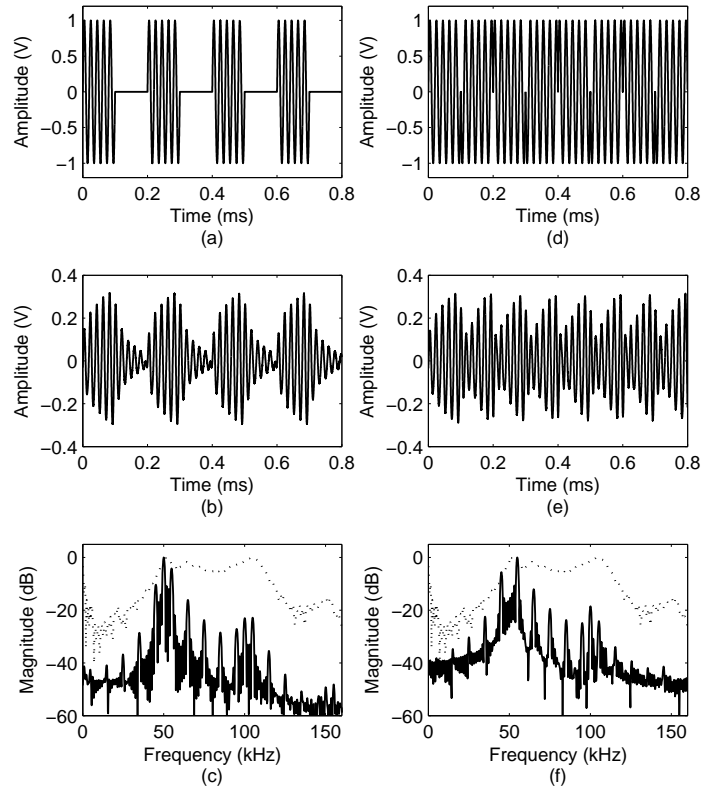
Figure 2.6: OOK modulation of a binary stream ("10101010") with a symbol duration of 0.1 ms at 50 kHz: (a) transmitted OOK signal; (b) received OOK signal at 2 m; (c) its spectrum. BPSK modulation with a symbol duration of 0.1 ms at 50 kHz: (d) transmitted BPSK signal; (e) received BPSK signal at 2 m; and (f) its spectrum. The dotted lines in (c) and (f) show the overall channel frequency response.

through an air gap of 2 m as illustrated in Fig. 2.5(b) and (e), respectively. Accordingly, their spectra in Fig. 2.5(c) and (f) show significant sidelobes around the carrier frequency. In addition, it is obvious that the received BPSK signal was heavily distorted as its spectrum in Fig. 2.5(f) peaked at about 75 kHz instead of 50 kHz. By increasing the symbol duration to 0.1 ms, there are 5 cycles of 50 kHz sinusoids in one single bit, and the data rate is, therefore, 10 kb/s. Note that this is deliberate to ensure an integer number of cycles exists in each symbol so that a symbol signal starts and ends at zero. As a result, both the transmitted and received OOK and BPSK signals in Fig. 2.6(a), (b) and Fig. 2.6(d), (e) show more distinctive amplitude and phase changes in the time

50
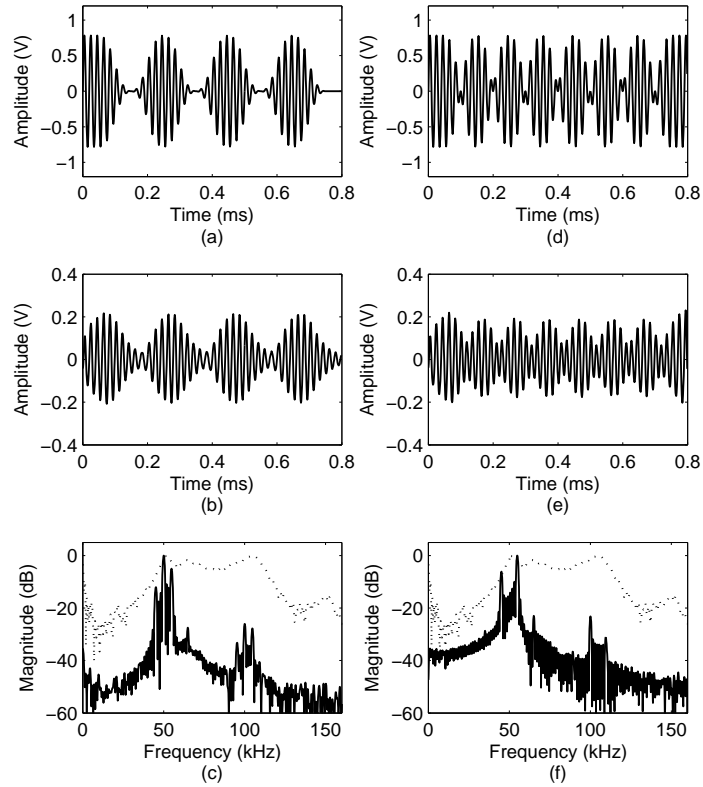
Figure 2.7: Pulse-shaped ($\alpha = 0$) OOK modulation of a binary stream ("10101010") with a symbol duration of 0.1 ms at 50 kHz: (a) transmitted OOK signal; (b) received OOK signal at 2 m; (c) its spectrum. Pulse-shaped ($\alpha = 0$) BPSK modulation with a symbol duration of 0.1 ms at 50 kHz: (d) transmitted BPSK signal; (e) received BPSK signal at 2 m; and (f) its spectrum. The dotted lines in (c) and (f) show the overall channel frequency response.

domain. The corresponding spectra are shown in Fig. 2.6(c) and (f), with a number of significant sidelobe peaks at both upper and lower sidebands. This is due to the sharp discontinuities at the transition points of the OOK signal, and the sudden phase changes of the BPSK signal, which result in unnecessary spectral leakage.

In a multichannel system, limiting the power of every modulated carrier to just the carrier bandwidth is important as the transmission power is reduced when the signal has a more concentrated frequency range. On the other hand, limiting a channel to a certain frequency band eliminates adjacent channel interference. Fig. 2.7(a), (b) and Fig. 2.7(d), (e) show both the transmitted and

received OOK and BPSK signals after applying a raised-cosine filter with a roll-off factor of zero in the time domain. As can be seen, the sharp transitions have been smoothed and it is also easier for an ultrasonic transducer with limited bandwidth to generate such fade-in and fade-out signals. Accordingly, the frequency responses of the pulse-shaped OOK and BPSK signals are illustrated in Fig. 2.7(c) and (f). It is evident from both the spectra that the sidelobes have been mostly eliminated in both lower and higher frequencies, thus most of the energy has been concentrated within the defined bandwidth. Note that the two low peaks at 100 kHz in Fig. 2.7(c) and (f) are the second harmonics of the original signal with the fundamental frequency of 50 kHz.

In summary, for narrowband ultrasonic transducers, the electro-mechanical inertia leads to long signal transient time. To allow sufficient time for both signal generation and detection while maintaining the highest data rate possible, a 0.1 ms bit duration was used for all subcarrier signals throughout Chapter 2.

2.3.2   Signal generation and synchronization
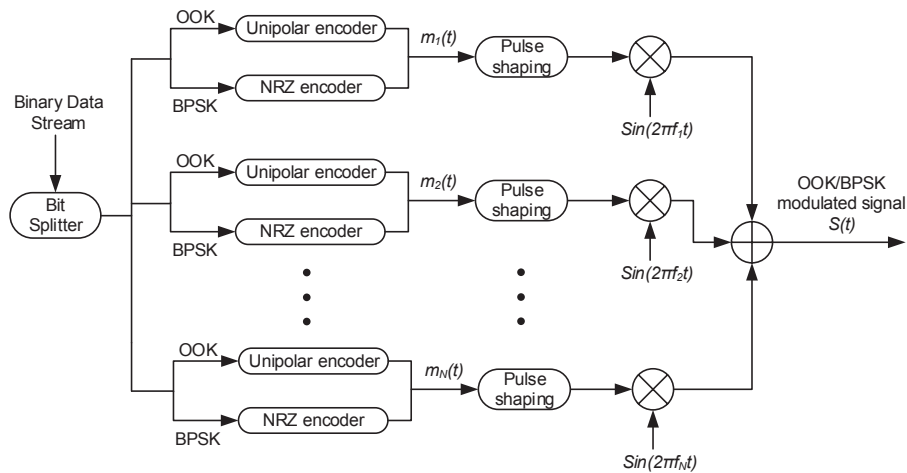
Figure 2.8: Schematic diagram of the multichannel OOK and BPSK modulator.

The diagram of a multichannel OOK and BPSK modulator used to generate a suitable transmission digital waveform is shown in Fig. 2.8. The binary

stream to be transmitted was sent into a bit splitter before distributing to different parallel channels. The split binary data were then encoded using a unipolar encoder and a non-return-zero encoder for OOK and BPSK schemes, respectively. For OOK, the voltage level used for a bit "1" was $+1$ V and a bit "0" was 0 V. For BPSK, a bit "1" was equal to $+1$ V and a bit "0" was equal to -1 V to provide a $180°$ phase change before being modulated to different carrier waves. The message sequences $m_1(t)$ to $m_N(t)$ were then filtered by a raised cosine filter before simultaneously modulating to different carrier frequencies. All these modulated signals were finally added together, giving a single waveform $S(t)$.

The space between two adjacent subchannels was determined by the width of the mainlobe of the modulated signal spectrum. As the amplitude of the OOK message signal varies from 0 V to $+1$ V, the modulated signal $y_{OOK}(t)$ can then be expressed as

$$
\begin{aligned}
y_{OOK}(t) &= [1 + m(t)] \cdot c(t) \\
&= [1 + cos(2\pi f_m t)]sin(2\pi f_c t) \\
&= sin(2\pi f_c t) + \frac{1}{2}sin[2\pi(f_c - f_m)t] + \frac{1}{2}sin[2\pi(f_c + f_m)t],
\end{aligned}
\tag{2.4}
$$

where $m(t)$ is the message signal at a rate of f_m and $c(t)$ is the carrier wave with a frequency of f_c. As can be seen from (2.4), the modulated signal has a carrier frequency component, and there are two sidebands with reduced power at frequencies $f_c + f_m$ and $f_c - f_m$. Since a bit duration of 0.1 ms was used, one complete cycle length of the message signal was then 0.2 ms, giving a message rate (f_m) of 5 kHz. It is also evident from Fig. 2.7(c) that three peaks at 45 kHz, 50 kHz and 55 kHz can be found from the spectrum of the 50 kHz OOK modulated signal. For BPSK, as the message signal varies from -1 V to $+1$ V, the modulated signal $y_{BPSK}(t)$ can be given as

$$y_{BPSK}(t) = m(t)c(t) = \frac{1}{2}sin[2\pi(f_c - f_m)t] + \frac{1}{2}sin[2\pi(f_c + f_m)t]. \qquad (2.5)$$

Here the modulated BPSK signal contains power only at the sum and difference of f_c and f_m. Accordingly, the spectrum in Fig. 2.7(f) shows two distinct peaks at both 45 kHz and 55 kHz. In this case, the subchannels should be evenly spaced with a gap of at least 10 kHz to prevent severe inter-channel interference. Initially, six frequency channels from 50 to 110 kHz with a channel spacing of 12 kHz were used as shown in Fig. 2.9.
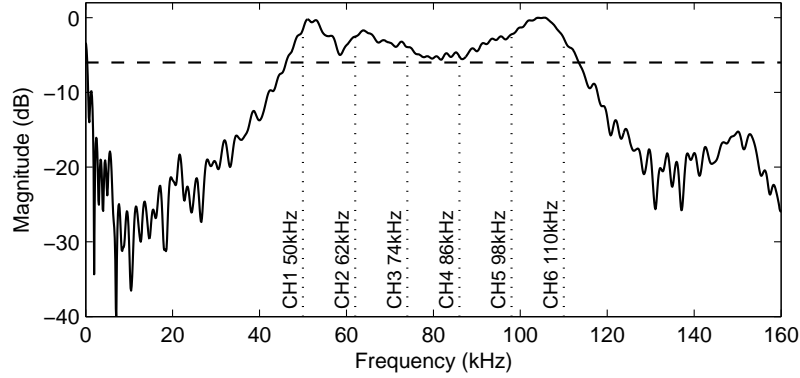
Figure 2.9: Channel allocation.

Synchronization is a fundamental requirement for any wireless communication system to work properly. Once an ultrasonic signal packet is detected, it is critically important for the receiver to identify the starting point of the arriving packet. Synchronization can be achieved by correlating the received signal with a known pilot signal being transmitted in front of the information data packets. As widely used in practical radar systems for range detection, a linear frequency modulation (LFM) signal whose frequency sweeps from low to high within a certain time is used as the pilot for wireless synchronization [9]. The LFM signal is described by the following equation

54

$$s(t) = 0.5[1 - cos(\frac{2\pi t}{T})]cos[2\pi t(f_0 + \frac{k}{2}t) + \phi]. \tag{2.6}$$

Here, f_0 is the starting frequency and k is the rate of frequency change. Note that in order to smooth out the sudden changes in signal amplitude and improve the resolution of the received signal during signal processing, the LFM signal is multiplied by a Hanning window $0.5[1 - cos(2\pi t/T)]$ which starts and ends with zero. Fig. 2.10 (a) shows a time-domain LFM signal with a frequency changes from 50 to 150 kHz within 0.5 ms, multiplied by a Hanning window, showing a bell-shaped amplitude with a fade-in and fade-out characteristic. Its frequency spectrum in Fig. 2.10 (b) presents a concentrated shape without any redundant sidelobes.
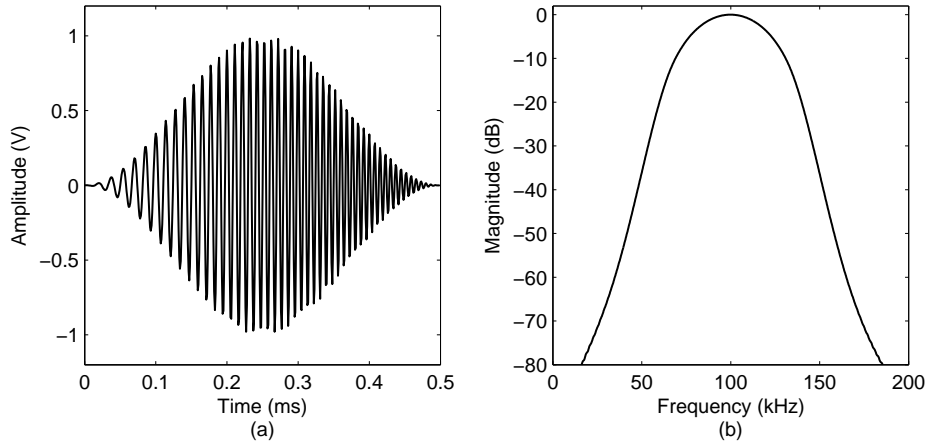
Figure 2.10: Hanning windowed LFM signal in (a) time domain; and (b) frequency domain.

By performing correlation of a known LFM signal and the received signal using a matched-filter at the receiver, the maximum energy of the matched-filter output indicates the start of the arriving data sequence. The response of the matched filter to a signal $s(t)$ is defined as [8]

$$g(t) = \int_{-\infty}^{\infty} s(\tau)h(t - \tau)d\tau, \tag{2.7}$$

55

whose impulse response is $h(t) = s^*(T-t)$, where $s(t)$ is assumed to be confined to the time interval $[0, T]$. The matched filtering of a received signal $r(t)$ then produces the output signal

$$
\begin{aligned}
y_{MF}(t) &= \int_{-\infty}^{\infty} r(\tau)h(t-\tau)d\tau \\
&= \int_0^T r(\tau)s^*(\tau)d\tau.
\end{aligned}
\tag{2.8}
$$

The main advantage of using a LFM signal is that it provides precise timing resolution for frame synchronisation as the matched-filter is the optimal linear filter that maximises the signal-to-noise ratio (SNR) in the presence of additive stochastic noise [8, 10].

2.3.3 Simulation model

When modelling ultrasonic signal transmissions in air, three filters to compensate for absorption of sound in air, beam divergence and transducer frequency response were included. The atmospheric absorption factor α in dB/m was introduced in (1.12), Section 1.3.2. Due to diffraction effects, the ultrasound beam diverges from the transmitter aperture. Hence, different amounts of the transmitted energy will be intercepted by the receiver depending on the receiver area, propagation range and the frequencies used. According to the angle of divergence, γ_0, defined in (1.16), the energy loss due to beam spreading, L_{sprd}, in dB can then be calculated in terms of the ratio of the transducer radius, $D/2$, and the beam spread radius at a particular range, d,

$$
L_{sprd} = 20 log_{10} \left(\frac{D}{2d \, tan\gamma_0} \right).
\tag{2.9}
$$

Recent work [11] recorded experimental results when different off-axis trans-
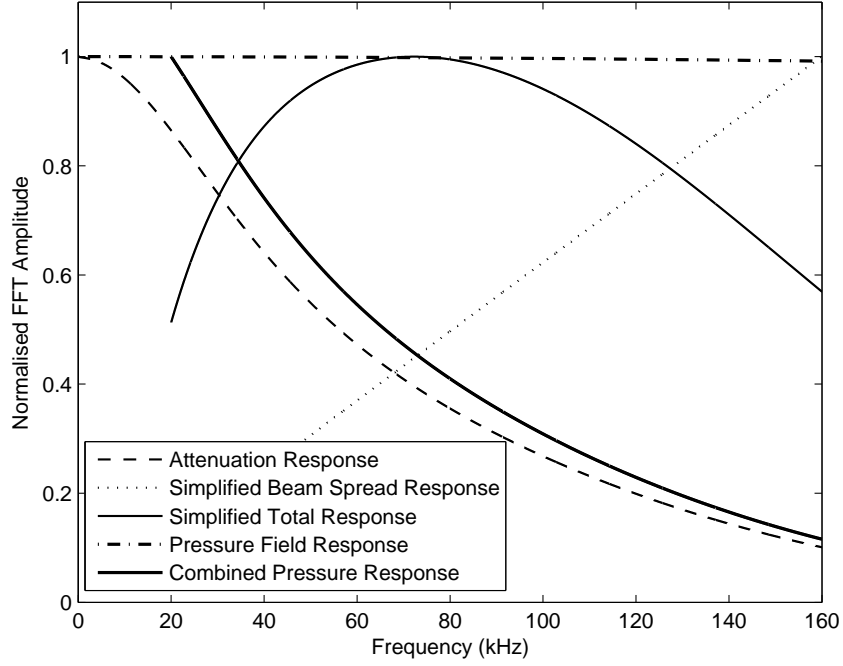
Figure 2.11: Comparison of simulated response for attenuation, simplified beam spread, pressure field at 3 m.

ducer displacements occurred that gave a reasonable match with the pressure-field model introduced in Section 1.3.3 for an ultrasonic communication channel at relatively short ranges. Fig. 2.11 compares the on-axis responses at 3 m using both the simplified beam spread model (2.9) and the full pressure field model (1.21), including their combined responses with the effects of attenuation. As can be seen, the simplified model shows that there should be less beam spreading at higher frequencies while the pressure field model gives almost a constant response at all frequencies. As a result, their combined responses after adding attenuation produced two different response curves which may affect the simulations significantly. The two models are compared with experimental results in Section 2.3.4. The received signal is also shaped by both the transmitter and receiver transducer responses at different sub-carrier frequencies. To simplify the simulation, a pulse signal was sent from the transmitter to the receiver transducer over an air gap of 50 mm. Note that 50 mm is the mini-
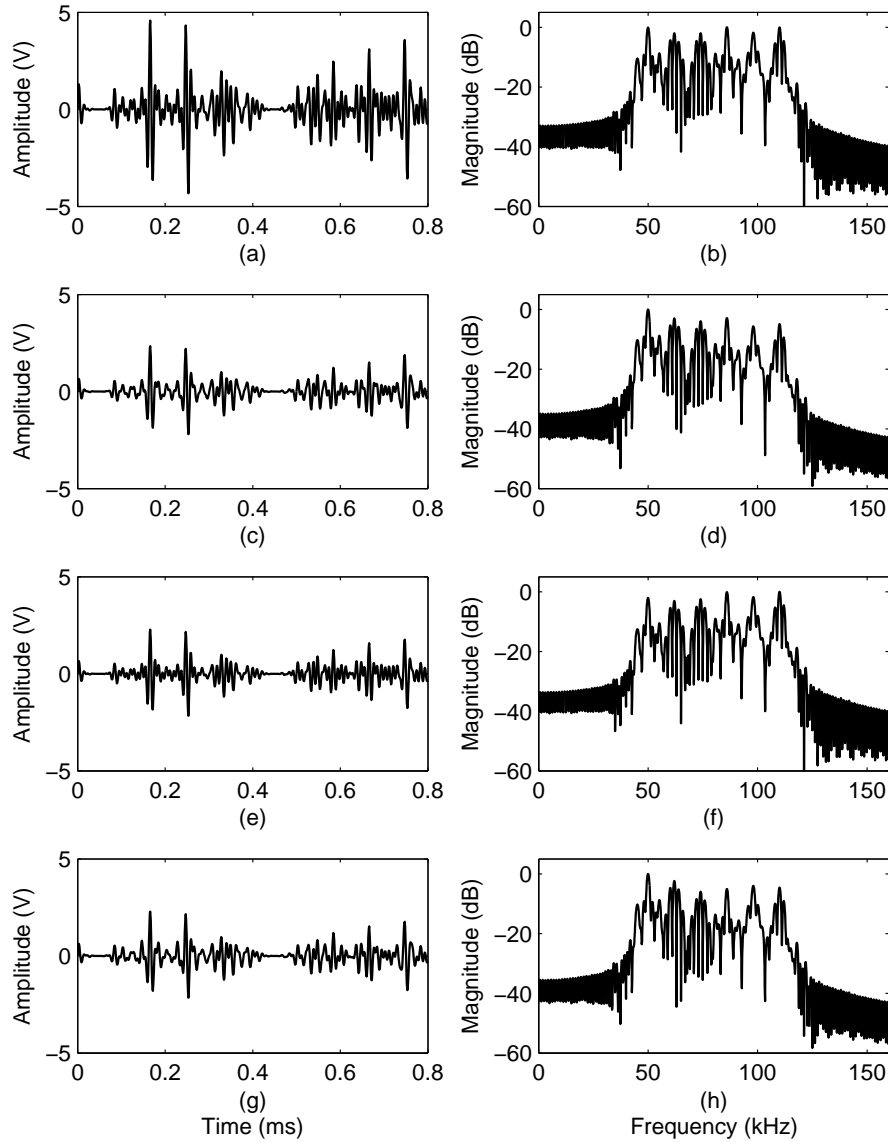
Figure 2.12: Simulation of a filtered multichannel OOK signal at 3 m: (a) original signal in the time domain , (b) its spectrum, (c) shaped by the atmospheric absorption filter, (d) its spectrum, (e) shaped by atmospheric absorption + beam spreading filter, (f) its spectrum, (g) shaped by atmospheric absorption + beam spreading + system response filter, and (h) its spectrum.

mum separation of the transducers that can distinguish the original pulse signal from its reflected echoes from the surface of the transmitter. The transducer frequency response was then calculated based on the pulse signal captured by the receiver. The received signal over different transmission ranges can then be

simulated and predicted by implementing the above three filters. In addition, the background noise in the air channel was adequately represented by additive white Guassian noise (AWGN), and was added to simulate electronic noise to match the experimental conditions more closely.

Fig. 2.12 (a) and (b) illustrate a representative multichannel OOK signal waveform before transmission in the time domain and frequency domain, respectively. Fig. 2.12 (c), (e) and (g) then show the predicted effects on the OOK signal that contributed by different filters using the simplified model after transmitting through an air gap of 3 m. Accordingly, their spectra are shown in Fig. 2.12 (d), (f) and (h). The original signal is firstly filtered by the attenuation response, giving a time-domain signal with reduced amplitude in Fig. 2.12 (c). Its spectrum in Fig. 2.12 (d) gradually declines with the increase of frequency. By applying both attenuation and beam spreading filters, the signal looks more dense in Fig. 2.12 (e) compared with the one in Fig. 2.12 (c). This is because low frequencies suffer more energy loss than high frequencies in terms of beam spreading. It brings the high-frequency components back to a higher amplitude level than that of the low-frequency ones as can be seen in the spectrum in Fig. 2.12 (f). System response is then introduced, it boosts the energy at 50 kHz channel and further shapes the overall channel response as shown in Fig. 2.12 (h).

2.3.4 Signal detection

All experiments were carried out in an indoor laboratory with negligible air turbulence and a low multi-path interference set-up. Room temperature was measured at 20°C under an atmospheric pressure of approximately 1 atm, and the relative humidity recorded was around 72%. Transmitter and receiver transducers were laser aligned to have coincident centre normals, allowing ease of simulation. Fig. 2.13(a) shows a received Hanning-windowed LFM synchro-
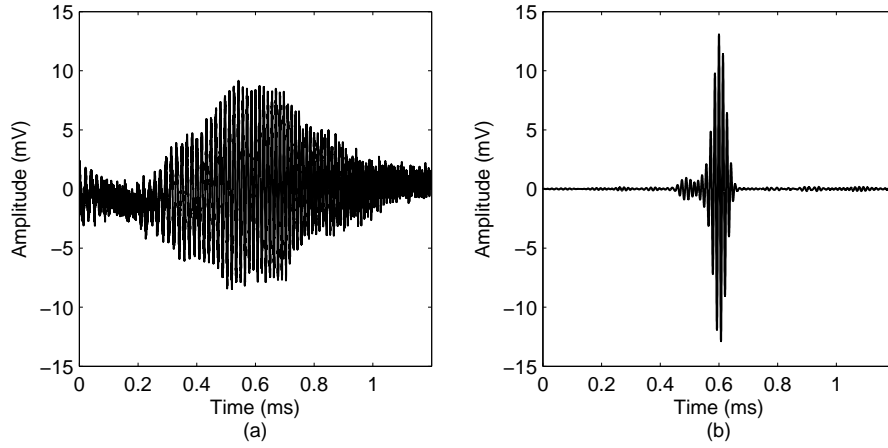
Figure 2.13: Wireless synchronization: (a) received LFM signal at 10 m; and (b) its matched filter output.

nization signal at 10 m with low SNR. The signal had a duration of 1 ms with its frequency swept from 50 kHz to 100 kHz. By performing cross-correlation of a known signal and the received signal in noise using a matched filter, the resulting waveform in Fig. 2.13(b) shows a large enhancement of SNR which enables a precise and robust detection of the starting point of the incoming signal packets. Example ASCII characters "Hello!" were encoded and modulated using the OOK modulation scheme described previously. Each character was represented by 8 bits with a bit duration of 0.1 ms. Since there were 6 channels transmitted simultaneously, the system data rate achieved was 60 kb/s. Fig. 2.14 illustrates simulated received OOK signals using both simplified and pressure field models compared to the experimental signal in the time and frequency domains over 3 m, respectively. As can be seen, all three time domain signals in Fig. 2.14 (a), (c) and (e) are visually similar. In the frequency domain, good agreement between the simulated signal using the simplified beam spread model and the actual experimental signal can be seen in Fig. 2.14 (d) and (f). However, the simulated signal spectra using the full pressure field model in Fig. 2.14 (b) gives a steeper decay along the frequency axis which does not match the experiment well. Therefore, to predict different frequency signals more accurately and also

60
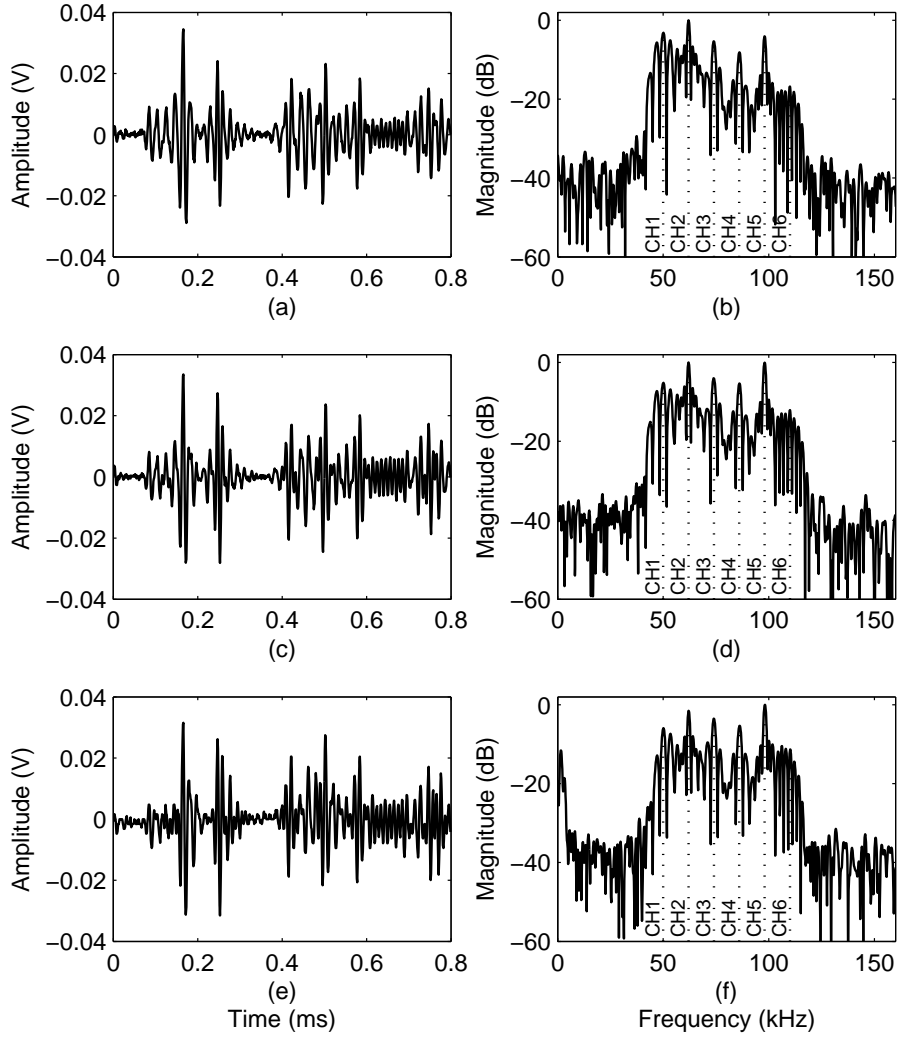
Figure 2.14: Comparison of simulated and experimental signals over 3 m: (a) time domain simulated received OOK signal using pressure field model, (b) its spectra, (c) time domain simulated received OOK signal using simplified model, (d) its spectra, (e) time domain received OOK signal and (f) its spectra. Note that CH1 - CH6 are channel 1 to channel 6.

to save computational effort, the simplified model was used instead of the full pressure field model for on-axis transducer set-ups. Note that only OOK signals and spectra are presented here as illustrative examples; similar good agreement was achieved with BPSK.

61

2.3.5 Signal demodulation

A typical multichannel OOK and BPSK demodulator is shown in Fig. 2.15. The received six-channel signal $S_n(t)$ was band-pass filtered by a Butterworth filter to extract the different frequency channels. Phase shift was minimised by implementing a zero-phase filter which processed the input data in both forward and reverse directions. For multichannel OOK, the filtered signals at individual channels were envelope detected using a Hilbert transform [12] before being decoded by bit comparators. For BPSK demodulation, the filtered signal was multiplied by a coherent reference carrier with the corresponding frequency in that channel. The resultant waveform was low-pass filtered before being sent to a bit judge. All decoded bits were then combined into a single bit sequence. The demodulation process of both simulation and experiment for OOK signals over 3 m is illustrated in Fig. 2.16. The simulated filtered signal in Fig. 2.16 (a) represents the second character 'e' as an illustrative example. As can be seen, amplitude peaks can be clearly identified to distinguish logic "1"s and "0"s.
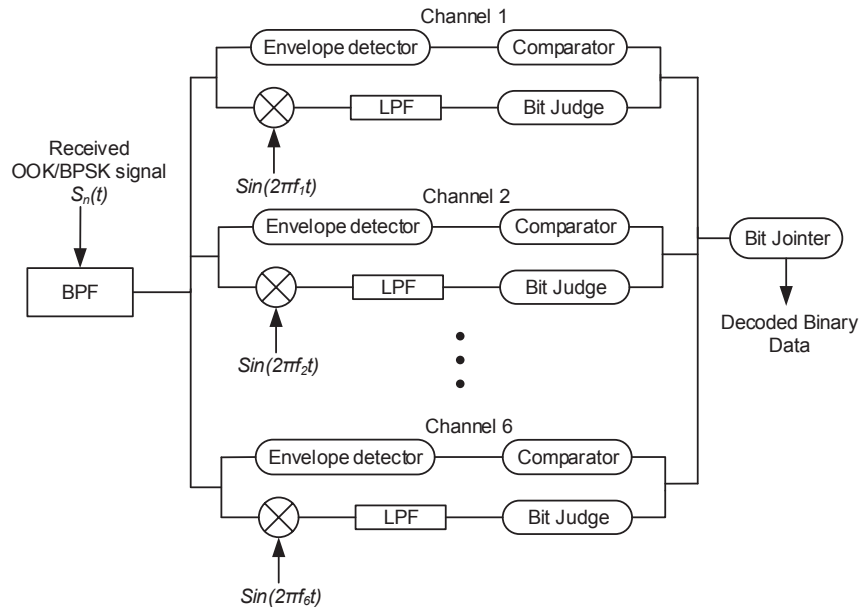
Figure 2.15: Schematic of the multichannel OOK and BPSK demodulator.
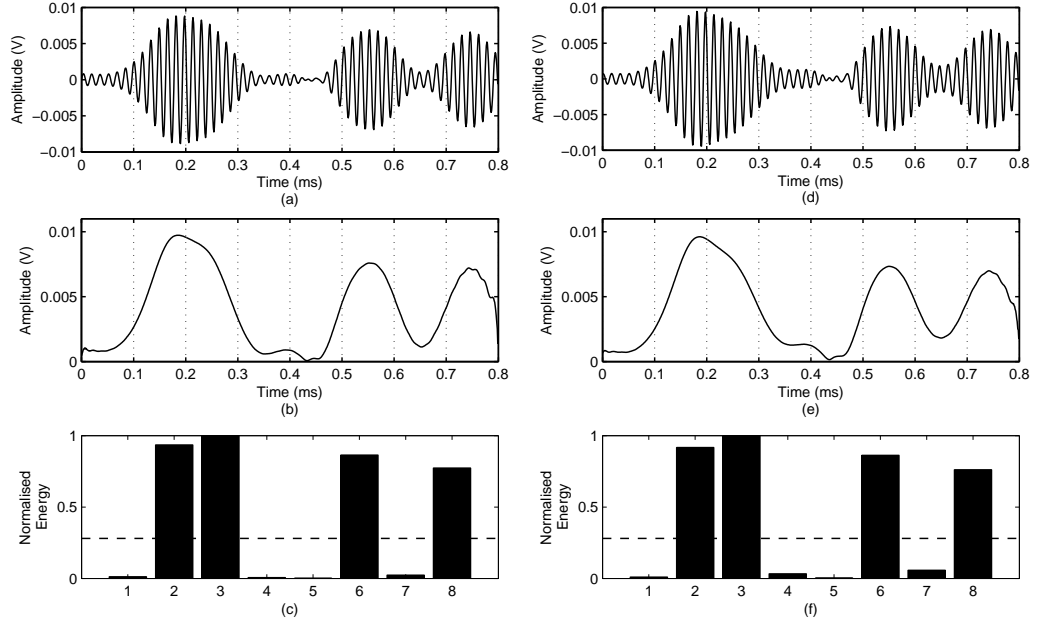
Figure 2.16: Simulated OOK demodulation process over 3 m: (a) band-pass filtered OOK signal for letter 'e', (b) envelope of the filtered signal, (c) normalised energy bar plot under the curve of each bit duration. Experimental OOK demodulation process: (d) band-pass filtered OOK signal for letter 'e', (e) envelope of the filtered signal, (f) normalised energy bar plot under the curve of each bit duration.

Fig. 2.16 (b) presents the plotted envelope by taking its absolute value. Afterwards, the energy under the curve over the central 20% of each bit period was calculated and normalised, giving the bar plot shown in Fig. 2.16 (c). This is to minimise the energy leakage effects so that the differences between energies of "1"s and "0"s are sufficiently distinct to deliver correct decoding results when compared with a threshold value. The threshold value was determined by a large number of error tests over short, medium and long ranges. Twelve thousand packets of six 8-bit random ASCII code sequences were modulated and simulated over distances of 0.2 m, 2 m and 5 m with SNR values of 3 dB, 25 dB and 35 dB respectively. Numbers of errors were collected in terms of different energy threshold values from 0 to 1 with a step of 0.01. The minimal numbers of errors all occurred when using a threshold value of 0.28 over the three different distances. Therefore, the demodulation threshold value was

set at 0.28. Accordingly, the experimental demodulation in Fig. 2.16 (d), (e) and (f) show a good match with the simulation. Simulated and experimental demodulations of the BPSK scheme described previously are also compared in Fig. 2.17. The figures show a good prediction by the simulation. Fig. 2.17 (b) shows the simulated result after the coherent multiplication of the band-pass filtered signal in Fig. 2.17 (a). If the amplitude of the low-pass filtered signal in Fig. 2.17 (c) detected at the centre of each bit duration was larger than 0, a bit "1" is extracted; conversely, an amplitude smaller than 0 implies a bit "0" was decoded. As can be seen in the experimental demodulation in Fig. 2.17 (e) and (f), the opposite phases for "1"s and "0"s are clearly displayed after coherent multiplication and it is straightforward to decode the low-pass filtered signals.
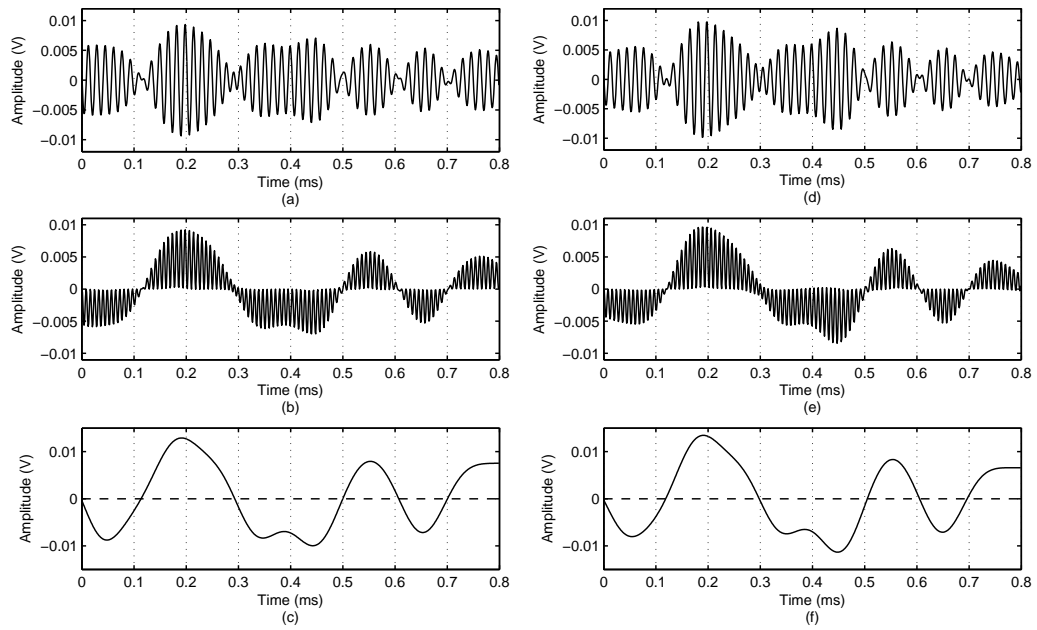
Figure 2.17: Simulated BPSK demodulation process over 3 m: (a) band-pass filtered BPSK signal for letter 'e', (b) waveform after coherent multiplication, (c) low-pass filtered signal of the waveform in (b). Experimental BPSK demodulation process: (d) band-pass filtered OOK signal for letter 'e', (e) waveform after coherent multiplication, (f) low-pass filtered signal of the waveform in (e).

Over propagation distances ranging from 0.5 m to 8 m with a step of 0.5 m, the rms values of both the experimental OOK and BPSK signals at different
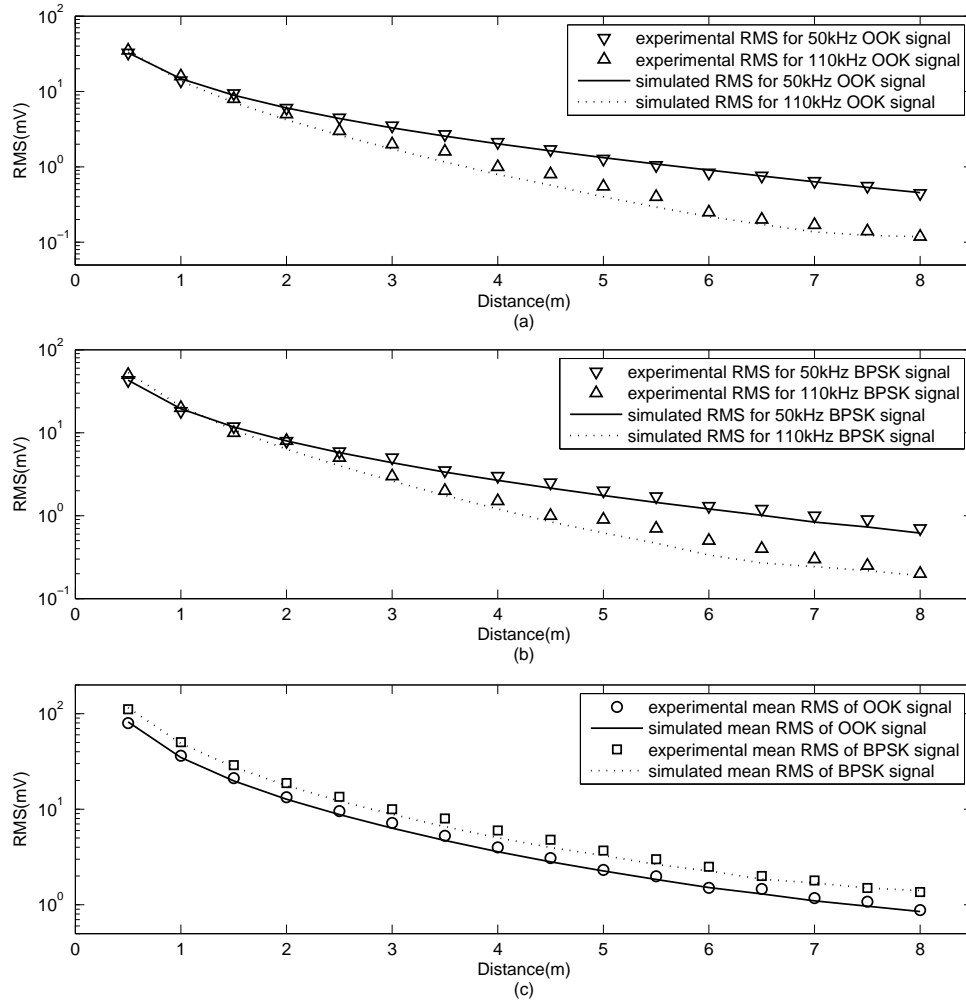
Figure 2.18: Comparison of experimental signal rms values with theoretical predictions over different distances for: (a) 50 kHz and 110 kHz OOK signals, (b) 50 kHz and 110 kHz BPSK signals and (c) combined 6-channel OOK and BPSK signals.

frequencies can be accurately predicted by the theory as Fig. 2.18 (a) and Fig. 2.18 (b) show. The figures again illustrate that the low frequency signals have smaller rms values over short ranges than high frequency signals for both OOK and BPSK modulation schemes due to beam spreading. However, at longer propagation ranges, atmospheric absorption starts to increase and become dominant. The mean rms curve for the combined signal of all six channels over different ranges is simulated in Fig. 2.18 (c). It should be noted that as a

constant-envelope modulation, the BPSK scheme produces signals with higher rms values over all ranges than the OOK scheme. It also indicates that the model in this work can be used to simulate other modulation schemes and predict signals as the simulated curves match the experimental data well.

2.4 System reliability

To investigate the reliability of the system, it was necessary to look at the BER of both modulation schemes over different ranges. Therefore, 1200 packets of six 8-bit random binary ASCII code streams were generated and transmitted continuously through the channel. BER information was recorded over transducer separations of up to 8 m with increments of 0.5 m. The process was repeated 10 times, and the results were then averaged. The BER results for OOK and BPSK schemes using different roll-off factors are illustrated in Fig. 2.19 (a) and Fig. 2.19 (b) respectively. As can be seen in Fig. 2.19 (a), the OOK scheme started to have decoding errors at 5 m using different roll-off factors from 0 to 1. The BER increases with the transmission distance for all roll-off factors after that. It is obvious that with a zero roll-off the errors were at the lowest level at all distances, and it gave the system error-free transmission up to 5.5 m. However, in Fig. 2.19 (b), the BER for the BPSK scheme drops from a high level at short distances before rising up again after 5 m. It is been proved that most of the errors occurring at short ranges are due to the echo signal reflected from the surface of the transmitter, as the number of errors drops significantly when the receiver is placed with an oblique angle to the transmitter centreline. It is noticed that the number of errors using the BPSK scheme over long ranges is much smaller than that using the OOK scheme. Again, a roll-off factor of 0.2 which provides the lowest BER for the BPSK scheme can be determined from this figure. It is intuitive to visualize the signal distortion using eye diagrams as shown
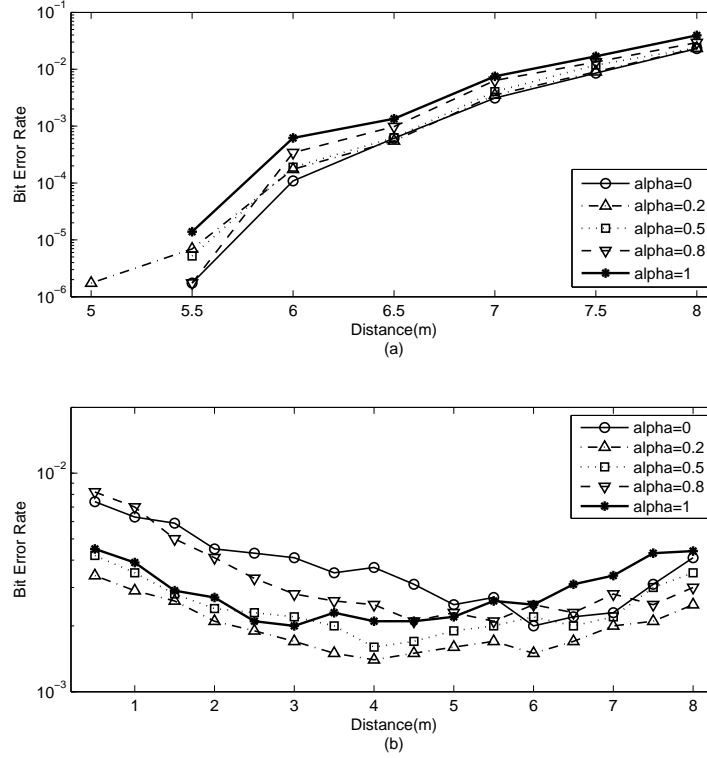
Figure 2.19: Comparison of the experimental BER for both (a) OOK and (b) BPSK signals over different transmission distances using different roll-off factors.

in Fig. 2.20. An eye diagram is the synchronised superposition of all possible bit transitions within a certain signalling interval. As can be seen, over 3 m, both the 50 kHz and 110 kHz OOK signals have more open eyes in Fig. 2.20 (a) and (b) than those of the BPSK signals in Fig. 2.20 (c) and (d). Therefore, it indicates that the OOK signals in both low and high frequency channels are less distorted than the BPSK signals. The eye of the 110 kHz BPSK signal in Fig. 2.20 (d) is completely closed. Note that narrow-band transducers have a relatively high-Q resonant response so that there is insufficient channel spacing to accurately represent fast phase changes, especially for high frequency BPSK signals in a multichannel scheme.

Previous work on multichannel communication investigated high frequency ASK at 250 kHz with only a 0.5 m transmission distance and achieved an
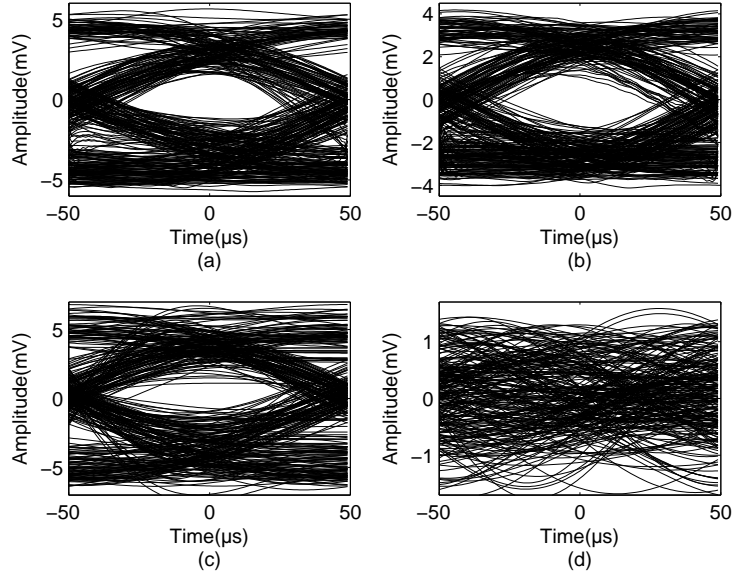
Figure 2.20: Eye diagrams for OOK signals in 50 kHz (a) and 110 kHz (b) channels and BPSK signals in 50 kHz (c) and 110 kHz (d) channels over 3 m.

80 kb/s data transfer rate using prototype transducers [13]. The spectral efficiency of the system measured in b/s/Hz was 0.76. However, in this work, the over-all system data rate achieved was up to 60 kb/s using a pair of commercially available SensComp 600 ultrasonic transducers. The bandwidth efficiency was 1 b/s/Hz, which is 32% higher compared to the previous work. System performance was tested in terms of the BER characteristics. The BER results shows that the OOK modulation scheme implemented here was capable of achieving error free decoding over ranges of up to 5 m. Previous short-range work by other authors [14] suffered from much higher BER (50% at 2.38 m) at a data rate of 83 kb/s using a single-band OOK modulation scheme, with error-free transmission only at ranges below 1.6 m.

2.5 Range-dependent modulation scheme

In order to have more effective transmission, a multichannel scheme is proposed using different modulation schemes depending on the range to ensure

Table 2.1: Channel arrangement over error-free ranges up to 2 m

	CH1	CH2	CH3	CH4	CH5
Operating frequency (kHz)	50	63	78	94	110
Number of cycles	5	5	5	7	10
Data rate (kb/s)	10	12.6	15.6	13.4	11

Table 2.2: Channel arrangement over error-free ranges up to 10 m

	CH1	CH2	CH3
Operating frequency (kHz)	60	80	100
Number of cycles	6	8	10
Data rate (kb/s)	10	10	10

error-free transmission. Over short ranges, data rates for different channels can be slightly increased using reduced bit times and different channel spacings. The channel arrangement detail is shown in Table 2.1. As can be seen, only five channels were used, and all of them were sampled at an integer number of cycles during each bit period. This prevents signal discontinuities, thus reducing unnecessary spectral leakage. The lowest frequency channel (Channel 1) and highest frequency channel (Channel 5), which most suffered from beam spreading loss and ultrasonic absorption respectively, contributed slightly lower data rates than the medium frequency channels so they had relatively longer bit durations. The total system data rate achieved using this channel arrangement was 63 kb/s. It is 5% higher than the data rate achieved by using the previous fixed-bit-duration and fixed-channel-spacing multichannel OOK modulation scheme with six channels. This scheme experienced error-free decoding over ranges up to 2 m. For long range ultrasonic transmission, the most distorted channels (50 kHz channel and 110 kHz channel) were not used and a larger channel spacing was assigned between medium frequency channels as shown in Table 2.2. The data rate achieved was half of the original OOK scheme. However, this new scheme only started to experience transmis-
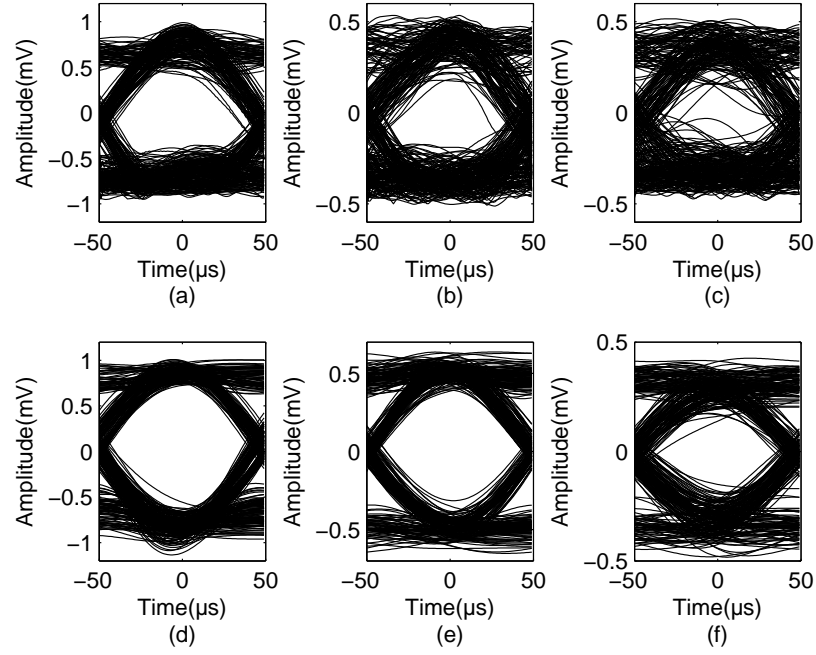
Figure 2.21: Eye diagrams for OOK signals in 60 kHz (a), 80 kHz (b) and 100 kHz (c) channels and BPSK signals in 60 kHz (d), 80 kHz (e) and 100 kHz (f) channels over 8 m.

sion errors beyond 7.5 m. As Fig. 2.19 (b) indicates, much less error occurs when using a multichannel BPSK scheme than when using a multichannel OOK scheme over long ranges. Therefore, it is possible to re-use BPSK modulation over longer ranges with a reduced data rate. The same channel allocation in Table 2.2 was implemented using BPSK modulation, and the error-free range was extended to 10 m according to the experimental results. The eye diagrams of 3-channel OOK and BPSK signals over 8 m are compared in Fig. 2.21. As can be seen, BPSK signals have better eye shapes with less jitter and amplitude variation in all three channels than OOK signals.

The BER results of different schemes can be used as an indicative guide in a two-way communication system when distance measurement is available. Within 2 m, 5-channel OOK with a data rate of 63 kb/s could be used. Between 2 and 5 m, the system switched to 6-channel OOK with 60 kb/s data transfer rate. Beyond 5 m, the transmission range without measurable errors could be

achieved using 3-channel BPSK modulation scheme with a reduce data rate of 30 kb/s. The transmission distance can be estimated based on the received signal strength (RSS) [15, 16]. As the rms values of the received signal in different propagation ranges can be predicted by the simulation model, different schemes are chosen in terms of the distance measured. Token signals according to the scheme used should be added and sent with the output signal to initialize the corresponding demodulation scheme. Therefore, a reliable two-way indoor ultrasonic link up to 10 m should be possible using the range-dependent scheme.

2.6   Transducer misalignment

The situation when the transducer centre normals are not coincident over long ranges was also studied in this work. As Fig. 2.22 shows, the receiver transducer (Rx) was placed away from the transmitter transducer (Tx) at a distance $d = 5$ m. The maximum distance of lateral displacement for error-free transmission using the 3-channel scheme illustrated in Table 2.2 for both OOK and
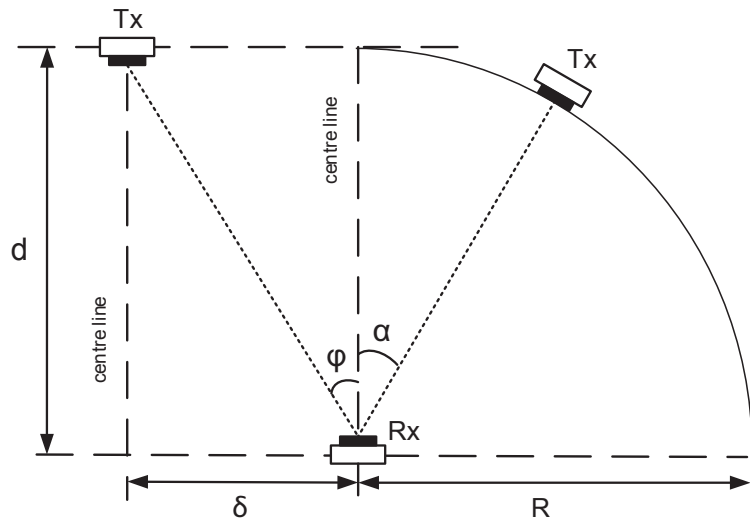
Figure 2.22: Diagram of transducer arrangements with lateral displacement δ, and oblique angle α.

71

Table 2.3: Comparison of BER using OOK and BPSK schemes at 0.4 m lateral displacement

BER	Over-all	Channel 1	Channel 2	Channel 3
OOK	1.79e-2	0	1.18e-4	1.78e-2
BPSK	1.17e-3	0	0	1.17e-3

Table 2.4: Comparison of BER using OOK and BPSK schemes at $7°$ oblique angle

BER	Over-all	Channel 1	Channel 2	Channel 3
OOK	8.12e-3	0	0	8.12e-3
BPSK	9.43e-4	0	0	9.43e-4

BPSK modulation was found to be 0.35 m, i.e. $\delta = 0.35$ m or 7% of "d". At this distance, the transducers were separated at an angle $\varphi = 4°$. The beam spreading angle for the highest frequency channel (100 kHz channel) is $6.3°$, and for the lowest frequency channel (60 kHz channel) is $10.5°$. In this case, all frequency channel signals can still be detected by the receiver transducer. As Table 2.3 shows, the 3-channel BPSK scheme has a much better performance than the 3-channel OOK scheme at 0.4 m lateral displacement in terms of the BER results over all channels. The BER reduces with decreasing channel frequency for both schemes as expected, as less high frequency energy can reach the receiver transducer. Apart from the lateral displacement experiment, it is also interesting to study the bit error tolerance when the two transducers are placed with different oblique angles as also shown in Fig. 2.22. The transmitter was separated from the receiver by a radius of $R = 5$ m, and the BER tests were carried using different oblique angles α with $1°$ increment. The results show that the bit errors started to occur at an oblique angle α of $7°$ for both 3-channel OOK and BPSK schemes. Bit error details are shown in Table 2.4. As can be seen, the high frequency channels are more prone to error, and the BPSK scheme is more robust than the OOK scheme in terms of BER characteristics. Fig. 2.23 (a) and (b) compare the signal rms values with theoretical predic-
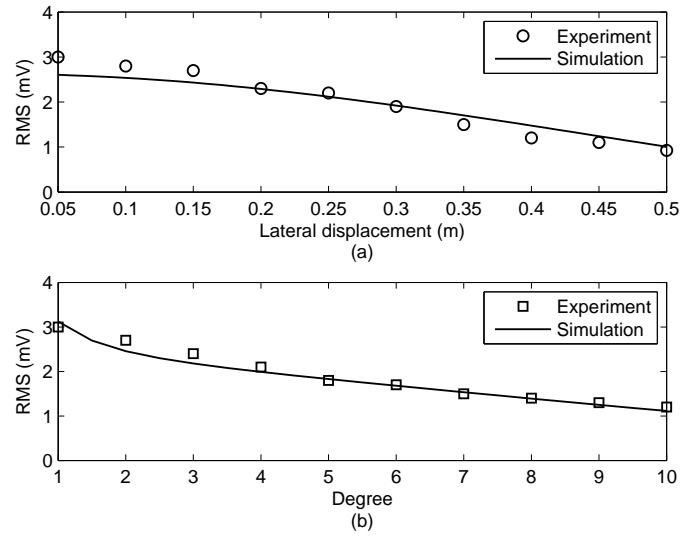
Figure 2.23: Comparison of experimental signal rms values with theoretical predictions with different: (a) lateral displacements and (b) oblique angles at a transducer separation of 5 m.

tions using the full pressure field model with different lateral displacements and oblique angles respectively, and good agreements were found between the two.

From both lateral displacement and oblique angle experiments, it suggests that alignment for ultrasonic communication is important though the system can tolerate errors with a small amount of lateral displacement and oblique angle. Thus, divergent or omnidirectional transducers are preferred. It also shows that low frequency signals are a better choice than high frequency signals for error-free transmission with off-centreline transducers.

2.7 Conclusions

It has been shown, in both simulation and experiment, that multichannel error-free data communication using both OOK and BPSK modulation schemes was practical over ranges up to 10 m. By using a pair of commercially available ultrasonic transducers with a nominal frequency of 50 kHz, all results were

73

based on multichannel transmission operating within frequencies from 50 kHz to 110 kHz in terms of 6 dB bandwidth. The maximum data rate achieved using a single modulation scheme was 60 kb/s, with 6 parallel 8-bit channels being represented by 0.8 ms duration time signals. System bandwidth efficiency was 100% in b/s/Hz. Ultrasonic signals were simulated including the effects of ultrasonic absorption in air, beam spreading loss, transducer response and AWGN. Simulation predicted the signals successfully, and had an excellent agreement with the experimental results based on signal characteristics in both time and frequency domains, the demodulation process and rms values over different transmission ranges. BER performance was characterised over different distances, and error-free decoding was achieved at ranges of up to 5 m using a multichannel OOK scheme. More reliable long-range links were also achieved by using a range-dependent multichannel modulation scheme. Individual bit times were assigned to each channel to achieve error-free transmission over all ranges up to 10 m using a combination of OOK and BPSK schemes. Transducer arrangements with lateral displacements and oblique angles were tested using both multichannel OOK and BPSK giving error-free transmission at reduced data rates. It was concluded that 3-channel BPSK was more robust than 3-channel OOK in both aligned and misaligned conditions. Wireless synchronization was also achieved by ultrasonic means, instead of by hard-wired link as used in previous works.

The major contribution of the work in this chapter is that a multiple-channel airborne ultrasonic communication system using basic baseband modulation schemes was characterised in both simulation and experiment, achieving practical transmission ranges and reasonable data transfer rates for indoor applications as compared with the previous works in Fig. 2.24. However, there are more advanced multichannel modulation formats available to maximise the system throughput for ultrasonic use. The studies of these modulations will

be described in the next chapter.
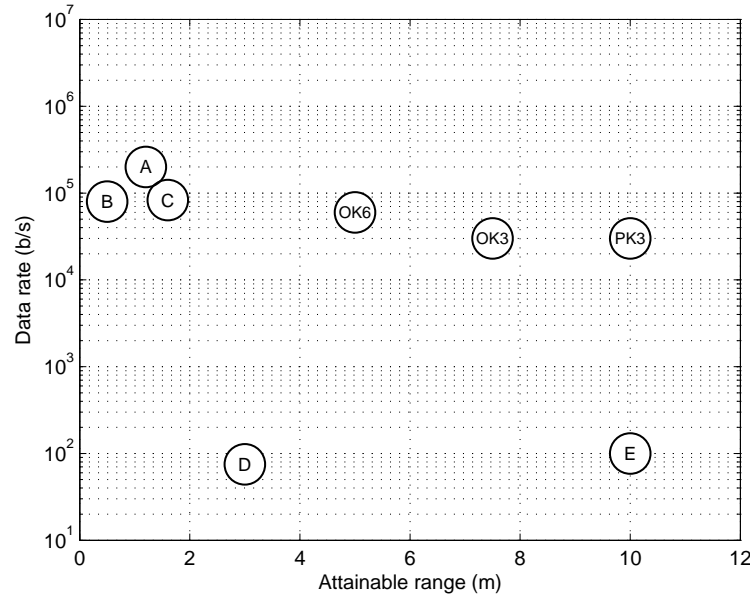
Figure 2.24: Comparison of different airborne ultrasonic data communication systems and their data rates at attainable transmission ranges. OK6 and OK3 represent 6-channel OOK and 3-channel OOK modulations, respectively, and PK3 represents 3-channel BPSK modulation. A, B, C, D, E refer to the works referenced in [17], [13], [14], [18] and [19], respectively.

2.8 References

[1] SensComp, Inc. [Online]. Available: `http://www.senscomp.com/pdfs/series-600-environmental-grade-sensor.pdf`. accessed Aug. 2015.

[2] A. Jiménez, Álvaro Hernández, J. Ureña, M. C. Pérez, F. J. Álvarez, C. D. Marziani, J. J. García, and J. M. Villadangos, "Emfi-based ultrasonic transducer for robotics applications," *Sensor. Actuat. A: Phys.*, vol. 148, no. 1, pp. 342 – 349, 2008.

[3] H. Choi and J. S. Popovics, "NDE application of ultrasonic tomography to a full-scale concrete structure," *IEEE Trans. Ultrason., Ferroelectr, Freq. Control*, vol. 62, pp. 1076–1085, June 2015.

[4] R. J. Imani and E. Robert, "Acoustic separation of submicron solid particles in air," *Ultrasonics*, vol. 63, pp. 135 – 140, 2015.

[5] H. E. Bass and L. N. Bolen, "Ultrasonic background noise in industrial environments," *J. Acoust. Soc. Amer.*, vol. 78, no. 6, pp. 2013–2016, 1985.

[6] E. McCune, *Practical digital wireless signals*. Cambridge, U.K.: Cambridge University Press, 2010.

[7] J. Gibson, *The Communications Handbook*. The electrical engineering handbook series, Boca Raton, FL, USA: CRC Press, 2002.

[8] J. Proakis and M. Salehi, *Digital Communications*. New York, NY, USA: McGraw-Hill, 2008.

[9] M. Skolnik, *Introduction to Radar Systems*. Electrical engineering series, New York, NY, USA: McGraw Hill, 2001.

[10] P. Lazik and A. Rowe, "Indoor pseudo-ranging of mobile devices using ultrasonic chirps," in *Proc. 10th ACM Conf. Embed. Netw. Sens. Syst. (SenSys)*, pp. 99–112, 2012.

[11] C. Li, D. Hutchins, and R. Green, "Response of an ultrasonic communication channel in air," *IET Commu.*, vol. 6, pp. 335–343, Feb. 2012.

[12] Y. Shmaliy, *Continuous-time signals*. New York, NY, USA: Springer, 2006.

[13] W. M. D. Wright, O. Doyle, and C. T. Foley, "Multi-channel data transfer using air-coupled capacitive ultrasonic transducers," in *Proc. IEEE Int. Ultrason. Symp. (IUS)*, pp. 1805–1808, 2006.

[14] C. Li, D. Hutchins, and R. Green, "Short-range ultrasonic digital communications in air," *IEEE Trans. Ultrason., Ferroelectr., Freq. Control*, vol. 55, no. 4, pp. 908–918, 2008.

[15] S. Holm, "Ultrasound positioning based on time-of-flight and signal strength," in *Proc. Int. Conf. Indoor Position. Indoor Navigat. (IPIN)*, pp. 1–6, Nov. 2012.

[16] C. Medina, J. Segura, and S. Holm, "Feasibility of ultrasound positioning based on signal strength," in *Proc. Int. Conf. Indoor Position. Indoor Navigat. (IPIN)*, pp. 1–9, Nov. 2012.

[17] C. Li, D. Hutchins, and R. Green, "Short-range ultrasonic communications in air using quadrature modulation," *IEEE Trans. Ultrason., Ferroelectr., Freq. Control*, vol. 56, no. 10, pp. 2060–2072, 2009.

[18] H. D. Haynes, M. A. Akeman, and V. M. Baylor, "Ultrasonic communication project, phase 1, FY 1999," tech. rep., Oak Bridge, TN, USA, Jun. 2000.

[19] S. Holm, O. Hovind, S. Rostad, and R. Holm, "Indoors data communications using airborne ultrasound," in *Proc. IEEE Int. Acoust. Speech. Signal (ICASSP)*, vol. 3, pp. 957–960, 2005.

Chapter 3

Evaluation of Orthogonal Frequency Division Multiplexing (OFDM) Schemes in Ultrasonic Communications

3.1   Introduction

Orthogonal frequency division multiplexing (OFDM) is a highly efficient form of multicarrier modulation which is extensively used in modern telecommunications, ranging from asymmetric digital subscriber line (ADSL) modem technology to 802.11 Wi-Fi wireless systems [1]. OFDM can eliminate the need for pulse shaping filtering and maximise the system throughput, therefore the work in this chapter investigated different OFDM methods applied to air-coupled ultrasonic communication, using both custom-made and commercially available capacitive ultrasonic transducers. Section 3.2 will describe the OFDM system including modulation, demodulation, phase correction and equalisation technique. The ultrasonic propagation model for signal prediction is also used to

78

simulate received signals, and compare them with the experimental results. In Section 3.3 and 3.4, system performance in both LOS and multipath scenarios will be evaluated, respectively. Section 3.5 gives the conclusions of this chapter.

3.2 OFDM system description

3.2.1 OFDM modulation

To enable the largest amount of data to be communicated using a finite frequency range, conventional FDM modulation uses relatively small symbol durations. The system then becomes more susceptible to loss of information from impulse noise, multipath distortion and other impairments. FDM also allows each channel to be band-limited to a specific frequency range by implementing a pulse-shaping filter [2]. However, this technique introduces unnecessary waste of the frequency spectrum in guard spaces between the sub-channels. It also increases the complexity of each sub-carrier modulator. OFDM is a special form of multicarrier transmission using a relatively longer symbol time, and with all the sub-carriers orthogonal to each other, meaning that cross-talk between the sub-channels is eliminated and guard bands are not required. The
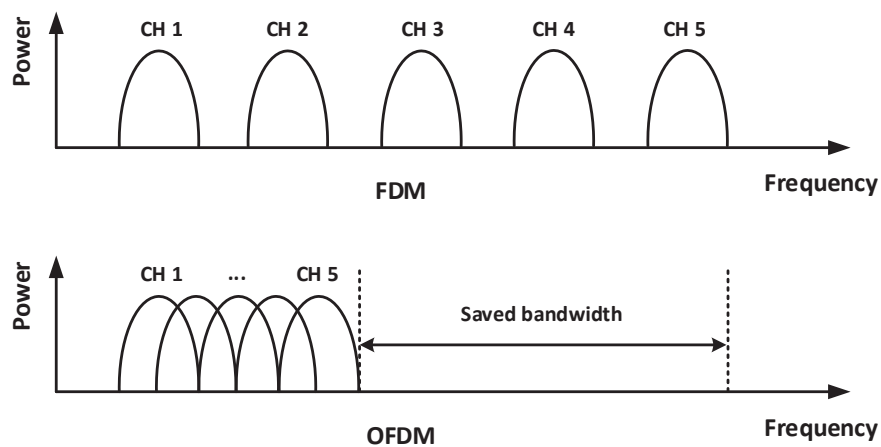
Figure 3.1: Comparison of FDM and OFDM in spectrum usage.

use of orthogonal sub-carriers allows sub-carrier spectra to overlap, thus significantly increasing the spectral efficiency. As illustrated in Fig. 3.1, compared with the FDM modulation, OFDM method uses the given bandwidth more efficiently. The orthogonality requires that the sub-carrier spacing in frequency is [3]

$$f_d = i/T_s \tag{3.1}$$

in Hertz, where T_s is the symbol time in seconds, and i is a positive integer. For minimum overall signal bandwidth, i is usually set to 1. A typical base-band OFDM signal, $s(t)$, can be written mathematically as the sum of N modulated carriers

$$s(t) = \sum_{k=0}^{N-1} s_k e^{j2\pi k f_d t} \Pi(t), \tag{3.2}$$

$$\Pi(t) = \begin{cases} 1, & 0 < t \leq T_s \\ 0, & otherwise. \end{cases} \tag{3.3}$$

Here s_k represents the OFDM symbol. Each transmitted symbol s_k takes on one of M possible signal states, and can be denoted as $s_k \in [s^{(1)}, s^{(2)}, ..., s^{(M)}]$. For example, $M = 4$, if QPSK modulation is used. $\Pi(t)$ represents a rectangular pulse with a duration of T_s. The rectangular window has a sinc-shape spectrum which makes a sub-channel spectrum heavily overlap its neighbours. Fig. 3.2 shows an illustrative frequency spectrum of five overlapped sub-channel carriers from 50 kHz to 54 kHz. As can be seen, each sub-carrier is represented by a different peak with the maximum power, and the peak of each sub-carrier corresponds directly with zero crossings of all adjacent channels.
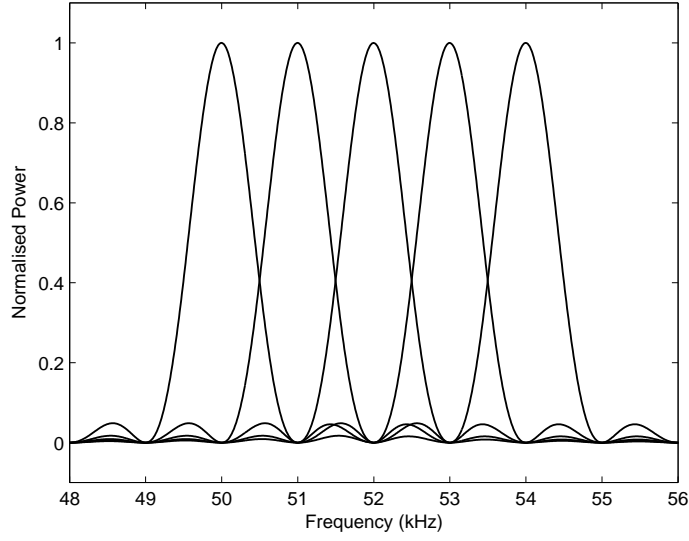
Figure 3.2: Orthogonality of OFDM sub-channel carriers.

In practice, both modulation and multiplexing are achieved digitally using an inverse fast Fourier transform (IFFT). As a result, the required orthogonal signals can be generated precisely and in a very computationally efficient way. Taking N sampling points of the signal $s(t)$ which is of symbol duration T_s, discrete values may be obtained at $t_n = n \cdot T_s/N$, $n = 0, 1, ..., N-1$, where T_s/N is the sample interval. This yields

$$s(n) = s(t_n) = \sum_{k=0}^{N-1} s_k e^{j\frac{2\pi}{N}kf_d nT_s}. \tag{3.4}$$

As $f_d = 1/T_s$, $s(n)$ may then be expressed by

$$\begin{aligned} s(n) &= \sum_{k=0}^{N-1} s_k e^{j\frac{2\pi}{N}kn} \qquad for\ n \in [0, N-1] \\ &= N \times IFFT[s_k]. \end{aligned} \tag{3.5}$$

Therefore, the OFDM signal $s(n)$ can be calculated very efficiently by applying an IFFT to the set of OFDM symbols s_k.

A typical OFDM modulator [4] is described in Fig. 3.3. In the digital domain, a series of input binary data is collected and converted to parallel combinations

81
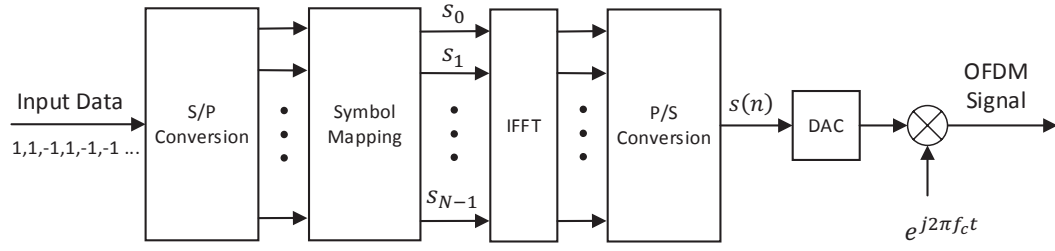
Figure 3.3: Schematic diagram of an OFDM modulator.

before mapping to corresponding constellation points on a constellation diagram, which is the two-dimensional plot of the signal states from a sequence of symbols. If the binary bits are modulated using a QPSK scheme, the OFDM symbols, s_k, can be presented as random-value complex numbers from the QPSK constellation $(\sqrt{2}/2) \cdot \{1 + j, 1 - j, -1 + j, -1 - j\}$. An IFFT operation is then performed on the parallel complex data, and a parallel-to-serial converter is then applied to produce the base-band OFDM signal, $s(n)$, which contains the original band of frequencies before it is modulated for transmission at a higher frequency. After that, a digital-to-analogue converter (DAC) is used to transform time-domain digital data to time-domain analogue data before up-converting the signal to the transmission frequency, f_c. At this point in time, the input data are OFDM modulated and ready to be transmitted.

3.2.2 OFDM signal transmission

The structure of the transmitted signal sequence is presented in Fig. 3.4. The sequence contains two major parts: preamble and data. In the preamble section, a LFM signal is transmitted at the start of the sequence for wireless synchronisation. By performing correlation of a known LFM signal and the received signal using a matched-filter at the receiver, the maximum energy of the matched-filter output indicates the start of the arriving data sequence as shown in Fig. 3.4. The LFM preamble is followed by the OFDM pilot signal. This is used for channel

82
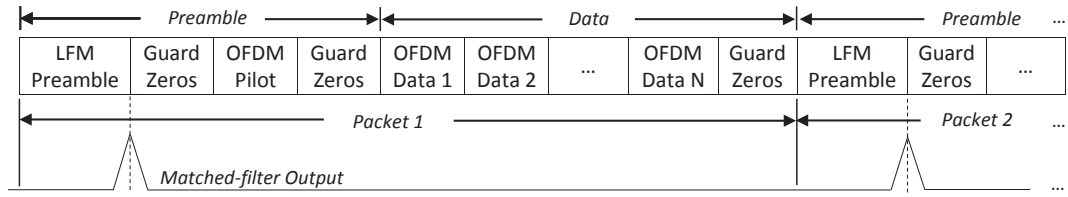
Figure 3.4: Data structure of transmitted sequence.

equalisation, and will be explained in detail in Section 3.2.3. Note that zero padding is inserted between each type of signal packet to help distinguish one from another.

All experiments were carried out in an indoor laboratory with negligible air turbulence using the same set-up and equipment as described in Chapter 2, Section 2.2.1. To better characterise ultrasonic signals over a wider range of frequency channels, a pair of prototype broadband capacitive ultrasonic transducers was investigated in the communication system. The laboratory-made transducer [5], as shown in Fig. 3.5, had a pitted backplate covered by a metallized PET membrane, and assembled into a screened casing with a 10 mm diameter aperture. Fig. 3.6 shows a schematic cross-section of the capacitive ultrasonic transducer. The backplate had small symmetric square pyramid shaped
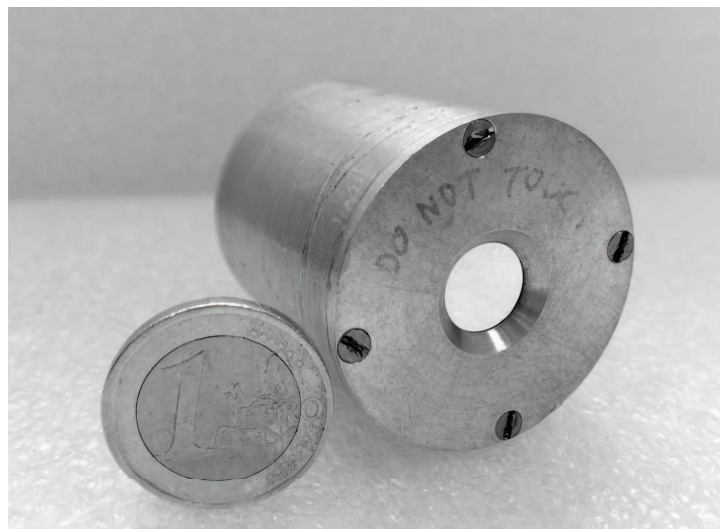
Figure 3.5: Laboratory-made air-coupled capacitive ultrasonic transducer.
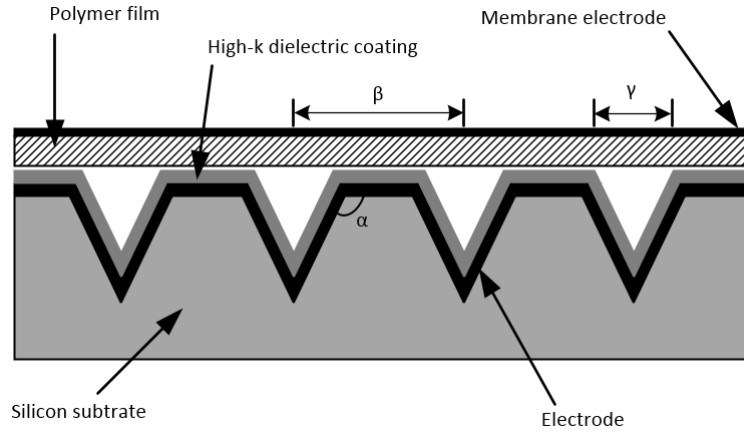
Figure 3.6: Schematic cross-section of a high-k capacitive ultrasonic transducer.

air cavities etched into a silicon substrate with edge length $\gamma = 40$ μm, pit separation $\beta = 80$ μm and sidewall incline $\alpha = 125.264°$. A HfO$_2$ high-k layer with a thickness of 800 nm was uniformly distributed across the pitted backplate, and covered by a 5-μm metallized polymer film. Here, k is the dielectric constant, and a high-k material allows increased capacitance of a parallel plate capacitor [6].

The overall system characteristics including impulse response, frequency response and phase response over an air channel at 0.5 m are illustrated in Fig. 3.7 (a), (b) and (c) respectively. As can be seen in Fig. 3.7 (b), the spectrum peaks at about 250 kHz, with a significant decline in response above 500 kHz. The 6-dB bandwidth is about 240 kHz from 150 kHz to 390 kHz. Compared to the Senscomp transducers described in Chapter 2, the high-k transducers have much wider bandwidth at higher frequencies. Fig. 3.7 (c) shows that the phase response of the channel is nearly linear at frequencies under 700 kHz. The time-domain background noise was also measured in Fig. 3.8 (a). Its frequency spectrum in Fig. 3.8 (b) behaves like Gaussian white noise across the 6-dB bandwidth. The recorded received signal amplitude was typically around 8 mV rms at 0.5 m, and the rms amplitude of the background noise was about 450 μV giving an SNR of 25 dB at this range.
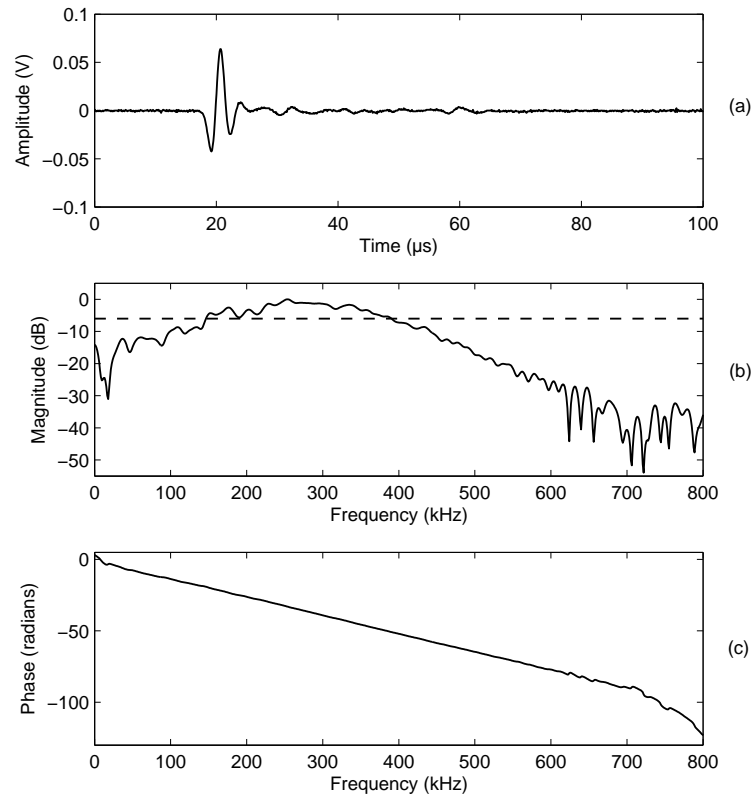
Figure 3.7: System characteristics using high-k transducers over 0.5 m: (a) impulse response; (b) frequency response; and (c) phase response.
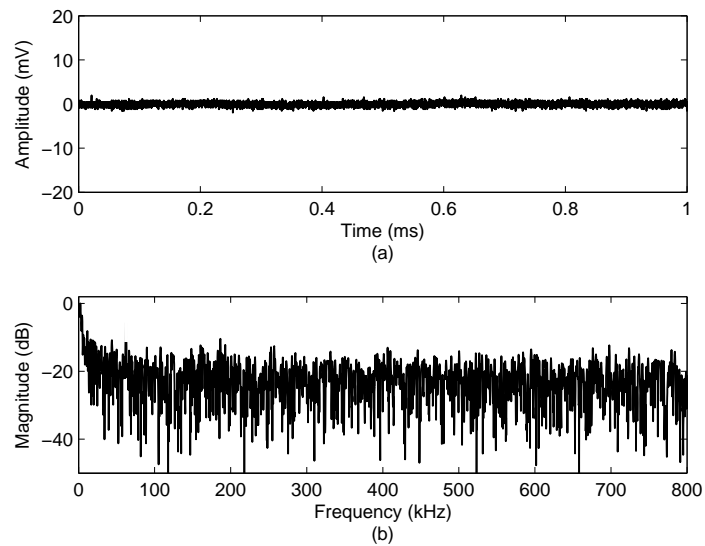
Figure 3.8: Background noise in: (a) time domain; and (b) frequency domain.
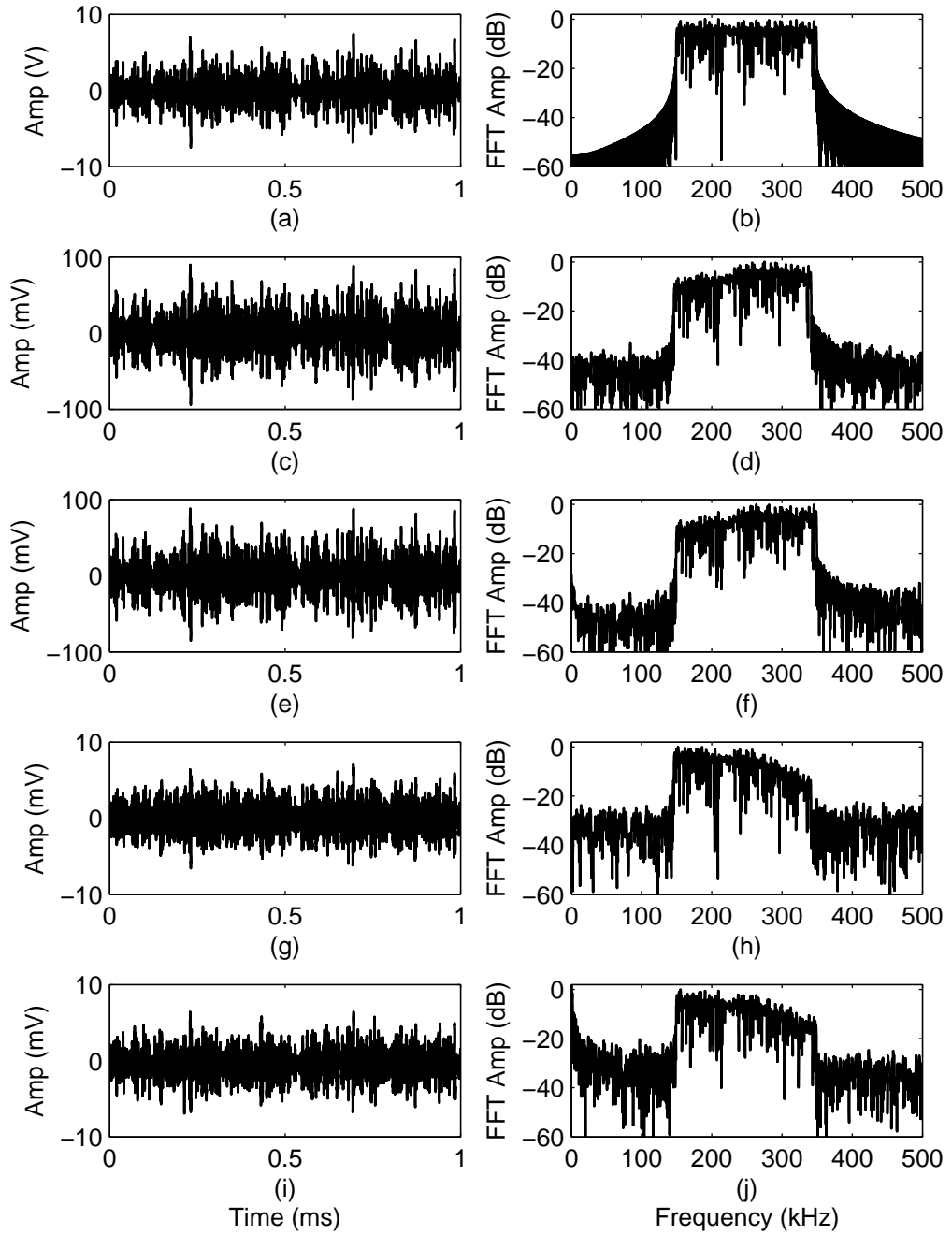
Figure 3.9: Comparison of transmitted signal, simulated received signal and actual received signal over 0.5 m and 1.6 m: (a) time domain transmitted signal, (b) its spectra, (c) time domain simulated received signal at 0.5 m, (d) its spectra, (e) actual received signal in time domain at 0.5 m, (f) its spectra, (g) time domain simulated received signal at 1.6 m, (h) its spectra, (i) actual received signal in time domain at 1.6 m, (j) its spectra.

Transmitter and receiver transducers were separated in a LOS manner, and the transmission bandwidth used was from 150 kHz to 350 kHz. The OFDM symbol T_s was set at 1 ms, giving a subcarrier spacing f_d of 1 kHz in order to retain the orthogonality. Fig. 3.9 compares the transmitted signal (QPSK-OFDM modulated), simulated received signal and actual received signal at transmission distances of 0.5 m and 1.6 m in both time domain and frequency domain. As can be seen, there is good agreement between the simulation predictions and actual experimental signals. In particular, at a short transmission range (0.5 m), it can be observed that the positive slope of the spectra outline from 150 kHz to 350 kHz in Fig. 3.9 (d) and (f) indicate that low frequency channel signals suffer from more significant loss due to beam divergence. However, over longer ranges (1.6 m), atmospheric absorption contributes more attenuation to high frequency channel signals as the spectra outlines have a negative slope along the frequency axis as shown in Fig. 3.9 (h) and (j).

3.2.3 OFDM demodulation

The demodulation for an OFDM signal is essentially the reverse process of the modulation as illustrated in Fig. 3.10. After receiving the OFDM signal, the receiver down-converts it and transforms it to the digital domain using an analogue-to-digital converter (ADC). After ADC conversion, the time-domain base-band OFDM signal is demodulated and converted to the frequency domain by executing a fast Fourier transform (FFT), avoiding the need for complex sub-channel filters. A phase offset recovery scheme together with channel equalisation is performed with the aid of the OFDM pilot signal. How these schemes work will be explained later in this section. After that, corrected OFDM symbols are de-mapped according to the transmission constellation pattern. In digital communications, a graphical representation of the received signal symbols modulated in different modulation modes is usually used to observe interfer-
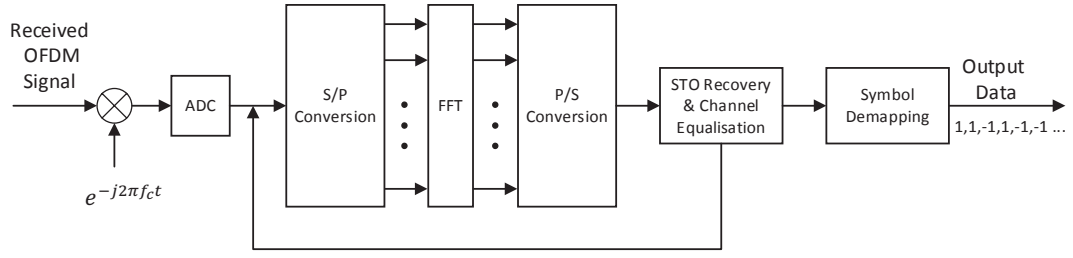
Figure 3.10: Schematic diagram of an OFDM demodulator.

ence and distortion in a signal. This is known as the constellation diagram. It displays the signal as a two-dimensional scatter diagram in the complex plane at symbol sampling instants. The real and imaginary axes are often called the in phase and the quadrature, respectively. Fig. 3.11 shows three constellation diagrams of the received OFDM signals using BPSK, QPSK and 16-QAM with an SNR of 5 dB in simulation. As can be seen, after introducing AWGN, the demapped OFDM symbols are scattered around their target points, but all the constellation points are grouped and well separated. As long as no demapped symbol crosses the detection boundaries, all the transmitted bits can be correctly decoded.

Generally, it is critical to perform an accurate time synchronisation to allow a receiver to recover an OFDM signal. An N-point FFT at the receiver processes
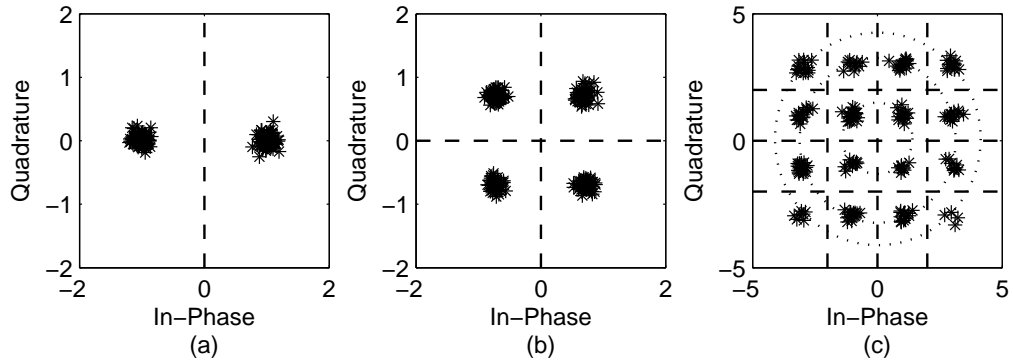
Figure 3.11: Simulated OFDM signal constellation diagrams for an SNR of 5 dB. (a) BPSK, (b) QPSK, and (c) 16-QAM. The detection boundaries are indicated by dashed lines. The circles in (c) indicate three different amplitudes of $\sqrt{2}$, $\sqrt{10}$ and $3\sqrt{2}$.

data in blocks of N samples at a time. Ideally, the N samples taken in by the FFT will correspond to the N samples of a single transmitted OFDM symbol. As described in Fig. 3.4, a known LFM preamble is located at the start of the data sequence for frame synchronisation. By processing the correlation operation, this aids the receiver to detect the OFDM symbol boundary. However, the OFDM signal is very sensitive to even small defects, and this is known as symbol timing offset (STO). The result is that the N samples sent to the FFT do not line up with the corresponding OFDM symbol. Thus, this offset can also be viewed as a shift of the FFT window. Assuming the symbol timing offset is δ samples, the received signal, $r(n)$, will then be a shifted version of $s(n)$ in (3.5), expressed as:

$$
\begin{aligned}
r(n) &= s(n + \delta) \\
&= \sum_{k=0}^{N-1} s_k e^{j\frac{2\pi}{N}k(n+\delta)}, \qquad for\ n \in [0, N-1].
\end{aligned}
\tag{3.6}
$$

Applying an FFT to both sides of (3.6) allows the recovered complex number sequence for each OFDM symbol to be derived as:

$$
\begin{aligned}
y_k &= \sum_{n=0}^{N-1} \left\{ \sum_{k=0}^{N-1} s_k e^{j\frac{2\pi}{N}k(n+\delta)} \right\} \cdot e^{-j\frac{2\pi}{N}kn} \\
&= s_k \cdot e^{j\frac{2\pi}{N}k\delta}, \qquad for\ k \in [0, N-1].
\end{aligned}
\tag{3.7}
$$

As equation (3.7) shows, an STO of δ samples in the time domain incurs a phase offset of $\frac{2\pi}{N}k\delta$ in the frequency domain, which is proportional to the sub-carrier index k, as well as the STO. This means that the STO error does not destroy the orthogonality of the sub-carriers, and the effect of the timing error is a phase rotation which linearly changes with carrier index. A simulated example of a QPSK-OFDM signal shifted by 2 samples is shown in Fig. 3.12. As can be seen in Fig. 3.12 (b), constellations of sub-carriers corresponding to high frequencies
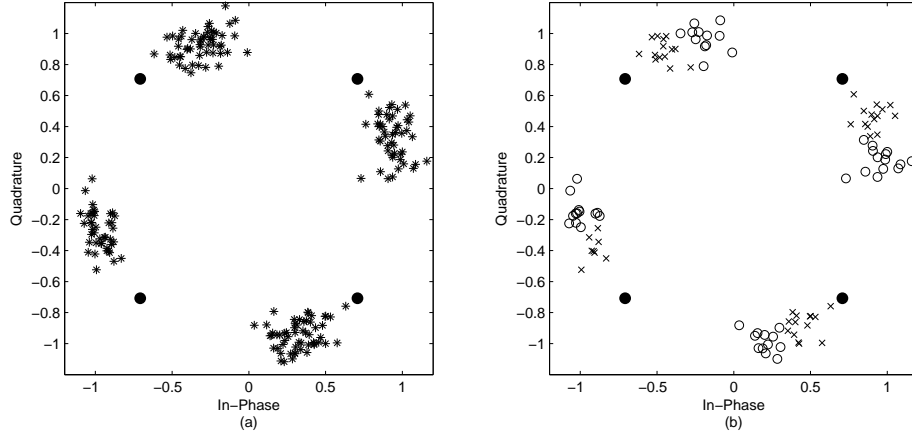
Figure 3.12: Effect of STO on received constellation. (a) Phase shift with 2 samples of symbol offset, SNR=5 dB, (b) Phase shift with 2 samples symbol offset showing only the lowest and the highest frequency constellation points: low frequencies ($\times$) and high frequencies ($\circ$).

experience a larger rotation than low frequency ones. Note that only the highest and the lowest 50 subcarrier signal constellations are plotted, showing different effects in terms of STO phase rotation at different frequencies.

STO can be corrected by applying the maximum likelihood (ML) approach [2] to the data-aided phase recovery scheme. Mathematically, it is to minimise the difference between the received pilot signal $s(n + \delta)$ and the signal of interest $s(n)$:

$$
\begin{aligned}
\hat{\delta} &= \arg\min_{\delta} \left\{ \sum_{n=0}^{N-1} [s(n) - s(n + \delta)]^2 \right\} \\
&= \arg\min_{\delta} \left\{ \sum_{n=0}^{N-1} s^2(n) + \sum_{n=0}^{N-1} s^2(n + \delta) - 2 \sum_{n=0}^{N-1} s(n)s(n + \delta) \right\}.
\end{aligned}
\tag{3.8}
$$

Note that the first term of the expansion in equation (3.8) does not depend on the unknown parameter δ, thus it will not affect the optimisation process. In the second term, the parameter is present, however, the sum is the energy of the signal, and when δ changes, the energy is still the same. Thus the second term of the expansion does not depend on δ either, and it can be removed from

90
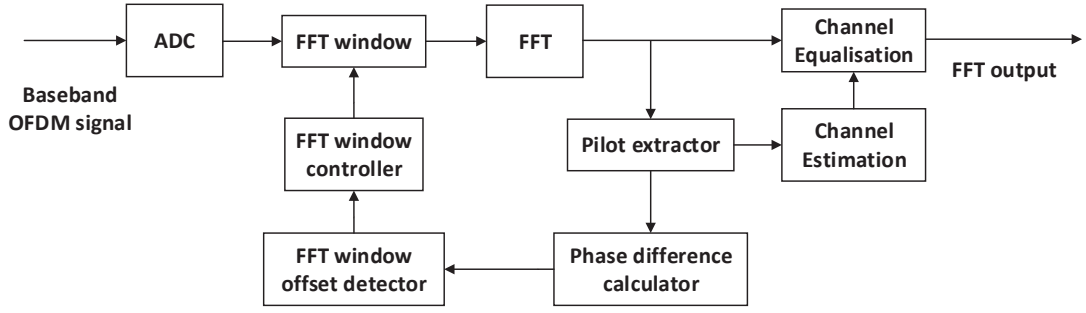
Figure 3.13: Structure of symbol timing offset (STO) synchronisation.

the optimisation process. Therefore, the maximisation becomes:

$$\hat{\delta} = \arg\max_{\delta} \left\{ \sum_{n=0}^{N-1} s(n)s(n+\delta) \right\}. \tag{3.9}$$

The sum in equation (3.9) is actually the time-correlation between the received signal and the signal of interest. Therefore, in this particular case, the ML approach is equivalent to the maximisation of the correlation. In practice, this optimisation process is performed using functional blocks as depicted in Fig. 3.13. An ADC converter samples a received OFDM signal. An FFT window is controlled by an FFT window controller to recover an FFT window position. A phase difference calculator calculates a phase difference between the original pilot and the received pilot signal extracted by a pilot extractor. An FFT window offset detector then detects the position of the FFT window by the phase difference output from the phase difference calculator. After that, the FFT window controller controls the position of the FFT window by the FFT window offset. Apart from the STO recovery, channel equalisation is also carried out based on the received pilot signal to equalise the amplitudes of the signals at different sub-carriers as the air channel has a non-flat frequency response.

As an illustrative example, the constellation diagram of a received QPSK-OFDM signal before phase correction is illustrated in Fig. 3.14. As can be seen, the received signal was completely corrupted as all the constellation points are
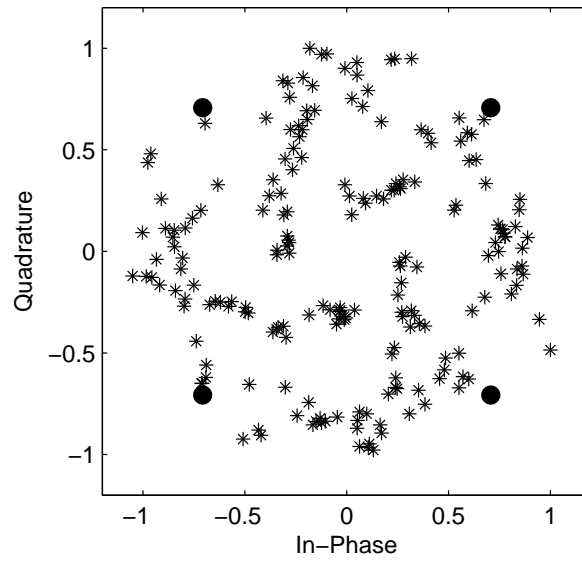
Figure 3.14: Received signal constellation before STO recovery and equalisation.
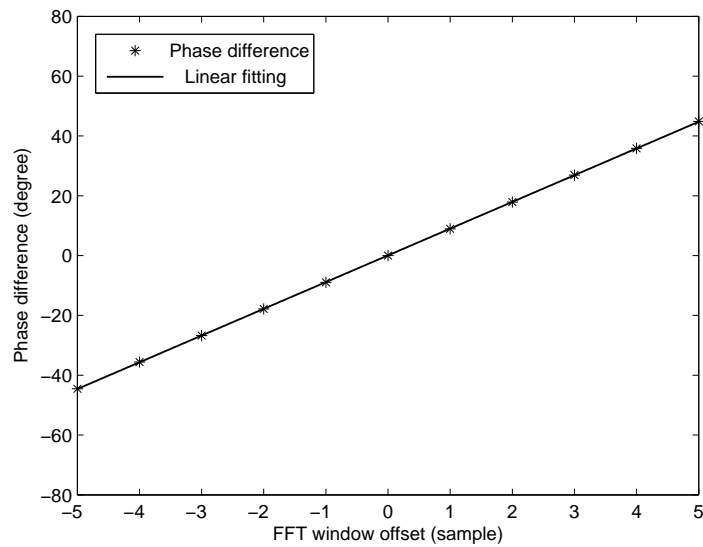
Figure 3.15: Phase difference calculator outputs according to FFT window offset.

spread across the quadrature boundary. In this case, it could not be correctly decoded. Fig. 3.15 shows the output of the phase difference calculator after pilot signal extraction. As can be seen, it is clear that the phase offset is directly proportional to the shift of the FFT window. After phase noise correction, the signal constellations are well presented in four constellation regions at
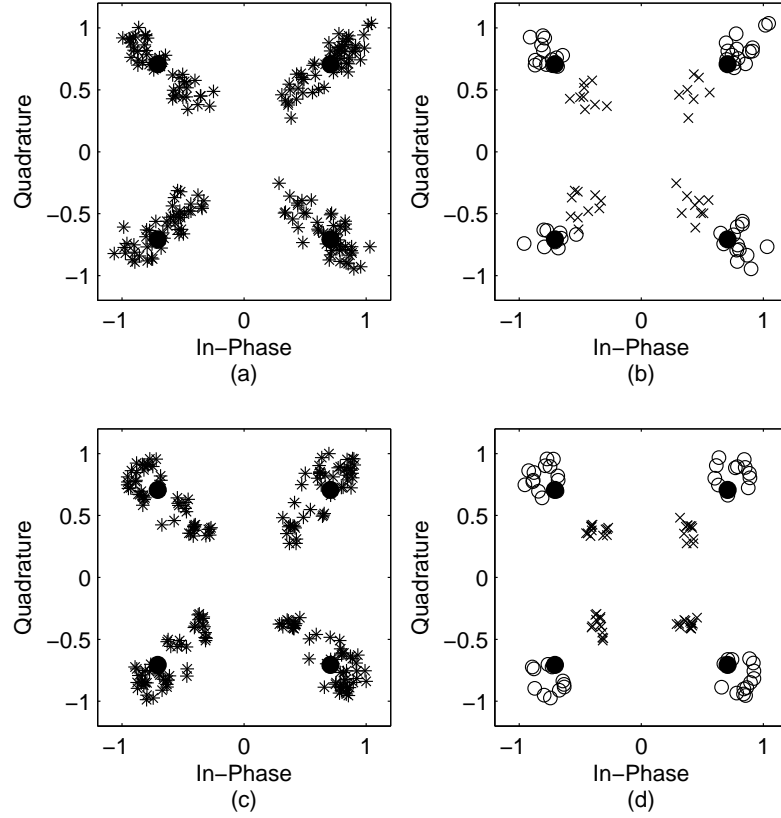
Figure 3.16: Comparison of received signal constellation after phase correction in simulation at a transmission distance of 0.5 m: (a) signal constellations at all sub-carrier channels, (b) received signal constellation showing only the lowest and the highest frequency constellation points: low frequencies ($\times$) and high frequencies ($\circ$). Corresponding constellations of experimental signals (c) and (d) at a transmission distance of 0.5 m.

both 0.5 m and 1.6 m ranges, as shown in Fig. 3.16 and Fig. 3.17 respectively. The actual received signal constellations in Fig. 3.16 (c) and Fig. 3.17 (c) are compared with the simulated constellations in Fig. 3.16 (a) and Fig. 3.17 (a). It can be seen that the theoretical predictions match the experimental signals well. The highest and the lowest 50 channel constellations are clustered into two groups with different amplitude levels due to both atmospheric attenuation and beam divergence. As can be seen from Fig. 3.16 (b) and (d), when the transmission range is short, low frequency constellations present lower amplitudes than high frequency ones. In Fig. 3.17 (b) and (d), as transmission
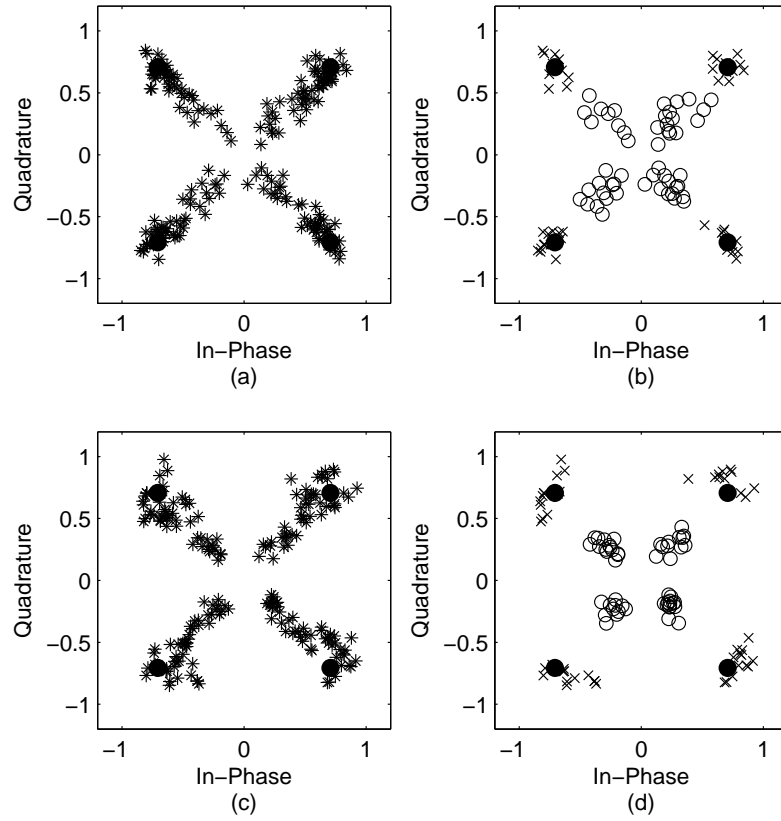
Figure 3.17: Comparison of received signal constellation after phase correction in simulation at a transmission distance of 1.6 m: (a) signal constellations at all sub-carrier channels, (b) received signal constellation showing only the lowest and the highest frequency constellation points: low frequencies ($\times$) and high frequencies ($\circ$). Corresponding constellations of experimental signals (c) and (d) at a transmission distance of 1.6 m.

range increases, the amplitudes of high frequency constellations start to decrease and become smaller than low frequency constellation amplitudes. To perform a better identification of symbols, channel equalisation was applied to provide tightly clustered constellation points. This can either be done with the aid of the pilot signal or using the simulation model. But in practice, the pilot signal should be used, as some unknown effects which are not considered in the simulation may be included in the communication channel. Fig. 3.18 (a) and (b) compares the outputs of the phase difference calculator when using the pilot signal and using the simulation model at transmission distances of 0.5 m

94
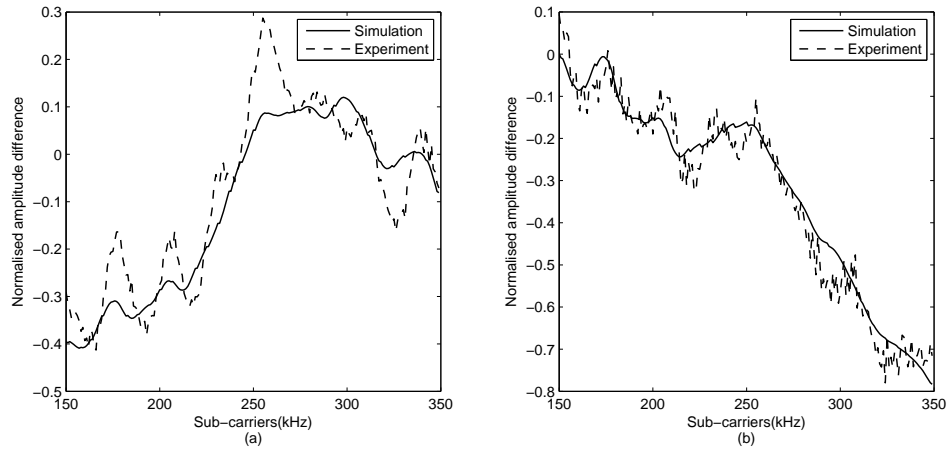
Figure 3.18: Amplitude difference estimated by the experimental pilot signal and by the simulation model in transmission distances of (a) 0.5 m and (b) 1.6 m.
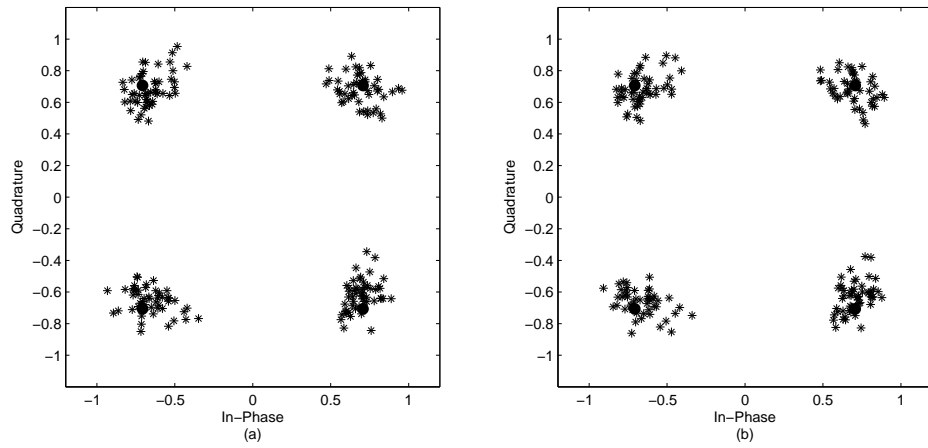
Figure 3.19: (a) Received signal constellation after channel equalisation using the simulation model, and (b) received signal constellation after channel equalisation with the aid of the experimental pilot signal.

and 1.6 m respectively. It shows an excellent agreement between the prediction of the simulation and the actual experimental phase difference calculated using the pilot signal. In Fig. 3.18 (a), when the transmission distance is 0.5 m, the amplitude differences increase in both simulation and experiment as the sub-carrier frequency increases. This trend confirms the results shown in both Fig. 3.9 and Fig. 3.16 at the same transmission distance. For the increased transmission distance (1.6 m), the opposite trend occurs, as shown in 3.18 (b) for both simulation and experiment. It again demonstrates that atmospheric

absorption dominates the total attenuation with the increase of the sub-carrier frequency. Fig. 3.19 (a) and (b) present the constellation diagrams after channel equalisation using theoretical prediction and the experimental pilot signal, respectively, at 1.6 m. As can be seen, constellations are clustered together in their individual regions in the same way as the constellation pattern shown in Fig. 3.11 (b). The equalisation compensates the amplitude difference between different sub-carrier signals. This is also necessary for correct decoding of higher-order quadrature modulation schemes such as 16-QAM, 64-QAM and so on.

3.3   Experimental results

The experiment was carried out in an indoor laboratory with no distinct ultrasonic background noise. The centre normals of the transmitter and receiver transducers were laser aligned to provide a direct LOS transmission link. Three different baseband modulation methods, BPSK, QPSK and 16-QAM, were used to modulate the subcarrier signals from 55 kHz to 99 kHz using the SensComp transducers, and 200 kHz to 399 kHz using the high-k transducers. Note that Gray coding was used for generating both QPSK and 16-QAM symbols. This was to minimise the decoding error as every two adjacent symbols differ from each other by only one bit [3]. It should also be noted that QAM usually has square constellations, thus the most common forms are 16-QAM, 64-QAM and 256-QAM. Higher order QAM can carry more bits per symbol, but they are more susceptible to noise as the constellations must be closer to each other. Due to the memory limitation of the arbitrary waveform generator, only 90 packets of 1-ms OFDM signals could be sent through the air channel.

3.3.1 Sampling frequency offset and correction

As all the subchannel spectra of an OFDM signal are overlapping with each other, the channel spacing becomes extremely narrow, resulting in a system that is highly sensitive to phase noise. Fig. 3.20 shows the received 16QAM-OFDM signal constellations before and after channel equalisation using SensComp and high-k ultrasonic transducers. Note only 16QAM-OFDM signal constellations are presented as illustrative examples. As can be seen from Fig. 3.20 (a) and (b), both the constellations are heavily distorted with corrupted phases and amplitudes. After channel equalisation, both constellations in Fig. 3.20 (c) and (d) form three circular rings with three different radii. This is because the
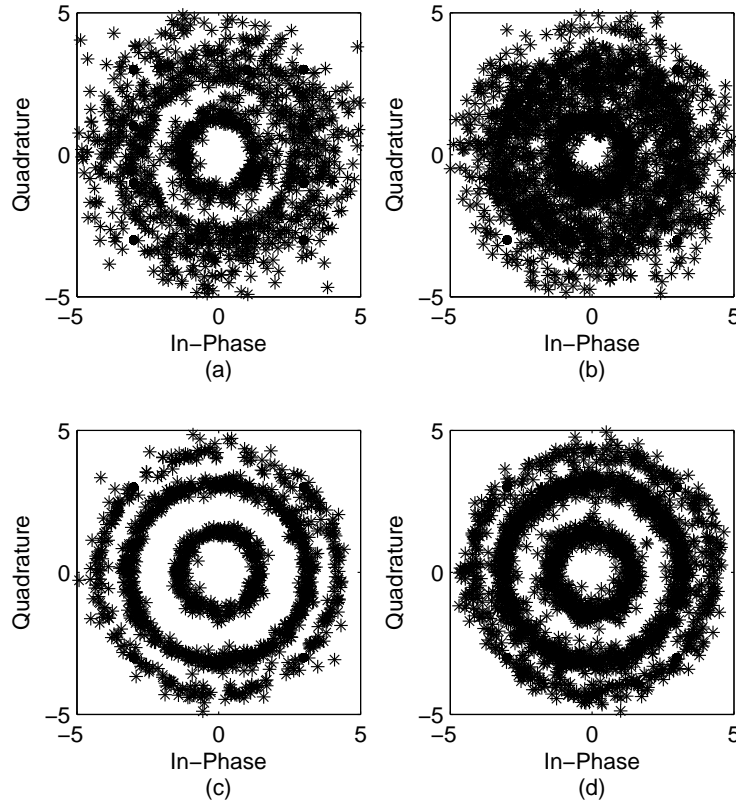
Figure 3.20: Received OFDM constellations using SensComp transducers before (a) and after (c) channel equalisation for 16-QAM at 2 m, and constellations using high-k transducers before (b) and after (d) channel equalisation for 16-QAM at 0.5 m.

amplitudes of the 16 constellation points have three different values $\sqrt{2}$, $\sqrt{10}$ and $3\sqrt{2}$ as shown in Fig. 3.11 (c). However, the two constellation diagrams indicate that the amplitude distortion has been recovered while the phase distortion is still retained. This phase rotation was introduced by the Picoscope oscilloscope as the sampling rate of the transmitted OFDM signal was 10 MHz precisely while the received signal was actually sampled at 9.7656 MHz resulting in 9765.6 OFDM samples in 1 ms.

To tackle this sampling frequency offset problem, the received signal was interpolated until it had the same number of samples in 1 ms as that of the transmitted signal, as MATLAB can only process an integer number of samples. Fig. 3.21 (a) and (b) show the received constellations when using SensComp
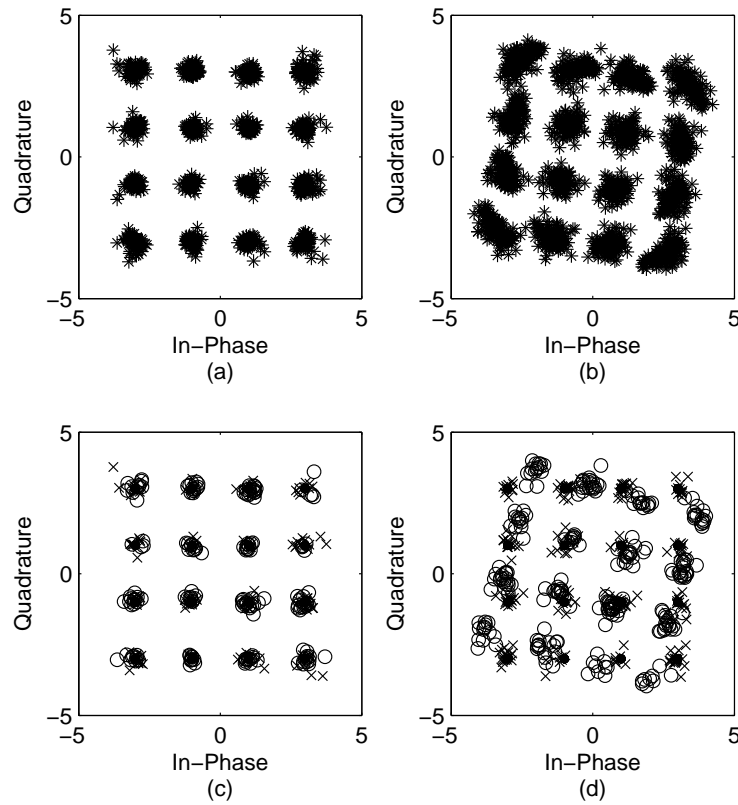
Figure 3.21: Received OFDM constellations using (a) SensComp transducers at 2 m and (b) high-k transducers at 0.5 m after interpolation and channel equalisation. (c) and (d) Corresponding signal constellations showing the first 10 ($\times$) and last 10 ($\circ$) OFDM data packets.

98

and high-k transducers, respectively, after applying interpolation and channel equalisation. As can be seen, the constellations shown in Fig. 3.21 (a) were well located around their original points when using SensComp devices at relatively low frequency subcarriers. However, in Fig. 3.21 (b), the constellations of demapped symbols at higher frequencies when using high-k transducers still had a certain amount of group phase rotation which moved part of the constellations across the detection boundaries. It indicates that OFDM signals were more sensitive to phase distortion especially at high frequency channels. This phase rotation was also accumulating with time as the constellations in Fig. 3.21 (d) show that the last 10 out of 90 OFDM signal packets received had larger phase rotations than the first 10 packets. In comparison, both the first 10 and last 10 packets of the received OFDM signal constellations at low frequencies were clustered within the 16 individual detection regions with negligible phase rotation as shown in Fig. 3.21 (c). The group phase offsets, $\Delta\phi$, of different OFDM data packets when using both SensComp and high-k transducers
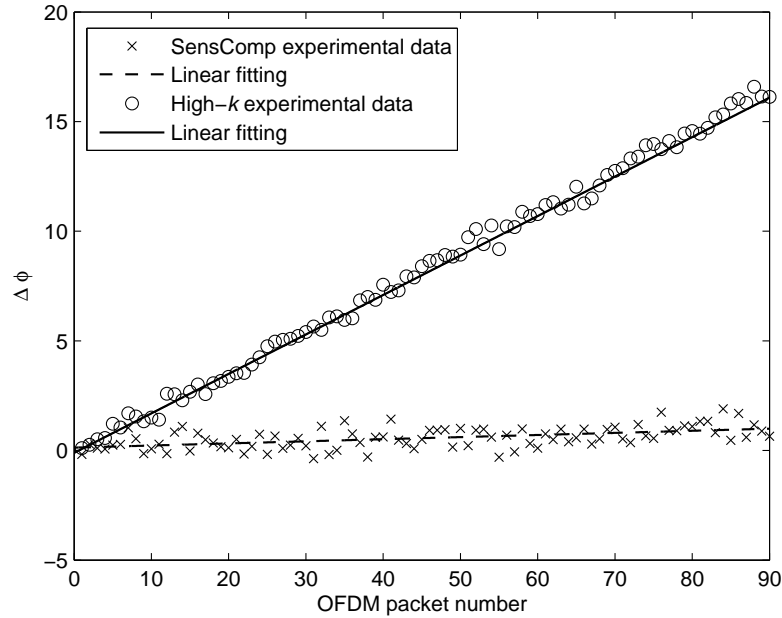
Figure 3.22: The trend of the group phase offset when using SensComp and high-k ultrasonic transducers with their individual linear fittings.

99

were calculated and plotted in Fig. 3.22. As can be seen, the phase offset of the received signal when using SensComp transducers had a minor increment with time from $0°$ up to about $1°$ at the 90th data packet. When using high-k transducers at high frequency subcarriers, the phase offset gradually increased from $0°$ for the first OFDM packet to approximately $16°$ when the last packet was received.

The phase offset was a cumulative hardware sampling error but it could still be compensated for as there was a predictable linear relationship, as seen from the trendlines in Fig. 3.22. The linear fitting equations for the high-k and SensComp experimental data are $y = 0.18x - 0.11$ and $y = 0.0096x + 0.13$ with the correlation coefficient R-squared values of 0.995 and 0.264, respectively. The high R-squared value indicates that the linear fitting fits the high-k experimental data very well. The SensComp experimental data was more fluctuated with a relatively low R-squared value because the group phase offset, $\Delta\phi$, for each OFDM data packet, was averaged over only 45 subcarriers compare to that of 200 for the high-k transducers. However, in practice, this group phase offset when using SensComp transducers is negligible as the maximum was less than $1°$ at the 90th data packet. Fig. 3.23 (a) and (b) illustrate the received
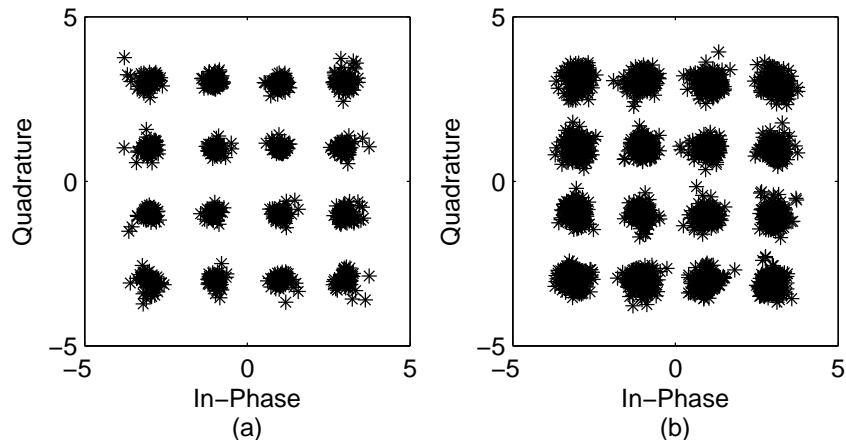
Figure 3.23: Received OFDM constellations using (a) SensComp transducers at 2 m and (b) high-k transducers at 0.5 m after interpolation, channel equalisation and phase offset correction using linear fitting equations.
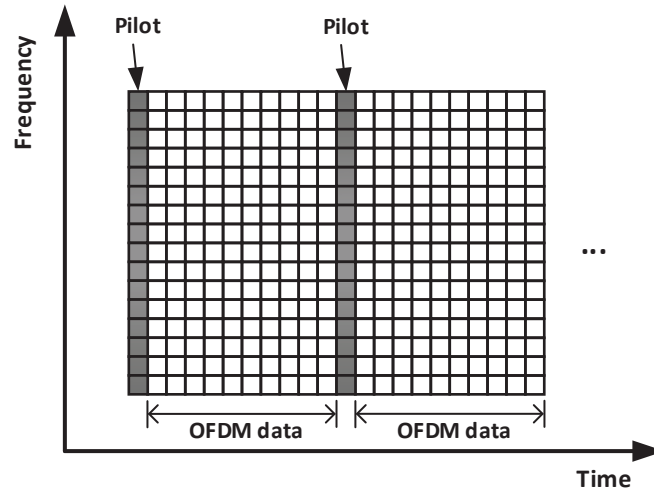
Figure 3.24: An illustrative diagram of the pilot arrangement for OFDM signal transmission.

OFDM constellations using SensComp and high-k transducers after the phase offset compensation with the aid of linear fitting equations, respectively, showing good correction outcomes. As an alternative to compensate the phase offset for high-frequency OFDM signals using high-k devices, the pilot signal was periodically inserted between the OFDM data packets. Fig. 3.24 shows the pilot arrangement used in this work. As can be seen, all subcarriers were used as pilot signals, and the pilots were inserted every 10 OFDM data packets. This limited the group phase offset within about $2°$ which was considered a safe decoding range. However, the overall system data transfer rate was reduced by 10% at the same time after the pilot insertion.

3.3.2 Performance evaluation

The performances including bandwidth efficiency, data rate, attainable transmission range, SNR and BER of all three modulation schemes were evaluated and compared using SensComp and high-k ultrasonic transducers in the experiments. The bit errors of the OFDM signals were measured with increasing range, and each 90-packet signal was transmitted 10 times before averaging.

101

Table 3.1: Experimental OFDM transmission

Ultrasonic Transducers	Modulation Format	f_c [a] (kHz)	Bandwidth (kHz)	Data Rate [b] (kb/s)	Bandwidth Efficiency (b/s/Hz)	Range (m)	SNR (dB)	BER [c]
SensComp	BPSK	77	45	45	1	11	0.63	<2.47E-5
	QPSK			90	2	9	11.78	<1.23E-5
	16-QAM			180	4	6	15.62	<6.17E-6
High-k	BPSK	300	200	200 (180)	1	1.2	12.27	<5.56E-6
	QPSK			400 (360)	2	1.1	15.93	<2.78E-6
	16-QAM			800 (720)	4	0.7	24.69	<1.39E-6

[a] Central carrier frequency;
[b] Reduced data rate if sampling frequency offset occurs;
[c] The values are of BERs with only one bit error.

The maximum attainable transmission distances with no measurable errors are listed in Table 3.1. As can be seen, much larger SNRs for error-free transmission (i.e. no measurable errors) were required by higher order modulation schemes compared with low-order modulations as they had smaller noise margins. The achieved error-free ranges using 16-QAM at low and high frequencies were up to 6 m and 0.7 m, and at 180 kb/s and 800 kb/s, respectively. These ranges were extended to 11 m and 1.2 m when BPSK modulation was used at 45 kb/s and 200 kb/s. Apparently, the most reliable OFDM link was transmitting BPSK modulated signals with the minimum SNR required. But when the system throughput is a priority, 16QAM-OFDM signals which are four times more efficient than those of BPSK-OFDM are suggested for a higher data transfer rate. Besides, as high-frequency ultrasound suffers severe atmospheric absorption in air, more energy was needed for a successful signal transmission, and the attainable ranges were also significantly restricted. It indicates that a trade-off should be made between the attainable range and data transfer rate for airborne ultrasonic communication as the transmission range is significantly restrained by the high-frequency attenuation of ultrasound while at the same time broader bandwidth at high frequency is needed for higher system data rates. Fig. 3.25 compares this work with the prior airborne ultrasonic data communication systems described in Chapter 1.5.2 in terms of their data rates
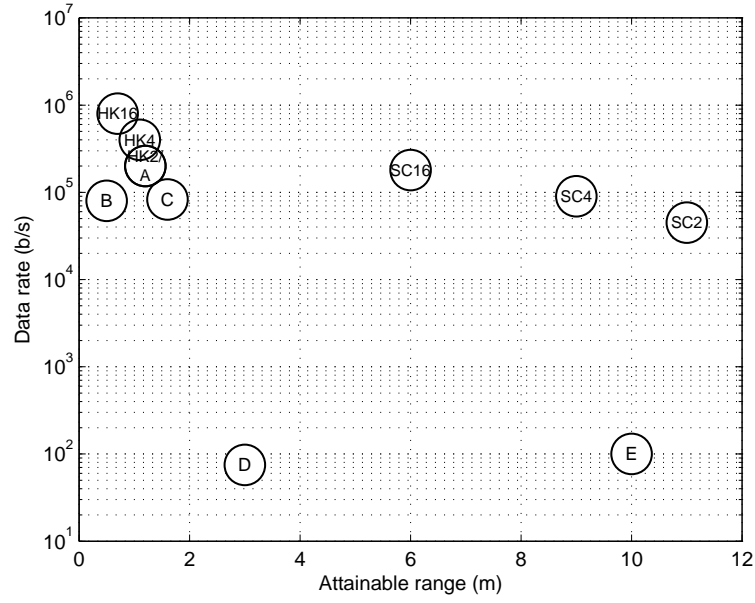
Figure 3.25: Comparison of different airborne ultrasonic data communication systems and their data rates at attainable transmission ranges. SC2, SC4 and SC16 represent BPSK-OFDM, QPSK-OFDM and 16QAM-OFDM when using SensComp transducers, respectively, and HK2, HK4 and HK16 represent BPSK-OFDM, QPSK-OFDM and 16QAM-OFDM when using high-k transducers, respectively. A, B, C, D, E refer to the works referenced in [7], [8], [9], [10] and [11], respectively.

and attainable transmission ranges. As can be seen, when SensComp transducers are used for OFDM signal transmission, this work has improved the data rates at longer ranges when compared with the prior works. By using high-k transducers, this work has also improved the overall system data rate at short ranges.

To better visualise the received OFDM signal conditions before and after the channel equalization, constellation diagrams of BPSK, QPSK and 16-QAM are given in Fig. 3.26 and Fig. 3.27 when using the SensComp and high-k transducers, respectively. As can be seen from Fig. 3.26 (a) - (c), the raw signal constellations after the demodulation process are completely corrupted as the constellation points are rotated and spread across the detection boundaries. By analysing the received pilot signal which was previously known by the receiver, the phase and amplitude shifts due to the effect of the ultrasonic channel in air
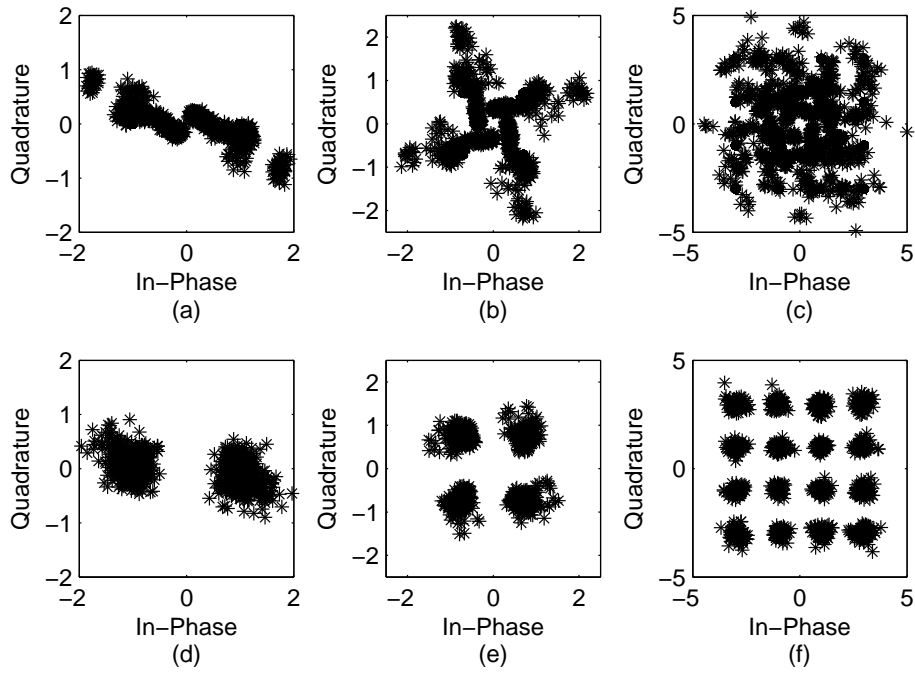
Figure 3.26: Received OFDM constellations using SensComp transducers before (a) - (c) and after (d) - (f) channel equalisation for BPSK, QPSK and 16QAM at 11 m, 9 m and 6 m, respectively.
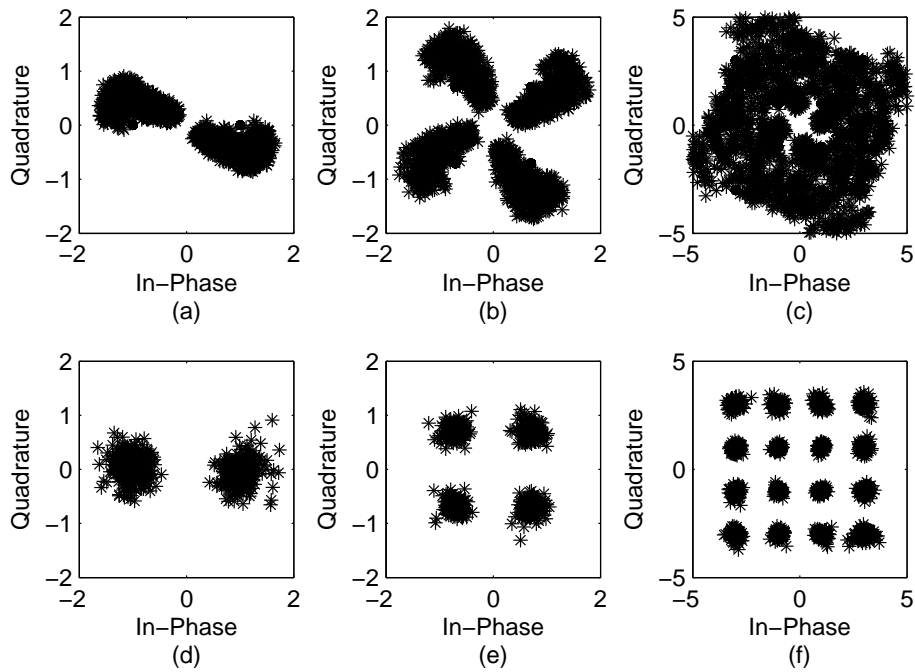
Figure 3.27: Received OFDM constellations using high-k transducers before (a) - (c) and after (d) - (f) channel equalisation for BPSK, QPSK and 16QAM at 1.2 m, 1.1 m and 0.7 m, respectively.

could then be compensated for before decoding. Fig. 3.26 (d) - (f) illustrate the three constellations after channel equalisation. As can be seen, all constellations of BPSK, QPSK and 16-QAM were recovered and clustered around their target points. Similarly, when the signals were transmitted and received using high-k ultrasonic transducers, considerable phase and amplitude noise can be observed from the raw received data after the OFDM symbols were demapped as shown in Fig. 3.27 (a) - (c) for different modulation schemes. Again, Fig. 3.27 (d) - (f) show three individual well located constellation patterns after channel equalisation as the inserted pilot signal provided the measurement of actual noise at each ultrasonic channel to correct the distortions and separate different constellation points.

3.4   OFDM in a multipath environment

The main advantage of OFDM over other forms of modulation is that it is much easier to make it immune to inter-symbol interference (ISI) caused by multipath propagation. In a linear dispersive channel, the received signal sequence, $r(n)$, can be expressed as the sum of several versions of the transmitted signal with different gains and delays:

$$r(n) = \sum_{i=0}^{L-1} \alpha_i s(n - \delta_i),$$
(3.10)

where L is the number of multipath components, α_i are path attenuation factors and δ_i are path delays. ISI could be easily eliminated by adding guard intervals (GI) between different OFDM symbols. As long as the length of the GI is larger than the maximum estimated delay spread, the effect of ISI can then be completely removed. However, if the GI is left empty, it will lead to another type of interference called inter-carrier interference (ICI) as the zero-padded waveform would destroy the orthogonality between sub-carriers. Therefore, to

prevent both ISI and ICI, an OFDM symbol is usually cyclically extended into the GI. This is achieved by taking the last few samples at the end of each symbol, and adding these samples to the start of the symbol. This cyclic prefix (CP) preserves the sub-carrier orthogonality at the expense of wasting some energy, as the power transmitted in the added symbols is not used at the receiver. At the same time, the system data rate is also reduced due to the extension of the total OFDM packet length.

To analyse the effects of a multipath channel on an OFDM signal, a simplified model was developed ignoring GI and background noise. Considering only the direct path signal and one reflected signal with a time delay δ and an attenuation factor of α, the following signal $r(n)$ is detected by the receiver:

$$
\begin{aligned}
r(n) &= s(n) + \alpha s(n - \delta) \\
&= \sum_{k=0}^{N-1} s_k e^{j\frac{2\pi}{N}kn} + \alpha \sum_{k=0}^{N-1} s_k e^{j\frac{2\pi}{N}k(n-\delta)} \\
&= \sum_{k=0}^{N-1} s_k (1 + \alpha e^{-j\frac{2\pi}{N}k\delta}) e^{j\frac{2\pi}{N}kn}, \qquad k \in [0, N-1].
\end{aligned}
\tag{3.11}
$$

Applying demodulation by the FFT, the transmitted data y_k can be recovered from the received signal $r(n)$:

$$
\begin{aligned}
y_k &= FFT\{r(n)\} \\
&= s_k (1 + \alpha e^{-j\frac{2\pi}{N}k\delta}) \\
&= s_k H(k),
\end{aligned}
\tag{3.12}
$$

where $H(k) = 1 + \alpha e^{-j\frac{2\pi}{N}k\delta}$ for $k \in [0, N-1]$. As equation (3.12) indicates, the delayed signal only changes the amplitude $|H(k)|$ and the phase $arg\{H(k)\}$ of each sub-carrier. If the path delay δ is smaller than the length of the GI, no ICI
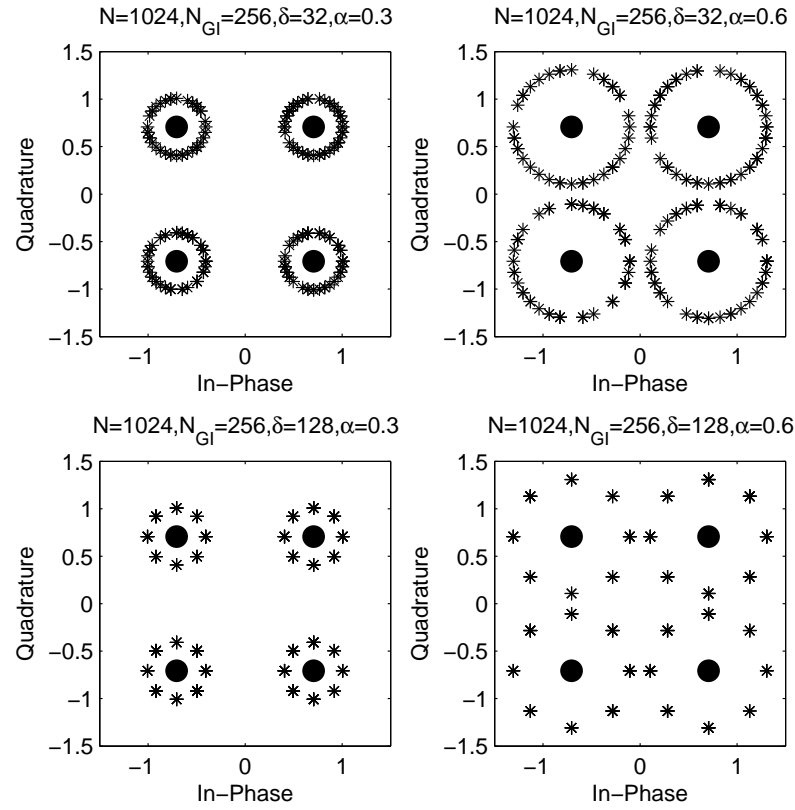
Figure 3.28: Spread of the QPSK-OFDM constellations with different delay and amplitude of the reflected signal.

is introduced, and the orthogonality between sub-carriers still holds. Assuming that a QPSK modulated signal is being transmitted through this channel, the constellations with different delay spread and attenuation of the detected signal are shown in Fig. 3.28. As can be seen, the effect of the multipath channel is to expand the constellations on each sub-carrier into different circles surrounding the target points. The number of points on each circle depends on the values of δ and N, and the radius of each circle depends on the value of α. If α is small, the transmitted data can still be correctly decoded. If α is large, and the circles cross over each other, an equaliser is then required to correct the channel distortion. According to equation (3.12), each received sub-carrier experiences a complex gain $H(k)$ due to the channel. In order to undo this effect, the transmitted data can be recovered from the received signal by multiplying s_k by

$1/H(k)$ which is just a single complex multiplication in the frequency domain. It greatly simplifies the equalisation process, especially compared to the adaptive filtering used in single carrier demodulations.

In practice, the effect of multipath reflections cannot be ignored. It can lead to the superposition of several time-delayed and attenuated copies of the transmitted signal at the receiver. As a result, it may introduce spreading of the received signal in time and constructive and destructive interference at various frequencies, leading to frequency selectivity. Depending on the size of the ultrasonic transducers and the operating frequencies used, the ultrasonic beams from the high-k devices are very directional and the transmission ranges are small. As a result, in an indoor laboratory environment, multi-path reflections are relatively low. Therefore, lower-frequency ultrasonic waves with much longer transmission ranges generated by the SensComp transducers are studied in a multipath environment. The experimental set up for multipath reflection is shown in Fig. 3.29. As can be seen, three solid reflectors R1, R2 and R3 were placed at both side of the transmission path to generated reflected signals. The
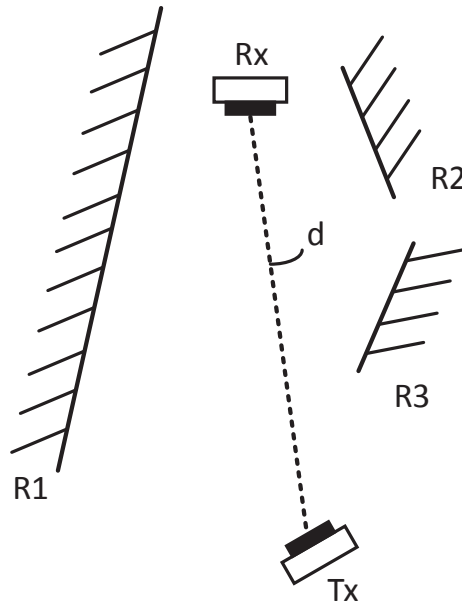
Figure 3.29: Experiment layout of multipath reflections.
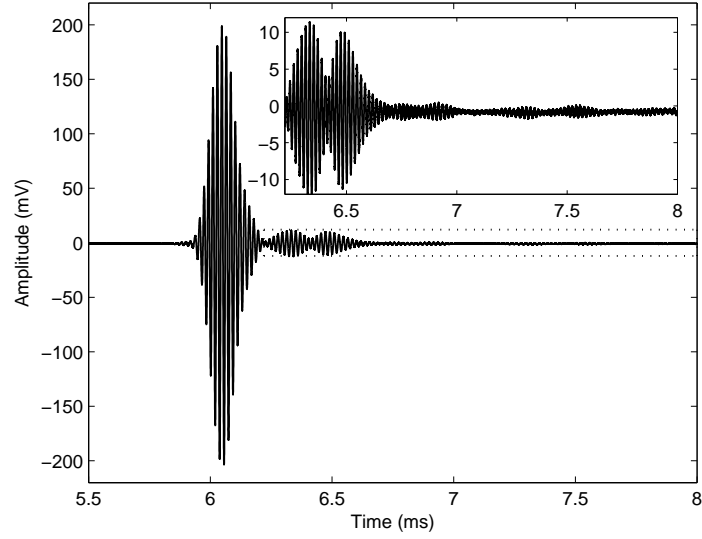
Figure 3.30: Received direct signal and reflected signals in a multipath environment.

Table 3.2: Experimental multipath reflections

Correspondence	Path distance (m)	Arrival time (ms)
Reflector R1 reflection	2.132	6.218
Floor reflection	2.198	6.408

direct LOS distance d from the transmitter to the receiver was 2 m, and both the transducers were 0.45 m above the floor. A typical reflection pattern in the time domain is shown in Fig. 3.30 when a Hanning-windowed 10-cycle 55 kHz sinusoid signal was transmitted through the system in the presence of reflecting surfaces. The enlarged region in Fig. 3.30 shows two strong reflections followed by additional signals with much smaller amplitudes within 2 ms of the direct signal. Each pattern of peaks corresponded to the arrival of acoustic reflections at the receiver at different moments in time. In this particular case, two possible reflections are from the reflector R1 and the floor of the laboratory. The details are shown in Table 3.2. It should be noted that all the reflections are relatively weak compared with the direct signal due to the directivity of the receiver.

To combat both ISI and ICI, a CP with a length of 2 ms was then added to

Table 3.3: Parameters of the OFDM signal used in the experiment in a multipath environment

Parameters	Settings
Sampling rate	$f_s = 10$ MHz
Centre frequency	$f_c = 77$ kHz
Signal bandwidth	$B = 45$ kHz
OFDM symbol duration	$T_s = 8$ ms
Cyclic prefix length	$T_{cp} = 2$ ms
Subcarrier spacing	$f_d = 125$ Hz
Number of subcarriers	$N = 360$
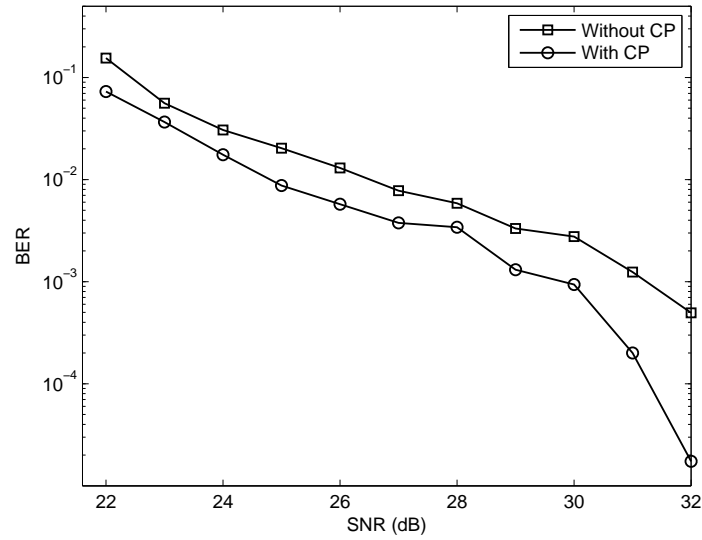
Figure 3.31: Bit error rate performance for 16-QAM OFDM modulation with and without cyclic prefix..

the OFDM symbols. Accordingly, the length of the OFDM symbols should also be extended. Details of the parameter settings are listed in Table 3.3. Since the OFDM symbol length was extended to 8 ms, to preserve subcarrier orthogonality, the subchannel width was reduced to only 125 Hz with a total number of 360 subcarriers in the range of 55 kHz to 99 kHz. The tested error-free decoding ranges for BPSK, QPSK and 16-QAM were maintained the same as listed
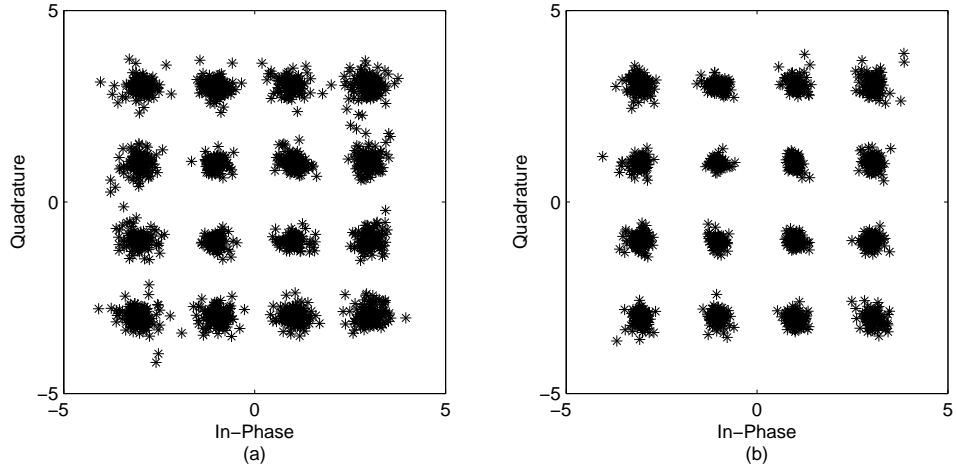
Figure 3.32: Received 16-QAM OFDM signal constellations after equalisation (a) without CP and (b) with CP at a SNR value of 32 dB.

in Table 3.1 using this new channel arrangement. However, after adding the CP, total data transfer rates for all three modulation schemes were reduced by 20%. To evaluate the performance of using CP in a multipath environment, BERs of the OFDM signals with CP and without CP are compared in Fig. 3.31. It is observed that there was an improvement in BER after adding CP, especially when the received signal had a large SNR. Note that only the performance of 16QAM-OFDM signals are presented here as an illustrative example. Accordingly, the constellations of the equalised 16-QAM signals without and with CP at an SNR value of 32 dB are shown in Fig. 3.32 (a) and (b), respectively. As can be seen, more concentrated constellation points with less spreading were extracted from the OFDM signal after adding CP.

It should be mentioned that two potential problems may raise with the extension of OFDM symbol time in order to use CP. One is that the system will be more sensitive to Doppler shift when the receiver is moving. The Doppler spread Δf can be calculated as [12]

$$\Delta f = \frac{\Delta v}{c} f_c, \tag{3.13}$$

where Δv is the relative velocity, f_c is the emitted frequency and c is the speed

of sound in air. Assuming in an indoor environment that a fast moving speed of the receiver is 2.5 m/s, the maximum Doppler shift spread is then up to 722 Hz which is much larger than the subcarrier spacing (125 Hz) used in the experiment. This may lead to significant decoding errors, therefore degrading the system performance. The other issue is the increase of peak-to-average power ratio (PAPR) as the OFDM signal with CP contains many more subcarriers. The PAPR of a transmitted signal $x(n)$ in dB can be given by [13]

$$PAPR[x(n)] = 10log_{10}\left\{\frac{\max\limits_{0\leq n\leq N-1}|x(n)|^2}{E[|x(n)|^2]}\right\}, \qquad (3.14)$$

where $E\{.\}$ denotes the expectation operator. When transmitting all '1's, the calculated PAPR of the 8-ms OFDM signal was 28.57 dB compared with 19.54 dB of the 1-ms OFDM signal. The high PAPR of the OFDM signal occurs due to the summation of the subcarrier signals. In order to transmit signals with such high PAPRs without distortion, linear power amplifiers with wide dynamic ranges are required. This may also result in the reduction of transmission power efficiency. Therefore, a well-balanced trade-off should be made to maintain the overall system performance.

3.5   Conclusions

Compared with FDM modulation, OFDM methods virtually eliminate the need for pulse shaping, and makes the demodulation process and channel equalisation much easier to implement, using multiplication rather than subchannel filtering. They also provide a data transmission robust against both ICI and ISI caused by the multipath channel. Due to hardware limitations, most air-coupled capacitive ultrasonic transducers have a relatively narrow bandwidth to provide data communication with an acceptable transfer rate. OFDM modulation can maximise bandwidth utilisation by allowing sub-carriers to overlap

each other.

This chapter presented a successful implementation of a pilot-aided OFDM data communication in air using both commercially available and prototype capacitive ultrasonic transducers. Phase and amplitude distortion due to STO and the effect of the ultrasonic channel in air was explained and corrected in advance of OFDM demodulation and demultiplexing by executing a pilot-aided channel estimation algorithm. The commercially available and prototype ultrasonic transducers had different operating frequencies at 77 kHz and 300 kHz, and bandwidths of 45 kHz and 200 kHz, respectively. Baseband modulations chosen were BPSK, QPSK and 16-QAM, and their performances in terms of data rate, range, spectral efficiency, SNR and BER were evaluated. The experimental results have shown that a 16-QAM modulation can be used to transmit ultrasonic signals in air at 180 kb/s over a range of 6 m in a direct LOS manner using SensComp transducers, and at 800 kb/s over 0.7 m using high-k transducers. It was also shown that the BPSK approach can provide the most reliable communication link up to 11 m at a reduced system transfer rate of 45 kb/s using SensComp transducers, and 1.2 m at 200 kb/s using high-k transducers. In a dispersive environment with multipath interference, system BER can be significantly reduced by adding CP to the OFDM symbols, however, at the expense of losing 20% of the transmitted signal power and overall data transfer rate.

The study in this chapter focused on LOS simplex communications. Non-LOS conditions may also occur in an indoor environment and the effects of reflection and diffraction will be presented in the next chapter. In addition, to enable the system for more practical use, full-duplex transmissions are also investigated in Chapter 4.

3.6 References

[1] S. Weinstein, "The history of orthogonal frequency-division multiplexing [history of communications]," *IEEE Commun. Mag.*, vol. 47, pp. 26–35, November 2009.

[2] J. Proakis and M. Salehi, *Digital Communications*. New York, NY, USA: McGraw-Hill, 2008.

[3] E. McCune, *Practical digital wireless signals*. Cambridge, U.K.: Cambridge University Press, 2010.

[4] J. Bingham, "Multicarrier modulation for data transmission: an idea whose time has come," *IEEE Commun. Mag.*, vol. 28, pp. 5–14, May 1990.

[5] S. G. McSweeney and W. M. D. Wright, "HfO2 high-k dielectric layers in air-coupled capacitive ultrasonic transducers," in *Proc. IEEE Int. Ultrason. Symp. (IUS)*, pp. 864–867, 2011.

[6] G. D. Wilk, R. M. Wallace, and J. M. Anthony, "High-k gate dielectrics: Current status and materials properties considerations," *J. Appl. Phys.*, vol. 89, no. 10, pp. 5243–5275, 2001.

[7] C. Li, D. Hutchins, and R. Green, "Short-range ultrasonic communications in air using quadrature modulation," *IEEE Trans. Ultrason., Ferroelectr., Freq. Control*, vol. 56, no. 10, pp. 2060–2072, 2009.

[8] W. M. D. Wright, O. Doyle, and C. T. Foley, "Multi-channel data transfer using air-coupled capacitive ultrasonic transducers," in *Proc. IEEE Int. Ultrason. Symp. (IUS)*, pp. 1805–1808, 2006.

[9] C. Li, D. Hutchins, and R. Green, "Short-range ultrasonic digital communications in air," *IEEE Trans. Ultrason., Ferroelectr., Freq. Control*, vol. 55, no. 4, pp. 908–918, 2008.

[10] H. D. Haynes, M. A. Akeman, and V. M. Baylor, "Ultrasonic communication project, phase 1, FY 1999," tech. rep., Oak Bridge, TN, USA, Jun. 2000.

[11] S. Holm, O. Hovind, S. Rostad, and R. Holm, "Indoors data communications using airborne ultrasound," in *Proc. IEEE Int. Acoust. Speech. Signal (ICASSP)*, vol. 3, pp. 957–960, 2005.

[12] J. Seybold, *Introduction to RF Propagation*. Hoboken, NJ, USA: John Wiley & Sons, 2005.

[13] S. H. Han and J. H. Lee, "An overview of peak-to-average power ratio reduction techniques for multicarrier transmission," *IEEE Wirel. Commun.*, vol. 12, pp. 56–65, Apr. 2005.

Chapter 4

Non Line-of-Sight (NLOS) Transmissions and Duplex Communication

4.1 Introduction

The studies in Chapter 2 and Chapter 3 were both performed in a direct LOS manner. However, non-LOS (NLOS) propagation paths may exist in an indoor environment. Section 4.2 and Section 4.3 will investigate the effects of reflection and diffraction during signal transmissions. Full-duplex data communication using two pairs of ultrasonic transducers is also studied for more practical use in Section 4.4. Section 4.5 gives the conclusion of this chapter.

4.2 Reflection

4.2.1 Specular reflection

When an ultrasonic wave travelling through air encounters a solid boundary medium, reflection and refraction may occur. Due to the large acoustic

116

impedance mismatch between air and most solid materials, much of the energy of the ultrasonic waves may be reflected. If the reflection occurs at relatively large, regular shaped objects with smooth surfaces, the echoes can be relatively intense and angle dependent. This type of reflection is called specular reflection. Typical building materials with highly reflective surfaces are, for example, wood, metal, plastic and glass.

According to Snell's law of refraction [1], for the reflected wave in the same medium, the angle of incidence θ_i is equal to the angle of reflection θ_r with respect to the surface normal, as shown in Fig. 4.1. It holds for a flat reflection boundary and homogeneous media where the dimensions of any features on the reflective surface is large compared to the wavelength of the emitted ultrasound.
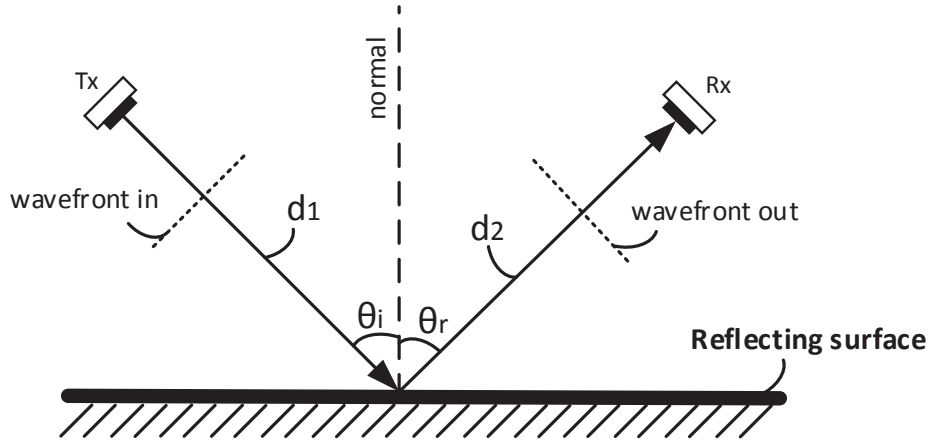
Figure 4.1: Reflection from a specular surface with the incidence angle θ_i equal to reflection angle θ_r.

To evaluate the effects of specular reflection on signal transmissions, 16QAM-OFDM modulated signals were transmitted and received using the SensComp ultrasonic sensors with equal incidence and reflection angles in front of a specular reflector made of polyethylene. Note that the distances d_1 and d_2 in Fig. 4.1 were both set at 1 m. By using the same parameter settings in Table 3.1,

Table 4.1: Received signal strength at different incidence angles

θ_i, θ_r $(\theta_i = \theta_r)$	10°	20°	30°	40°	50°	60°	70°	80°
rms (dBmV)	35.7	35.2	35.3	35.7	35.5	35.7	35.2	35.5

the averaged received signal strength from 10 measurements with 90 packets of OFDM signals in dBmV at different angles from $10°$ to $80°$ with a step of $10°$ was measured as shown in Table 4.1. As listed in the table, the received signal strength of OFDM signals at all angles are very close to each other, and the variations are due to alignment errors and background noise. The averaged signal strength at all angles was at 35.48 dBmV, and this is compared with the received signal strength (36 dBmV) when the transmitter and the receiver transducers are separated at a direct LOS distance of 2 m in air. There is only an approximately 0.5 dBmV drop in terms of the signal energy. This part of energy was transmitted through the air/solid interface. Therefore, most of the ultrasonic energy was reflected from a specular reflecting surface at all incidence angles. The received 16QAM-OFDM signal constellations at incidence angles of $20°$ and $80°$ are compared with those of a direct LOS signal, as shown in Fig. 4.2. As can be seen, there is visually little difference between the LOS signal constellation
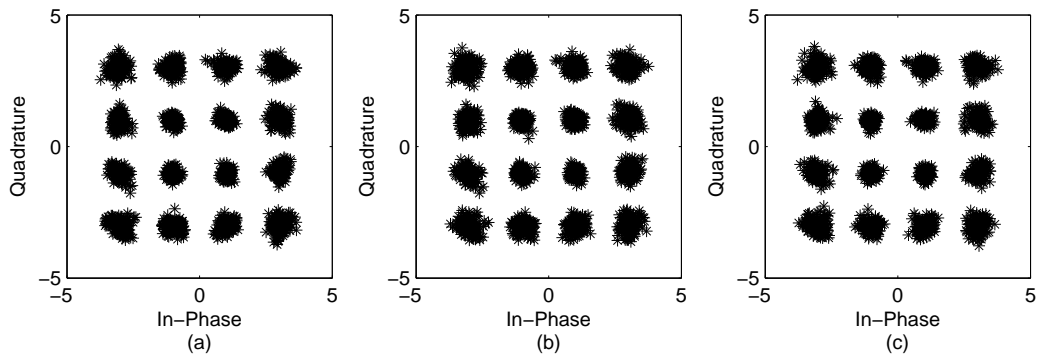
Figure 4.2: Received 16-QAM signal constellation diagrams (a) at 2-m direct LOS, (b) incidence angle of $20°$, and (c) incidence angle of $80°$.
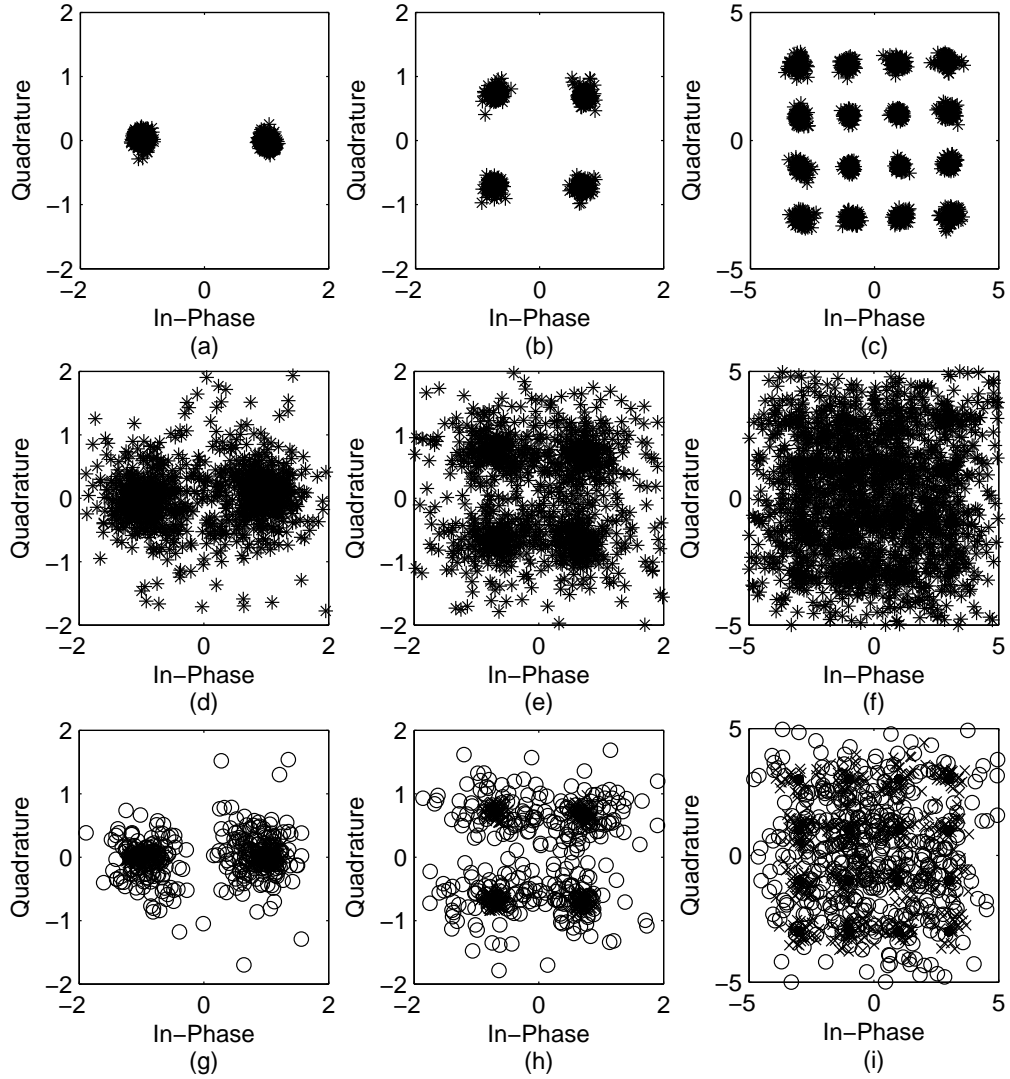
Figure 4.3: Received constellations with transducers aligned (a) - (c) and in front of a melamine sponge reflector (d) - (f) for BPSK-OFDM, QPSK-OFDM and 16QAM-OFDM, respectively. (g)-(i) are the corresponding constellations for (d)-(f) showing low frequencies ($\times$) and high frequencies (o).

and reflected signal constellations at both small and large incidence angles. It is concluded that specular reflections do not distort ultrasonic data signals when the incidence and reflected angle are the same.

In practise, ultrasonic waves inside a room may also be reflected by relatively soft, weakly reflective surfaces such as carpets, curtains and textiles that have absorbing and scattering properties. By replacing the specular reflector in

Fig. 4.1 with melamine sponge, signal performance for the three OFDM modulations were analysed with an incidence and reception angle of $45°$. The received reflected signal constellation diagrams for the three modulation schemes are compared with those of the directly received signals through an air gap of 2 m in Fig. 4.3. The result shows three heavily distorted constellation patterns with most of the constellation points spread across the detection boundaries, as illustrated in Fig. 4.3(d)-(f). Fig. 4.3(g)-(i) present the corresponding constellation diagrams with only high-frequency symbols marked in 'o' and low-frequency symbols marked in '×'. The constellations indicate that most decoding errors were occurred at high-frequency channels for all three different modulations as many of their symbols are laying across the detection boundaries. Compared with the received signals in a direct LOS manner, the averaged signal intensity has dropped by about 25.8 dBmV. Therefore, in an indoor environment with porous absorbent surfaces, a considerable amount of the incident signal energy will be absorbed, and the amount of the absorption goes up with frequency. In this case, the received reflected signals could not be correctly decoded. This
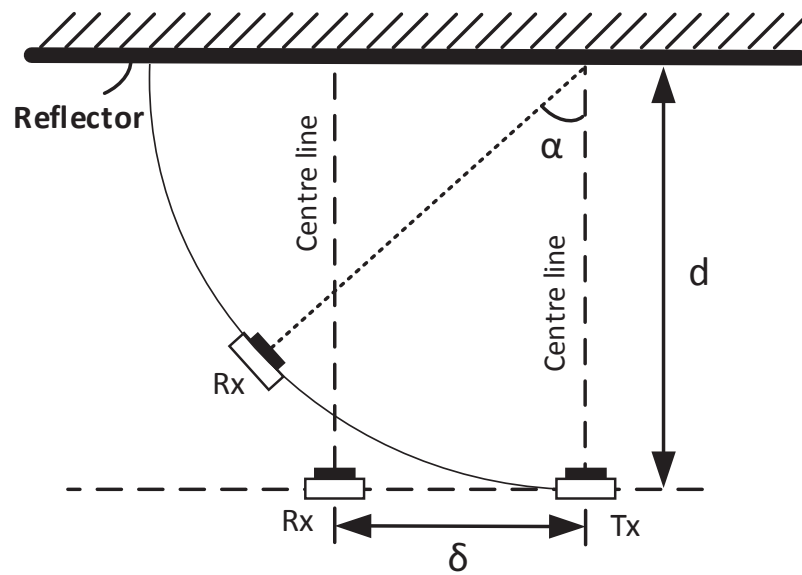
Figure 4.4: Diagram of transducer arrangements with lateral displacement δ and oblique angle α at a separation of d in front of a solid specular reflector.
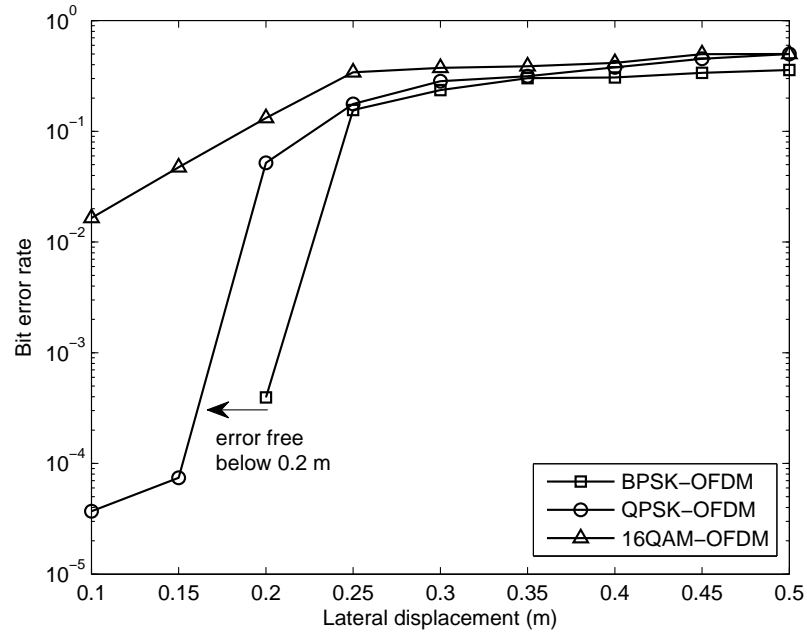
Figure 4.5:   BERs with lateral displacement in a reflection setup using BPSK, QPSK, and 16-QAM modulations.

may prove beneficial by reducing multipath reflections.

The situation when the transducer centre normals are not coincident in front of a specular reflector was also studied. The transmitter transducer (Tx), as shown in Fig. 4.4, was placed away from the solid reflector at a distance of $d = 1$ m. The front face of the receiver transducer (Rx) was facing the reflector in parallel, and with a varied lateral displacement δ. The BER results for BPSK-OFDM, QPSK-OFDM and 16QAM-OFDM modulations with increasing lateral displacements up to 0.5 m are shown in Fig. 4.5. As can be seen, all three BER curves ascend rapidly with lateral displacement. The lowest order modulation scheme, BPSK, achieved signal transmission with no measurable errors below 0.2 m. When the lateral displacement increased to 0.25 m, the BERs for all three modulations reached a level of about 20%. The received signal constellations for all three modulation schemes at lateral displacements of 0.1 m and 0.25 m are shown in Fig. 4.6. The received constellations at 0.1 m in Fig. 4.6(a)-(c) are compared with the ones at 0.25 m in Fig. 4.6(d)-(f). It can be seen that the
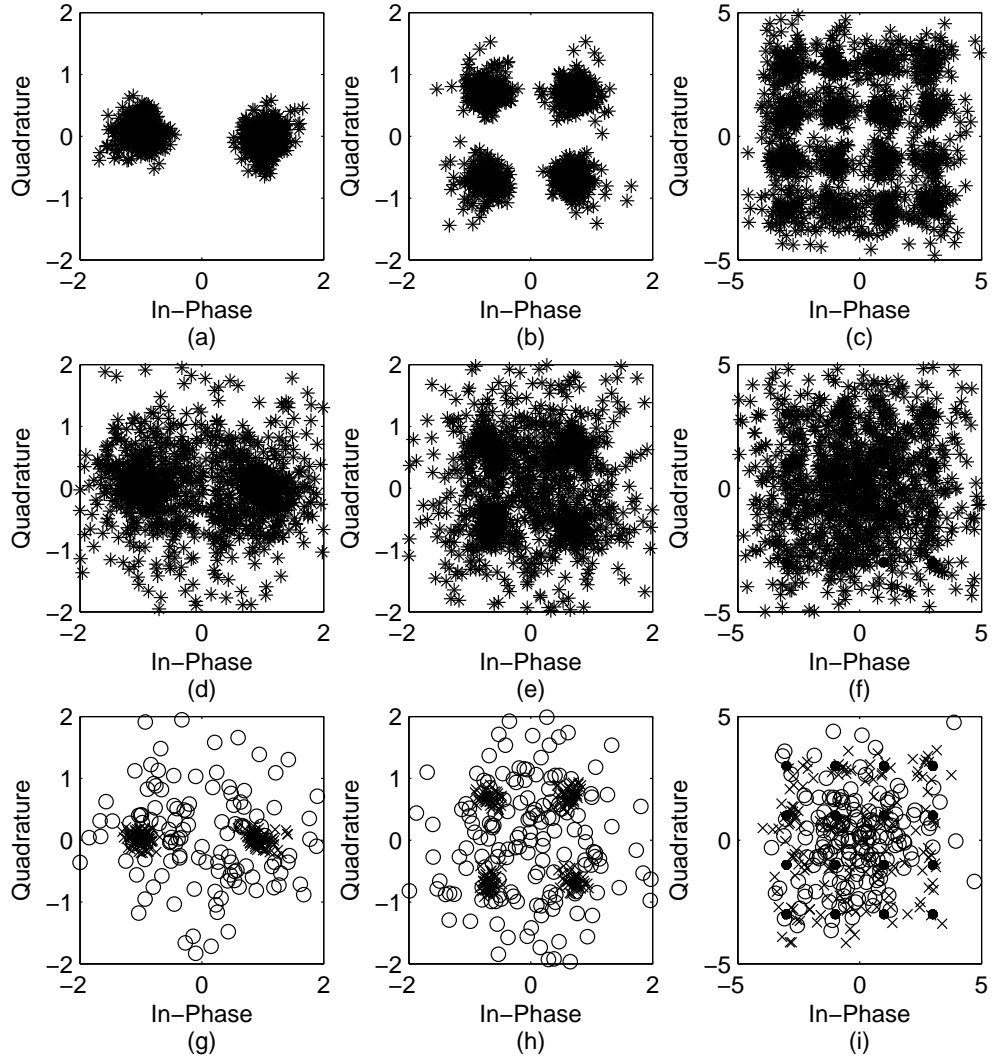
Figure 4.6: Received signal constellations with lateral displacements of 0.1 m for (a)-(c), and 0.25 m for (d)-(f) in a reflection setup using BPSK, QPSK, and 16-QAM modulations. (g)-(i) are the corresponding constellations for (d)-(f) showing low frequencies (×) and high frequencies (o).

constellations became more distorted with more spreading around the target points. In Fig 4.6(g)-(i), the high-frequency channel constellations as marked in 'o' are more scattered compared with the low-frequency channel constellations marked in '×' for all three modulations. As a result, high-frequency channels contributed much more decoding error as less high-frequency energy can be intercepted by the receiver transducer with a large lateral displacement. The bit
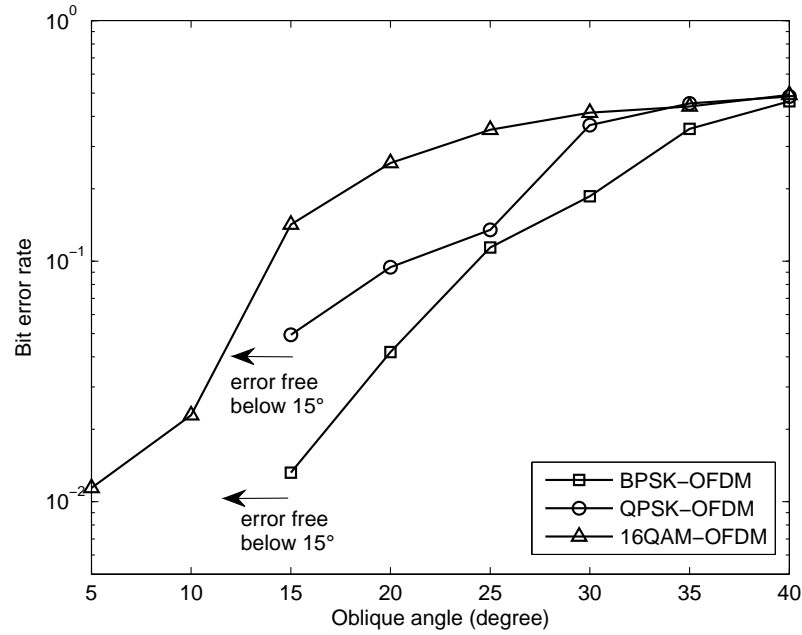
Figure 4.7: BERs with oblique angles in a reflection setup using BPSK, QPSK, and 16-QAM modulations.

error tolerance when the receiver transducer was placed with different angles α for the three modulations was also evaluated, as shown in Fig. 4.7. The three BER curves present a similar trend as the curves illustrated in Fig. 4.5. For BPSK and QPSK, these two modulation methods experienced error-free decoding with an oblique angle up to $15°$. Accordingly, the received signal constellations at $5°$ and $15°$ for the three modulations are compared in Fig. 4.8. Again, high-frequency channel constellations were more dissipated around target points compared with low-frequency ones as shown in Fig. 4.8(g)-(i). This is because the receiver started to miss high-frequency ultrasonic beams at a large oblique angle.

Fig. 4.9 presents the transducer arrangement in front of a solid specular reflector with source image (Tx') and beam contours indicated. As can be seen, the theoretical beam divergence angles when using SensComp sensors at 55 kHz and 99 kHz are $11.4°$ and $6.3°$, respectively. Therefore, the maximum lateral displacement of the receiver transducer that can receive the 99 kHz sig-
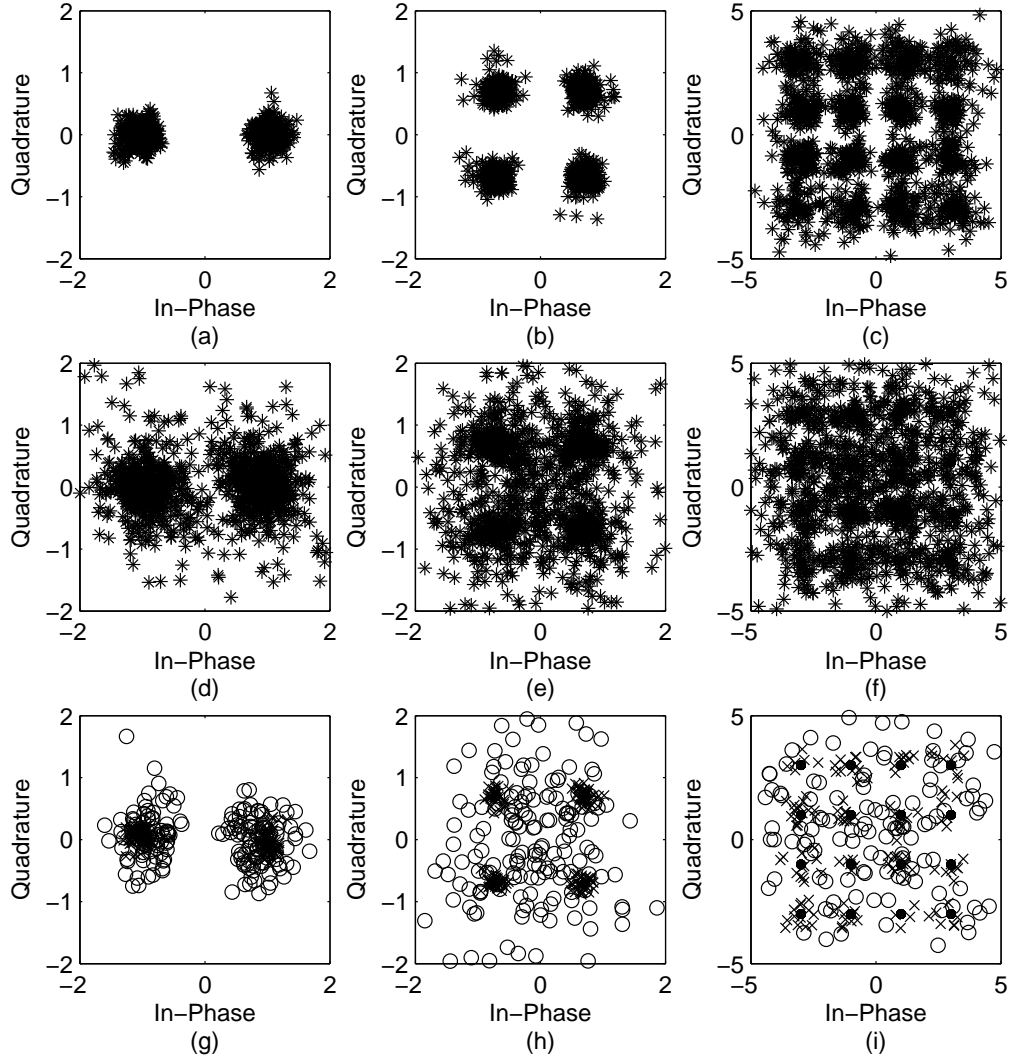
Figure 4.8: Received signal constellations with oblique angles of $5°$ for (a)-(c), and $15°$ for (d)-(f) in a reflection setup using BPSK, QPSK, and 16-QAM modulations. (g)-(i) are the corresponding constellations for (d)-(f) showing low frequencies ($\times$) and high frequencies (o).

nal is 0.22 m at a separation of 2 m. The receiver starts to miss the reception of high-frequency signals beyond this range. This is the reason that the curves for all three modulations in Fig. 4.5 reached a high level of BER over 10% at 0.25 m. If the lateral displacement reaches the boundary of the lowest-frequency signal beam contour at 0.4 m, the receiver may fail to receive any signal from the transmitter at all. Similarly, for the setup of the receiver transducer with an
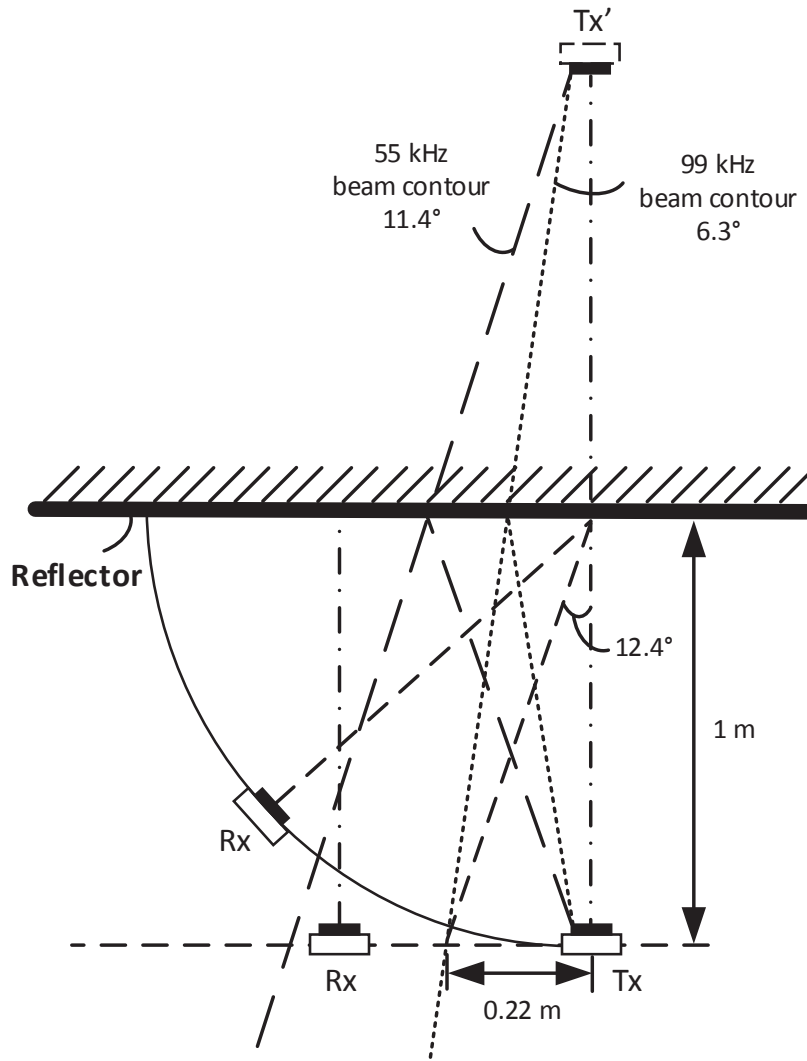
Figure 4.9: Diagram of transducer arrangement in front of a solid specular reflector with source image and beam contours indicated.

oblique angle, the maximum angle for the receiver to intercept the 99 kHz signal was $12.4°$. According to Fig. 4.7, both QPSK and BPSK started to have error decoding at $15°$. Note that due to the interference between the transmitted signal and the reflected signal across the air gap, 16-QAM modulation with relatively small noise margins still has error decoding even with a small lateral displacement or oblique angle. The specular reflection experiments suggest that ultrasonic data transmissions using low-order modulation schemes at low-frequency channels are preferred when the transmitter and receiver are in front of a solid specular reflector in the case that only a NLOS path is available.

4.2.2 Diffuse reflection

Some material surfaces inside a room are not perfectly flat. When the surface irregularities have dimensions similar to the ultrasonic wavelength, an incident wave will be reflected into many different directions, which is called diffuse reflection. When diffuse reflections dominate the specular reflection, the reflected ultrasonic signals are becoming much weaker and less predictable as each of them has its own particular amplitude, phase and direction.

Fig. 4.10 shows an aluminium diffuser with uneven surface irregularities of varying depths used as a possible reflector in the experiment. The diffuser has groove sizes of about 2 mm to 10 mm compared to the signal wavelengths of 3 mm to 6 mm. The OFDM signal performances for BPSK, QPSK and 16-QAM modulations were evaluated with an equal incident and reflected angle of $45°$ in front of the diffuser panel. The resulting received signal constellations for all three modulation schemes are compared with the ones reflected from a polyethylene surface as illustrated in Fig. 4.11. The constellation diagrams in Fig. 4.11 (d)-(f) clearly show the decrease of received signal SNR as the symbol points are more scattered around their target points due to amplitude and

Figure 4.10: Aluminium diffuser panel.
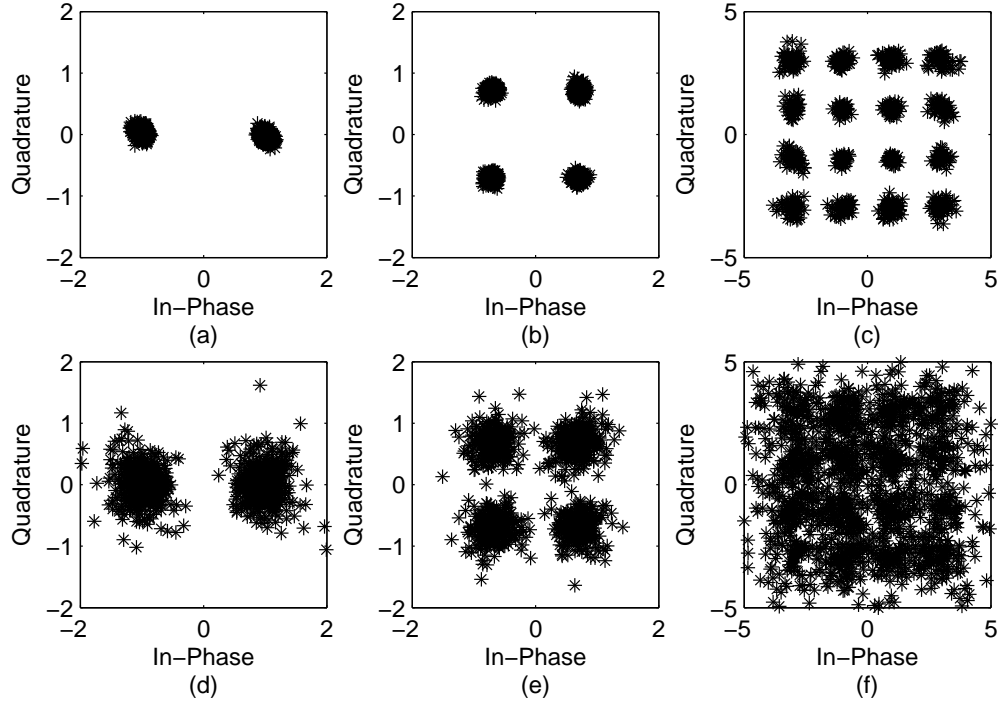
Figure 4.11: Received constellations with transducers in front of a polyethylene plastic reflector (a) - (c) and a aluminium reflector (d) - (f) for BPSK-OFDM, QPSK-OFDM and 16QAM-OFDM, respectively.

phase distortion. 16-QAM, which offers much faster data rate and higher levels of spectral efficiency for the system, however, is considerably less resilient to noise. Therefore, it obtained the most bit errors among the three modulation schemes. The BPSK signal, which carries the least bits of information per symbol was decoded without errors after reflecting from a solid diffuser. The averaged reduction of the received signal energy was about 11.06 dBmV compared with that of the received signal reflected from the specular reflector. It should be noted that the signal strength after diffuse reflection was 14.22 dBmV higher than that after reflected from a absorbing material. Therefore, using low-order modulation such as BPSK, is still feasible for data communication in the situation when diffuse reflection occurs.

4.3 Diffraction

In reality, any free edge of an object will diffract some sound energy in all directions. This is caused by an obstacle in the propagation path or by inhomogeneity of the air [2]. The effects of diffraction can be evaluated by measuring signal levels for different frequencies diffracted from a sharp-edged screen. Fig. 4.12 shows the configuration of transmitter transducer (Tx), receiver transducer (Rx), and a blocking screen, where the lateral displacement u of the receiver can vary with the transmitter and receiver transducer faces in parallel (position A). It should be noted that the screen still occluded half of the transmitted aperture when $u = 0$, and only diffracted signals could be obtained when $u \geq 0.0192$ m (i.e. half the aperture diameter) and no LOS signal could be received. Fig. 4.13 shows the resulting signal attenuation at the receiver Rx as a function of u, for the highest signal frequency (99 kHz) and the lowest signal frequency (55 kHz) used in the experiment. It can be seen that for both low and high frequency signals, the larger the lateral displacement, the smaller amount of diffracted energy that is received, as expected. In addition, the low frequency signals are diffracted more than the high frequency signals and can
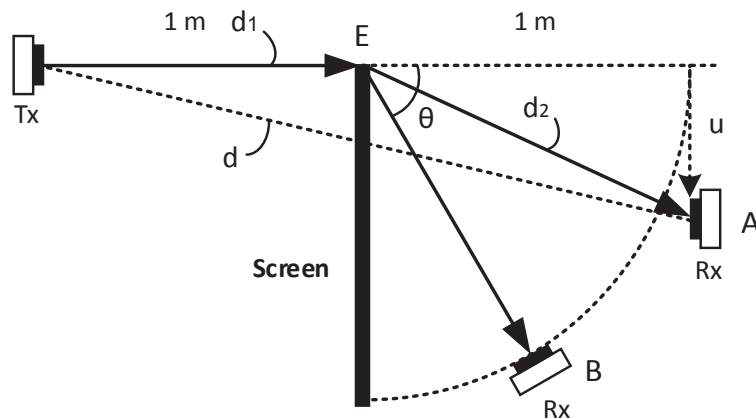
Figure 4.12: Configuration of transmitter Tx and receiver Rx where ultrasonic waves diffract around the edge of a blocking screen. Position A: transducer faces parallel, position B: receiver rotates and faces the edge E.
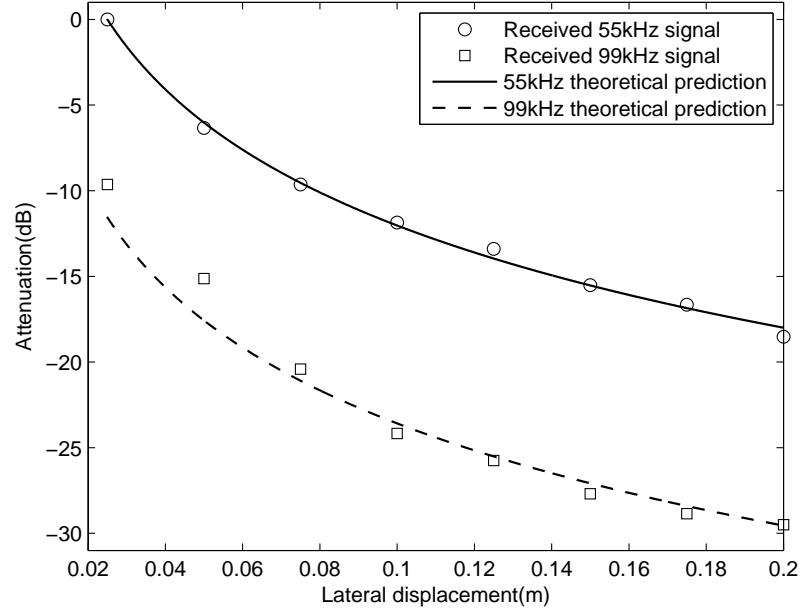
Figure 4.13: Theoretical and experimental signal attenuation for 55 kHz and 99 kHz ultrasonic waves with varied lateral displacement in a diffraction setup consisting of a sharp-edged screen.

be detected at larger values of lateral displacement. However, when the lateral displacement is as small as 0.2 m for example, the signal strength for high- and low-frequency waves were approximately -30 dB and -19 dB, respectively.

The reduction of sound pressure level due to diffraction around the edge of a barrier can be described in terms of a Fresnel number [2, 3], which is given by

$$N = \frac{2}{\lambda}(d_1 + d_2 - d) \tag{4.1}$$

where λ is the wavelength of sound and lengths d_1, d_2, and d are as shown in Fig. 4.12. Note that this equation is only valid for point sources and receivers. The attenuation by diffraction A_d, in dB, is then approximated as a function of the Fresnel number

$$A_d = 10log_{10}(20N). \tag{4.2}$$

129

Equation (4.2) yields the two attenuation curves for 55 kHz and 99 kHz signals in Fig. 4.13. As can be seen, the theoretical prediction matches the experimental data well. Note that the model only considers a point source and receiver, therefore the actual received signal energy may decrease faster than the theoretical prediction with the increase of lateral displacement as the effective reception area of the receiver is an ellipse rather than a circle. By using the same diffraction setup in Fig. 4.12, the BER results for all three modulation schemes with increasing lateral displacements up to 0.2 m are shown in Fig. 4.14. As can be seen, the BER curves for all three modulations ascend rapidly with lateral displacement. 16-QAM, with the most spreading of the spots in the constellation and hence with reduced noise immunity, experienced the most error decoding at all ranges. Lower-order modulation schemes, QPSK and BPSK, proved their superiority over 16-QAM when signals are diffracted around a sharp-edged screen, with first bit errors occurring at 0.1 m and 0.125 m, re-
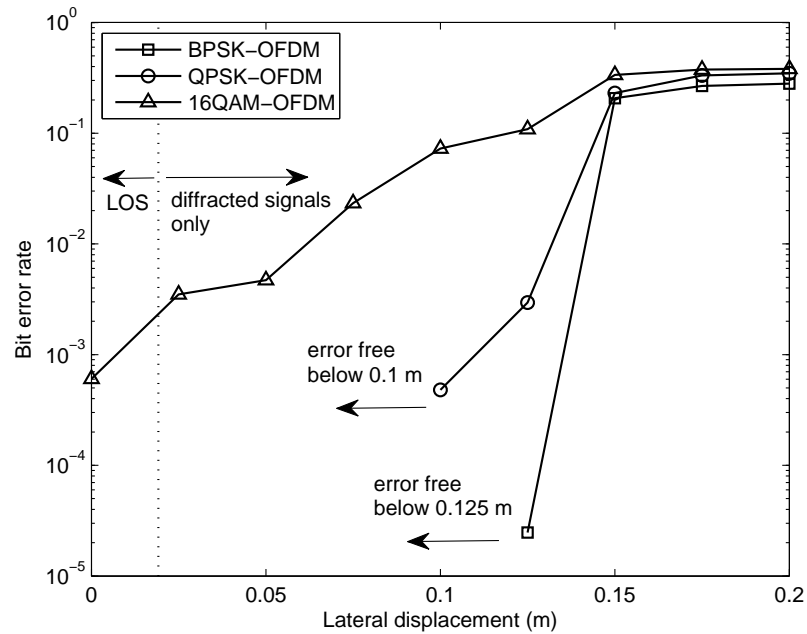
Figure 4.14: BERs with varied lateral displacement in a diffraction setup consisting of a sharp-edged screen using BPSK, QPSK and 16-QAM modulations, showing error-free NLOS transmission ranges for BPSK-OFDM and QPSK-OFDM.

spectively. When the lateral displacement of the receiver increased to 0.2 m, the BERs for all three modulations reached a level close to 30%. It indicates that BPSK and QPSK modulation schemes work better using only diffracted signals than 16-QAM in terms of BER performance. However, NLOS transmission with no measurable errors was achieved with BPSK-OFDM and QPSK-OFDM.

One situation that occurs when the face of the receiver is angled towards the edge of the screen barrier is illustrated in Fig. 4.12 position B. Note that there will be no LOS signal intercepted by the receiver when the oblique angle θ is larger than $1.1°$. The theoretical signal attenuation for 55 kHz and 99 kHz signals with an increasing oblique angle θ from $0°$ to $40°$ in a $5°$ step is compared with experimental results in Fig. 4.15, and good agreement was found between the two. Low-frequency signals are again diffracted more than the high-frequency ones in terms of the measured signal energy. Accordingly, the BER results for the three modulation schemes are illustrated in Fig. 4.16. It
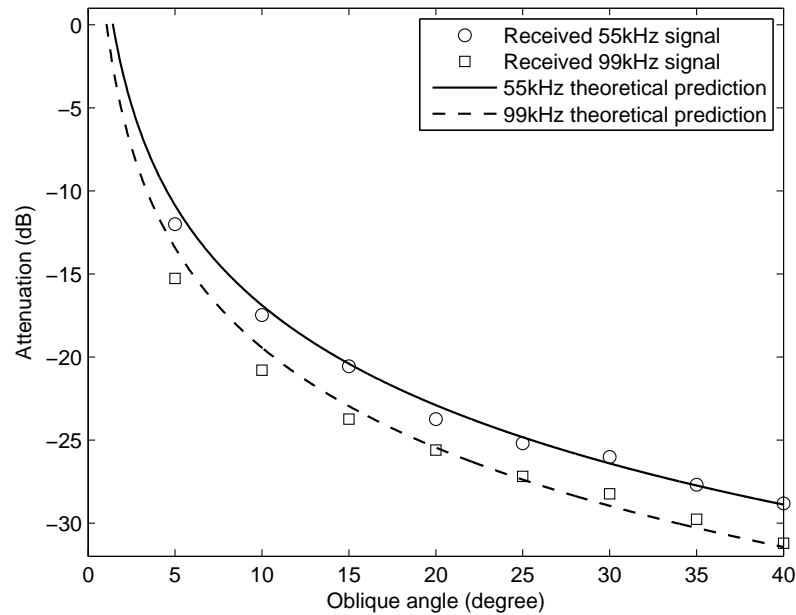
Figure 4.15: Theoretical and experimental signal attenuation for 55 kHz and 99 kHz ultrasonic waves with varied oblique angles in a diffraction setup consisting of a sharp-edged screen.

131
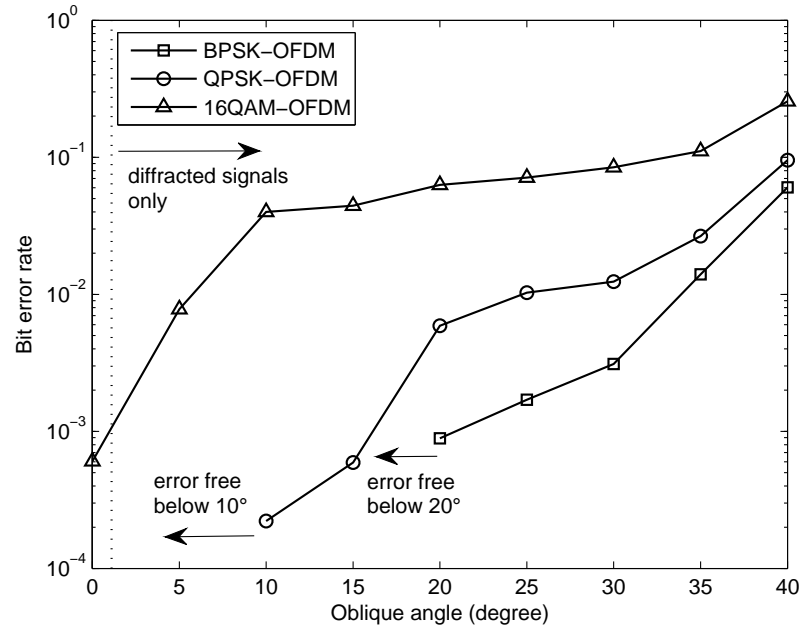
Figure 4.16: BERs with varied oblique angles when the receiver is facing towards the edge of the blocking screen using BPSK, QPSK and 16-QAM modulations.

shows a similar overall trend as the curves in Fig. 4.14. For QPSK and BPSK, the two modulation methods experienced error-free decoding with oblique angles up to $10°$ and $20°$, respectively. It was found from both diffraction experiments that ultrasonic data transmissions are possible after bending around obstacles using low-order modulations, and low frequencies are highly valued for better signal reception.

4.4   Full-duplex communication

In previous chapters, only simplex channels whose direction of transmission is unchanging are described. In other words, the data transmission has taken place in one direction, for example, a radio station is a simplex channel as it transmits the signal to its listeners and never allows them to transmit back. The advantage of simplex mode of transmission is that the entire bandwidth can be used, allowing more data to be transmitted at the same time. However, for more

practical wireless communications, a duplex channel should be considered. It consists of two simplex channels, a forward channel and a backward channel, linking at the same points. If the data is transmitted at a single time in only one direction, it is called half duplex transmission. If the message is flowing at the same time in both directions, the established link is full duplex. The main problem of the full-duplex mode of transmission is the bandwidth of the channel is decreased as two channels are used.

In this section, full-duplex ultrasonic data transmission is described using the SensComp transducers. The experimental arrangement of full-duplex communication is shown in Fig. 4.17. As can be seen, two pairs of ultrasonic sensors are used to transmit data simultaneously in opposite directions. Due to a possible manufacturing adjustment, more recently obtained SensComp transducers had a more concentrated frequency response at the nominal frequency of 50 kHz than the SensComp devices used in earlier chapters, as shown in Fig. 4.18 (b). The system impulse response and phase response over a range of 2 m are also illustrated in Fig. 4.18 (a) and (c), respectively. The measured peak-to-peak amplitude of the impulse signal was about 386 mV, and there is no phase distortion across the ultrasonic bands from 20 kHz to 150 kHz. The background noise was also analysed in both the time and frequency domains
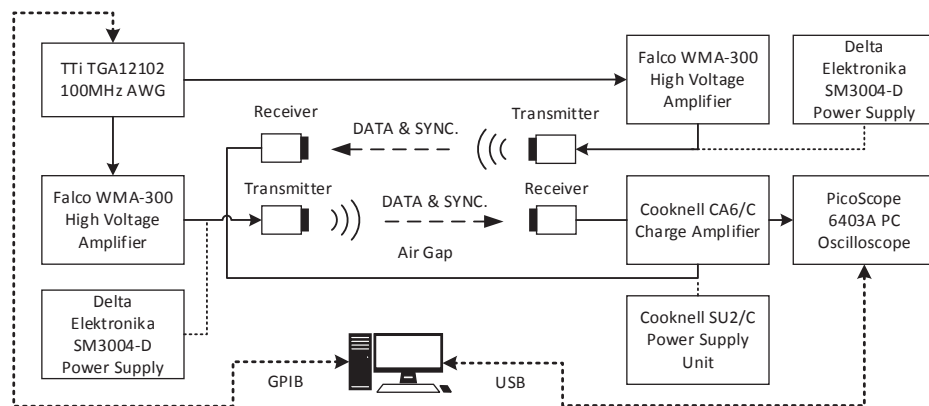
Figure 4.17: Schematic diagram of the full-duplex communication set-up.
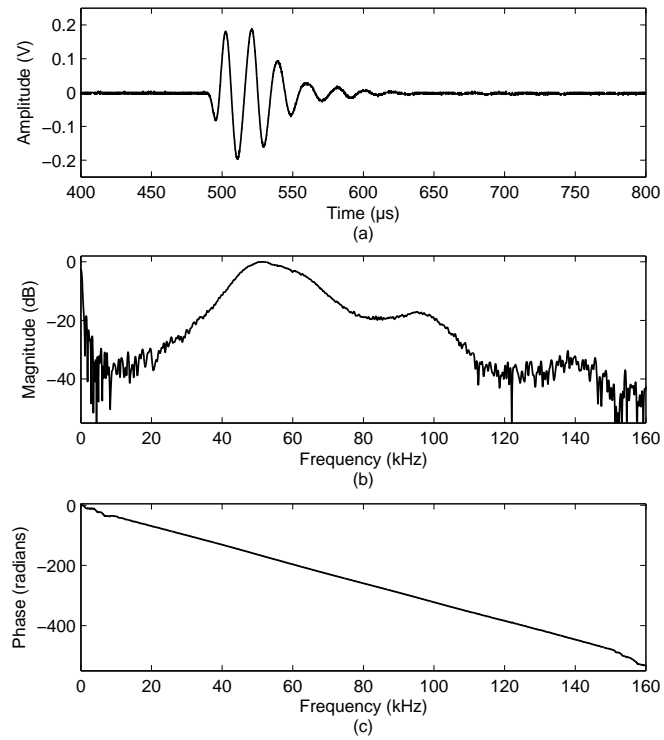
Figure 4.18: System characteristics over 2 m: (a) impulse response; (b) frequency response; and (c) phase response.
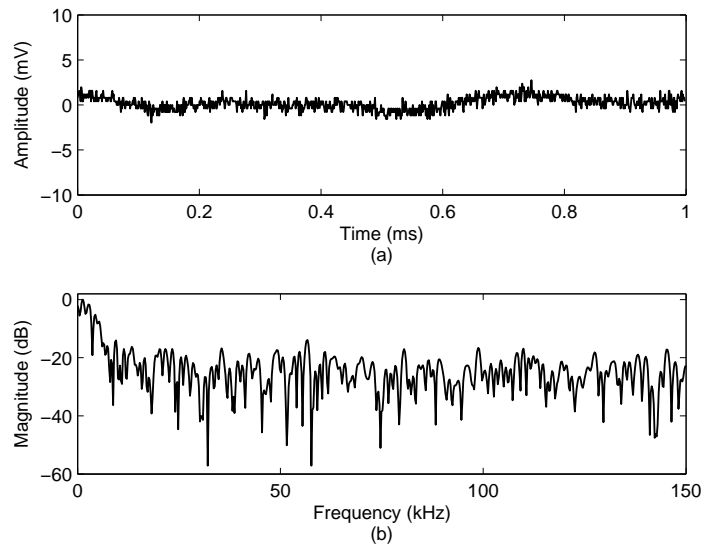
Figure 4.19: Background noise in: (a) time domain; and (b) frequency domain.

as shown in Fig. 4.19 (a) and (b), respectively. A relatively flat frequency spectrum was observed at ultrasonic frequencies as can be seen from Fig. 4.19 (b).

The recorded noise level was approximately 4.7 mV. Therefore, the SNR value of the new SenComp transducers at this range was 38.3 dB.

As the new SensComp transducers had higher sensitivity while narrower bandwidth than the old ones when compare their frequency responses in Fig. 4.18 and Fig. 2.3, fewer subcarriers could be used to transmit data. The experiment was initially conducted using 16QAM-OFDM modulation over frequencies from 30 kHz to 79 kHz. The symbol time was again set at 1 ms, so that there were 50 subchannel signals with an overall data rate of 200 kb/s being
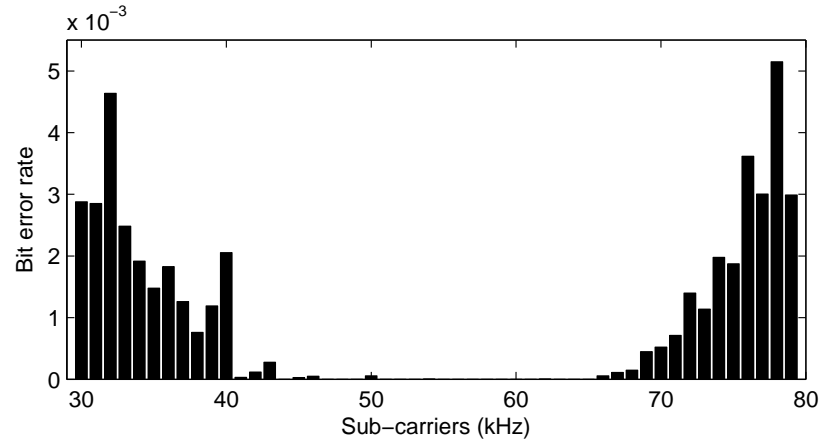
Figure 4.20: Error distribution at different sub-carriers from 30 kHz to 79 kHz over 5 m.
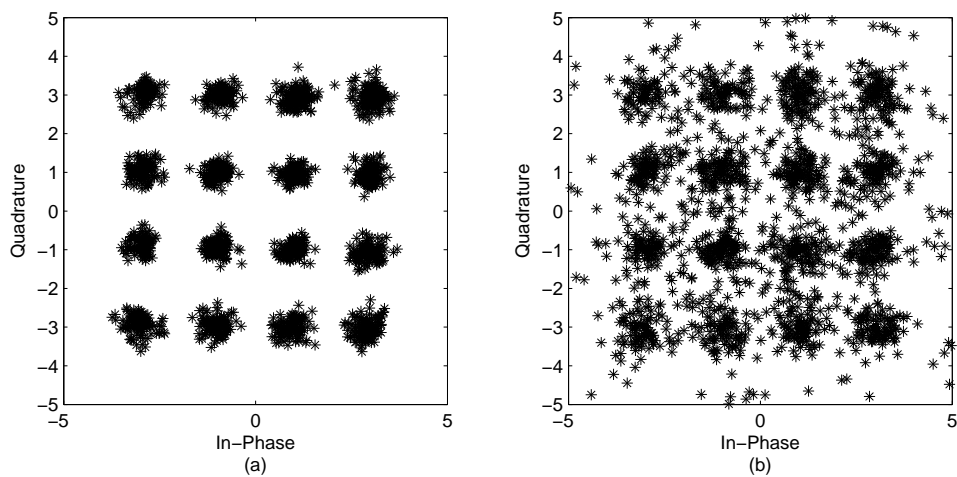
Figure 4.21: Received signal constellation at 5 m in (a) simplex, and (b) full-duplex mode.

transmitted through the air gap. The decoding bit errors of the received signal at 5 m were calculated as the error distribution at different subcarriers is shown in Fig. 4.20. As can be seen, the error distribution presents a U-shape pattern corresponding to the shape of the system frequency response in Fig. 4.18(b). More bit errors occurred at less responsive subchannels. According to the BER result in Fig. 4.20, subchannels from 45 kHz to 65 kHz with the minimum number of decoding errors were used to transmit 16-QAM modulated signals at 80 kb/s in both simplex and full-duplex configurations. The resulting received signal constellation diagrams are shown in Fig. 4.21 (a) and (b), respectively. As can be seen, in simplex mode, all decoded sub-carrier signal constellations are clustered around the target points with no measurable errors, while the received constellations are dispersed across the detection boundaries in full-duplex mode. This may be due to the interference between the two signals propagating simultaneously across the air gap. By splitting the frequency bands for signals transmitting in opposite directions, this interference may be eliminated.

4.4.1 Transmission in separate bands

One solution to achieve a reliable full-duplex communication link with two pairs of transducers is to use separate frequency bands for outward and return signals. The spectra for both outward and return OFDM modulated signals are shown in Fig. 4.22. As can be seen, distinctive peaks can be found at all orthogonal sub-carriers, and they are divided into two groups with a 1-kHz guard band at 55 kHz. In this case, the data rate was reduced to 40 kb/s for the transmission in each direction. By using the channel allocation illustrated in Fig. 4.22, both the received outward and return signal constellations in simplex and full-duplex transmission modes over 5 m are compared in Fig. 4.23. As can be seen, there is visually little difference between the diagrams in simplex and
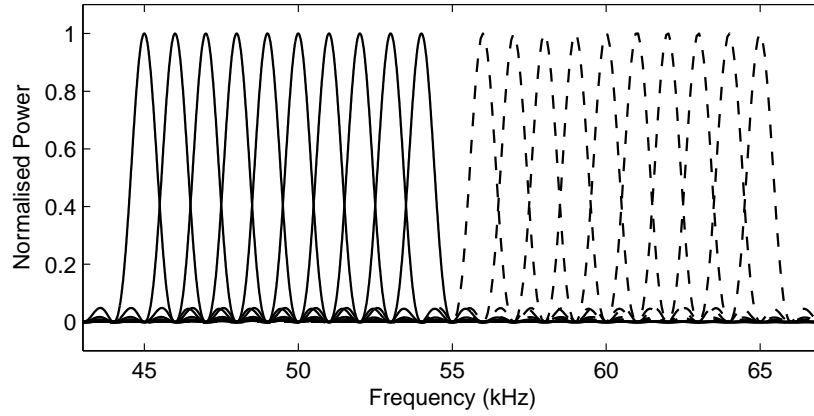
Figure 4.22: Outward (solid line) and return (dashed line) signal spectra at separate bands.
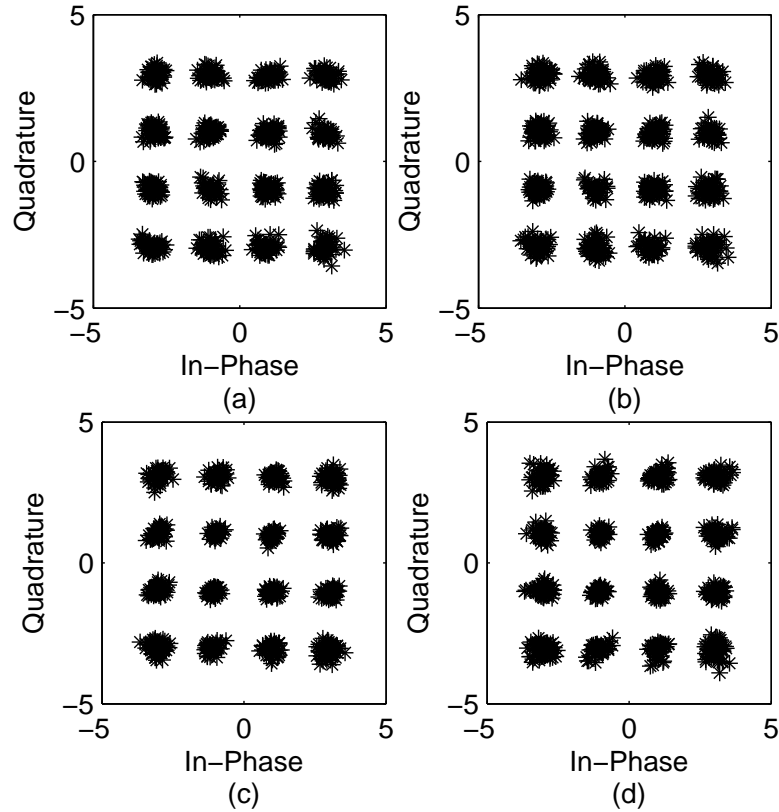
Figure 4.23: Comparison of received outward signal constellation in (a) simplex mode and (b) full-duplex mode at a transmission distance of 5 m. Corresponding constellations of received return signals (c) and (d) at a transmission distance of 5 m.

duplex mode with all constellations points well located around their target

points. As a result, no decoding bit errors were detected. Fig. 4.24 (a) and (b)
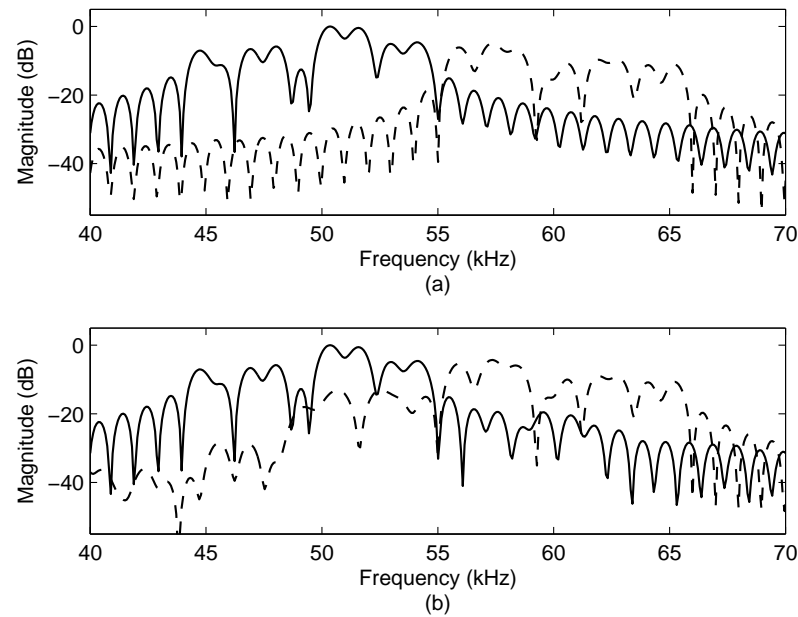
Figure 4.24: Received outward (solid line) and return (dashed line) signal spectra over 5 m in (a) simplex mode, and (b) full-duplex mode.

shows overlapped received outward and return signal spectra at 5 m in simplex and full-duplex mode, respectively. In simplex mode, both the outward and return signal spectra are well located in their given bands with side-lobes spread across each other. In duplex mode, the side-lobes of both outward and return signal spectra increased, especially the ones between 50 and 55 kHz from the return signal are increased about 15 dB compare to those in the simplex mode. Fig. 4.25 shows the spectra of the received outward and return signal by the receiver on the same side as the transmitter. As can be seen, both the outward and return signal spectra stand out at their frequency bands above -30 dB. The peak of the outward signal spectra reached at around -10 dB as the 50 to 55 kHz sub-carriers are at the most responsive bands of the new Senscomp transducers. It indicates that the crosstalk between the transmitter and receiver on the same side are strong though no decoding errors were detected in the full-duplex mode. Therefore, transducer casings should be better shielded to prevent potential interference due to crosstalk for better signal transmission. It should also

138
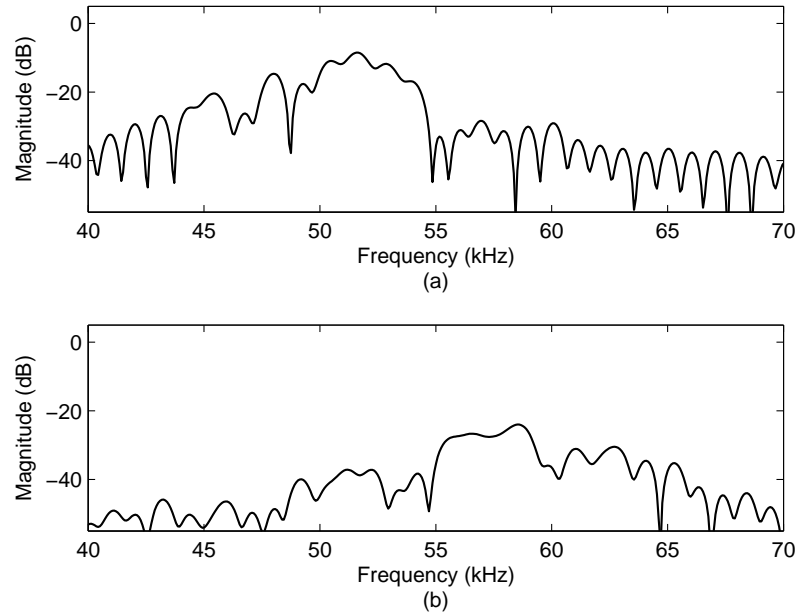
Figure 4.25: Received (a) outward (solid line) and (b) return (dashed line) signal spectra when the receiver is on the same side as the transmitter.

be noted that over longer ranges, the return signal at high-frequency bands will be disproportionally affected due to the frequency-dependent attenuation. Interleaving shares all the channels between the uplink and downlink, and could still maintain full-duplex transmissions at reduced data rates. This technique is investigated in the next section.

4.4.2 Transmission in interleaved bands

The orthogonality is still maintained if the OFDM subchannel spacing is doubled. Therefore, it is possible to transmit the outward and return OFDM signals in an interleaved method without interfering each other. Fig. 4.26 shows an illustrative spectrum pattern of both the outward and return signals. This is to maintain the full-duplex transmission over long ranges as similar channels at all available frequencies are shared by both outward and return links. Otherwise, the link which occupies high-frequency channels may be completely destroyed due to the signal attenuation at high frequencies while the link us-
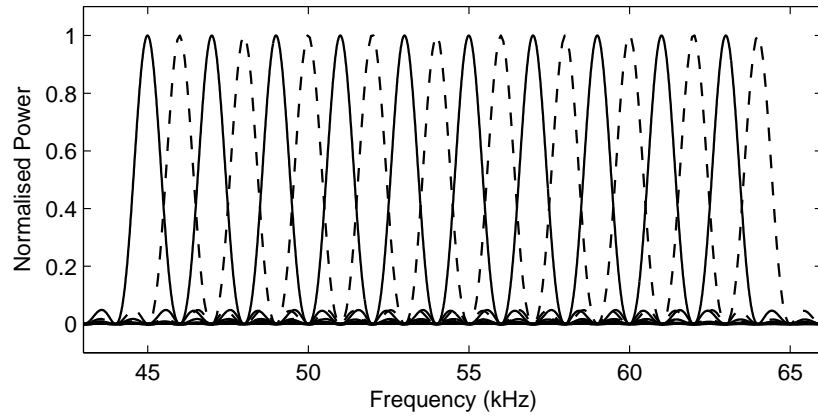
Figure 4.26: Interleaved outward (solid line) and return (dashed line) spectra with an orthogonal spacing of 1 kHz.
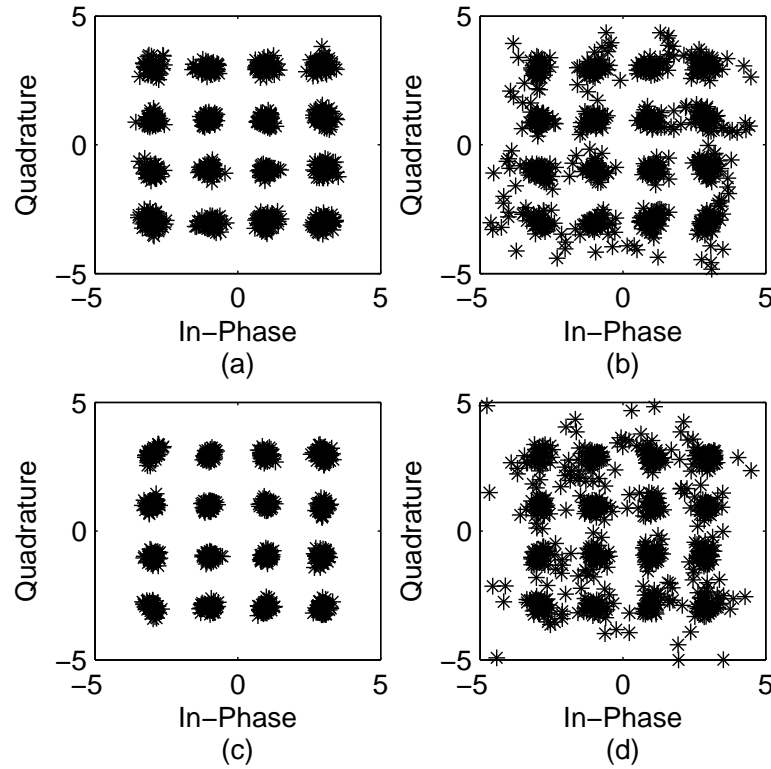
Figure 4.27: Comparison of received outward signal constellation in (a) simplex mode and (b) full-duplex mode at a transmission distance of 5 m. Corresponding constellations of received return signals (c) and (d) at a transmission distance of 5 m.

ing low-frequency channels is still functioning properly. As can be seen from

Fig. 4.26, the outward and return signal subcarriers are alternately loaded and

evenly spaced at 1 kHz in an orthogonal way, achieving a data rate of 40 kb/s in each direction. Accordingly, the received outward and return signal constellations in simplex and full-duplex modes are compared in Fig. 4.27. As the constellation diagrams presented in Fig. 4.27(a) and (c), no decoding bit errors were reported for both outward and return transmissions in simplex mode. However, both the constellation diagrams are more noisy and a small number of constellations points dropped across the detection boundaries in full-duplex mode as shown in Fig. 4.27 (b) and (d). It was found that the sub-channels that introduced decoding errors were at 50 kHz, 51 kHz, 52 kHz and 54 kHz. The received outward and return signal spectra in simplex and full-duplex mode are also illustrated in Fig. 4.28(a) and (b), respectively. As can be seen in Fig. 4.28(a), in simplex transmission mode, no bit errors were detected though the peak of subchannel 51 kHz for the outward was slightly distorted, and the peak of subchannel 52 kHz for the return was right-shifted by about 0.5 kHz. However, in duplex transmission mode, the two subchannels includ-
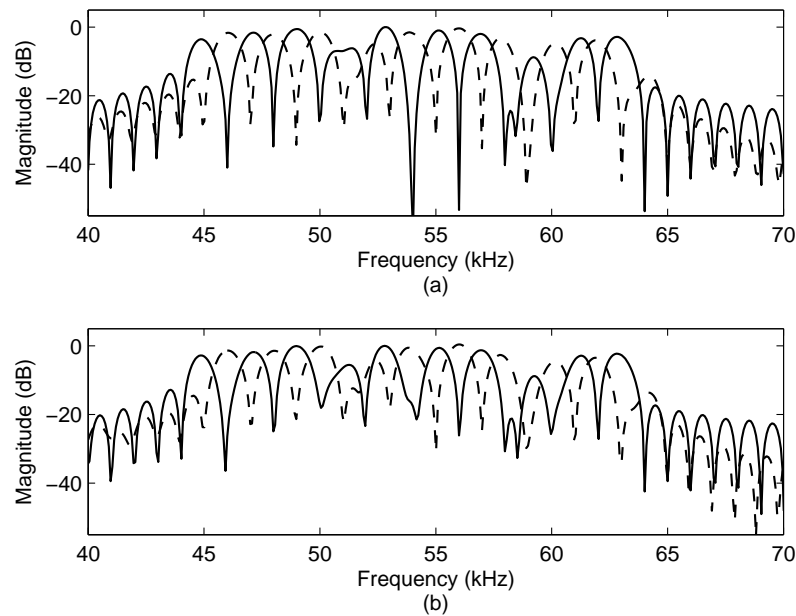
Figure 4.28: (a) Received outward (solid line) and return signal (dashed line) spectra in (a) simplex mode, and (b) full-duplex mode.

ing the neighbouring ones were more distorted according to the spectra shown in Fig. 4.28(b). It indicates that the OFDM signals are more sensitive to inter-channel interference (ICI) using interleaved bands with 1 kHz channel spacing in full-duplex transmission mode.

When the channel spacing of the interleaved bands was doubled as illustrated in Fig. 4.29, the system was more robust to ICI and lack of orthogonality as the received outward and return signal constellations at 5 m clustered tightly around their target symbol points with no decoding errors as shown in Fig. 4.30 (a) and (b), respectively. It should be noted that by increasing the channel spac-
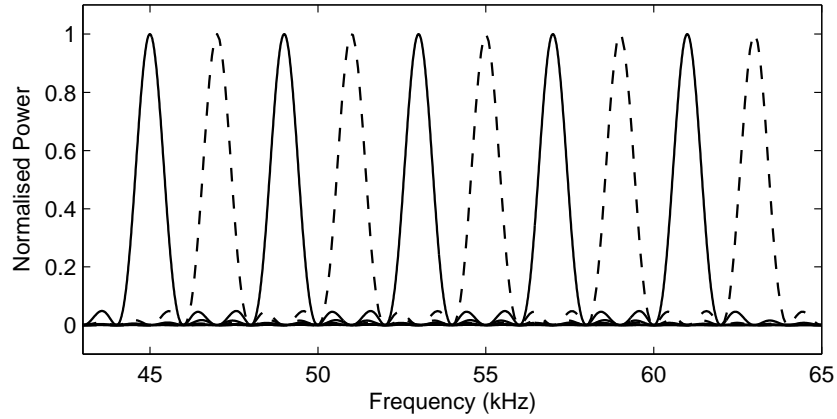
Figure 4.29: Interleaved outward (solid line) and return (dashed line) spectra with an orthogonal spacing of 2 kHz.
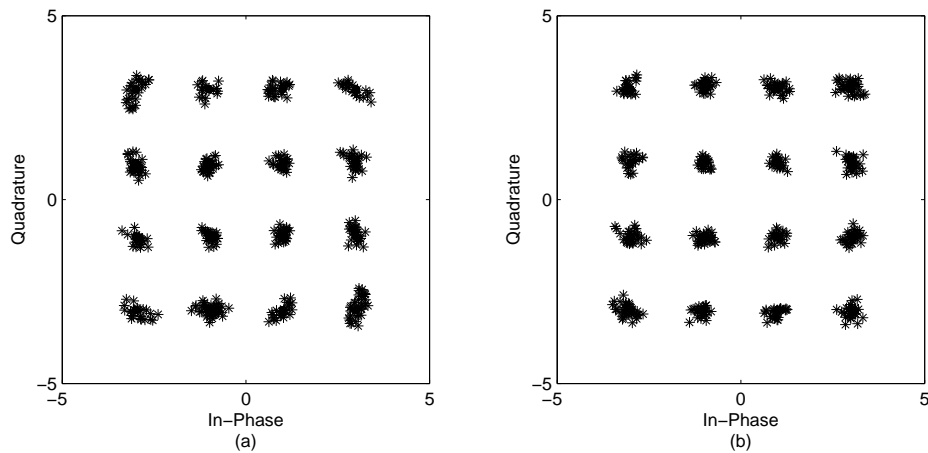
Figure 4.30: Comparison of received outward (a) and return (b) signal constellations with a channel spacing of 2 kHz in full-duplex mode at a transmission distance of 5 m.

142

ing to 2 kHz for better ICI characteristics, the achieved one-way data rate was reduced to 20 kb/s.

4.5   Conclusions

Ultrasonic signal transmissions in NLOS conditions including reflection and diffraction were studied. When the transmitted signal was reflected from a specular surface, the received signal strength kept almost the same as long as the incidence angle was equal to the reflection angle. Approximately 0.5 dBmV of signal energy loss was measured at all different incidence angles. 16QAM-OFDM signals were transmitted without measurable errors when the reflection path length was 2 m in front a specular reflector. BPSK-OFDM signal was proven to return the best BER performance and high frequency sub-channels were prone to errors when the transducer centre normals were not coincident. When the ultrasonic signal was transmitted towards a soft absorbent material surface, the received signal intensity dropped by about 25.8 dBmV. It was found that the OFDM signals experienced a significant amount of decoding errors especially in high-frequency channels due to this energy loss. When the signal was reflected by a diffuse reflector, the received energy dropped by about 11.06 dBmV compared with that of the signal reflected from the specular reflector. BPSK-OFDM signal again was proved to be more robust than the modulation schemes with higher-order formats after diffuse reflection. It was shown by the experiment that all three OFDM modulation schemes investigated could operate after diffracting around a sharp-edged screen, and that BPSK-OFDM was proven to return the best BER performance when only diffracted signals were received in the channel. The diffraction effects were incorporated into a model of the ultrasonic channel that also accounted for beam spread and attenuation in air. The simulations were a good match to the measured signals and

diffracted signals could be demodulated successfully.

By using new SensComp devices with a reduced bandwidth, full-duplex data transmission was implemented in experiment. It was shown that the reliable OFDM channels were from 45 kHz to 65 kHz using separate outward and return frequency bands with a guard band of 1 kHz in between. Crosstalk was detected by the receiver from a neighbouring transmitter on the same side, however, error-free transmission still held using 16QAM-OFDM over 5 m. The achieved unidirectional data transfer rate was 40 kb/s. By using interleaved channel allocation, the connections in both directions could still be maintained with reduced data rates over long ranges as high-frequency channels were shared by both outward and return links. However, OFDM signals were found to be more sensitive to distortion and frequency shift with a channel spacing of 1 kHz. By increasing the channel spacing to 2 kHz, the system was able to perform full-duplex signal transmission without decoding errors at a unidirectional data rate
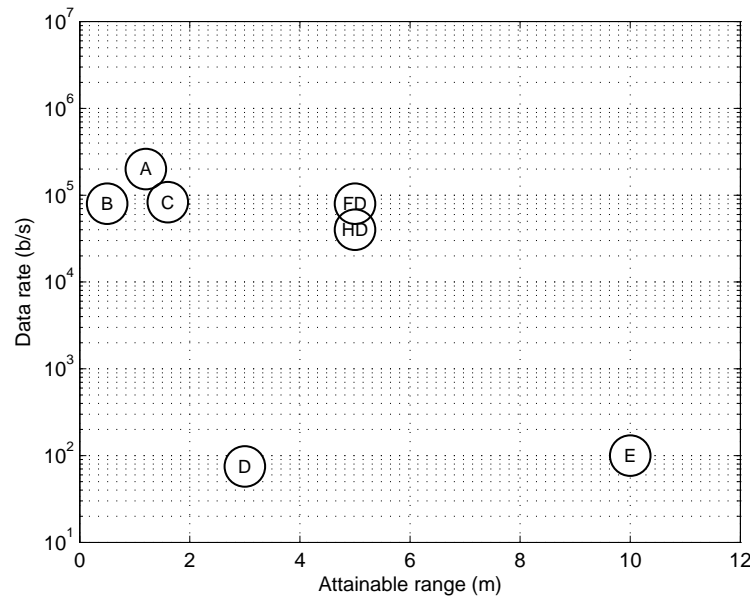
Figure 4.31: Comparison of different airborne ultrasonic data communication systems and their data rates at attainable transmission ranges. HD and FD represent 16QAM-OFDM modulation in half-duplex and full-duplex modes, respectively. A, B, C, D, E refer to the works referenced in [4], [5], [6], [7] and [8], respectively.

of 20 kb/s over 5 m. Again, Fig. 4.31 compares both half-duplex and full-duplex communications with the prior works in terms of the achieved range and data rate, showing improvement by using the new Senscomp ultrasonic transducers.

4.6   References

[1] D. Blackstock, *Fundamentals of Physical Acoustics*. Hoboken, NJ, USA: John Wiley & Sons, 2000.

[2] M. J. Crocker, *Handbook of acoustics*. Hoboken, NJ, USA: John Wiley & Sons, 1998.

[3] N. H. F. Thomas D. Rossing, *Principles of Vibration and Sound*. New York, NY, USA: Springer, 2004.

[4] C. Li, D. Hutchins, and R. Green, "Short-range ultrasonic communications in air using quadrature modulation," *IEEE Trans. Ultrason., Ferroelectr., Freq. Control*, vol. 56, no. 10, pp. 2060–2072, 2009.

[5] W. M. D. Wright, O. Doyle, and C. T. Foley, "Multi-channel data transfer using air-coupled capacitive ultrasonic transducers," in *Proc. IEEE Int. Ultrason. Symp. (IUS)*, pp. 1805–1808, 2006.

[6] C. Li, D. Hutchins, and R. Green, "Short-range ultrasonic digital communications in air," *IEEE Trans. Ultrason., Ferroelectr., Freq. Control*, vol. 55, no. 4, pp. 908–918, 2008.

[7] H. D. Haynes, M. A. Akeman, and V. M. Baylor, "Ultrasonic communication project, phase 1, FY 1999," tech. rep., Oak Bridge, TN, USA, Jun. 2000.

[8] S. Holm, O. Hovind, S. Rostad, and R. Holm, "Indoors data communications using airborne ultrasound," in *Proc. IEEE Int. Acoust. Speech. Signal (ICASSP)*, vol. 3, pp. 957–960, 2005.

Chapter 5

Indoor Ultrasonic Communication Network

5.1 Introduction

Up to this point, appropriate modulations and their performances have been investigated. This chapter will describe the implementation of an indoor ultrasonic communication network with full-duplex connections. To enable the system to switch between different modulation schemes for more efficient and reliable signal transmission, the user location must be determined. Section 5.2 discusses the architecture planning of the communication network based on experimental results. Section 5.3 gives a brief review of the ultrasonic positioning system in the literature, followed by the description of the positioning method used, the generation of the ranging signal, and the evaluation of the location accuracy. After that, the handover scheme for a system with a moving mobile device will be introduced. The last section gives the conclusions of this chapter.

5.2   Network architecture

The basic idea of building an indoor communication network structure is to have ceiling-mounted or wall-mounted base stations with transceivers and one or more mobile devices within the network area. It is preferred to install the minimum number of base stations to cover the largest area possible whilst achieving the best data rate possible. The ultrasonic beam coming out from a transducer aperture can be considered as a cone, therefore the projection at any normal distance away from the aperture is a circle with a certain radius which due to diffraction and beam spreading depends on the transmitted signal frequency. Therefore, any network configuration will be a compromise between coverage and data rate. Over short ranges, a higher data rate can be achieved with a small coverage area, however, requiring a higher number of transceivers. On the contrary, over long ranges, the achieved data rate might be lower with relatively large signal coverage, but a smaller number of transceivers is needed. Thus, a reasonable compromise between the two needs to be considered when designing an indoor ultrasonic communication network.
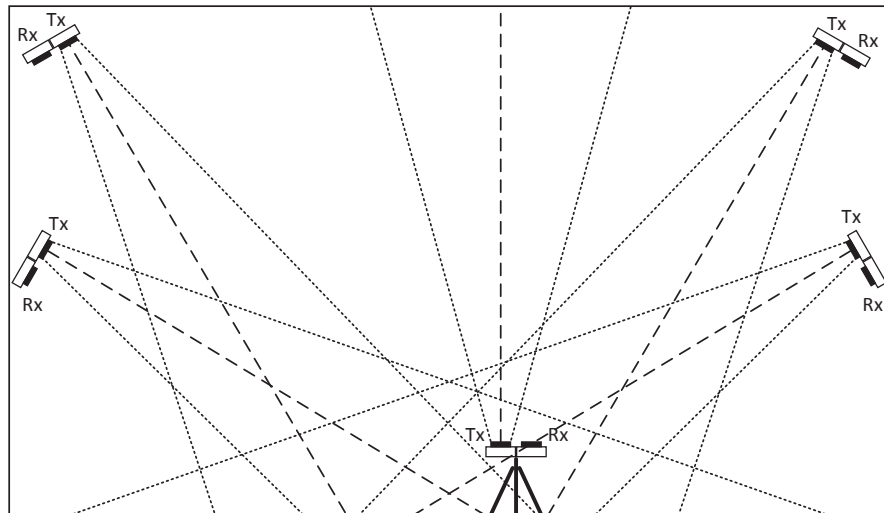
Figure 5.1:   Side view of the indoor network setup including corner base stations and a ground mobile unit with their transmitting beam contours indicated.
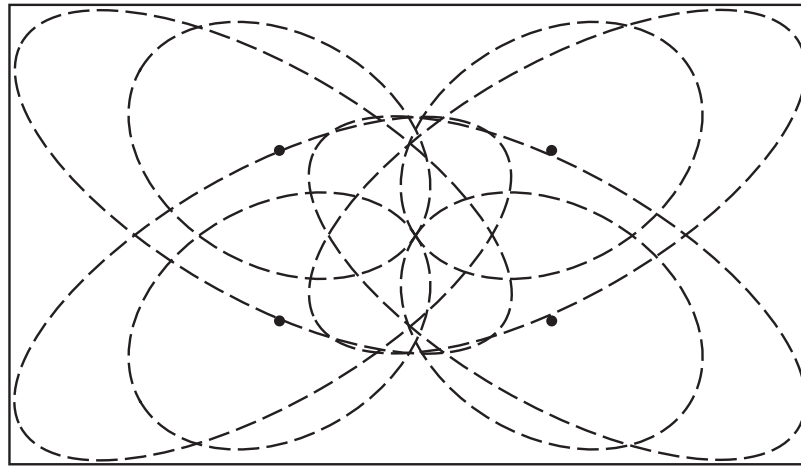
Figure 5.2: Cell planning using ellipse shapes.

One possible network setup inside a room is to install base stations on the walls or the ceiling as the side view in Fig. 5.1 shows. With this setup, a relatively large area can be covered by using small number of transducers. The effective coverage area becomes an ellipse instead of a circle as illustrated in Fig. 5.2. The area that is serviced by one base station with one transceiver (one transmitter and one receiver) is regarded as one cell. One of the drawbacks of this ellipse cell planning is that it uses ceiling base stations very inefficiently as a large overlapping area between two neighbouring cells is introduced. It is also difficult to cover the rest of the room in an organised arrangement using ellipse cell shapes. Besides, the base stations on the wall or the ceiling may miss the transmitting signal beam if the transmitter of the mobile unit is not facing the base station as shown in Fig. 5.1. As shown earlier in Chapter 2, if the transducers are misaligned by more than $7°$, transmission errors will occur. Unless the mobile unit changes its orientation to have direct LOS to a base station or uses omnidirectional transceivers, a full-duplex communication link will be impractical.

There is another popular network architecture which divides the geographic service area into hexagonal zones, as employed in modern cellular mobile com-
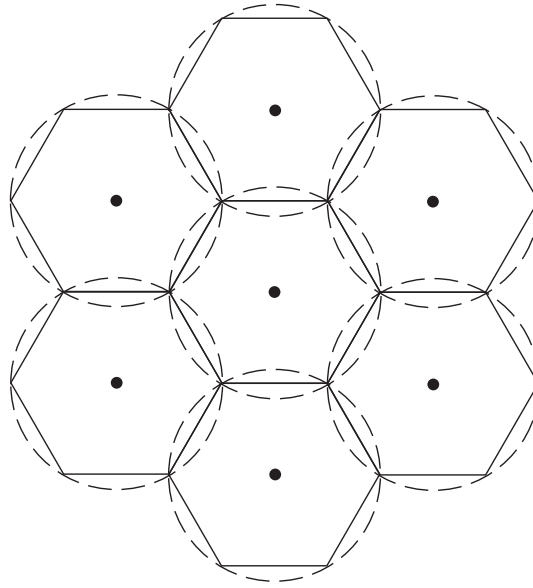
Figure 5.3: Cell planning using hexagonal shapes.
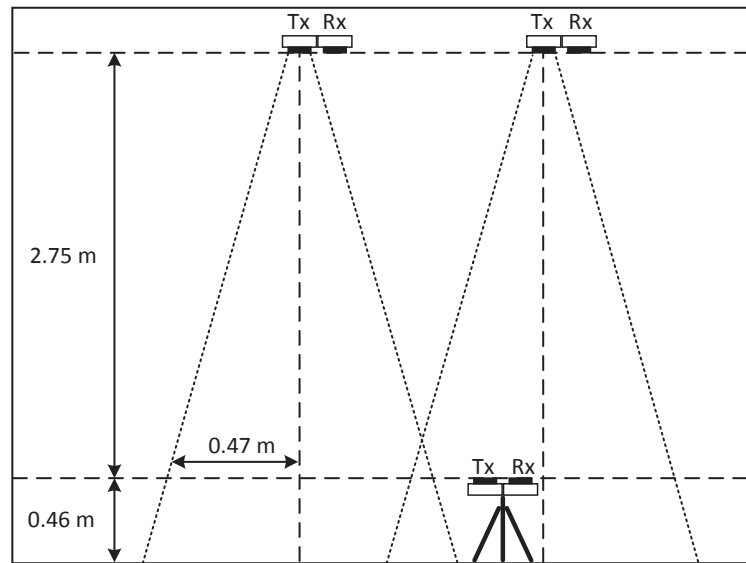
Figure 5.4: Side view of the indoor network setup including ceiling-mounted base stations and a ground mobile unit with their transmitting beam contours indicated.

munication systems [1]. Fig. 5.3 shows a typical cell plan using hexagonal divisions. As can be seen, each cell has the same size, and the coverage region overlaps at the outer boundaries. Since a hexagonal cell has an equal distance to all adjacent cells, it provides the most efficient coverage with the least number of required base stations. The corresponding side view of the base station

149

and mobile unit setup is shown in Fig. 5.4. As can be seen, the base stations are placed on the ceiling with their transducers facing down to the ground. The mobile device is placed under the coverage area with its transducers facing the ceiling. As the highest frequency channel used for data transmission is 65 kHz using separate bands for uplink and downlink which is described in Section 4.4.1, the maximum possible theoretical angle of divergence at this frequency is $9.65°$, giving a coverage circle with a radius of 0.47 m when the height of the base stations relative to the height of the mobile unit is fixed at 2.75 m. Therefore, the maximum separation between the two base stations should be 0.47 m or less.

To maximise the system throughput, data transmissions were carried out using 16QAM-OFDM modulation at different lateral displacements in full-duplex
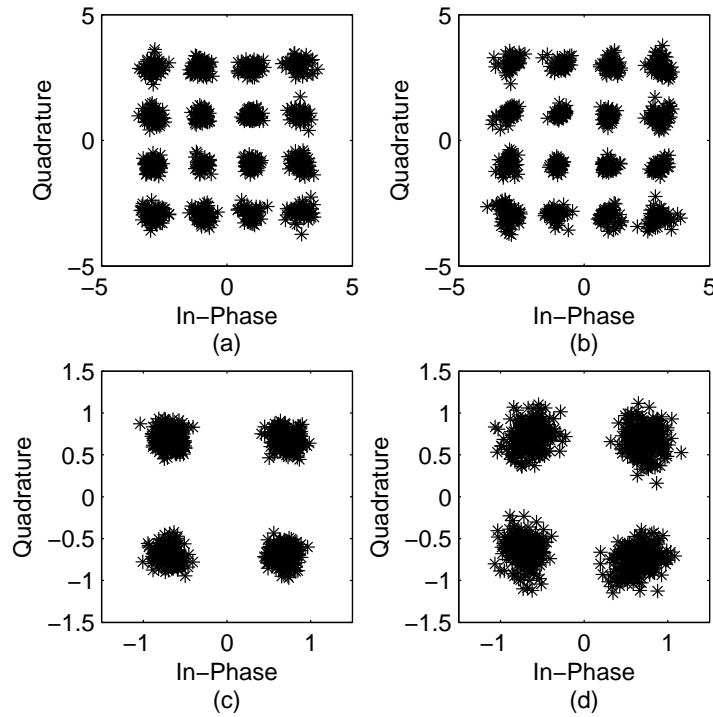
Figure 5.5: The received 16QAM-OFDM uplink (a) and downlink (b) signal constellation at a lateral displacement of 0.15 m; and QPSK-OFDM uplink (c) and downlink (d) signal constellation at a lateral displacement of 0.35 m in full-duplex mode.
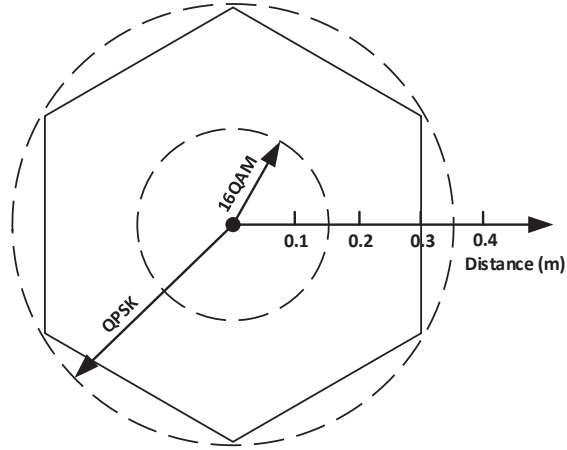
Figure 5.6: Error-free transmission area covered by using different OFDM modulation schemes.

mode. It was found that the maximum error-free lateral displacement was 0.2 m for both uplink and downlink with separated bands. By using a lower-order modulation scheme (QPSK-OFDM), the maximum lateral displacements with no measurable errors were extended up to 0.45 m and 0.4 m for uplink and downlink, respectively. These could be identically sized using interleaved uplink and downlink channels, but at the expense of the maximum data rate achievable. The received 16QAM-OFDM signal constellations for the uplink and downlink at a lateral displacement of 0.15 m were shown in Fig. 5.5 (a) and (b), respectively. Similarly, the received QPSK-OFDM signal constellations for the uplink and downlink at a lateral displacement of 0.35 m were also shown in Fig. 5.5 (c) and (d). As can be seen, both the downlink constellations using different modulations show larger variations in phase and amplitude than that of the uplink signals. This is because by using lower frequency bands the uplink signal has a wider angle of divergence for better signal reception at the same lateral displacement compared to the downlink signal. Therefore, to maintain a reliable full-duplex data transmission link, at least two different modulation methods should be used at different coverage regions as shown in Fig. 5.6. In

151
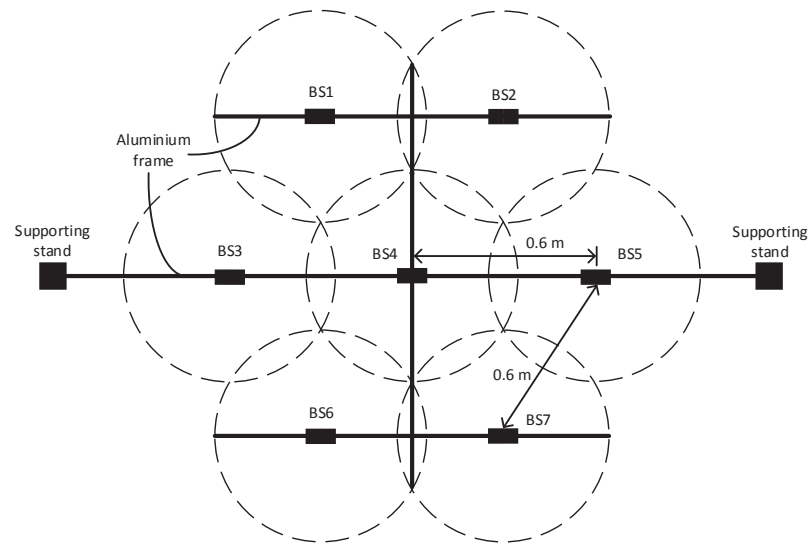
Figure 5.7: Schematic of the base stations installed on the ceiling.

this case, 16QAM-OFDM can provide a maximum data transfer rate of 40 kb/s for both uplink and downlink within a circle radius of 0.15 m. For a larger reliable coverage area, the radius can be extended up to 0.35 m using QPSK-OFDM at a reduced data rate of 20 kb/s for both uplink and downlink. A larger error-free region may achieved by using BPSK-OFDM modulation, but it is not recommended for data transmission in this work due to its low transfer rate of 10 kb/s. In this work, the horizontal separation of two different cell centres was set at 0.6 m to achieve seamless and reliable connectivity between the mobile device and the base stations. The experiment setup of the ceiling mounted base station network is illustrated in Fig. 5.7. Each base station has one transmitter and one receiver that are attached to an aluminium frame. All transducers can move along the metal bar to adjust their positions. The actual constructed metal frame with on-ceiling base stations is shown in Fig. 5.8. As can be seen, there are seven pairs of ultrasonic transducers being installed, covering an area of about 2.2 m^2.

As the SensComp ultrasonic sensors were originally used for camera ranging at a nominal frequency of 50 kHz, only very limited bandwidth could be used
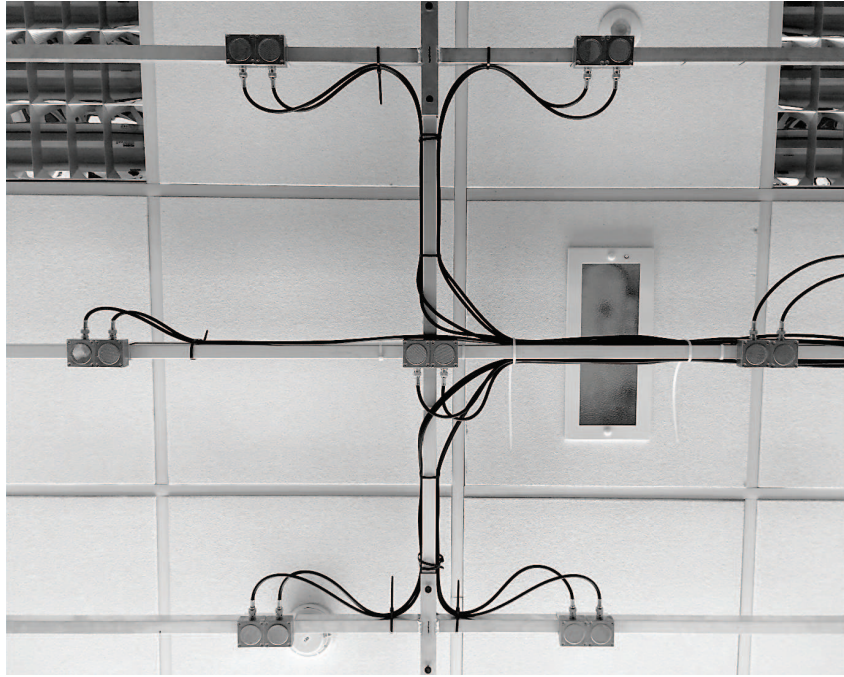
Figure 5.8: Installed ceiling-mounted base stations.

for data transmission. In addition, the emitted sound beam had a highly directional radiation pattern due to the relatively small value of λ/D. It reduced the effective horizontal coverage area, and affected the accuracy of the data exchange with large lateral displacement. Therefore, wideband ultrasonic transducers with an omnidirectional design are preferred for better performance of an indoor communication system.

5.3   Ultrasonic indoor positioning

For an indoor communication network, the knowledge of user location is important for efficient and effective data transmissions. The user location in a cell can be used to select and optimise the modulation scheme. Due to the low propagation speed of ultrasound in air compared with radio waves, ultrasonic systems can provide more accurate measurement of time-of-flight (TOF) for location estimation.

A number of ultrasonic indoor positioning and localization systems have

been reported in the literature. The Bat system [2] consists of mobile wireless devices known as Bats and a network of fixed ceiling-mounted receivers. The users carry tag devices which emit an ultrasonic pulse when radio-triggered by a controller. The system then measures the TOFs of the pulse intercepted by different receivers and calculates the 3D position of the tag device by triangulation. The achieved positioning accuracy was within 3 cm at 40 kHz with a maximum location update rate of 150 Hz. A Cricket system [3] allows mobile and static nodes to learn their physical locations by receiving and analysing concurrent radio and ultrasonic signals at 40 kHz from beacons spread throughout the building. In order to minimise the effects of noise and reflections of ultrasound in the environment, the receiver collects up to 25 distinct distance samples from each of the four beacons, achieving a relatively slow location update rate of approximately 0.16 Hz [4]. It is also found that the 3D position estimates can be accurate to between 5 cm and 25 cm. Another similar indoor position sensing system [5] allows wearable and mobile computers to determine their positions in a 3D space by receiving precisely timed 40 kHz ultrasonic signals triggered by a RF pulse from four transmitters installed on the ceiling using TOF methods. The resulting 3D position estimation accuracy was between 10 cm and 25 cm with a system update rate of a few hertz. A later study has looked at an indoor positioning system using prototype Dolphin transmitters and receivers at 50 kHz without radio triggering [6]. This centralised system with ceiling receivers and roaming transmitters was shown to have 2 cm location accuracy with an increased update rate of 20 kHz. In [7], a reference-free ultrasonic indoor location system with a receive-only mobile device which determines its own position based on ultrasonic signals in frequency bands between 36 kHz and 45 kHz sent by at least three transmit-only ultrasonic beacons was proposed. The mobile device consists of three receivers placed in a triangle, allowing angle-of-arrival (AOA) and TOF estimation with-

out the use of synchronising RF. The system provides 3D location accuracy of about 9.5 cm with update rates between 5 Hz and 20 Hz. A recent work has implemented an ultrasonic local positioning system that allows a robot mobile to navigate in an indoor area [8]. Each ceiling-mounted beacon contains five ultrasonic transducers which send positioning signals modulated using orthogonal codes at 40 kHz. The ultrasonic signals were synchronised by RF pulses, and the achieved position accuracy was below 3 cm. By merging the odometer and ultrasonic positioning information using a H-Infinite filter, the entire path of the moving robot on the floor can be obtained.

5.3.1 Positioning method

It is common to take advantage of the slow propagation speed of ultrasound to estimate its TOF between a transmitter and a receiver. The TOF is then used to calculate the distance between the two nodes based on the measured speed of sound in air. A receiver collects a set of transmitter-to-receiver distances to estimate its position by using the mathematical method of trilateration. More specifically, a roaming receiver's 3D position (u, v, w) is a function of the measured distance d_i to a given ceiling transmitter i, and the preassigned location (x_i, y_i, z_i) of the fixed beacon transmitter, described as

$$d_i = \sqrt{(u - x_i)^2 + (v - y_i)^2 + (w - z_i)^2}. \tag{5.1}$$

In order to perform trilateration, at least three different values of d_i are required. In addition, the receiver needs to know the exact time that the ranging signals depart from the transmitters to calculate the absolute TOFs. Therefore, a wireless RF synchronization signal is usually sent synchronously to achieve good accuracy [2, 3, 5]. However, the inclusion of this synchronization link to provide a timing reference adds more hardware resources, power consumption,

and signal processing complexity to the system. It also requires the use of RF which may not be permitted in certain areas.

There is another TOF method associated with a different mode of receiver operation. In this mode, the mobile receiver only knows the time differences of the arriving signals with respect to each other rather than the absolute time of arrivals. Since the receiver has to pick up an arbitrary point of time as a reference of signal TOF measurements, a set of pseudo-ranges are gathered, however, with an equal offset from the true transmitter-to-receiver distances [9]. This approach is called pseudoranging which is also performed by Global Positioning System (GPS) receivers [10]. The relationship can be expressed as

$$\tilde{d}_i = \sqrt{(u - x_i)^2 + (v - y_i)^2 + (w - z_i)^2} + \Delta d, \qquad (5.2)$$

where $\tilde{d}_i$ is the pseudo-range to a certain transmitter and Δd is the distance offset common to all pseudo-ranges. If Δd is positive, the start time that was arbitrarily chosen by the receiver was before the transmitters began sending their ranging signals, and the pseudo-ranges are longer than the actual ranges. Otherwise, if Δd has a negative value, then the receiver's chosen time point was behind the true starting point, and the pseudo-ranges become shorter than the actual ones. To perform trilateration, at least four pseudo-ranges are required as there are four unknowns in (5.2). Compared to the receivers in synchronous systems, these asynchronous receivers do not need additional wireless radio-triggered synchronization links to perform position estimation. However, the disadvantage of pseudo-ranging is that it takes one more signal TOF measurement to compute the location, making the estimation potentially less accurate.

5.3.2 Ranging signal

Multiple ceiling beacons should transmit their unique ranging signals simultaneously at the same frequency to have the same coverage area and similar received signal strength at the receiver. In order to provide the multiple simultaneous access to the various ranging signals that are to be received from different base stations, a code division multiple access (CDMA) method was used. CDMA is a spread-spectrum technique that transmits the signals at the same time with different spreading code sequences [11]. Code sequences that have good autocorrelation properties are called pseudorandom noise sequence as their autocorrelation function is similar to that of random noise which has a sharp peak and low sidebands [12].

A pseudorandom noise sequence with desirable autocorrelation characteristics can be created using a series of shift-registers with feedback-taps that are logically combined and fed into the bit input [13]. Fig. 5.9 shows one type of three-stage linear feedback shift register (LFSR) synchronised by a unique clock signal. A shift register simply copies its input D to its output Q on each step. Based on different tap connection arrangements, the binary bits are then fed back to the input of the first register after the exclusive-OR (XOR) operation. Table 5.1 presents the truth table of function $f = A \oplus B$ where the symbol $\oplus$ is
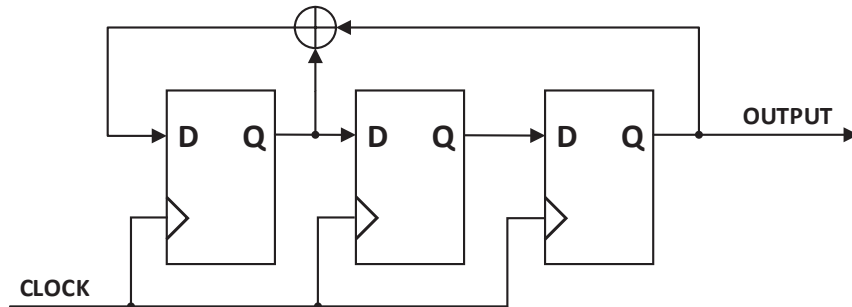
Figure 5.9: Three-stage LFSR generating m-sequence of length 7, using taps 1 and 3.

Table 5.1: Truth table for XOR function

A	B	f
0	0	0
0	1	1
1	0	1
1	1	0

used to indicate the XOR operation. As can be seen, XOR of two inputs is true if only one of the two inputs is true. LFSR taps can be mathematically described by a characteristic polynomial, for example, $1 + x + x^3$, for the arrangement in Fig. 5.9. Each configuration of n-stage registers is able to produce all possible combinations of binary sequences in $2^n - 1$ cyclic shifts. The sequence created with a maximum length of $2^n - 1$ is then called maximum-length sequence, or m-sequence. If the taps are changed, a new sequence is produced with the same length. In general, the m-sequences are found to have excellent autocorrelation properties [14]. However, for applications in spread spectrum communication systems, a uniformly low cross-correlation value for a code sequence is also required so that the receiver can be able to pick out signals from individual transmitters with minimal cross interference between any pair of code sequences sharing the same spectrum [15]. Unfortunately, the cross-correlation function between two m-sequences of the same period may have relatively high peaks that are undesirable in CDMA [16]. Depending on the different sequence pairs used, it is still possible to find ones that have smaller cross-correlation peaks, but the size of such a set of sequences is usually too small for practical CDMA applications [17].

Even though the cross-correlations of m-sequences are generally high, it has been found [18] that certain pairs of well-picked m-sequences with length $2^n - 1$ exhibit a smooth three-valued cross-correlation function with values $\{-1,$

$-t(n)$, $t(n) - 2$}, where

$$t(n) = \begin{cases} 2^{(n+1)/2} + 1 & (\text{odd } n) \\ 2^{(n+2)/2} + 1 & (\text{even } n) \end{cases} \tag{5.3}$$

These m-sequences are called preferred sequences. For example, consider the case where $n = 7$, then $t(7) = 2^4 + 1 = 17$ and the three possible values of the periodic cross-correlation function are $\{-1, -17, 15\}$. Therefore, the worst-case cross-correlation is 17. Table 5.2 [17] lists the peak values θ_c of the cross-correlation between pairs of m-sequences for $3 \leq n \leq 10$. Here, θ_u represents the maximum value of autocorrelation for two m-sequences. As can be seen, the number of m-sequences with a length of m increases rapidly with n. It can also be observed that θ_c takes a larger percentage of θ_u compared with $t(n)$ when $n \geq 5$, and the difference between the two increases with n. Thus, these preferred pairs of m-sequences can be used to produce families of binary sequences with good cross-correlation properties.

Gold codes, which were invented by Dr. Robert Gold in 1967 [19], can be used to generate the ranging signal as they obtain both good auto and cross-

Table 5.2: Cross-correlation of m-sequences and Gold sequences

n	Length of code sequence $m = 2^n - 1$	Number of m-sequences	Peak cross-correlation θ_c	θ_c/θ_u	$t(n)$	$t(n)/\theta_u$
3	7	2	5	0.71	5	0.71
4	15	2	9	0.60	9	0.60
5	31	6	11	0.35	9	0.29
6	63	6	23	0.36	17	0.27
7	127	18	41	0.32	17	0.13
8	255	16	95	0.37	33	0.13
9	511	48	113	0.22	33	0.06
10	1023	60	383	0.37	65	0.06

correlation properties. The Gold codes are a particular set of pseudo-random sequences that are constructed by the XOR of two preferred m-sequences using the same clock signal [15]. As the cell size is relatively small, a fast positioning update rate is needed. Therefore, the length of the m-sequence should be as small as possible. As Table 5.2 shows, for $n = 3$ and $n = 4$, the values of θ_c and $t(n)$ are the same. When n increases to 5, the peak cross-correlation $t(n)$ using the preferred sequences starts to be superior to that of the general pairs. Fig. 5.10 illustrates the Gold code generator used in this work, consisting a pair of five-stage LFSRs. The initial contents of the LFSR are called the seed, and each seed gives a different Gold code. Therefore, by using all different possible seeds (except for all '0's), a class of $2^n - 1$ Gold sequences of length $2^n - 1$ can be generated. If the original two m-sequences are included, a total of $2^n + 1$ Gold sequences can be constructed in one family. In this case, 33 ($2^5 + 1$) Gold codes with a length of 31 ($2^5 - 1$) from the same family can be used by 33 different base stations to transmit ranging signals at the same time. The Gold codes can also be expressed in the form of characteristic polynomial for the two LFSRs, such as GC($1 + x^2 + x^5$, $1 + x^2 + x^3 + x^4 + x^5$, 00011) according to the circuit diagram in Fig. 5.10. Note that a seed of '00...001' is always used by the first
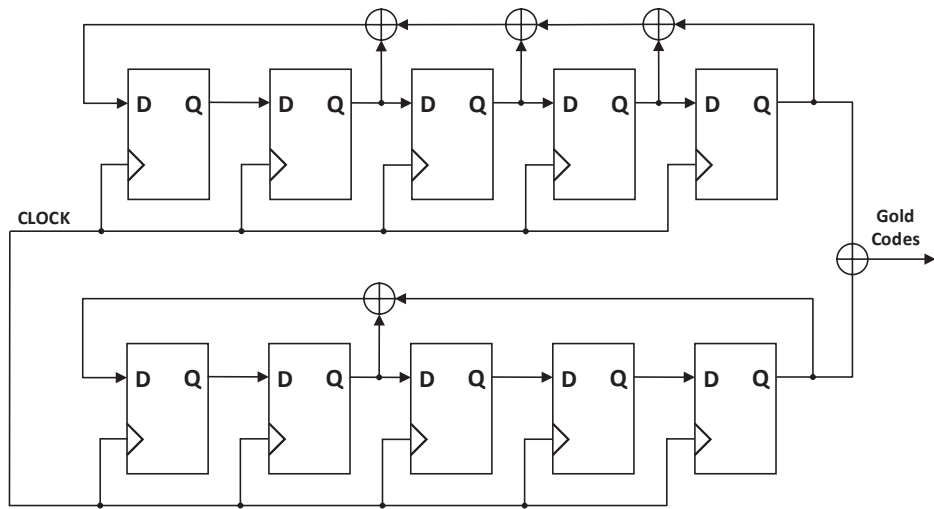
Figure 5.10: Circuit of a Gold code generator.
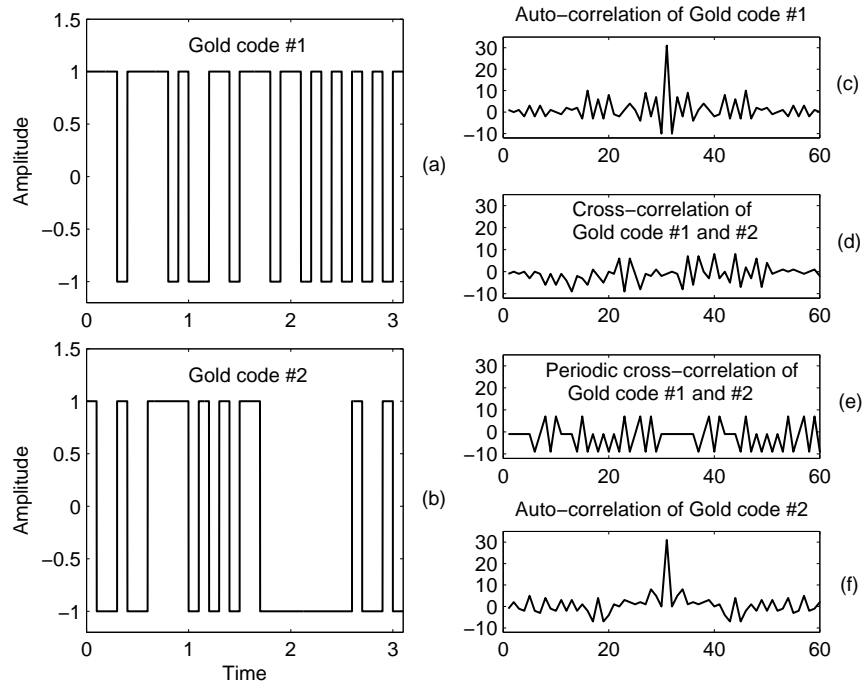
Figure 5.11: Gold code and its correlation properties.

LFSR, and '00011' is the user defined seed for the second LFSR. Fig. 5.11(a) and (b) show two of the 31-bit Gold sequences from the same family generated by the circuit in Fig. 5.10. Their auto-correlations are illustrated in Fig. 5.11(c) and (f), respectively. As can be seen, both show an impulse-like curve, indicating high similarities with themselves. Their cross-correlation property is compared in Fig. 5.11(d), showing very low correlation with each other. Fig. 5.11(e) illustrates their periodic cross-correlation results with three values $\{-1, -9, 7\}$, as (5.3) predicts. Since Gold codes have low cross-correlation in addition to excellent auto-correlation characteristics, they are widely used in applications in telecommunication and satellite navigation [20]. The Gold codes with a length of 511 bits have also been used for indoor location systems using both acoustic [21] and ultrasonic [6] methods.

Other well-known pseudo-random sequences used in CDMA systems are Walsh-Hadamard codes [22] and Kasami codes [23]. Walsh-Hadamard codes are orthogonal codes with nonzero cross-correlation only if the two sequences

161

are the same. The major drawback of the Walsh-Hadamard codes is that the sequences have poor autocorrelation properties, making the family unsuitable for asynchronous CDMA systems [24]. Since the time-of-arrivals (TOAs) of the signals at the receiver are different, orthogonal codes cannot be separated from each other. Therefore, Walsh-Hadamard codes are not used in this work. Kasami codes have similar properties to the Gold codes with preferred pairs of m-sequences. There exist small and large sets of Kasami sequences. The small set has a family of $2^{n/2}$ binary sequences with a period of $2^n - 1$ for even n. Their maximum cross-correlation is $2^{n/2} + 1$. The large set includes both the small set of Kasami sequences and a set of Gold sequences as its subsets. The autocorrelation and cross-correlation characteristics of the large Kasami set are inferior to those of the small set, but the large set has a larger number of sequences [24]. As the generation of small set Kasami codes is restrained by using only even number of shift registers, they are not investigated in this work, either.

5.3.3 Ranging accuracy evaluation

Location measurements were performed in a laboratory environment as before, using three ceiling base stations and one mobile receiver. The base station transmitters were placed near the ceiling in the centre of the room at known positions, with their apertures facing down to the floor. This reduced the effect of multipath reflections from the walls. The mobile receiver was placed in different known coordinate points inside the area that was covered by the transmitting ultrasonic beams with its transducer facing the ceiling.

To have a relatively large signal coverage area, a sinusoid with a low ultrasonic frequency of 25 kHz outside the communication channels (45 to 65 kHz) was used as the carrier wave, modulated by a Gold code using BPSK. The Gold code had a length of 31 bits and was applied at a rate of 5 kHz, yielding a ranging signal duration of 6.2 ms. Each transmitter from the ceiling base stations
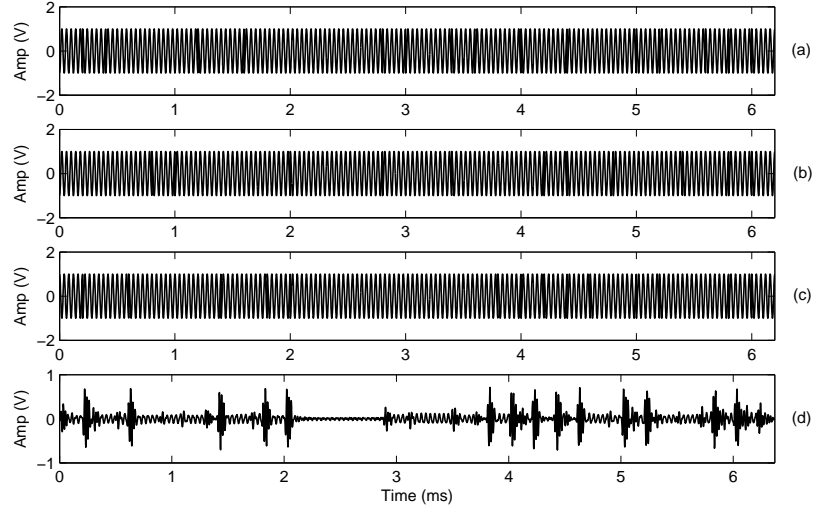
Figure 5.12: Transmitted signals (a), (b), (c), carrying Gold codes from three different ceiling-mounted transmitters and the received signal (d) by the mobile device.

was assigned a unique Gold code from the same family. The mobile receiver was placed at a fixed height of 0.46 m above the floor to simplify the positioning process. Therefore, only three ranging signals were needed to estimate the location of the mobile device as w and z_i in (5.2) are known. Equation (5.2) can then be simplified as

$$\tilde{d}_i = \sqrt{(u - x_i)^2 + (v - y_i)^2 + c} + \Delta d, \tag{5.4}$$

where c is a constant, and is equal to $(w - z_i)^2$. Fig. 5.12 (a), (b) and (c) show transmitted Gold code modulated signals from three different base stations. The transmitters were configured to broadcast their ranging signals simultaneously. These signals with different amplitudes and TOAs were then received as a single waveform by the mobile device as illustrated in Fig. 5.12 (d). As can be seen, the effect of constructive and destructive interference can be visually identified as its amplitude varies with time.

In order to detect the TOAs of different ranging signals, the receiver needs to correlate the received waveform with the different corresponding Gold code

163
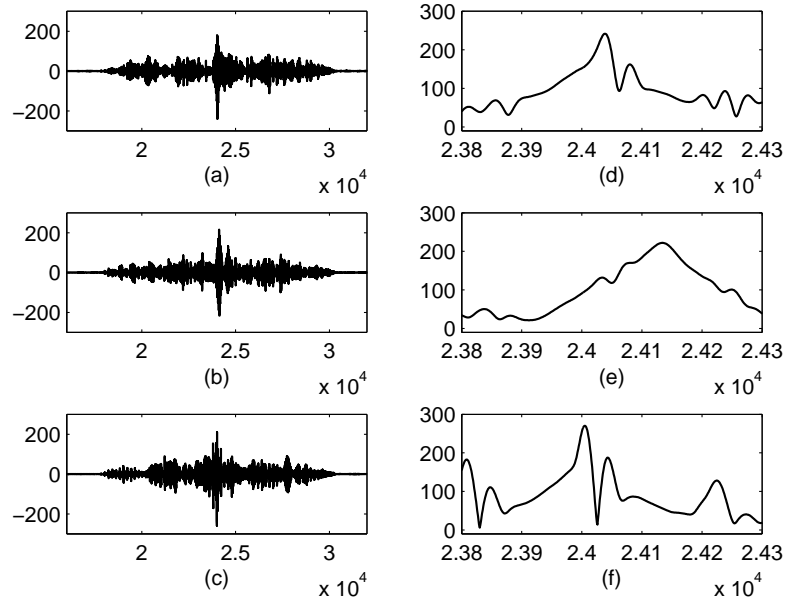
Figure 5.13: Cross-correlation of the received ranging signal with different Gold code modulated signals (a), (b), (c), and the resulting curves after peak detection (d), (e), (f).

modulated signals locally generated, and identical to the transmitted ones. The cross-correlation results of the received signal against three different ranging signals are shown in Fig. 5.13 (a), (b) and (c). As can be seen, three distinct peaks are produced in the centre after correlation. After peak detection, the highest peaks of the resulting curves illustrated in Fig. 5.13 (d), (e) and (f) can then be used to identify the TOAs of the ranging signals. It can also be observed that the signal that arrived at the receiver earlier than the others had a higher peak as the transmission distance was shorter thus less attenuation occurred.

The location accuracy of the system was evaluated at ten different positions

Table 5.3: Base station coordinates in (m)

Base station	(x_i, y_i, z_i)
BS1	0.3, 0.5196, 0
BS2	0, 0, 0
BS3	0.6, 0, 0

164
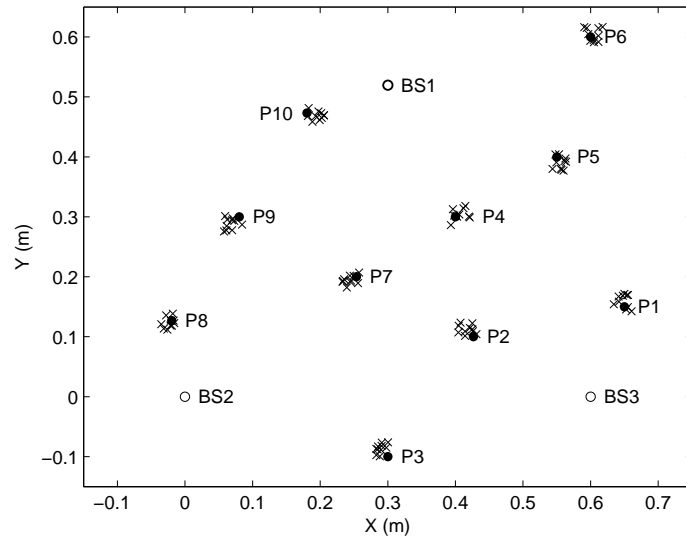
Figure 5.14: Estimated 2D positions (x) using asynchronous ranging algorithm in coordinates (X,Y). The solid points correspond to the positions where the receiver transducer was physically placed, and the unfilled points were the positions of the ceiling base stations.
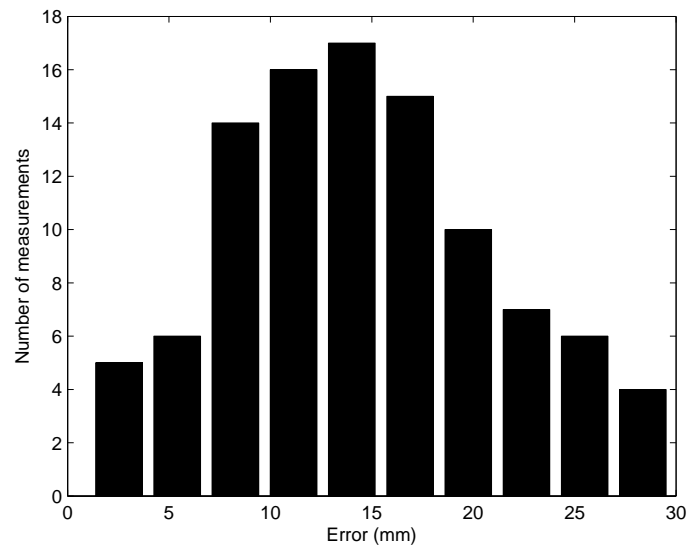
Figure 5.15: Histogram of the absolute positioning error from the measurements carried out at all ten testing points.

for the mobile receiver at a fixed height. The measurements were taken 10 times at each test position. The locations of the base stations at known coordinates are listed in Table 5.3. To better visualise the distribution of the measured locations, the 2D coordinate of the evaluated test points are shown in Fig. 5.14.

As can be seen, the measured points are scattered around or close to the reference points, demonstrating the effectiveness of the positioning system proposed in this work. The locations of base stations and mobile unit were projected on to the floor using a plumb bob before taking the measurement. Therefore, the uncertainty of the hand-measured positions may contribute a small amount of error at ± 1 mm given that the minimum scale of the measuring tape used was is 1 mm. The histogram of the absolute positioning error from the measurements at all ten test points is shown in Fig. 5.15. It shows that all the error readings of the estimated locations are within 28.37 mm which is 2.13% of the theoretical radius (1332 mm) that is covered by the cone of an emitted 25 kHz ultrasonic signal sent from a 2.75 m-height ceiling, and 72% of the measuring errors are between 8.28 mm and 19.76 mm. Note that the transducer radius (19.2 mm) is approximately 50% of the maximum measuring error. It indicates that the ultrasonic positioning system using an asynchronous ranging method is feasible with reasonably good accuracy.

5.4   Handover between base stations

In a practical cellular wireless communication system, a mobile device should be able to move between different cells while still keeping the connection with at least one of the base stations through an automatic and seamless mechanism, called a handover [25]. It represents a switching process from one serving base station to a candidate base station. As the mobile unit has a fixed height in this work, the handover allows connectivity switching when the mobile device moves from one active cell to the other horizontally without changing the service network.

In cellular mobile systems with multiple users, base stations in adjacent cells are assigned to different frequencies to prevent co-channel interference.
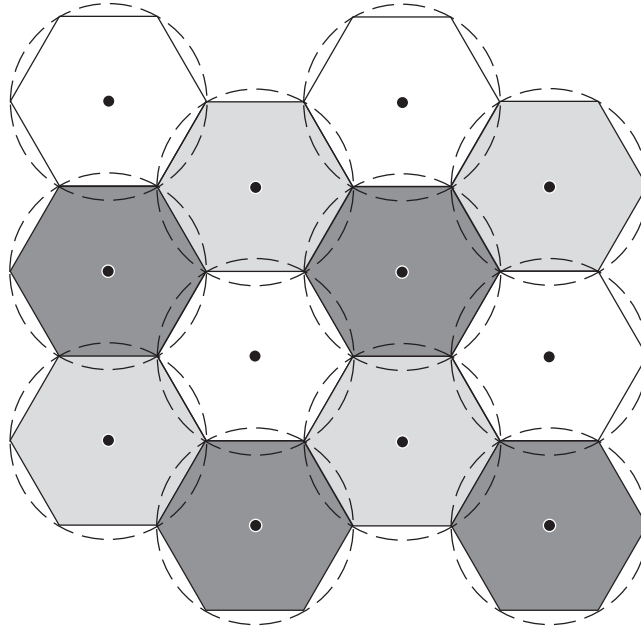
Figure 5.16: Employment of frequency re-use plan for a re-use factor of 3 (cells with the same shading use the same frequencies).

Meanwhile, to use the frequency spectrum more efficiently, the corresponding frequencies are re-used in a regular pattern over the entire service area [26]. Fig. 5.16 shows a cell arrangement with a frequency re-use factor of 3. Note that the cells with the same shading use the same frequencies. With this re-use pattern, the available frequency spectrum is then divided into three different channel groups for each cluster that contains three adjacent cells. However, a narrowband system, as used in this work, does not have the bandwidth to further split the limited spectrum into different frequency groups. Therefore, identical uplink and downlink channels were used by all base stations in different cells. The handover process is then to switch off the downlink channels of the current base station, and switch on those of the candidate base station based on the estimated location and trajectory of the mobile device. Note that only one mobile user was assigned in this system for simplicity, to show proof of concept and to achieve a more reasonable data transfer rate.

Assuming that the mobile unit moves at a constant speed, v, and the lo-

cation update rate is η, the minimum detectable distance that the mobile unit has moved is then υ/η. As described in Section 5.2, there is a 50 mm gap left between the maximum error-free displacement and the planned cell coverage radius. The minimum detectable moving distance should then be less than 50 mm. This is to ensure reliable signal transmissions when switching between different modulation methods within the cell and the handover between adjacent cells. Fig. 5.17 shows the transmitted signal structure of a base station. The ranging signal modulated by a Gold code at 25 kHz was sent every 31 ms with a duration of 6.2 ms, thus the achieved system location update rate was around 32.3 Hz. This was to transmit as many OFDM data packets as possible within a certain time period so that the maximum data rate could be obtained. At the same time, the value of υ/η was 46.4 mm which was just below 50 mm when the moving speed of the mobile unit was assumed to be 1.5 m/s. Fig. 5.17 also shows the base station that transmitted signals using the downlink frequency bands from 56 kHz to 65 kHz every 31 ms. Each signal packet contained a synchronization signal, a pilot signal and 29 OFDM signals carrying data information. Therefore, the actual data rates using 16-QAM and QPSK were 37.4 kb/s and 18.7 kb/s, respectively. For the mobile device, the signal structure is illustrated in Fig. 5.18. The transmission used uplink frequency bands from 45 kHz to 54 kHz with the same signal contents as for the base
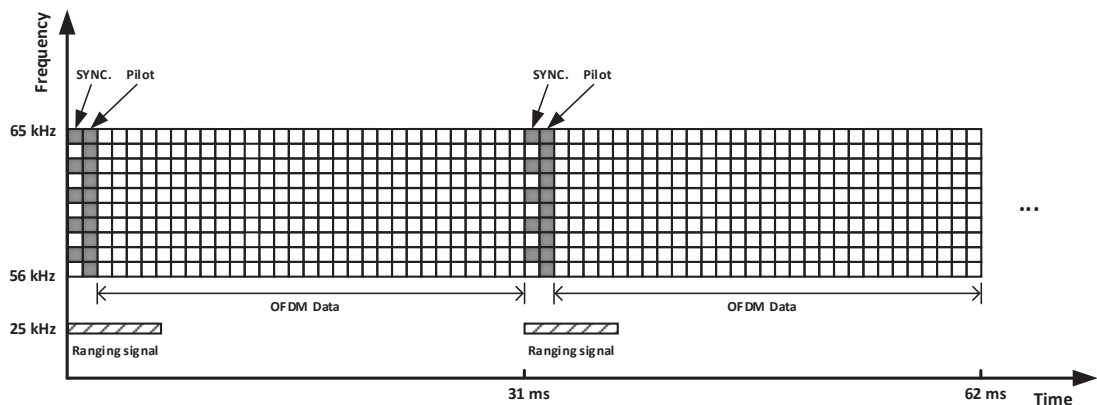
Figure 5.17: Signal structure of base stations.

168
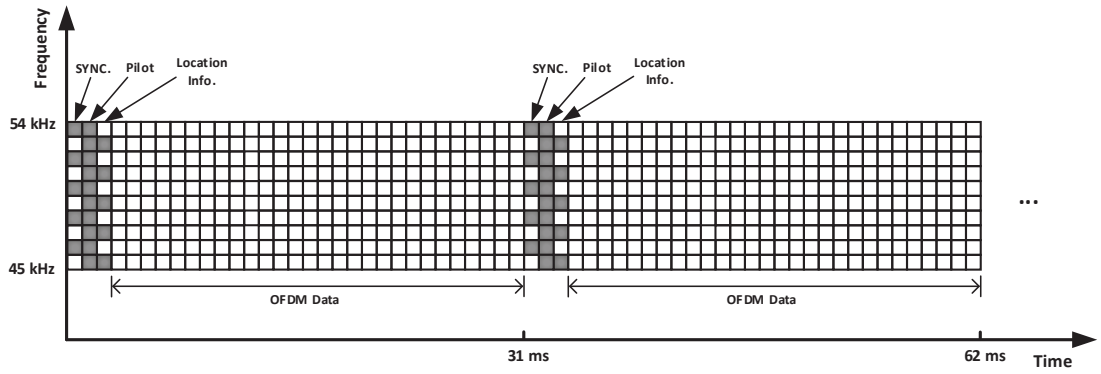
Figure 5.18: Signal structure of the mobile device.

stations, and sent signals every 31 ms as well. Note that the first packet of the data signals was reserved for sending the calculated location information of the mobile unit to the base stations so that the system was able to switch between different modulation schemes within the same cell and perform the handover when the mobile unit moved from one cell to another. The achieved uplink data rates using 16-QAM and QPSK were 36.1 kb/s and 18.1 kb/s, respectively.

Ultrasonic transducers with a smaller aperture opening, or omnidirectional transducers, would have wider beam divergence, therefore providing a larger signal coverage area. The location update rate could also be reduced to improve the overall data transfer rate as a smaller number of handovers are needed. When broadband ultrasonic transducers with sufficient transmission
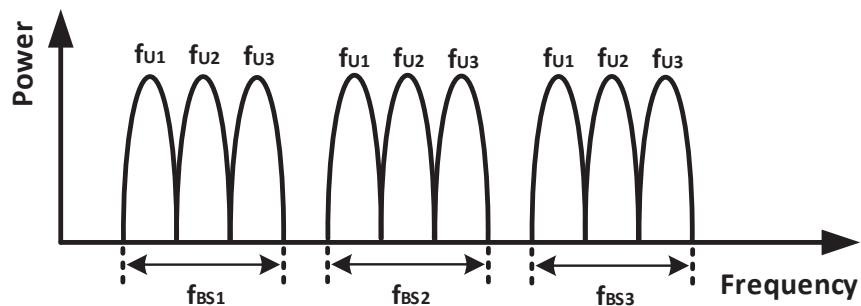
Figure 5.19: Channel arrangement for multiple users. f_{U1}, f_{U2} and f_{U3} represent frequency bands for user 1, user 2 and user 3, respectively, and f_{BS1}, f_{BS2} and f_{BS3} represent frequency bands for base station 1, base station 2 and base station 3, respectively.

169
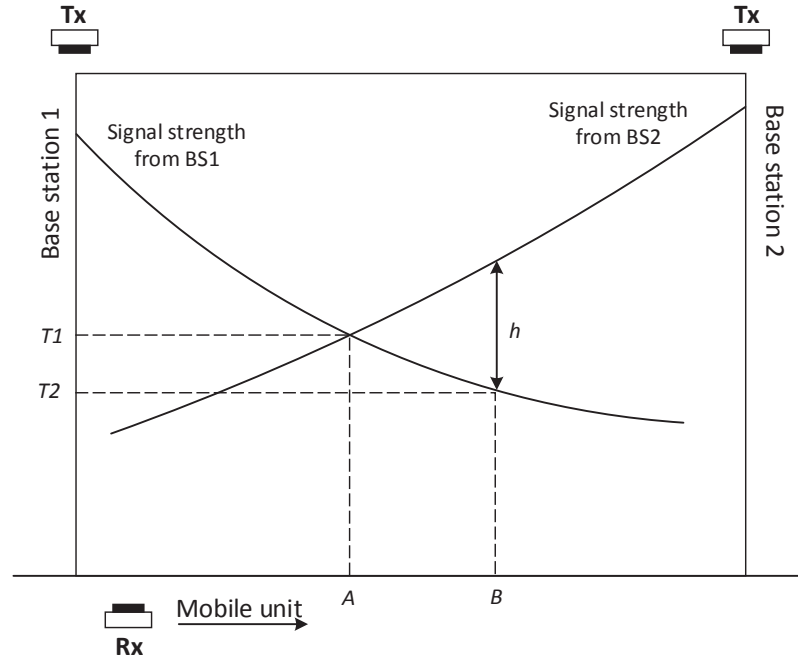
Figure 5.20: Handover design for ceiling-mounted network configuration.

bandwidth are used, a frequency re-use scheme would become executable for providing services to multiple mobile users. For example, a cellular system with a frequency re-use factor of 3 would need to share the overall available frequency bands as illustrated in Fig. 5.19. If there are three mobile users registered in the system, each base station needs to reserve three subbands (f_{U1}, f_{U2} and f_{U3}) for each of the users. An alternative handover technique can be approached by detecting the received signal strength from the current and the adjacent base stations. As Fig. 5.20 shows, as the mobile user moves from the current base station to an adjacent base station, it keeps detecting the received signals that operate at different frequency bands from both base stations. If the handover occurs at position A when the received signal strength from two base stations are equal, any fluctuation of the received signal strength may stimulate too many unnecessary handovers when the current base station is still able to provide adequate service. The fluctuation in signals may be introduced by multipath reflections or the orientation of the receiver transducer surface of the

mobile unit. When the mobile unit is passing position A and moving towards the adjacent base station (BS2), the received signal strength from the current base station (BS1) may become sufficiently weaker than that from the adjacent base station. The handover occurs at position B with a certain amount of hysteresis, h, which could effectively prevent a "ping-pong" effect (the repeated handover between the two base stations caused by the fluctuations in the received signal strengths from both base stations) that happens at position A.

5.5   Conclusion

An indoor ultrasonic communication network with ceiling-mounted base station transceivers and one mobile device was proposed and constructed. The communication cells were structured using hexagonal shapes to cover the service area more efficiently. The separation of different base stations was set at 0.6 m according to the experimental maximum lateral displacement for data transmissions with no measurable errors. An asynchronous positioning method was implemented for the system to determine the location of the mobile unit. The ranging signals were phase modulated by different 31-bit Gold codes from the same family using a non-communication channel at 25 kHz. The achieved ranging accuracy was within 28.37 mm with a maximum update rate of 32.3 Hz. According to the measured location of the mobile device moving from one cell to another, the system executed the handover of the communication link on a switch on and off basis as all base stations used the same frequency bands for data transmission. Within a circular range of 0.15 m, 16QAM-OFDM was used to achieve a higher uplink data transfer rate of 37.4 kb/s while the range was extended up to 0.35 m by using QPSK-OFDM with a data rate of 18.7 kb/s. For the uplink connection, the achieved data rates using 16QAM-OFDM and QPSK-OFDM were 36.1 kb/s and 18.1 kb/s, respectively. The spec-

Table 5.4: Specifications of the ultrasonic indoor communication network

System Throughput (kb/s)	Downlink: 37.4, 18.7
	Uplink: 36.1, 18.1
Frequency Band (kHz)	Positioning: 25
	Data: 45 - 65
Modulation Format	Positioning: BPSK
	Data: 16QAM-OFDM, QPSK-OFDM
Cell Size (m)	Hexagonal: 0.6 (side to side)

ifications of the indoor ultrasonic communication network implemented in this work are summarised in Table 5.4. A more robust handover technique using received signal strength with hysteresis was also proposed to improve the system efficiency when multiple mobile users subscribed to the service.

5.6 References

[1] S. Jones, *The Basics of Telecommunications*. Basics Books Series, Chicago, IL, USA: International Engineering Consortium, 2004.

[2] M. Addlesee, R. Curwen, S. Hodges, J. Newman, P. Steggles, A. Ward, and A. Hopper, "Implementing a sentient computing system," *Computer*, vol. 34, pp. 50–56, Aug. 2001.

[3] N. B. Priyantha, A. Chakraborty, and H. Balakrishnan, "The cricket location-support system," in *Proc. 6th Annu. Int. Conf. Mobile Comput. Netw. (MobiCom)*, pp. 32–43, Aug. 2000.

[4] N. B. Priyantha, A. K. Miu, H. Balakrishnan, and S. Teller, "The cricket compass for context-aware mobile applications," in *Proc. 7th Annu. Int. Conf. Mobile Comput. Netw. (MobiCom)*, pp. 1–14, Jul. 2001.

[5] C. Randell and H. Muller, "Low cost indoor positioning system," in *Proc. Ubiquitous Computing*, pp. 42–48, Sept. 2001.

[6] M. Hazas and A. Hopper, "Broadband ultrasonic location systems for improved indoor positioning," *IEEE Trans. Mobile Comput.*, vol. 5, pp. 536–547, May 2006.

[7] M. M. Saad, C. J. Bleakley, T. Ballal, and S. Dobson, "High-accuracy reference-free ultrasonic location estimation," *IEEE Trans. Instrum. Meas.*, vol. 61, pp. 1561–1570, Jun. 2012.

[8] D. Ruiz, E. García, J. Ureña, D. de Diego, D. Gualda, and J. C. García, "Extensive utrasonic local positioning system for navigating with mobile robots," in *Proc. 10th Workshop Positioning Navigat. Commun. (WPNC)*, pp. 1–6, Mar. 2013.

[9] R. J. Milliken and C. J. Zoller, "Principle of operation of NAVSTAR and system characteristics," *Navigation*, vol. 25, no. 2, pp. 95–106, 1978.

[10] B. W. Parkinson and S. W. Gilbert, "NAVSTAR: Global positioning system - Ten years later," *Proc. IEEE*, vol. 71, pp. 1177–1186, Oct. 1983.

[11] E. McCune, *Practical digital wireless signals*. Cambridge, U.K.: Cambridge University Press, 2010.

[12] A. Bensky, *Wireless Positioning Technologies and Applications, Second Edition*. Norwood, MA, USA: Artech House, 2016.

[13] F. J. MacWilliams and N. J. A. Sloane, "Pseudo-random sequences and arrays," *Proc. IEEE*, vol. 64, pp. 1715–1729, Dec. 1976.

[14] N. Zierler, "Linear recurring sequences," *J. Soc. Ind. Appl. Math.*, vol. 7, pp. 31–48, Mar. 1959.

[15] R. Pickholtz, D. Schilling, and L. Milstein, "Theory of spread-spectrum communications - a tutorial," *IEEE Trans. Commun.*, vol. 30, pp. 855–884, May 1982.

[16] D. V. Sarwate and M. B. Pursley, "Crosscorrelation properties of pseudo-random and related sequences," *Proc. IEEE*, vol. 68, pp. 593–619, May 1980.

[17] J. Proakis and M. Salehi, *Digital Communications*. New York, NY, USA: McGraw-Hill, 2008.

[18] R. Gold, "Maximal recursive sequences with 3-valued recursive cross-correlation functions," *IEEE Trans. Inf. Theory*, vol. 14, pp. 154–156, Jan. 1968.

[19] R. Gold, "Optimal binary sequences for spread spectrum multiplexing," *IEEE Trans. Inf. Theory*, vol. 13, pp. 619–621, Oct. 1967.

[20] K. Lakhtaria, *Next Generation Wireless Network Security and Privacy*. Advances in Information Security, Privacy, and Ethics, Hershey, PA, USA: IGI Global, 2015.

[21] C. Sertatil, M. A. Altinkaya, and K. Raoof, "A novel acoustic indoor localization system employing CDMA," *Digit. Signal Process.*, vol. 22, no. 3, pp. 506 – 517, 2012.

[22] H. Chen, *The Next Generation CDMA Technologies*. Hoboken, NJ, USA: John Wiley & Sons, 2007.

[23] T. Kasami, S. Lin, and W. Peterson, "Some results on cyclic codes which are invariant under the affine group and their applications," *Inform. Control*, vol. 11, no. 5, pp. 475 – 496, 1967.

[24] K. Du and M. Swamy, *Wireless Communication Systems: From RF Subsystems to 4G Enabling Technologies*. Cambridge, U.K.: Cambridge University Press, 2010.

[25] G. P. Pollini, "Trends in handover design," *IEEE Commun. Mag.*, vol. 34, pp. 82–90, Mar. 1996.

[26] V. Vij, *Wireless Communication*. New Delhi, India: Laxmi Publications Pvt Limited, 2010.

Chapter 6

Conclusions and Future Work

The research work described in this thesis has investigated the development and characterisation of multiple-channel airborne ultrasonic data communications using capacitive transducers. This chapter summarises this work and its conclusions, and suggestions for future research are also highlighted.

6.1 Conclusions

The introductory chapter firstly presented the historical use of ultrasound in different fields. It was followed by the basic properties of ultrasound including propagation through a medium, atmospheric absorption and radiated field patterns, which are the main considerations of the simulation model used in Chapter 2 and Chapter 3. Two popular ultrasonic transducers were also described in Chapter 1 with their characteristics discussed. It was found that capacitive ultrasonic transducers are more efficient for signal transmissions in air. Previous research on airborne ultrasonic communications were reviewed later in Chapter 1, which gave a good initial guidance for expanding the research in the area.

In Chapter 2, the investigation on multichannel wireless ultrasonic communication using basic baseband modulation methods (OOK and BPSK) was

described. It was shown that 6-channel OOK was practical over transmission ranges up to 5 m with a data transfer rate of 60 kb/s when the transducer centre normals were aligned. This range was extended to 10 m using 3-channel BPSK, however, at a reduced data rate of 30 kb/s. A simulation model was created including three filters to compensate for atmospheric absorption in air, beam spreading and transducer frequency response. Good agreement was found between the simulation predicted signal and the experimental signal in both time and frequency domains, indicating that the simulation model could be used to characterise ultrasonic signals through an air gap. According to the experimental results obtained when transducers were arranged with lateral displacements and oblique angles, it was found that error-free data transmissions were still attainable with a small amount of displacement and angle offset. It was also concluded that 3-channel BPSK was more robust than 3-channel OOK in both aligned and misaligned conditions in terms of the BER performance. In this work, wireless synchronization was achieved by ultrasonic means instead of a hard-wired link. The work in this chapter has added the knowledge of airborne ultrasonic wireless systems using multiple parallel channels, and formed a solid basis for developing other more efficient ultrasonic data communication methods. Aspects of this work have been published in [1, 2].

Chapter 3 looked at more advanced modulation schemes based on OFDM methods to maximise the system throughput. Compared with conventional FDM modulations, OFDM significantly improved the bandwidth utilisation and achieved the multichannel modulation process by means of an efficient IFFT computation instead of using pulse-shaping, multiplication and summation. The use of the FFT during demodulation had a profound effect on subchannel filtering and equalisation problems arising with the previous FDM systems. It was seen that all these processes were greatly simplified. By implementing 16QAM-OFDM in ultrasonic bands from 200 kHz to 399 kHz, a maximum

800 kb/s system data rate was achieved over ranges up to 0.7 m using a pair of prototype capacitive transducers with a HfO_2 high-k layer. Phase and amplitude noise were compensated using a pilot-aided estimation algorithm for correctly decoding OFDM signals. Good agreements were again found between the predictions of the simulation and the actual experimental signals. Different order baseband modulations from BPSK, QPSK and 16-QAM were also investigated using SensComp devices with subchannels from 55 kHz to 99 kHz. By using 16QAM-OFDM, a high bandwidth utility of 4 b/s/Hz was achieved at a data rate of 180 kb/s over ranges up to 6 m. Meanwhile, BPSK-OFDM experienced the lowest BER with the longest transmission range up to 11 m at 45 kb/s. In a dispersive environment with multipath reflections, OFDM was proved to be able to reduce system decoding errors by adding cyclic prefix, however, at the expense of wasting a certain amount of transmitted power and overall data rate. Aspects of this work have been published in [3–5].

In Chapter 4, data transmissions in non-line-of-sight conditions including reflections and diffractions were evaluated. For specular reflection, there was little signal energy drop when the incidence and reflection angles were the same so that successful signal decoding was retained. When the ultrasonic signal reflected from a soft and weakly reflective surface, most of the energy was absorbed, and the high-frequency channels were found to be more affected by the absorbent surface. BPSK-OFDM modulation was proven to return the best BER performance and high-frequency signals were prone to errors when the transducer centre normals were not coincident. For diffuse reflection, less signal energy was received compared with specular reflection, and BPSK-OFDM was again shown to be more robust than modulation methods with higher orders. The diffraction experiments also showed that the signal could still be correctly decoded when diffracted around a sharp-edged corner, however, with only a small amount of displacement. Low-order modulations at low frequen-

cies were better for signal transmission when diffraction occurred. Full-duplex communication with two pairs of transducers transmitting and receiving signals in opposite directions simultaneously was also investigated in Chapter 4. Transmissions with no measurable errors were achieved by splitting the frequency bands for forward and reverse signals at a data rate of 40 kb/s using recently-manufactured SensComp transducers, which had a different usable bandwidth when compared to those used in Chapter 2 and Chapter 3. To maintain connections for both outward and return links in the case when all high-frequency channels were corrupted, interleaved channel allocation was used. The corresponding experimental results indicated that the OFDM signals were more sensitive to ICI unless a larger channel spacing was used. Aspects of this work were published in [4].

An indoor data communication network with ceiling-mounted base stations and a mobile unit was investigated in Chapter 5. The wireless network was structured using hexagonal shapes to efficiently cover the service area. The separation of different base stations was set at a relatively small distance of 0.6 m to compensate the directionality of the ultrasonic beam from the SensComp transducers. An asynchronous positioning method was evaluated in the system using Gold code modulated signals, achieving ranging accuracy within 28.37 mm with a maximum update rate of 32.3 Hz. The location information of the mobile device was used to help optimise modulations within individual cells and seamless handover between neighbouring cells. Under the coverage of each cell base station, 16QAM-OFDM and QPSK-OFDM were used to transmit data at different transfer rates depending on different lateral displacements. The data signals were transmitted and received based on packets in every 31 ms, achieving downlink data rates from 18.7 kb/s to 37.4 kb/s and uplink data rates from 18.1 kb/s to 36.1 kb/s. A wall-mounted base station setup would have been a good alternative to cover a relatively larger area using a smaller number of

transducers. However, wide-angled or omnidirectional ultrasonic transducers would be needed to establish effective full-duplex communication links.

6.2 Future work

The ultrasonic data communication system described in this thesis was an operational prototype, and additional work will need to be undertaken before it can be deployed as part of a practical indoor communication network.

There exits an inherent lag from the PC to the arbitrary waveform generator as it takes a finite amount of time to upload the digitally modulated signals through a GPIB interface. This could possibly be replaced by a more efficient digital to analogue converter. Similar issues occur at the receiver side as there is a delay between the oscilloscope and the PC when reading the data, therefore this set up does not facilitate real-time data streaming.

Regarding the mobility and flexibility of the system, the physical size of the equipment needs to be reduced for practical use. Thus, programmable integrated circuit boards that function as modulator and demodulator could replace the bulky waveform generator and amplifiers. The sizes of both the SensComp and high-k transducers are relatively large especially as part of a portable mobile receiver. New designs or alternative transducers with small size while obtaining similar characteristics could be used. Both the transducers rely on a 200 V bias to drive the signal, therefore ultrasonic transducers powered by low-voltage batteries should be used for future systems. There are broadband CMUTs designed with 5 V [6] and zero [7] bias voltage operating in water at about 7 MHz. Unfortunately, no such capacitive ultrasonic transducer with adequate sensitivity has been reported in the literature for the operation in air. Therefore, the development and characterisation of new airborne ultrasonic transducers with low bias voltage for practical indoor data communication

would be another direction of future investigation.

It would be desirable to have omnidirectional [8] or wide-angle [9] ultrasonic transducers as transmitters in an indoor communication network so that a larger coverage area can be achieved with a smaller number of base stations. This can be done by using an external mirror or reflective cone to disperse the ultrasonic beam. Besides, multiple directional devices, suitably arranged to give omnidirectional coverage, have already been constructed and used in a 3D ultrasonic location system [10]. It is also beneficial to the signal reception as both the oblique angle and lateral displacement tolerance is increased when using such types of transducer as the receiver.

Finally, error control coding should be widely adopted to enable reliable delivery of digital data over unpredictable wireless channels. This would build a communication system that could automatically detect some of the decoding errors and reconstruct their original data for more robust performances, i.e. lower BER. Redundancies such as parity bits, checksums and cyclic redundancy checks (CRCs) are usually introduced into the data to be transmitted for error detection [11]. Once the errors are detected, the system conducts either a retransmission until the data can be verified or a recovery of the original data with the aid of an error-correcting code prior to transmission. The drawbacks of using error detection and correction schemes are the complexity of their implementation and the reduction of the information transmission rates as additional bits are added. Therefore, the tradeoffs between channel efficiency and system robustness should be realised.

6.3   References

[1] W. Jiang and W. M. D. Wright, "Wireless communication using ultrasound in air with parallel OOK channels," in *Proc. 24th IET Irish Signals Syst.*

Conf. (ISSC'13), pp. 1–6, Jun. 2013.

[2] W. Jiang and W. M. D. Wright, "Multichannel ultrasonic data communications in air using range-dependent modulation schemes," *IEEE Trans. Ultrason., Ferroelectr., Freq. Control*, vol. 63, pp. 147–155, Jan. 2016.

[3] W. Jiang and W. M. D. Wright, "Full-duplex airborne ultrasonic data communication using a pilot-aided QAM-OFDM modulation scheme," *IEEE Trans. Ultrason., Ferroelectr., Freq. Control*, vol. 63, pp. 1177–1185, Aug. 2016.

[4] W. Jiang and W. M. Wright, "Evaluation of multiple-channel OFDM based airborne ultrasonic communications," *Ultrasonics*, vol. 71, pp. 288 – 296, Sept. 2016.

[5] W. Jiang and W. M. D. Wright, "Indoor wireless communication using airborne ultrasound and OFDM methods," in *Proc. IEEE Int. Ultrason. Symp. (IUS)*, pp. 1–4, Sept. 2016.

[6] Y. S. Tien, P. C. Ku, F. Y. Lin, P. C. Li, L. H. Lu, P. L. Kuo, and W. C. Tian, "A low voltage CMOS-based capacitive micromachined ultrasonic sensors development," in *Proc. IEEE Sensors*, pp. 1–4, Oct. 2012.

[7] F. Y. Lin, W. C. Tian, and P. C. Li, "CMOS-based capacitive micromachined ultrasonic transducers operating without external dc bias," in *Proc. IEEE Int. Ultrason. Symp. (IUS)*, pp. 1420–1423, Jul. 2013.

[8] J. L. Ealo, A. R. Jimenez, F. Seco, C. Prieto, J. Roa, F. Ramos, and J. Guevara, "Broadband omnidirectional ultrasonic transducer for air ultrasound based on EMFi," in *Proc. IEEE Int. Ultrason. Symp. (IUS)*, pp. 812–815, Oct. 2006.

[9] W. Manthey, N. Kroemer, and V. Magori, "Ultrasonic transducers and transducer arrays for applications in air," *Meas. Sci. Technol.*, vol. 3, no. 3, pp. 249–261, 1992.

[10] A. Nishitani, Y. Nishida, and H. Mizoguch, "Omnidirectional ultrasonic location sensor," in *Proc. IEEE Sensors*, pp. 684–687, Oct. 2005.

[11] K. Prasad, *Principles of Digital Communication Systems and Computer Networks*. Hingham, MA, USA: Charles River Media, 2004.

Publications arising from the work in this thesis

[1] W. Jiang and W. M. D. Wright, "Wireless communication using ultrasound in air with parallel OOK channels," in *Proc. 24th IET Irish Signals Syst. Conf. (ISSC'13)*, pp. 1-6, Jun. 2013.

[2] W. Jiang and W. M. D. Wright, "Multichannel indoor wireless data communication using high-k capacitive ultrasonic transducers in air", in *Proc. IEEE Int. Ultrason. Symp. (IUS)*, pp. 1606-1609, Jul. 2013.

[3] W. Jiang and W. M. D. Wright, "Ultrasonic wireless communication in air using OFDM-OOK modulation", in *Proc. IEEE Int. Ultrason. Symp. (IUS)*, pp. 1025-1028, Sept. 2014.

[4] W. Jiang, "'Sound of silence': a secure indoor wireless ultrasonic communication system", *The Boolean*, pp. 38-42, Sept. 2014.

[5] W. Jiang and W. M. D. Wright, "Multichannel ultrasonic data communications in air using range-dependent modulation schemes", *IEEE Trans. Ultrason., Ferroelectr., Freq. Control*, vol. 63, pp. 147-155, Jan. 2016.

[6] W. Jiang and W. M. D. Wright, "Full-duplex airborne ultrasonic data communication using a pilot-aided QAM-OFDM modulation scheme", *IEEE Trans. Ultrason., Ferroelectr., Freq. Control*, vol. 63, pp. 1177-1185, Aug. 2016.

[7] W. Jiang and W. M. D. Wright, "Evaluation of multiple-channel OFDM based airborne ultrasonic communications", *Ultrasonics*, vol. 71, pp. 288-296, Sept. 2016.

[8] W. Jiang and W. M. D. Wright, "Progress in airborne ultrasonic data communications for indoor applications", in *Proc. IEEE Int. Conf. Ind. Inform. (INDIN)*, 2016.

[9] W. Jiang and W. M. D. Wright, "Indoor wireless communication using airborne ultrasound and OFDM methods", in *Proc. IEEE Int. Ultrason. Symp. (IUS)*, pp. 1-4, Sept. 2016.

[10] W. Jiang and W. M. D. Wright, "Indoor airborne ultrasonic wireless communication using OFDM methods", submitted for publication in *IEEE Trans. Ultrason., Ferroelectr., Freq. Control, Special Issue*, 2017.

[11] W. Jiang and W. M. D. Wright, "Indoor ultrasonic wireless communication network", to be submitted to *Ultrasonics*.

Appendix A

Equipment Specifications

Cooknell CA6/C charge amplifier

Input impedance	100 Ω above 10 kHz
Charge sensitivity	250 mV per pico-coulomb
Bandwidth	<10 kHz to >10 MHz
Maximum output level	1 V rms into 50 Ω
Series noise voltage generator	0.6 nV/Hz typical

Falco WMA-300 high voltage amplifier

Amplification	50×, fixed
Bandwidth	DC - 5 MHz @-3 dB
Slew rate	2000 V/μs typical
Delay time	140 ns input to output
Output voltage	-150 V to +150 V
Current	300 mA typical with limiter
Noise and offset	12 mV rms noise, 100 mV offset
Input impedance	50 Ω
Output impedance	50 Ω

PicoScope 6403A oscilloscope

Number of channels	4 (BNC connectors)
Bandwidth (-3 dB)	DC - 350 MHz
Rise time	1.0 ns
Voltage ranges	± 50 mV to ± 20 V
Sensitivity	10 mV/div
Input impedance	50 Ω
Timebases	10 ns/div to 1000 s/div
ADC resolution	8 bits
Maximum sampling rate	5 GS/s

SensComp series 600 environmental grade transducer

Transmitting sensitivity	110 dB min. at 50 kHz
Receiving sensitivity	-42 dB min. at 50 kHz
Distance range	0.15 to 10.7 m
Resolution	± 3 mm to 3 m
Suggested DC bias voltage	200 V
Suggested AC driving voltage	200 V peak

TTi TGA 12102 arbitary waveform generator

Waveform memory	1 M points/channel
Waveform length	8 to 1,048,576 points
Vertical resolution	12 bits (4096 levels)
Sample clock rate	0.1 Hz to 100 MHz
Output impedance	50 Ω
Amplitude range	5 mV to 20 Vpk-pk

Appendix B

Matlab$^{\text{TM}}$ program listings

Modulation and demodulation of multichannel OOK

```matlab
% Written by Wentao Jiang 2014
% Ultrasonics Research Group
% Univeristy College Cork

% Multichannel OOK modulation and demodulation

clear all

%%%%%%%%%%%%%
% Modulation %
%%%%%%%%%%%%%

% Number of subchannels
m=6;

% Number of bits per subchannel
n=8;

% Input data
datain=round(rand(1,m*n));

% Bit duration
t_bit=0.1e-3;

% Sampling frequency
fs=1e6;

% Generate baseband signal
amp=zeros(1,length(0:1/fs:m*n*t_bit-1/fs));
for i=1:m*n
    if datain(i)==1
        amp(1+(i-1)*fs*t_bit:i*fs*t_bit)=1;
    end
end

% Pulse shaping
% The order n must be even
b=firrcos(50,10e3,0,fs,'rolloff');
ps_amp=filtfilt(b,1,amp);

% Carrier frequency of the lowest subchannel
fc=50e3;
```

```matlab
% Channel spacing
fd=12e3;

% Generate passband signal
t=0:1/fs:t_bit*n-1/fs;
ook=zeros(1,length(t));
for i=1:m
    carrier=sin(2*pi*(fc+(i-1)*fd)*t);
    temp=ps_amp(1+(i-1)*n*fs*t_bit:n*i*fs*t_bit).*carrier;
    ook=ook+temp;
end

% Adding AWGN
snr=5;
nook=awgn(ook,snr,'measured');

%%%%%%%%%%%%%%%%
% Demodulation %
%%%%%%%%%%%%%%%%

% BPF window width
dif=6e3;

% Bandpass filtering
nook=[nook,zeros(1,2.5*t_bit*fs)];
fsig=zeros(1,m*length(t));
for i=1:m
    wn=[(fc+(i-1)*fd-dif)/(fs/2) (fc+(i-1)*fd+dif)/(fs/2)];
    [b,a]=butter(3,wn,'bandpass');
    temp=filtfilt(b,a,nook);
    temp=temp(1:length(t));
    fsig(1+(i-1)*length(t):i*length(t))=temp;
end

% Envelope detection
envelope=abs(hilbert(fsig));

% Normalised energy bar
for i=1:m*n
    amp(i)=sum(envelope(1+0.4*t_bit*fs+(i-1)*length(envelope)/(m*n)...
            :i*length(envelope)/(m*n)-0.4*t_bit*fs).^2);
end
maxamp=zeros(1,m);
for i=1:m
    maxamp(i)=max(amp(1+(i-1)*n:i*n));
end
for i=1:m
    nor(1+(i-1)*n:i*n)=amp(1+(i-1)*n:i*n)/maxamp(i);
end

% Decoding
for i=1:m
    data_out=zeros(1,n);
    for j=1:n
        if nor((i-1)*n+j)>0.28
            data_out(j)=1;
```

```
        end
    end
    dataout(1+(i-1)*n:(i-1)*n+n)=data_out;
end

% Display input and output binary bits
disp('Input:');
disp(datain);
disp('Output:');
disp(dataout);
```

Modulation and demodulation of multichannel BPSK

```
% Written by Wentao Jiang 2014
% Ultrasonics Research Group
% Univeristy College Cork

% Multichannel BPSK modulation and demodulation

clear all

%%%%%%%%%%%%%%
% Modulation %
%%%%%%%%%%%%%%

% Number of subchannels
m=6;

% Number of bits per subchannel
n=8;

% Input data
datain=round(rand(1,m*n));

% Bit duration
t_bit=0.1e-3;

% Sampling frequency
fs=1e6;

% Generate baseband signal
amp=ones(1,length(0:1/fs:m*n*t_bit-1/fs));
for i=1:m*n
    if datain(i)==0
        amp(1+(i-1)*fs*t_bit:i*fs*t_bit)=-1;
    end
end

% Pulse shaping
% The order n must be even
b=firrcos(50,10e3,0,fs,'rolloff');
ps_amp=filtfilt(b,1,amp);
```

```matlab
% Carrier frequency of the lowest subchannel
fc=50e3;

% Channel spacing
fd=12e3;

% Generate passband signal
t=0:1/fs:t_bit*n-1/fs;
bpsk=zeros(1,length(t));
for i=1:m
    carrier=sin(2*pi*(fc+(i-1)*fd)*t);
    temp=ps_amp(1+(i-1)*n*fs*t_bit:n*i*fs*t_bit).*carrier;
    bpsk=bpsk+temp;
end

% Adding AWGN
snr=5;
nbpsk=awgn(bpsk,snr,'measured');

%%%%%%%%%%%%%%%%
% Demodulation %
%%%%%%%%%%%%%%%%

% BPF window width
dif=6e3;

% Bandpass filtering
nbpsk=[nbpsk,zeros(1,2.5*t_bit*fs)];
fsig=zeros(m,length(t));
for i=1:m
    wn=[(fc+(i-1)*fd-dif)/(fs/2) (fc+(i-1)*fd+dif)/(fs/2)];
    [bb,aa]=butter(3,wn,'bandpass');
    temp=filtfilt(bb,aa,nbpsk);
    fsig(i,:)=temp(1:length(t));
end

% Coherent demodulation
dataout=zeros(1,m*n);
[b,a]=ellip(5,0.5,60,10e3/(fs/2));
for i=1:m
    carrier=sin(2*pi*(fc+(i-1)*fd)*t);
    coherent=carrier.*fsig(i,:);
    env=filtfilt(b,a,coherent);
    for j=1:n
        if env(round((j-0.5)*t_bit*fs))>0
            dataout((i-1)*n+j)=1;
        end
    end
end

% Display input and output binary bits
disp('Input:');
disp(datain);
disp('Output:');
disp(dataout);
```

190

Modulation and demodulation of 16QAM-OFDM

```matlab
% Written by Wentao Jiang 2015
% Ultrasonics Research Group
% Univeristy College Cork

% 16QAM-OFDM modulation and demodulation

clear all

%%%%%%%%%%%%
% Modulation %
%%%%%%%%%%%%%%

% Modulation order
M=4;

% Number of subcarriers
NumSubc=400;

% Generate random binary bits
msg=round(rand(1,M*NumSubc));

% Symbol mapping
constellation=[1+1i 1+3i 1-1i 1-3i 3+1i 3+3i 3-1i 3-3i -1+1i...
    -1+3i -1-1i -1-3i -3+1i -3+3i -3-1i -3-3i];
qam=[];
for j=1:M:length(msg)
    index=16-bi2de(fliplr(msg(j:j+3)));
    qam=[qam constellation(index)];
end

% Sampling frequency
fs=10e6;

% OFDM symbol time
Ts=1e-3;

% Carrier frequency of the lowest subchannel
fc=150e3;

% OFDM modulation
t=0:1/fs:Ts-1/fs;
K=fs*Ts;
Y=K*ifft(qam,K);
ofdm=Y.*exp(2*pi*1i*fc*t);

% Adding AWGN
snr=5;
nofdm=awgn(ofdm,snr,'measured');

%%%%%%%%%%%%%%%%
% Demodulation %
%%%%%%%%%%%%%%%%%
```

```matlab
% OFDM demodulation
rx=nofdm.*exp(-2*pi*1i*fc*t);
dk=fft(rx)/K;
demap=dk(1:NumSubc);
aa=real(demap);
bb=imag(demap);

% Demodulated OFDM symbol constellations
figure;
plot(real(constellation),imag(constellation),'.k','MarkerSize',12);
hold on
plot(aa,bb,'*k');
xlabel('In-Phase');
ylabel('Quadrature');
xlim([-5 5]);
ylim([-5 5]);
grid on

% Demapping
dataout=zeros(1,M*NumSubc);
for j=1:NumSubc
    if aa(j)>0&&aa(j)<2
        dataout(4*j-3:4*j-2)=[1 1];
    elseif aa(j)>2
        dataout(4*j-3:4*j-2)=[1 0];
    elseif aa(j)>-2&&aa(j)<0
        dataout(4*j-3:4*j-2)=[0 1];
    elseif aa(j)<-2
        dataout(4*j-3:4*j-2)=[0 0];
    end
end
for j=1:NumSubc
    if bb(j)>0&&bb(j)<2
        dataout(4*j-1:4*j)=[1 1];
    elseif bb(j)>2
        dataout(4*j-1:4*j)=[1 0];
    elseif bb(j)>-2&&bb(j)<0
        dataout(4*j-1:4*j)=[0 1];
    elseif bb(j)<-2
        dataout(4*j-1:4*j)=[0 0];
    end
end

% Display input and output binary bits
disp('Input:');
disp(msg);
disp('Output:');
disp(dataout);
```

Gold codes generation and their correlation properties

```matlab
% Written by Wentao Jiang 2016
% Ultrasonics Research Group
% Univeristy College Cork

% Gold codes generation and their correlation properties

clear all

%%%%%%%%%%%%%%%%%%%%%%%%%
% Gold codes generation %
%%%%%%%%%%%%%%%%%%%%%%%%%

% Characteristic polynomial of LFSR1
polyn1=[0 1 0 0 1];

% Define the length of the m-sequence
n=length(polyn1);
N=2^n-1;

% The seed of LFSR1
reg=[zeros(1,n-1) 1];

% Generate the first m-sequence
mseq1(1)=reg(n);
for i=2:N
    nreg(1)=mod(sum(polyn1.*reg),2);
    for j=2:n
        nreg(j)=reg(j-1);
    end
    reg=nreg;
    mseq1(i)=reg(n);
end

% Characteristic polynomial of LFSR2
polyn2=[0 1 1 1 1];

% Define the length of the m-sequence
n=length(polyn2);
N=2^n-1;

% The seed of LFSR2
reg=[zeros(1,n-2) 1 1];

% Generate the second m-sequence
mseq2(1)=reg(n);
for i=2:N
    nreg(1)=mod(sum(polyn2.*reg),2);
    for j=2:n
        nreg(j)=reg(j-1);
    end
    reg=nreg;
    mseq2(i)=reg(n);
end
```

```matlab
% Generate Gold codes
for shift_amount=0:N-1
    shift_mseq2=[mseq2(shift_amount+1:N) mseq2(1:shift_amount)];
    goldseq(shift_amount+1,:)=mod(mseq1+shift_mseq2,2);
end

%%%%%%%%%%%%%%%%%%%%%%%%%
% Correlation properties %
%%%%%%%%%%%%%%%%%%%%%%%%%

% Define sampling frequency and bit duration
fs=1e6;
t_bit=0.1e-3;
t=0:1/fs:t_bit*N-1/fs;

% NRZ encoder
g=zeros(N,round(N*t_bit*fs));
for i=1:N
    for j=1:N
        if goldseq(i,j)==1
            g(i,1+(j-1)*fs*t_bit:j*fs*t_bit)=1;
        elseif goldseq(i,j)==0
            g(i,1+(j-1)*fs*t_bit:j*fs*t_bit)=-1;
        end
    end
end

% Plot two Gold code sequences
figure;
subplot(4,2,[1 3]);
plot(t*1e3,g(8,:),'k','LineWidth',1);
xlim([0 3.1]);
ylim([-1.2 1.5]);
text(1,1.25,'Gold code #1');
ylabel('Amplitude');

subplot(4,2,[5 7]);
plot(t*1e3,g(4,:),'k','LineWidth',1);
xlim([0 3.1]);
ylim([-1.2 1.5]);
text(1,1.25,'Gold code #2');
xlabel('Time');
ylabel('Amplitude');

% NRZ encoder
gc=ones(N,N);
for i=1:N
    for j=1:N
        if goldseq(i,j)==0
            gc(i,j)=-1;
        end
    end
end

% Auto- and cross-correlation
```

```matlab
acr1=xcorr(gc(8,:),gc(8,:));
acr4=xcorr(gc(4,:),gc(4,:));
xcr=xcorr(gc(8,:),gc(4,:));

% Periodic cross-correlation
for i=1:2*N-1
    pxcr(i)=sum(gc(8,:).*gc(4,:));
    gc(8,:)=[gc(8,N) gc(8,1:N-1)];
end

% Plot the resultant curves
subplot(4,2,2);
plot(acr1,'k','LineWidth',1);
xlim([0 60]);
ylim([-12 35]);
title('Auto-correlation of Gold code #1');

subplot(4,2,4);
plot(xcr,'k','LineWidth',1);
xlim([0 60]);
ylim([-12 35]);
text(10,23,{'Cross-correlation of';'Gold code #1 and #2'});

subplot(4,2,6);
plot(pxcr,'k','LineWidth',1);
xlim([0 60]);
ylim([-12 35]);
text(10,23,{'Periodic cross-correlation of';'Gold code #1 and #2'});

subplot(4,2,8);
plot(acr4,'k','LineWidth',1);
xlim([0 60]);
ylim([-12 35]);
title('Auto-correlation of Gold code #2');
```